On the Emission Properties of Plasmonic Hybrid Systems and Polarimetric Spectroscopy of Planar Nanoantennas

DISSERTATION

der Mathematisch-Naturwissenschaftlichen Fakultät
der Eberhard Karls Universität Tübingen
zur Erlangung des Grades eines
Doktors der Naturwissenschaften
(Dr. rer. nat.)

vorgelegt von
Annika Mildner
aus Sigmaringen

Tübingen
2024

Gedruckt mit Genehmigung der Mathematisch-Naturwissenschaftlichen Fakultät der Eberhard Karls Universität Tübingen.

Tag der mündlichen Qualifikation:	31.10.2024
Dekan:	Prof. Dr. Thilo Stehle
1. Berichterstatterin:	Prof. Dr. Monika Fleischer
2. Berichterstatter:	Prof. Dr. Jannik Meyer

ABSTRACT

The umbrella term *plasmonics* describes a variety of phenomena, which are all dependent on the unique optical properties that arise when shrinking the dimensions of metals to the nanoscale.
Localized surface plasmon polaritons describe the interaction of light with collective oscillations of the free electron gas density in metal particles with sub-wavelength dimensions. The induced fluctuations of electric charges in turn lead to electromagnetic oscillations. The associated electromagnetic fields are strongly localized at the surfaces of the metallic nanostructures, even breaking the diffraction limit for the localization of light and therefore enabling strong field enhancements, compared with the excitation field. Additionally, plasmonic particles provide well-defined absorption and scattering cross sections, what makes them promising candidates in a variety of applications, such as in electro-optical devices or biosensing applications.
In this thesis, different plasmonic (hybrid) systems were investigated to study their optical properties in regards to enhancement effects and polarization dependencies.
To study the emission behavior of semiconductor nanocrystals bound to the apexes of resonantly-tuned plasmonic nanocones, hybrid systems consisting of CdSe/ZnS quantum dots and gold nanocones were fabricated. The system, and also its individual components, were investigated optically using dark-field scattering spectroscopy and confocal photoluminescence spectroscopy. (In cooperation with the group of Prof. A. Meixner, University of Tübingen.)
In a subsequent project, a similar hybrid system was incorporated into a metal-dielectric bullseye nanoantenna device, to pave the way towards ultra-bright single photon sources. The nanocone therein acts as a plasmonic resonator responsible for the Purcell enhancement and the bullseye structure as an optical Bragg grating for emission redirection. (In cooperation with the group of Prof. R. Rapaport, University of Jerusalem.)
In the last part of the thesis, the scattered far fields of different plasmonic nanostructures were investigated for their degree of optical chirality. Therefore, planar achiral gold nanorectangles and chiral rhomboids were investigated with a modified dark-field scattering spectroscopy set-up allowing for polarized excitation and subsequent analyzation of the scattered light. The polarization was extracted for each wavelength individually and the results compared to numerical simulations of the near and far field. Furthermore, a method was presented to extract the full set of Stokes parameters from the experimental data and compared to the ones obtained from simulations.

Finally, an analytical model was developed to describe the interplay of two or more spectrally overlapping plasmonic modes within an individual nanostructure. Comparison of measurement, simulation and analytical model showed an excellent accordance and, moreover, it could be shown that even achiral nanostructures can exhibit chiral far fields.

ZUSAMMENFASSUNG

Der Überbegriff Plasmonik beschreibt eine Vielzahl an Phänomenen, welche von den einzigartigen optischen Eigenschaften abhängig sind, die auftreten, wenn man die Größe von Metallen auf Dimensionen auf der Nanometerskala schrumpft. Lokalisierte Oberflächenplasmon-Polaritonen beschreiben die Wechselwirkung von Licht mit kollektiven Oszillationen der freien Elektronengasdichte in Metallpartikeln, die kleiner sind als die Wellenlänge des Lichts. Die induzierten Fluktuationen der elektrischen Ladungen wiederum führen zu elektromagnetischen Oszillationen. Die zugehörigen elektromagnetischen Felder sind stark an den Oberflächen der metallischen Nanostrukturen lokalisiert, sogar bis unterhalb der Beugungsgrenze von Licht. Daher ermöglichen sie im Vergleich zum anregenden Lichtfeld hohe Feldverstärkungen. Zusätzlich weisen plasmonische Partikel wohldefinierte Absorptions- und Streuquerschnitte auf, was sie zu vielversprechenden Kandidaten für vielfältige Einsatzmöglichkeiten macht, beispielsweise in elektrooptischen Bauteilen oder in biosensorischen Anwendungen.
In dieser Arbeit wurden verschiedene plasmonische (Hybrid-)Systeme analysiert, um ihre optischen Eigenschaften in Hinblick auf Verstärkungseffekte und Polarisationsabhängigkeiten zu untersuchen.
Um das Emissionsverhalten von Halbleiter-Nanokristallen zu ermitteln, welche an die Spitzen von resonant-gestimmten plasmonischen Nanokegeln gebunden wurden, wurden Hybrid-Systeme aus CdSe/ZnS Quantendots und Gold-Nanokegeln hergestellt. Sowohl die Systeme im Gesamten, als auch ihre einzelnen Komponenten wurden mittels Dunkelfeld-Spektroskopie und konfokaler Photolumineszenz-Spektroskopie optisch untersucht. (In Kooperation mit der Arbeitsgruppe von Prof. A. Meixner, Universität Tübingen.)
In einem nachfolgenden Projekt wurde ein ähnliches Hybrid-System in eine metallisch-dielektrische Bullseye Nanoantennenstruktur integriert, mit dem Ziel, den Weg zu ebnen für die Entwicklung besonders heller Einzelphotonenquellen. Der Nanokegel dient darin als plasmonischer Resonator, welcher für die Purcell-Verstärkung verantwortlich ist. Die Bullseyestruktur dient als optisches Bragg-Gitter, welches die Emission gezielt ausrichtet. (In Kooperation mit der Arbeitsgruppe von Prof. R. Rapaport, Universität Jerusalem.)

Im letzten Teil der Arbeit wurden die gestreuten Fernfelder verschiedener plasmonischer Nanostrukturen auf ihre optische Chiralität hin untersucht. Dafür wurden planare, achirale Gold-Nanorechtecke und chirale Rhomboide mit einem modifizierten Dunkelfeld-Spektroskopie-Aufbau untersucht. Dieser ermöglicht eine polarisierte Anregung und anschließende Analyse der gestreuten Lichtfelder. Die Polarisation wurde für jede Wellenlänge einzeln bestimmt und die Ergebnisse mit numerischen Simulationen des Nah- und Fernfeldes verglichen. Des Weiteren wurde eine Methode präsentiert, um den vollständigen Satz an Stokes-Parametern aus den experimentellen Daten zu bestimmen. Dieser wurde anschließend mit den Ergebnissen aus Simulationen verglichen. Abschließend wurde ein analytisches Model entwickelt, um das Zusammenspiel zweier oder mehrerer spektral überlappender plasmonischer Moden einer einzelnen Nanostruktur zu beschreiben. Der Vergleich zwischen Messung, Simulation und analytischem Modell zeigte eine herausragende Übereinstimmung und es konnte außerdem gezeigt werden, dass auch achirale Strukturen chirale Fernfelder aufweisen können.

CONTENTS

ACRONYMS

ND	Neutral density filter
NA	Numerical aperture
BFP	Back focal plane
RPM	Radially polarized mode
APM	Azimuthally polarized mode
APD	Avalanche photo diode
TCSPC	Time-correlated single photon counter
EBL	Electron beam lithography
ITO	Indium tin oxide
MIBK	Methyl isobutyl ketone
IPA	Isopropanol
PMMA	Polymethyl methacrylate
SEM	Scanning electron microscopy
AFM	Atomic force microscope
3-MPA	3-mercaptopropionic acid
HUJI	Hebrew University of Jerusalem, Israel
TM	Transverse magnetic
TE	Transverse electric
SNOM	Scanning near-field optical microscopy

1 INTRODUCTION

When firstly starting literature research on the field of *plasmonics* by going through scientific publications or other kinds of articles, e.g. in a popular scientific way or press releases, one might stumble across articles with titles such as "Why gold nanoparticles are more precious than pretty gold: Noble metal surface plasmon resonance and its enhancement of the radiative and nonradiative properties of nanocrystals of different shapes" [1], "Better living through plasmonics" [2] or "Applying plasmonics to a sustainable future: Plasmonics technologies may form components of a future clean and sustainable society" [3]. At first glance, the topic seems to be greatly exaggerated, yet raises highest expectations. By going down the rabbit hole, one can actually find that the implications are not as far-fetched as it might seem, as plasmonics is in the focus of a variety of scientific fields. Plasmonic materials offer a variety of versatile properties, such as their high optical tunability, or their unique ability to concentrate light into volumes on the nanometer scale, thus resulting in strong electric fields, highly energetic hot-electron generation and local heating effects, which can be exploited to manipulate, push or intensify interactions with their surroundings.

As is indicated in one of the articles above, plasmonic particles play an important role in energy related applications. They are implemented in many different manifestations in electro-optical devices [4], e.g. to enhance the efficiency of solar cells [5–8], but also as catalysts in water splitting approaches for hydrogen generation [9–11] or to reduce carbon dioxide into methanol and water [12–14]. The photocatalytic effect can also be exploited for water purification [15] or pollution detection [16]. Plasmonics also makes up an essential part in biomedical applications, as is reviewed for example in "The golden age: gold nanoparticles for biomedicine" [17] and many others [18–20]. Plasmonic nanoparticles are deployed, e.g. in *in vitro* diagnostics [21], where they are extensively used in lateral flow assay configurations. The most popular examples for such applications are probably Corona virus rapid tests, pregnancy tests or diabetic glucose meters [22], in which gold nanoparticles serve as highly visible optical indicators. The strongly enhanced optical properties of gold nanoparticles are also used in *in vivo* imaging applications, for example in cancer diagnostics, where the ligand shells of the deployed particles are modified with the respective (anti-)antibodies to specifically bind to cancerous cells [23] and facilitate detectability. However, plasmonic particles are not only useful in diagnostics, but also for therapeutic purposes, for example

in photothermal therapy or for drug delivery applications [24].
Many researchers pursue the search for new plasmonic materials and arrangements, to expand their usability to the terahertz regime, e.g. for facilitating telecommunication applications [25], such as components for signal conversion, i.e. to convert wireless telecommunication signals to the optical frequency domain [26–28] or integrated plasmonic circuits [29].
Another communication-related research topic including plasmonics is the rapidly growing field of quantum technologies [30], including efforts on quantum cryptography applications [31, 32]. An essential component in the development of quantum photonic applications are *on-demand*, deterministic single photon sources with fast operation speeds, high photonic emission rates and a well-defined polarization of the emitted single photons. Recent progress on the development of such sources includes, e.g. multiplexed sources, which are 'based on multiplexing multiple probabilistic photon-creation events' [33] or sources that are based on nonlinear frequency conversion in nonlinear crystals [34, 35]. Other approaches to develop (deterministic) single photon sources rely on the radiative properties of single emitters, e.g. atoms, molecules or semiconductor quantum dots, i.e. depend on the spontaneous emission from a two-level energy system [36, 37].

As set out above, plasmonic nanostructures play a key role in many different fields of science and in an enormous number of applications. The work presented in this thesis joins the ranks of research concerning fundamental questions, but also demonstrates an approach to combine different fundamental studies and takes the path towards the development of an application.
In this thesis, different plasmonic (hybrid) systems were investigated theoretically with the help of numerical simulations, and also experimentally, using different spectroscopy and imaging techniques. The term hybrid system herein denotes the combination of a plasmonic metal nanostructure with a colloidal semiconductor nanocrystal.
In the first place, hybrid systems consisting of three-dimensional gold nanocones and colloidal CdSe/ZnS quantum dots, bound to the apexes of the nanocones, were fabricated. This was done using standard nanofabrication techniques, i.e. electron beam lithography and a thermal evaporation process, and a self-aligned attachment process for the precise positioning of the quantum emitters. In cooperation with the group of Prof. A. Meixner from the Institute of Physical and Theoretical Chemistry, these hybrid structures were then characterized optically using dark-field scattering spectroscopy and confocal photoluminescence spectroscopy, to study the altered emission behavior and enhanced fluorescence of quantum emitters in the vicinity of photonic structures. The ability of metallic nanoparticles to enhance luminescence signals of fluorescent molecules has been known for

decades [38, 39], yet it is still topic of contemporary research, as the control over light emission is an enabling tool in technological application developments [40]. However, the mechanisms involved in the altered optical properties and the dependencies on geometrical parameters need to be identified and understood beforehand, to be able to efficiently make use of the described phenomenon.
The conical geometry of the nanostructures in this work was chosen for their strong ability to generate highly localized and enhanced near fields at their tips when illuminated with light and also the advantageous accessibility of the hot spots due to the three-dimensional geometry. With the applied attachment process, many hybrid structures can be fabricated in a single manufacturing step, which enables statistics on the investigated systems. The main results of this study can be condensed to the message, that the photoluminescence signals of the investigated quantum emitters were found to be enhanced compared to a reference quantum dot on a dielectric glass substrate, as their radiative lifetimes were found to be drastically decreased when coupled to a plasmonic nanocone, and also changes in their fluorescence intermittency behavior could be observed.
In a subsequent project, in cooperation with the group of Prof. R. Rapaport at the Hebrew University of Jerusalem, the concept was adapted, and a similar structure, consisting of nanocone and quantum dot, was implemented in an optical bullseye nanoantenna, for the simultaneous modification of the emission rate and emission directionality, respectively.
The investigated kind of nanostructure contributes to application-oriented research, as it faces some obstacles, currently arising during the development of nanocrystal-based single photon sources. For colloidal quantum dots, the radiative lifetime of such emitters is usually on the order of several to hundreds of nanoseconds in the absence of any photonic cavity. The photon emission rates are therefore initially limited intrinsically and as emission is usually also isotropic, the performance might be lowered, leading to severe restrictions in terms of usability. However, engineering both decay rate and emission directionality simultaneously is no trivial task, as it is quite challenging to combine high quality factors and large mode volumes at envisaged room-temperature operation [41]. The composite structure investigated here presents a solution to this trade-off, as the nanocone acts as a plasmonic resonator, which enhances the emission rate of the quantum emitter at the tip, and the circular Bragg grating redirects the emission in the out-of-plane direction. A high directivity of the emission leads in turn to a high collection efficiency of the emitted photons and minimizes losses. The functionality of the device was investigated with several optical experiments, and a Purcell factor of 20 could be demonstrated alongside extraordinary directionality of the emitted photons, resulting in projected photon rates approaching

the GHz regime.

Apart from single photon sources, also other photonic devices, so-called metamaterials or metasurfaces, offer potential for quantum cryptographic applications. They are also highly investigated in contemporary research, as they offer a broad range of novel approaches for the generation, manipulation and detection of classical light [31, 42, 43]. Metasurfaces, which are in general composed of specifically designed planar nanostructures arranged in so-called sub-wavelength unit cells, have shown to be ideally suited for polarization control applications [44, 45].

Another polarization related topic is the extensive topic of chiral plasmonics [46–48], which also plays a major role in biosensing applications, due to the varying sensitivity of some specimens to light fields with different handedness [49]. In contrast, some research also focuses on the investigation of light emitted from such chiral nanostructures. While the emergence of chiral far-field signals, however, is often associated with geometrically chiral nanostructures, the occurrence of chiral near fields also in achiral nanostructures has been demonstrated and is widely accepted [50–52].

In the last part of this thesis, single achiral planar gold nanorectangles were investigated using dark-field scattering spectroscopy with linearly polarized white light for excitation. A cross-like aperture was invented to maintain the linear polarization even for illumination with a dark-field condenser. Thus, for different incoming linear polarizations, the detected signals were analyzed and the polarization extracted for each wavelength. Depending on the orientation of the incoming polarization, also circular polarization could be demonstrated. Numerical simulations were performed, regarding the near field as well as the far field, to support the experimental findings and their interpretation. It could be shown through simulations that, as expected, the near fields surrounding the achiral nanostructure show chiral features and that the degree of circular polarization in the scattered far fields is already determined in the near field. A method to extract the full set of Stokes parameters from the experimental data was presented and compared to the ones extracted from simulations. According to literature [53], the third Stokes parameter is proportional to the chirality flux from the near field to the far field. It could be demonstrated both experimentally and theoretically, that achiral structures can exhibit chiral far-field signals if the nanostructure has two or more excitable and overlapping plasmonic modes. Finally, an analytical model could be developed to describe the interaction of the dipolar modes within the nanostructure. The validity was also tested in additional measurements on chiral planar nanostructures with increasing degree of geometrical chirality. Again, a remarkable correspondence between simulation, model and measurement could

be demonstrated.

The presented thesis is structured as follows: in a first chapter, fundamental physical concepts are introduced, such as Maxwell's equations or the Drude-Lorentz model to describe the dielectric function of gold, alongside with relevant information on the different components crucial for the understanding and interpretation of the results. In a second chapter, the experimental methods are presented, that were used to fabricate and characterize the samples. This includes details on different fabrication processes, but also detailed descriptions of the different optical set-ups that were used in different experiments. Also, a short introduction into the used numerical simulation software is given. The experimental results are finally presented alongside numerical simulations, and subsequently discussed in a third chapter, before the work closes with a summary and outlook.

2

BASIC THEORY

2.1 PLASMONICS

The field of *plasmonics* forms a major branch of *nanophotonics*, and fundamentally explores the interaction of electromagnetic waves with metallic surfaces or metallic particles with dimensions on the order of or even smaller than the wavelength of the incoming light fields.
A *plasmon* therein denotes a quantum of plasma oscillation, and can be interpreted as a quasi-particle, in analogy to phonons, which describe quantizations of mechanical vibrations. Upon compliance of some boundary conditions, dependent on material and its manifestation, a plasmon can couple to photons at optical frequencies and form another quasi-particle, namely a plasmon polariton. For the sake of simplification, the term *plasmon* is used throughout this thesis, even when speaking of plasmon polaritons.
In a classical picture, a plasmon can be described as an oscillation of the free electron gas density in a carrier material, and most of its properties can be derived directly from Maxwell's equations, as will be shortly recapped in the following. The reviews and explanations given in this section mostly rely on the textbooks [54–58], to which it shall also be referred for deeper insights.

2.1.1 *Maxwell's Equations*

The macroscopic Maxwell equations describe electromagnetic phenomena in the presence of matter, and are of the following form:

$$\nabla \cdot \vec{D} = \rho_{ext} \tag{2.1}$$

$$\nabla \cdot \vec{B} = 0 \tag{2.2}$$

$$\nabla \times \vec{E} = -\frac{\partial \vec{B}}{\partial t} \tag{2.3}$$

$$\nabla \times \vec{H} = \vec{J}_{ext} + \frac{\partial \vec{D}}{\partial t} \quad . \tag{2.4}$$

Therein, $\vec{D}$ denotes the dielectric displacement, and ρ_{ext} the external charge density. $\vec{B}$ is the magnetic induction, $\vec{E}$ and $\vec{H}$ denote the electric and magnetic fields, and $\vec{J}_{ext}$ is the current density. Fundamental interactions between the charged particles inside the medium and external electromagnetic fields are not taken into account, since the microscopic responses are averaged over large distances, resulting in

a macroscopic polarization $\vec{P}$ and magnetization $\vec{M}$. Those in turn are linked to the four macroscopic fields via

$$\vec{D} = \varepsilon_0 \vec{E} + \vec{P} \tag{2.5}$$

$$\vec{H} = \frac{1}{\mu_0}\vec{B} - \vec{M} \ , \tag{2.6}$$

where ε_0 denotes the electric permittivity and μ_0 the magnetic permeability of vacuum, respectively.
Since only non-magnetic media are part of this thesis, magnetic responses can be neglected and further discussions are therefore limited to electric polarization effects. The polarization $\vec{P}$ describes the averaged electric dipole moment per unit volume inside the medium, which is due to the alignment of microscopic dipoles with the electric field. It is therefore related to the internal charge density ρ via $\nabla \cdot \vec{P} = -\rho$, and conservation of charge ($\nabla \cdot \vec{J} = -\frac{\partial \rho}{\partial t}$) links the polarization to the current density via

$$\vec{J} = \frac{\partial \vec{P}}{\partial t} \ , \tag{2.7}$$

which can be interpreted in such a way that all polarization effects are included in the macroscopic electric field.
In conclusion, Maxwell's equations define the fields that are generated by currents and charges in a medium, yet they do not describe the origin of these quantities. In order to find a self-consistent solution for the electromagnetic fields, Maxwell's equations are accompanied by a set of constitutive relations that describe the behavior of matter under the influence of the fields. For linear, isotropic and non-magnetic media, one can relate the dielectric displacement to the electric fields and the magnetic induction to the magnetic fields via

$$\vec{D} = \varepsilon_0 \varepsilon \vec{E} \tag{2.8}$$

$$\vec{B} = \mu_0 \mu \vec{H} \ , \tag{2.9}$$

$\mu = 1$ for non-magnetic media

where ε is the relative permittivity and μ is the relative permeability of the medium.
The polarization is often also linked to the electric fields via the linear relationship

$$\vec{P} = \varepsilon_0 \chi \vec{E} \tag{2.10}$$

with the dielectric susceptibility χ, from which it can be concluded that $\varepsilon = 1 + \chi$ (by inserting equations 2.5 and 2.10 in 2.8).
It remains to be noted that the internal current density $\vec{J}$ is also linked to the electric field $\vec{E}$ via the conductivity σ according to

$$\vec{J} = \sigma \vec{E} \ . \tag{2.11}$$

2.1.1.1 *Time-Harmonic Fields*

In general conception, one often deals with monochromatic light excitations, i.e. electromagnetic fields oscillating with a single frequency ω. Such monochromatic electromagnetic fields in a linear medium can be written as

$$\vec{E}(\vec{r},t) = \Re\Big(\vec{E}(\vec{r})\exp(-i\omega t)\Big),\ \vec{B}(\vec{r},t) = \Re\Big(\vec{B}(\vec{r})\exp(-i\omega t)\Big)\ .$$

Here, $\vec{E}(\vec{r},t)$ and $\vec{B}(\vec{r},t)$ are real, while $\vec{E}(\vec{r})$ and $\vec{B}(\vec{r})$ denote complex amplitudes. In a majority of literature, the symbol $\vec{E}$ ($\vec{B}$) is used for both, the real, time-dependent electric (magnetic) field but also for the complex spatial part, yet it is always stated whether real fields are considered in the time domain or time-harmonic fields are used.
However, for time-harmonic fields and a linear medium, Maxwell's equations can be written as

$$\nabla\cdot\varepsilon\vec{E} = \rho \tag{2.12}$$
$$\nabla\times\vec{E} = i\omega\vec{B} \tag{2.13}$$
$$\nabla\cdot\vec{B} = 0 \tag{2.14}$$
$$\nabla\times\frac{1}{\mu}\vec{B} = \vec{J} - i\omega\varepsilon\vec{E}\ . \tag{2.15}$$

2.1.2 *Dielectric Function in Metals*

The simplest form to describe and explain the optical properties of metals is with the use of a *plasma model*, namely the *Drude model*, in which a gas of free electrons moves against a fixed background of positively charged ion cores. The model gives reasonable results over a wide frequency range, yet its validity is limited as interband transitions are not incorporated in this approach, even though they may occur at visible frequencies. For gold, the threshold energy for interband transitions is about $\sim 2.38\,\mathrm{eV}$ [59], i.e. already occurs for wavelengths $< 520\,\mathrm{nm}$. For a more apt description, the Drude model needs to be supplemented by an extended approach, which is given by the *Drude-Lorentz model*, in which interband transitions are considered by using the classical picture of a bound electron.

Bound electrons in metals can be found e.g. in lower-lying shells of the atoms.

An electron of the free electron gas in a metal can be described by solving the equation of motion for a driven oscillator according to

$$m_e\ddot{x} + m_e\gamma\dot{x} = eE(t)\ , \tag{2.16}$$

where e is the charge and m_e the effective mass of the free electrons. The problem can be considered in one dimension without loss of generality. The damping term γ is proportional to the Fermi velocity v_F divided by the mean free path l between scattering events. As driving source, a time-harmonic electric field $E = E_0\exp(-i\omega t)$ is

assumed with amplitude E_0 and frequency ω. After some initial time, the system oscillates with the same frequency ω, which leads to

$$-\omega^2 x = i\gamma\omega x + \frac{eE_0}{m_e} \ , \tag{2.17}$$

where the common exponential terms have been cancelled. The displacement can thus be written as

$$x = \frac{e}{m_e}\frac{1}{\omega^2 - i\gamma\omega}E_0 \ , \tag{2.18}$$

and is governed by the damping constant γ and the amplitude of the driving field E_0. By assuming that a displacement x leads to a dipole moment $p = ex$, the polarization P can be calculated and is given by

$$P = nex = \frac{ne^2}{m_e}\frac{1}{\omega^2 - i\gamma\omega}E_0 = \varepsilon_0\chi E_0 \ , \tag{2.19}$$

where n is the density of oscillators. The right-hand side of the equation above shows the relation between polarization P and electric susceptibility χ as given in equation 2.10. By using $\varepsilon = 1 + \chi$, an expression for the permittivity of the free electron gas density can be obtained according to

$$\varepsilon(\omega) = 1 - \frac{\omega_p^2}{\omega^2 + i\gamma\omega} \ , \tag{2.20}$$

where $\omega_p = \sqrt{\frac{ne^2}{\varepsilon_0 m_e}}$ denotes the volume plasma frequency. This expression can be separated into its real and imaginary parts according to

$$\varepsilon_1(\omega) = 1 - \frac{\omega_p^2}{\omega^2 + \gamma^2} \tag{2.21}$$

$$\varepsilon_2(\omega) = \frac{\gamma\omega_p^2}{\omega(\omega^2 + \gamma^2)} \ . \tag{2.22}$$

Here, it shall be noted that the real part of the dielectric constant is negative. As a consequence, metals can be penetrated only to a very small amount, since the refractive index is a complex quantity given by $n = \sqrt{\varepsilon}$, and a strong imaginary part denotes strong absorption.

Figure 2.1 shows the experimental data of the permittivity of gold from Johnson and Christy [61] together with the Drude model. While for wavelengths above 650 nm the thereof obtained expression 2.20 models the experimental data quite satisfactorily, the deviations below 650 nm are clearly unacceptable. As mentioned before, for higher frequencies the contributions of interband transitions need to be taken into account by extending the equation of motion for a bound electron. Similar to before, the description is therefore based on a driven and damped harmonic oscillator model, in which two oppositely charged

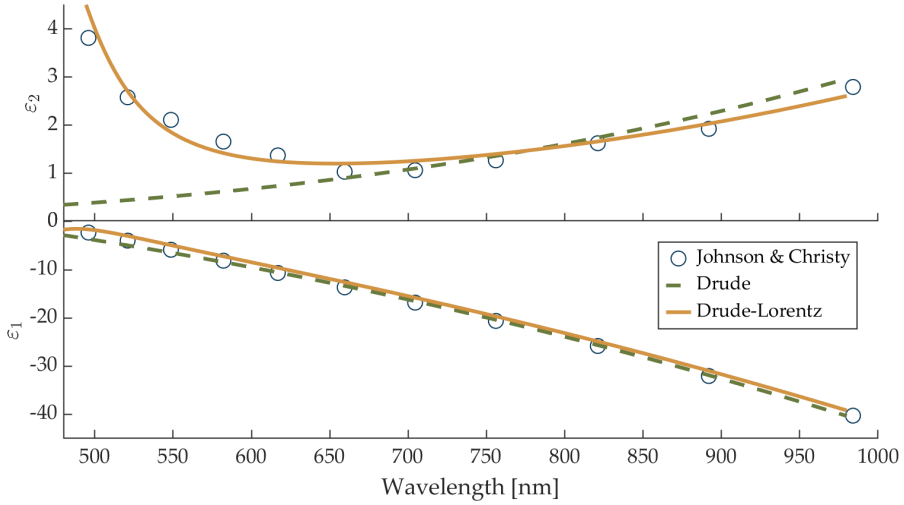

Figure 2.1: Real and imaginary part of the permittivity of gold. The dots show the experimental data obtained from Johnson and Christy, while the green dashed line shows the Drude model and the solid line the Drude-Lorentz model. The values used in the calculation of the models were obtained from [60].

particles are connected with a spring that holds the electron in place. This can be described according to

$$m\ddot{x} + m\gamma\dot{x} + \alpha x = eE(t) \quad , \tag{2.23}$$

where m denotes the effective mass of the bound electrons, γ is the damping and α is the spring constant. By choosing a similar ansatz as before, the contribution of the bound electrons to the dielectric function is found to be

$$\varepsilon_{Interband}(\omega) = 1 + \frac{\tilde{\omega}_p^2}{(\omega_0^2 - \omega^2) - i\gamma\omega} \quad , \tag{2.24}$$

where $\tilde{\omega}_p = \sqrt{\frac{\tilde{n}e^2}{\varepsilon_0 m}}$ is introduced in analogy to the plasma frequency and with $\tilde{n}$ being the density of the bound electrons. $\omega_0 = \sqrt{\frac{\alpha}{m}}$ denotes the resonance frequency. Consequently, the obtained expression can again be separated into its real and imaginary part, and the according terms show the typical resonance behavior of a harmonic oscillator, as it is graphically depicted in Figure 2.2. While the imaginary part shows a resonance peak at ω_0 and is associated with losses, the real part shows a dispersive behavior, which describes how the oscillator follows the driving field.

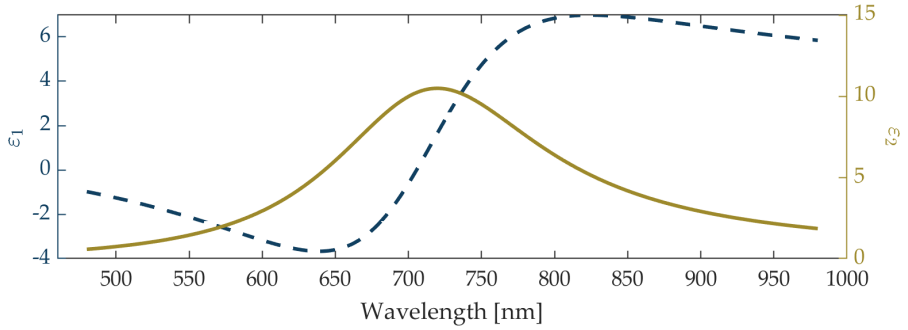

Figure 2.2: Real and imaginary part of the dielectric function for bound electrons. The imaginary part shows a resonance peak and is associated with losses, while the real part shows a dispersive behavior.

2.1.3 *Particle Plasmons*

The optical properties of metals under the influence of an external electromagnetic field have been discussed in the previous section. As has been mentioned before, an incoming electromagnetic wave can excite different kinds of plasmons, i.e. oscillations of the electron plasma in the considered material. One distinguishes between three kinds of plasmonic excitations, i.e. volume plasmons in bulk material [62], propagating surface plasmons at interfaces between a dielectric and a metal [63] and localized, i.e. *non-propagating* surface plasmons in *small* particles [55]. The latest kind is of interest in this thesis and is therefore discussed in more detail in the following.
If a small metallic nanoparticle, i.e. with dimensions much smaller than the wavelength of the incoming light, is irradiated with an oscillating electromagnetic field, oscillations of the free electron gas density can be excited inside the particle. These oscillations lead to a separation of charge carriers at the particle boundary, which in turn exerts a restoring force on the driven electrons, so that a resonance can arise. When excited at resonance, a strong dipole moment is induced, therefore leading to highly enhanced fields both inside and, close to the surface, also outside the particle. The situation is graphically depicted on the left-hand side in Figure 2.3[1], showing the influence of an incoming electromagnetic wave on the surface charge distribution of a sub-wavelength-sized spherical nanoparticle (not to scale). The image on the right-hand side shows the distribution of the amplification of the electric field intensity at the resonance wavelength in the near-field zone.

1 The Scientific color map *batlow* [64] is used throughout this thesis to prevent visual distortion of the data and exclusion of readers with color-vision deficiencies [65].

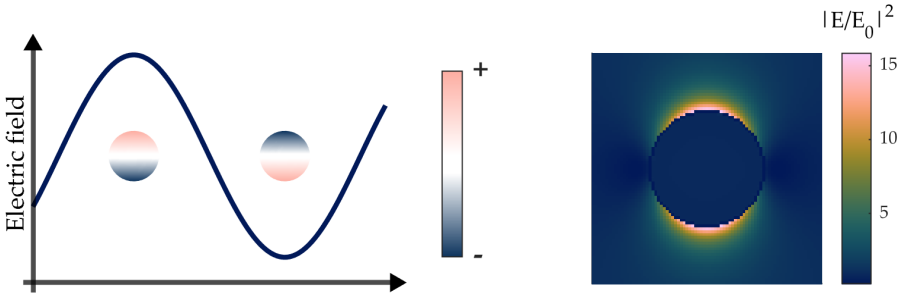

Figure 2.3: Excitation scheme of localized surface plasmons (left) and near-field intensity enhancement (right) for a spherical nanoparticle

2.1.3.1 *Quasi-Static Approximation*

The exemplarily chosen nanosphere offers an additional advantage, as the simple geometry allows for an analytical treatment to find a resonance condition in the *quasi-static approximation*. To make use of the quasi-static approximation, the diameter of the nanosphere is required to be much smaller than the wavelength of the incoming light ($d \ll \lambda$), so that the harmonically oscillating electromagnetic field can be considered constant over the particle volume. In this case, the problem can be simplified to a homogeneous, isotropic sphere surrounded by an isotropic and non-absorbing medium in a uniform, static electric field. As the electric field distribution is of interest, one needs to find a solution to the *Laplace equation* for the potential $\nabla^2\Phi = 0$, from which the electric field can then be calculated according to $\vec{E} = -\nabla\Phi$. Detailed calculations on the problem can be found in literature [54], here the results shall be shortly discussed.
The potential outside the sphere is found to be

$$\Phi_{out} = -E_0 r\cos\theta + \frac{\varepsilon - \varepsilon_m}{\varepsilon + 2\varepsilon_m} E_0 a^3 \frac{\cos\theta}{r^2} \quad , \tag{2.25}$$

which describes the superposition of the applied field with amplitude E_0 and that of a dipole located at the center of the sphere with radius a. The dielectric function of the particle's medium is given by ε, and ε_m denotes the dielectric constant of the surrounding medium.
By introducing the dipole moment $\vec{p}$, equation 2.25 can be rewritten as

$$\Phi_{out} = -E_0 r\cos\theta + \frac{\vec{p}\cdot\vec{r}}{4\pi\varepsilon_0\varepsilon_m r^3} \tag{2.26}$$

$$\vec{p} = 4\pi\varepsilon_0\varepsilon_m a^3 \frac{\varepsilon - \varepsilon_m}{\varepsilon + 2\varepsilon_m}\vec{E}_0 \quad , \tag{2.27}$$

which shows that an applied external field induces a dipole moment inside the sphere and its strength is proportional to $|\vec{E}_0|$. The dipole moment in turn can be rewritten as $\vec{p} = \varepsilon_0\varepsilon_m\alpha\vec{E}_0$ by introducing the complex polarizability α according to

$$\alpha = 4\pi a^3 \frac{\varepsilon - \varepsilon_m}{\varepsilon + 2\varepsilon_m} \quad . \tag{2.28}$$

From equation 2.28 it becomes clear that, e.g. for gold, the polarizability shows a resonant enhancement if the *Fröhlich condition* is met, i.e. the denominator is $\varepsilon + 2\varepsilon_m \to 0$ and therefore $\Re(\varepsilon(\omega)) = -2\varepsilon_m$. Consequently, the associated mode is the dipole surface plasmon of the metallic nanosphere. Moreover, equation 2.28 further shows the strong dependence of the resonance frequency on the dielectric constant of the environment. If ε_m increases, the resonance experiences a red shift. The occurrence of a resonance in the polarizability also implies that the electric fields (both inside and outside the particle), obtained from the potentials via $\vec{E} = -\nabla\Phi$, show a resonant enhancement.

$$\vec{E}_{in} = \frac{3\varepsilon_m}{\varepsilon + 2\varepsilon_m}\vec{E}_0 \tag{2.29}$$

$$\vec{E}_{out} = \vec{E}_0 + \frac{3\vec{n}(\vec{n}\cdot\vec{p}) - \vec{p}}{4\pi\varepsilon_0\varepsilon_m}\frac{1}{r^3} \tag{2.30}$$

These properties, the sensitivity to changes in the refractive index of the surrounding medium, as well as the highly enhanced fields at the plasmon resonance make metal nanoparticles ideal candidates for optical sensing devices.

2.1.3.2 *Scattering and Absorption Cross Sections*

As described above, an oscillating dipole moment is induced in the metallic nanosphere when illuminated with an oscillating electromagnetic field. This leads to scattering of the incoming plane wave and can be represented as radiation by a point dipole. The corresponding scattering cross section of the sphere can be obtained by dividing the total radiated power of the dipole by the intensity of the incoming plane wave and results in

$$C_{sca} = \frac{k^4}{6\pi}|\alpha|^2 = \frac{8\pi}{3}k^4a^6\left|\frac{\varepsilon - \varepsilon_m}{\varepsilon + 2\varepsilon_m}\right|^2 \quad , \tag{2.31}$$

where k is the wave vector in the surrounding medium. As the particle also dissipates power from the incident field inside the particle, the absorption cross section can be calculated by applying *Poynting's theorem*, and it can be found that the power dissipated by a point dipole is determined by $P_{abs} = \frac{\omega}{2}\Im(\vec{p}\cdot\vec{E}_0^*)$, which leads to

$$C_{abs} = k\Im(\alpha) = 4\pi k a^3 \Im\left(\frac{\varepsilon - \varepsilon_m}{\varepsilon + 2\varepsilon_m}\right) \quad . \tag{2.32}$$

The extinction cross section, describing the total amount of power removed from the incident beam, is consequently given by the sum of absorption and scattering. From the cross sections described above it can be seen that C_{abs} scales with a^3, whereas C_{sca} scales with a^6. Therefore, extinction is governed by scattering for larger particles, whereas absorption dominates for smaller ones.

2.1.4 *Optical Antennas*

As has been discussed in the previous sections, small metal nanoparticles interact with an incoming electromagnetic field in such a way that a resonance occurs, i.e. the electric fields can be highly amplified close to the nanostructure and also scattering at wavelengths close to the resonance wavelength is selectively enhanced. Such structures can therefore be considered as optical antennas, similar to their analogies in the microwave or radiowave regimes, and they enable the conversion of freely propagating light into highly localized energy, and vice versa [66]. This principle is graphically depicted in Figure 2.4, where on the left-hand side the antenna acts as a transmitting device for radiation originating from an inefficient photon source, while on the right-hand side it represents the receiving device for incoming optical radiation.

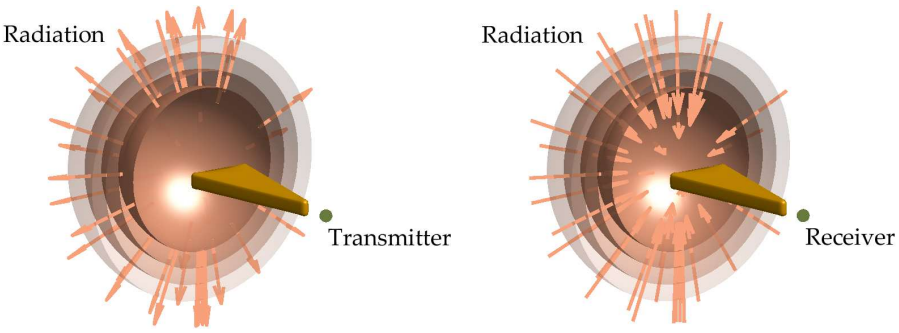

Figure 2.4: Optical antenna design, acting as transmitting device (left) and receiving device (right) for optical radiation. Image after [66].

Due to their capability to control light at sub-wavelength scales and enhance different photophysical processes, optical antennas find use in a variety of different applications, as it is outlined in Figure 2.5 [66–68]. The image on the left-hand side illustrates the process of photon emission in light-emitting devices, where charge carriers, i.e. electrons e^- and holes h^+, are recombined in a medium. The center image shows the reverse process, as it is applied in photovoltaics, where incoming light causes the separation of charge carriers. The task of the optical antenna in both cases is to make the transfer of energy more efficient, as it couples the propagating fields and the local electric fields, respectively. The image on the right-hand side illustrates the principle being crucial in spectroscopic applications, where the antenna acts as both, a receiving and a transmitting device. The presence of the antenna does have an influence on the emission rates of a photon emitter, such as fluorescent molecules or quantum dots, as it will be discussed in section 2.3.1. Also, dependent on the individual geometric design, antennas can also be used to simultaneously control the direction of emission, as it is done with so-called

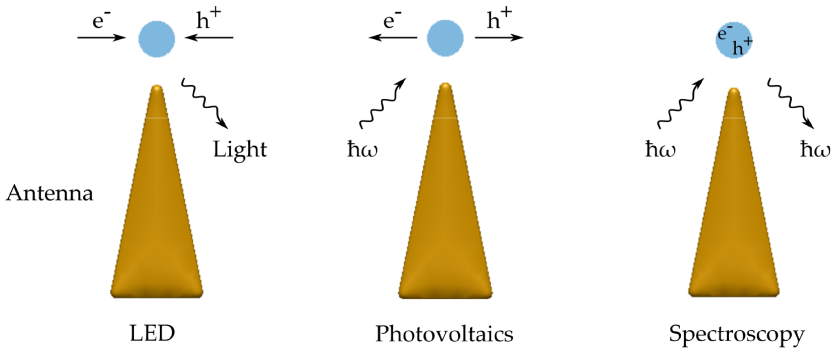

Figure 2.5: Scheme of photophysical processes used in antenna-based applications. (Left) Charge carrier recombination in light-emitting devices. (Center) Charge carrier separation in photovoltaics. (Right) Enhancement and directioning of light in spectroscopic applications. Image after [67].

directional antennas. A single resonant nanorod antenna can also act as a directional antenna, as is exemplarily depicted in Figure 2.6. The image illustrates the radiation patterns (bottom) for a dipolar emitter being placed close to the end of a resonant nanorod antenna on a glass substrate (top). The according surface charge distributions for the first two resonant modes are also depicted. If the antenna is designed in such a way that the emission matches the resonance frequency of the dipolar mode, the radiation pattern looks similar to what is expected for a dipole on a glass surface, the emitted light is radiated in the lateral direction compared to the charge oscillations in the antenna and mostly into the substrate. If the first higher order mode is excited, i.e the quadrupolar mode, the emission pattern rotates by 90° and the width of the lobes increases. Many antenna designs are based on a combination of such short metallic structures exhibiting plasmonic resonances. A well-known configuration is an optical *Yagi-Uda antenna*, consisting of a feed element responsible for emission enhancement of a nearby photon emitter and a reflection and several directing elements for wave guiding through constructive interference in a distinct direction [69, 70]. Other designs for example include waveguides to enable efficient directional coupling to plasmonic structures [71–73]. Another design to modify the emission directionality of a single quantum emitter, namely a hybrid metal-dielectric bullseye nanoantenna will be discussed in section 2.3.2.

2.2 SEMICONDUCTOR QUANTUM DOTS

As is stated in the name, semiconductor quantum dots or nanocrystals are small particles of a few nanometers in size, composed of compounds of semiconductors, such as lead selenide, cadmium selenide, cadmium sulfide, indium arsenide and many others [74]. They exhibit

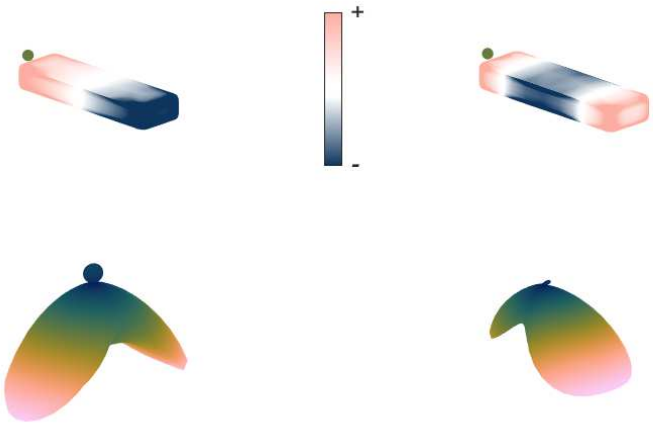

Figure 2.6: Radiation patterns of a dipole emitter coupled to the end of a nanorod antenna for the first two resonant modes, i.e. the dipolar mode (left) and the quadrupolar mode (right).

highly tuneable optical properties, covering the entire visible spectral range up to the near-infrared. The absorption- and emission properties can be accurately controlled by adjusting the size of the quantum dots and also by engineering the surface passivation by choosing from various ligands.
The different emission wavelengths of such nanocrystals occur due to the quantum confinement effect [75]. A schematic of the electronic energy structure of semiconductors of different sizes is illustrated in Figure 2.7. For bulk material, the valence band (VB) and conduction band (CB) are continuous and separated by a bandgap. The excitons, i.e. bound electron-hole pairs, can be described by a hydrogen-like Hamiltonian according to

$$\hat{H} = -\frac{\hbar^2}{2m_h}\nabla_h^2 - \frac{\hbar^2}{2m_e}\nabla_e^2 - \frac{e^2}{\varepsilon|r_e - r_h|} \quad , \tag{2.33}$$

where m_h and m_e are the effective masses of the hole and the electron and ε is the dielectric constant of the semiconducting material [57]. If the dimensions of the material decrease to sizes comparable to the Bohr radius of the exciton, the last term in equation 2.33, describing Coulomb interactions, can be neglected and the exciton states become discrete and shift to higher energies. This also results in an expanded bandgap, which enables tuning of the emission wavelength. The confinement energy increases due to Heisenberg's uncertainty principle, which states that the momentum of a particle increases if its position becomes well defined. This is given in small nanocrystals, as the electron-hole pairs are spatially limited, i.e. confined in the dimensions of the quantum dots.

The nanocrystals used in this thesis were CdSe/ZnS core/shell quantum dots, which are known to be spherical to slightly elongated

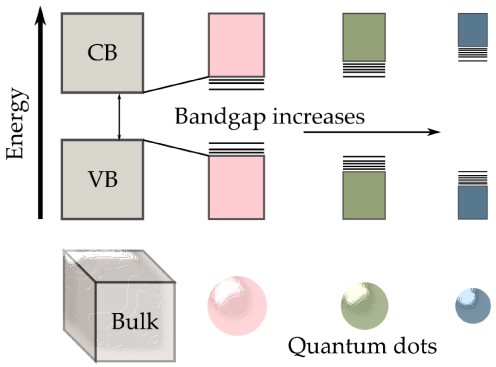

Figure 2.7: Schematic of the electronic energy structure in semiconductor materials. The dimensions of the semiconductor range from bulk material to nanocrystals with decreasing sizes, the energy states reach from continuous to discrete levels with increasing effective bandgaps.

in the direction of the crystal axis [76]. Due to their crystallographic properties they possess a *dark axis* in the direction of the crystal axis and a *bright plane* in the perpendicular direction, in which the two-dimensional emission transition dipole moment is degenerate, as is illustrated in Figure 2.8. In contrast to this emission anisotropy, the excitation transition dipole moment of a single CdSe/ZnS quantum dot is isotropic in three dimensions, i.e. such a nanocrystal can also be excited along the dark axis [77].

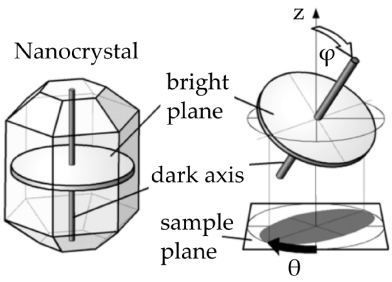

Figure 2.8: Sketch of a three-dimensional CdSe nanocrystal with its two-dimensional transition dipole moment (bright plane) and its one-dimensional dark axis. Image adapted with permission from [76].

The schematic on the left-hand side in Figure 2.9 illustrates the energy-level structure of electrons and holes confined in a spherical CdSe/ZnS quantum dot. As mentioned before, the effective energy gap of a quantum dot $E_g(QD)$ is larger than that of bulk material, as it is given by the distance between the lowest electron and highest hole confined energy levels. Depending on the energy of the incoming excitation light, excitons, i.e. electron-hole pairs can be excited, and op-

tical transitions allowed by selection rules are exemplarily highlighted with arrows. In semiconductor quantum dots the absorption strength increases towards shorter wavelengths, which is due to an increased density of states towards the center of the semiconductor conduction band [57]. The images in the center and on the right-hand side illustrate the processes involved in the radiative decay, i.e. the generation of the photoluminescence signal, and multiexciton generation, e.g. the excitation of biexcitons. Nanocrystals excited with excess energy fastly relax through the release of phonons to the lowest-energy excitonic state, from which they subsequently decay to the ground-state via the emission of a photon. Alternatively, the excess energy of the excited electron can be transferred to another exciton, whose excitation energy is therefore lowered by the presence of the first one.

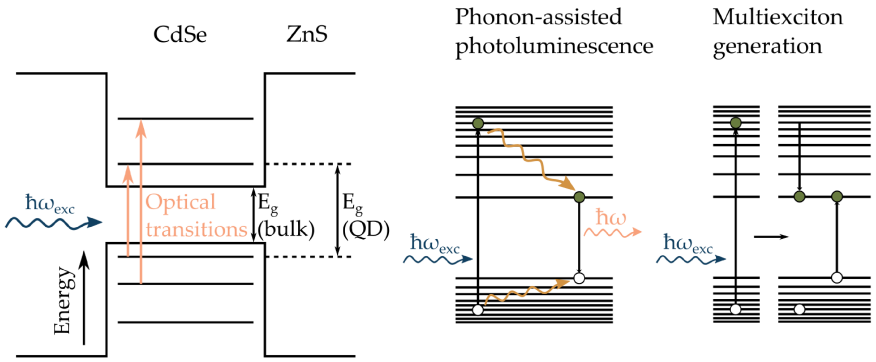

Figure 2.9: Schematic energy-level structure of a spherical CdSe/ZnS core/shell quantum dot (left). The effective energy gap E_g(QD) of the quantum dot is larger than that of bulk material E_g(bulk) due to the splitting into confined energy levels. Schematics of the relaxation processes after absorption of a photon with an energy $E_{exc} > E_g$. In the phonon-assisted relaxation process (center) the excess energy is released through phonons before the electron-hole pair recombines radiatively. Contrary, the excess energy can also be transferred to another exciton, i.e. excitation of a biexciton takes place (right).

Even though quantum dots are praised for their unique optical properties and high optical stability, they can show photoluminescence intermittency in their emission, so-called *blinking behavior*, which limits the usage in potential device applications. Although there are many works on the synthesization of quantum dots with suppressed blinking behavior [78–82], the mechanisms responsible for the emission intermittency are still subject to contemporary sciences [83]. There are two competing mechanisms identified to explain the blinking behavior, namely *Auger recombination* and *surface trap induced recombination* [84]. Auger recombination denotes a non-radiative process (in charged

nanocrystals) where the energy set free during electron-hole recombination is transferred to other electrons or holes rather than being emitted through a photon. The absorbing carriers are subsequently excited to higher energy levels in the same band from where radiative channels are open again. Surface trap induced recombination occurs when a charge carrier tunnels into a trap state on the surface of the quantum dot and is highly dependent on the shell thickness and choice of ligands for surface passivation [85, 86].

2.3 HYBRID SYSTEMS

Semiconductor quantum dots are sometimes referred to as *artificial atoms* due to their discrete electronic energy structure, which can be described similar to those of isolated atoms. The quantum system in free space can therefore be approximated by a three-level system [87], as it is displayed on the left-hand side in Figure 2.10. The third level is taken into account in order to include transitions to dark states. The diagram reads as follows: a quantum dot in the ground state $|g>$ is excited to an intermediate excited state $|i>$ upon absorption of an incident photon originating from illumination with a plane wave. The transition rate of this process is described by the excitation rate γ_{exc}^0. The system then decays immediately to the excited state $|e>$ through a non-radiative process, from where it can decay back to the ground state $|g>$, either radiatively by emitting a photon with a decay rate γ_{rad} or non-radiatively with a rate γ_{nr}. The red shift observed in the emission wavelength compared to the excitation is due to the energy loss during the transition from $|i>$ to $|e>$. By assuming that the intermediate state is only occupied for infinitesimally short times, the system can be described by a two-level system, and for the occupation of the initial states one can assume $X_e + X_g = 1$. The transition dynamics can then be written as

$$\begin{aligned} \dot{X}_e &= \gamma_{exc} - \gamma_{nr} - \gamma_{rad} \\ &= (1 - X_e)k_{exc} - X_e(k_{nr} + k_{rad}) \ , \end{aligned} \tag{2.34}$$

where the excitation rate is given by $\gamma_{exc} = X_g k_{exc}$, i.e. by the population X_g of the ground state times the rate constant k_{exc}, and the radiative decay rate is given by $\gamma_{rad} = X_e k_{rad}$, accordingly.
So for a quantum emitter being located at position $\vec{r}$ and being represented by a two-level system with transition dipole moment $\vec{p}$ and transition frequency ω, the excitation rate is found to be dependent on the local excitation field $\vec{E}(\vec{r}, \omega)$, i.e. $\gamma_{exc} \propto \left|\vec{p} \cdot \vec{E}\right|^2$. According to *Fermi's golden rule* the radiative transition rate is given by the transition probability [88]

$$\mathcal{W}_{g \to e} = \frac{2\pi}{\hbar^2} \left|M_{ge}\right|^2 \rho(\vec{r}, \omega) \ , \tag{2.35}$$

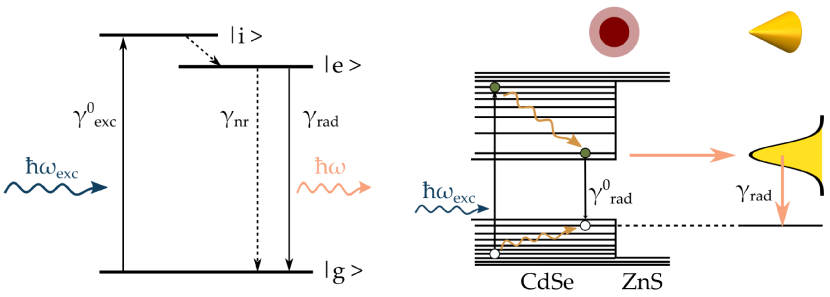

Figure 2.10: Term diagram of a three-level quantum system with ground state $|g>$, intermediate state $|i>$ and excited state $|e>$ (left). The solid lines represent radiative and the dotted lines non-radiative processes. Schematic energy level illustration of a CdSe/ZnS quantum emitter coupled to a plasmonic gold nanocone (right). The presence of the nanocone changes the local photonic density of states compared to that in free-space and therefore alters the absorption and emission rates of the quantum system. Energy can be transferred to the nanocone, from where a photon can be emitted through the plasmon mode or the energy can dissipate through ohmic losses in the metal.

where M_{ge} is the matrix element for the transition and $\rho(\vec{r},\omega)$ is the local density of states. The transition matrix element therein is given by

$$M_{ge} = \langle e|\hat{H}|g\rangle = \int \psi_e^*(\vec{r})\hat{H}(\vec{r})\psi_g(\vec{r})d^3\vec{r} \ , \tag{2.36}$$

where $\hat{H} = -\hat{p}\cdot\hat{E}$ is the interaction Hamiltonian in the dipole approximation. The electrons then respond to the electric field according to $\vec{p} = -e\vec{r}$ and the Hamiltonian can be written as $\hat{H} = e(xE_x + yE_y + zE_z)$, where $E_{x,y,z}$ are the electric field amplitudes in the according directions. With this, the transition matrix element, for e.g. x-polarized light, can be written as

$$M_{ge} = eE_x \int \psi_e^* x \psi_g d^3\vec{r} \tag{2.37}$$

with the transition dipole moment $p_x = -e\langle e|\hat{p}_x|g\rangle \equiv -e\int \psi_e^* x\psi_g d^3\vec{r}$. By applying Fermi's golden rule, the absorption, i.e. excitation rate, and the spontaneous decay rate of a quantum emitter in free space, i.e. in a homogeneous environment and an isotropic local density of states, can be calculated and are given by [88]

$$\gamma_{0,exc} = \frac{\pi|\vec{p}|^2}{3\varepsilon_0\hbar^2} \tag{2.38}$$

$$\gamma_0 = \frac{\omega^3|\vec{p}|^2}{3\pi\varepsilon_0\hbar c^3} \ , \tag{2.39}$$

wherein $\vec{p} = \langle e|\hat{p}|g\rangle$ is the transition dipole matrix element and the (*partial*) photonic density of states in free space is given by $\rho_0 = \frac{\omega^2}{\pi^2c^3}$.

For a quantum emitter placed in close vicinity to a metallic nanoparticle, the transition rates are modified due to the change in the electromagnetic environment, as will be explained in the section below following [87–89].

2.3.1 *Emission modification*

The transition scheme of a hybrid system, consisting of CdSe/ZnS quantum dots placed close to the tips of plasmonic gold nanocones, is illustrated on the right-hand side of Figure 2.10. The presence of the plasmonic nanocone leads to a modified photonic local density of states, which in turn modifies the decay rates of the quantum emitter. Also, in an inhomogeneous environment, the decay rates will be dependent on the orientation of the dipole moment of the emitter (cf. Figure 4.6). The Purcell factor F_i describes the enhancement of the modified decay rates in a modified environment compared to those in free space, i.e. $F_i = \frac{\gamma_i}{\gamma_{0,i}}$, where $i = x, y, z$ represents the dependence on the dipole orientation [90].
In general, two dominant effects on the transition rates, caused by the presence of a nanostructure, can be identified. Due to the enhanced near field at the tip of the nanocone, the absorption, i.e. excitation, is increased by a factor

$$F_{exc} = \frac{\gamma_{exc}}{\gamma^0_{exc}} = \frac{I}{I_0} \ , \tag{2.40}$$

where I is the intensity of the plasmonically enhanced incident light and I_0 is the intensity of the incident light without nanostructure, accordingly. Also, as mentioned before, the local density of optical states $\rho(\vec{r}, \omega)$ is highly enhanced in close proximity to the tip of the nanocone, therefore leading to an increase in γ_{em}, as according to Fermi's golden rule $\gamma_{em} \propto \rho$ (cf. section 2.3). In contrast to free space, where the emission rate is given by the sum of the radiative rate and intrinsic losses $\gamma^0_{em} = \gamma^0_{rad} + \gamma^0_{nr}$, the optical states near a plasmonic structure can also be non-radiative due to *quenching*. Quenching describes a non-radiative decay process which can be explained by ohmic losses in the metal particle [91]. The total decay rate can then be written as $\gamma_{em} = \gamma = \gamma_{rad} + \gamma_{nr}$, and the change in the emission rate can therefore be described by the enhancement factors

$$F_{rad} = \frac{\gamma_{rad}}{\gamma^0_{em}} \ , \ F_{nr} = \frac{\gamma_{nr}}{\gamma^0_{em}} \ . \tag{2.41}$$

By inserting the modified decay rates into equation 2.34, the excited state dynamics in an inhomogeneous environment can be written as

$$\begin{aligned} \dot{X}_e &= \gamma_{exc} - \gamma^0_{nr} - \gamma_{rad} - \gamma_{nr} \\ &= (1 - X_e) k^0_{exc} F_{exc} - X_e k^0_{rad} \left(\Phi_0^{-1} - 1 + F_{nr} + F_{rad} \right) \ . \end{aligned} \tag{2.42}$$

Here, Φ_0 denotes the fluorescence quantum yield of the quantum emitter in free space and is given by

$$\Phi_0 = \frac{k^0_{rad}}{k^0_{rad} + k^0_{nr}} \quad . \tag{2.43}$$

To find a solution to this differential rate equation, different excitation regimes need to be distinguished, depending on the incident intensity and e.g. the form of illumination, i.e. continuous wave or pulsed illumination [89]. If the system is excited with a continuous wave, simplifications can be made to obtain an analytical solution. As the incoming intensity is constant over time, the system will quickly reach an equilibrium state and the steady-state solution $\dot{X}_e = 0$ can be considered. The population probability of the excited state can then be written as

$$X_e = \frac{k^0_{exc} F_{exc}}{k^0_{exc} F_{exc} + k^0_{rad}(\Phi_0^{-1} - 1 + F_{nr} + F_{rad})} \quad , \tag{2.44}$$

and the intensity of the emitted light from such a quantum system, i.e. the total rate of radiative decay, is therefore given by

$$\gamma = X_e k^0_{rad} F_{rad} = \frac{k^0_{exc} F_{exc} k^0_{rad} F_{rad}}{k^0_{exc} F_{exc} + k^0_{rad}(\Phi_0^{-1} - 1 + F_{nr} + F_{rad})} \quad . \tag{2.45}$$

This radiative decay rate strongly depends on the enhancement regimes, i.e. on the illumination intensities, and can be further simplified in distinct cases [89]. In the saturation regime, i.e. for high incident intensities, the decay rate is given by $\gamma = F\gamma_0$ (cf. equation 4.5), as it will be discussed in section 4.2. The enhancement rates can therefore be obtained from experiments, by using a combination of lifetime and saturation measurements, and also the device quantum yields can be calculated by solving a set of rate equations describing the emission process in the respective system [41].

2.3.2 *Radiation modification*

As it has been mentioned before in section 2.1.4, not only the decay rates can be modified in a plasmonic hybrid system, but also the emission directionality can be influenced by the presence of an optical antenna. In the case of the hybrid metal-dielectric bullseye antenna described in section 4.2, the circular Bragg antenna is responsible for redirecting the emission. In addition, the structure is covered in a dielectric layer of polymethyl methacrylate, acting as a photonic waveguide, which allows long propagation distances along the grating [92]. The exact geometrical dimensions, as they are sketched in Figure 2.11, need to be optimized through simulations, as efficient photon extraction is dependent on many crucial geometrical parameters [93,

94]. Nevertheless, the basic working principle of the device shall be shortly explained in the following.

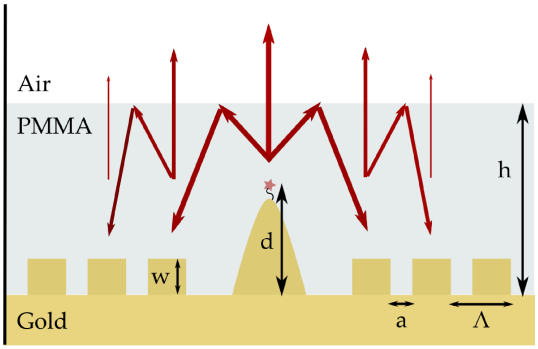

Figure 2.11: Cross-sectional illustration of the hybrid bullseye antenna defining the geometrical parameters. A second-order Bragg grating is located on top of a continuous gold film and encircles a nanocone with a quantum emitter attached to its tip. The whole device is embedded in a layer of PMMA acting as a photonic waveguide.

A semiconductor nanocrystal, placed at a certain distance d to the substrate gold layer and embedded in the dielectric PMMA layer with height h, emits photons with a certain emission wavelength preferentially into the high refractive index medium. The dielectric layer is adjusted to serve as a single-mode waveguide for the respective emission wavelength, i.e. contains a guided mode, which allows the light to cover long distances before being diffracted by the grating. Figure 2.12 schematically sketches a waveguide with refractive index n_1, surrounded by different media n_2 and n_3, where $n_1 > n_2 > n_3$. The image shows an intuitive picture of the optical path of a plane wave traveling in the waveguide. The wave inside the core, propagating in direction $\vec{k}$, is totally reflected at both interfaces and therefore trapped in the core, resulting in a guided mode. The propagation constant $\vec{k}$ can be decomposed into its orthogonal components, β and k_x, as is also sketched on the left-hand side. The transverse component therein is given by $k_x = n_1 \frac{\omega}{c} \cos\theta$ and the longitudinal component is given by $\beta = n_1 \frac{\omega}{c} \sin\theta$, so that $\beta^2 + k_x^2 = \left(n_1 \frac{\omega}{c}\right)^2$. The traveling wave can therefore be understood as the superposition of two orthogonal components traveling in the longitudinal (z) and transverse (x) directions, as it is depicted on the right-hand side of Figure 2.12. The transverse wave is thereby reflected back and forth between the two interfaces and *interferes* with itself. The phase accumulated during a trip back and forth of the transverse component is dependent on the core thickness and given by $\varphi = 2kh\cos\theta$. A guided mode can only exist when the transverse component interferes constructively with itself, i.e. a resonance condition is satisfied. This condition is

given by $2kh\cos\theta + \varphi_2(\theta) + \varphi_3(\theta) = 2m\pi$, where m is an integer and $\varphi_{2,3}(\theta)$ are phase shifts associated with the internal reflections at the interfaces of the waveguide [95].

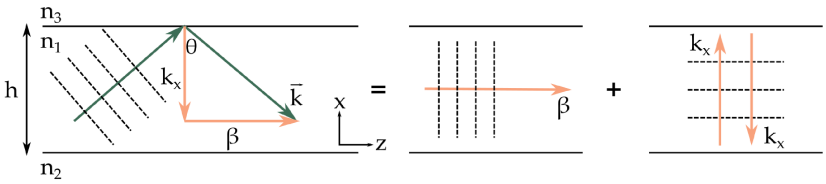

Figure 2.12: Schematic illustration of a waveguide with core refractive index n_1 and height h, surrounded by media n_2 and n_3. The green arrows depict the wave vector ($\vec{k}$), i.e. the path of a plane wave, which is reflected back and forth at the different interfaces. The k-vector and therefore the propagation of light can be decomposed in a transverse (k_x) and a longitudinal (β) component, as is illustrated on the right-hand side. A guided mode can only exist if the transverse component satisfies a resonance condition, i.e. interferes constructively with itself.

As the geometry of the wave-guiding structure is two-dimensional and the emitted photons propagate in radial direction, the geometry of the diffraction grating is also circular and consists of concentric rings with period Λ. The grating is designed in such a way that the second-order Bragg condition is fulfilled, i.e. $\Lambda = \frac{\lambda}{n_{eff}}$, where λ is the wavelength of light in free space and n_{eff} is the effective refractive index of the grating, respectively. The corresponding reciprocal lattice vector, i.e. the *Bragg vector*, is given by $G = \frac{2\pi}{\Lambda}$. To obtain a wave vector component $k_{||}$ parallel to the surface, the following two relations need to be satisfied [96]

$$k_{||} = k - mG \ , \tag{2.46}$$

$$k_{||} \leqslant nk_0 = n\frac{2\pi}{\lambda} \ , \tag{2.47}$$

where m is an integer, denoting different diffraction orders, and n is the refractive index of the surrounding medium. For a second-order Bragg grating, as it is displayed in Figure 2.13, it follows that $k = n_{eff}\frac{2\pi}{\lambda}$ and $G = \frac{2\pi}{\Lambda} = n_{eff}\frac{2\pi}{\lambda} = k$, so that $k_{||} = k - G = 0$ can be supported. This results in vertical propagation of light, i.e. perpendicular to the surface, which is desired for the efficient photon extraction from hybrid dielectric-metal bullseye antennas.

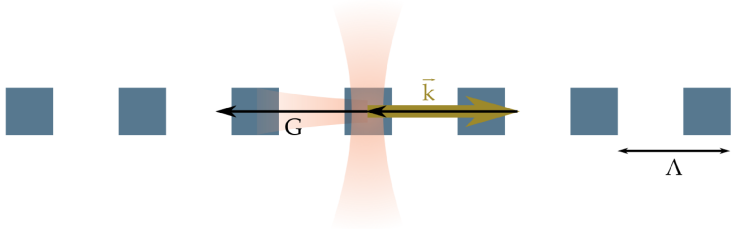

Figure 2.13: Schematic illustration of diffraction at a second-order Bragg grating. The bold arrow shows the propagation of the incoming light, while the thinner black arrows show the reciprocal lattice vector G, dependent on the lattice period Λ via $G = \frac{2\pi}{\Lambda}$. As the second-order Bragg condition is fulfilled, the diffracted light can also propagate in a vertical direction relative to the surface. Image after [96].

2.4 POLARIMETRIC SPECTROSCOPY

When investigating the multitude of optical properties of semiconductor nanocrystals, it is of increased interest to study as well the polarimetric properties of the emitted light. While spherical CdSe nanocrystals are known to emit partially polarized light dependent on their crystal orientation [76] (cf. Figure 2.8), elongated quantum rods clearly show linearly polarized luminescence [97]. The emission polarization can also be actively influenced by strong light-matter interactions, when a quantum emitter is placed close to a plasmonic nanostructure, as it has been shown for quantum dots [98] or fluorescent molecules [99, 100] in the vicinity of gold nanorods. Fluorescent labeling and measurements on the fluorescence polarization are one of the most widespread methods used in clinical and biomedical sciences [101], whereas the control of polarization in plasmonic nanostructures is subject of contemporary research further on [102–104]. While *metasurfaces* are designed to control the polarization of a light beam on the big scale [105], chiral plasmonics focuses as well on the polarization manipulation at the single particle level [47]. The experiments presented in section 4.3 of this thesis deal with the analyzation of the polarization of light scattered from achiral plasmonic nanostructures, and the polarization is found to vary from linear to circular depending on the polarization of the incident excitation light. In the following sections, the polarization ellipse of the electric field will be explained and the *Stokes parameters* will be introduced, which define a set of values to describe the polarization state of light [56]. Additionally, the concepts of optical and geometrical chirality will be presented, together with a description of the optical chirality flux to the far field.

2.4.1 *Polarization Ellipse and Stokes Parameters*

Polarization of light arises when two independent and orthogonal components contribute to the total electric field, $E_x(z,t)$ and $E_y(z,t)$, which have different phases and possibly different amplitudes and can be described by [106]

$$\begin{aligned} E_x(z,t) &= E_{0x}\cos(\omega t - kz + \varphi_x) \\ E_y(z,t) &= E_{0y}\cos(\omega t - kz + \varphi_y) \quad . \end{aligned}$$

Here, the term $\omega t - kz$ describes the propagation of light, where ω is the angular frequency, t represents time, $k = \frac{2\pi}{\lambda}$ is the wave number and z denotes a location in space. φ_x and φ_y denote phase constants, respectively. However, the electric field components cannot be directly observed, as the optical frequency is on the order of $10^{15}\frac{1}{s}$. A vivid description of the polarization behavior can yet be obtained by elimination of the fastly oscillating propagation term, which can be done by the separation of the terms into

$$\begin{aligned} \frac{E_x(z,t)}{E_{0x}} &= \cos(\omega t - kz) \\ \frac{E_y(z,t)}{E_{0y}} &= \cos(\omega t - kz + \Delta) \\ &= \cos(\omega t - kz)\cos\Delta - \sin(\omega t - kz)\sin\Delta \quad , \end{aligned} \tag{2.48}$$

where $\Delta = \varphi_y - \varphi_x$.
Thus

$$\frac{E_y(z,t)}{E_{0y}} - \frac{E_x(z,t)}{E_{0x}}\cos\Delta = -\sin(\omega t - kz)\sin\Delta \quad . \tag{2.49}$$

By rewriting equation 2.48 into

$$\sin(\omega t - kz) = \sqrt{1 - \left(\frac{E_x(z,t)}{E_{0x}}\right)^2}$$

and inserting into equation 2.49 one obtains

$$\frac{1}{\sin^2\Delta}\left[\left(\frac{E_x(z,t)}{E_{0x}}\right)^2 + \left(\frac{E_y(z,t)}{E_{0y}}\right)^2 - 2\frac{E_x(z,t)}{E_{0x}}\frac{E_y(z,t)}{E_{0y}}\cos\Delta\right] = 1 \tag{2.50}$$

which represents an ellipse equation with free parameters E_{0x}, E_{0y} and Δ. This electric field ellipse can also be expressed in rotated Cartesian coordinates via

$$\frac{(x\cos\Psi + y\sin\Psi)^2}{a^2} + \frac{(y\cos\Psi + x\sin\Psi)^2}{b^2} = 1 \quad , \tag{2.51}$$

as it is displayed in Figure 2.14. By comparing the coefficients of those two equations 2.50 and 2.51, one can connect the principal axes a and b of an ellipse with orientation Ψ with the relative amplitudes and phase of the electromagnetic fields. Under consideration of $E_x \mathrel{\widehat{=}} x$ and $E_y \mathrel{\widehat{=}} y$ one obtains

$$\frac{1}{E_{0x}^2 \sin^2 \Delta} = \frac{\cos^2 \Psi}{a^2} + \frac{\sin^2 \Psi}{b^2} \tag{2.52}$$

$$\frac{1}{E_{0y}^2 \sin^2 \Delta} = \frac{\sin^2 \Psi}{a^2} + \frac{\cos^2 \Psi}{b^2} \tag{2.53}$$

$$\frac{\cos \Delta}{\sin^2 \Delta} \frac{1}{E_{0x} E_{0y}} = \frac{\sin \Psi \cos \Psi}{b^2} - \frac{\sin \Psi \cos \Psi}{a^2} \tag{2.54}$$

By dividing equation 2.52 by equation 2.53, it follows for E_{0x} and E_{0y}

$$\frac{E_{0y}}{E_{0x}} = \frac{\sqrt{a^2 \sin^2 \Psi + b^2 \cos^2 \Psi}}{\sqrt{a^2 \cos^2 \Psi + b^2 \sin^2 \Psi}} \ . \tag{2.55}$$

An expression for the relative phase Δ can finally be obtained from equation 2.54 by substituting $\frac{1}{\sin^2 \Delta}$ with equation 2.52 and further

$$\frac{\cos \Delta}{E_{0x} E_{0y}} \left(\frac{\cos^2 \Psi}{a^2} + \frac{\sin^2 \Psi}{b^2} \right) E_{0x}^2 = \frac{\sin \Psi \cos \Psi}{b^2} - \frac{\sin \Psi \cos \Psi}{a^2}$$

Multiplying both sides with $a^2 b^2$ and substituting the numerator of equation 2.55 on the left hand side, it follows that

$$\begin{aligned}
\frac{\cos \Delta}{\cancel{E_{0x} E_{0y}}} \cancel{E_{0y}^2} \cancel{E_{0x}^2} &= a^2 \sin \Psi \cos \Psi - b^2 \sin \Psi \cos \Psi \\
&= (a^2 - b^2) \sin \Psi \cos \Psi \\
\cos \Delta \cdot 2 E_{0x} E_{0y} &= \frac{2 \sin \Psi \cos \Psi}{\underbrace{\cos^2 \Psi - \sin^2 \Psi}_{\tan 2\Psi}} (E_{0x}^2 - E_{0y}^2) \\
\cos \Delta &= \frac{E_{0x}^2 - E_{0y}^2}{2 E_{0x} E_{0y}} \tan 2\Psi \ .
\end{aligned} \tag{2.56}$$

As mentioned before, the electric field and therefore also the ellipse described in equation 2.50 cannot be observed directly. Yet, the intensity is a measurable quantity, which can be obtained from taking the time average of equation 2.50. The time average of the quadratic field components is defined by [106]

$$\langle E_i(z,t) E_j(z,t) \rangle = \lim_{T \to \infty} \frac{1}{T} \int_0^T E_i(z,t) E_j(z,t) dt \quad (i,j = x,y) \ .$$

This time averaging leads to the relation

$$S_0^2 = S_1^2 + S_2^2 + S_3^2 \ , \tag{2.57}$$

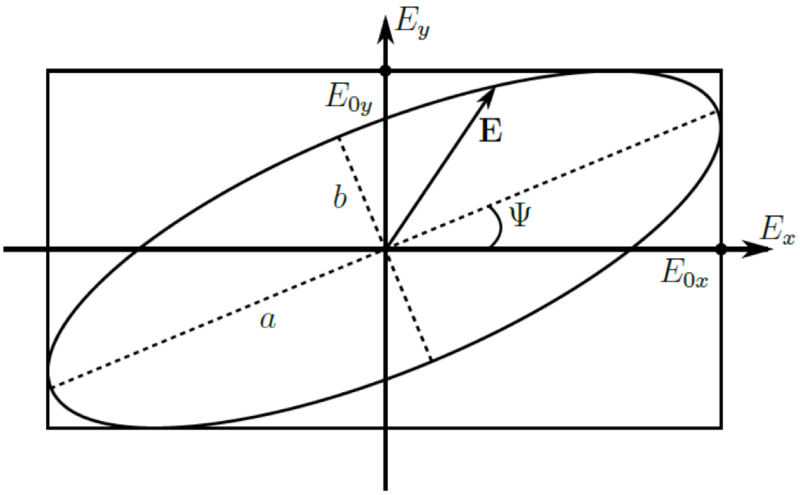

Figure 2.14: Polarization ellipse with major a and minor b axis and orientation Ψ.

where S_0 to S_3 denote the four Stokes parameters and are given by

$$S_0 = E_{0x}^2 + E_{0y}^2 = I_{0^\circ} + I_{90^\circ} \tag{2.58}$$

$$S_1 = E_{0x}^2 - E_{0y}^2 = I_{0^\circ} - I_{90^\circ} \tag{2.59}$$

$$S_2 = 2E_{0x}E_{0y}\cos\Delta = I_{45^\circ} - I_{135^\circ} \tag{2.60}$$

$$S_3 = 2E_{0x}E_{0y}\sin\Delta = I_{LCP} - I_{RCP} \quad . \tag{2.61}$$

The Stokes parameters can be described in terms of intensity, as shown above, and are therefore measurable quantities. S_0 describes the total intensity of the light field, while S_1 describes the preponderance of linearly horizontally polarized light over linearly vertically polarized light. S_2 and S_3 describe the predominance of linearly 45° over linearly 135° polarized light and of left-handed circularly polarized light over right-handed circularly polarized light, respectively.

2.4.1.1 *Intensity Pattern*

As discussed above, in standard optical experiments, the intensity of the electromagnetic field is measured rather than the electric field. To evaluate the obtained intensity patterns from analyzed dark-field scattering spectra, as it is described in section 4.3, an expression for the fitting procedure can be derived as described below, following the description given in the Supporting Information of Ref. [107].
The equation for the polarization ellipse of the electric field can also be described in polar coordinates (E, φ) according to

$$E(\varphi) = \sqrt{\frac{a^2 \cdot b^2}{a^2 \sin^2(\varphi - \Psi) + b^2 \cos^2(\varphi - \Psi)}} \quad .$$

Here, a and b again denote the major and minor axis of the ellipse, and Ψ represents the rotation (cf. Figure 2.14). When a linear polarizer is

inserted into the optical path, the time-dependent transmitted electric field $E(\varphi(t))$ becomes an orthogonal projection in the direction of the transmission axis Θ of the polarizer. The resulting intensity is then given by

$$\begin{aligned} I_\Theta(t) &= |E(\varphi(t)) \cdot \cos(\varphi(t) - \Theta)|^2 \\ &= \frac{a^2 \cdot b^2}{a^2 \sin^2(\varphi(t) - \Psi) + b^2 \cos^2(\varphi(t) - \Psi)} \cdot \cos^2(\varphi(t) - \Theta) \quad . \end{aligned} \tag{2.62}$$

The amplitude of this time-dependent oscillation can be determined by differentiating equation 2.62 with respect to φ, and finding the angle φ_Θ for which the condition

$$\left.\frac{\partial I}{\partial \varphi}\right|_{\varphi=\varphi_\Theta} = 0$$

is fulfilled.
By substituting $\varphi_\Theta - \Theta = \eta$ and $\varphi_\Theta - \Psi = \kappa$, the derivative can be written as

$$\begin{aligned} 0 = &[-2a^2b^2 \cos(\eta)\sin(\eta)] \cdot [a^2 \sin^2(\kappa) + b^2 \cos^2(\kappa)] \\ &+ [-2a^2b^2 \cos^2(\eta)] \cdot [a^2 \sin(\kappa)\cos(\kappa) - b^2 \cos(\kappa)\sin(\kappa)] \\ = &-2a^2b^2 \cos(\eta) \cdot \\ &(\sin(\eta) \cdot [a^2 \sin^2(\kappa) + b^2 \cos^2(\kappa)] \\ &+ \cos(\eta) \cdot [a^2 \sin(\kappa)\cos(\kappa) - b^2 \cos(\kappa)\sin(\kappa)]) \end{aligned}$$

The trivial solution to this equation can be easily identified and is given by $\cos(\eta) = 0$.
The non-trivial solution, however, can be obtained by solving

$$\begin{aligned} 0 = &a^2 \sin(\kappa) \cdot [\sin(\eta)\sin(\kappa) + \cos(\eta)\cos(\kappa)] \\ &+ b^2 \cos(\kappa) \cdot [\sin(\eta)\cos(\kappa) - \cos(\eta)\sin(\kappa)] \\ = &a^2 \sin(\kappa) \cdot \cos(\eta - \kappa) + b^2 \cos(\kappa) \cdot \sin(\eta - \kappa) \\ = &\underbrace{a^2 \cos(\Psi - \Theta)}_{\alpha} \cdot \sin(\kappa) + \underbrace{b^2 \sin(\Psi - \Theta)}_{\beta} \cdot \cos(\kappa) \quad . \end{aligned}$$

This equation has the form of $\alpha \sin(\kappa) + \beta \cos(\kappa) = 0$, which can be rewritten as $\gamma \sin(\kappa + \chi) = 0$ with $\gamma = \sqrt{\alpha^2 + \beta^2}$. Herein, χ denotes an additional phase that can be expressed as $\chi = \arcsin(\frac{\beta}{\gamma})$ or $\chi = \arccos(\frac{\alpha}{\gamma})$, respectively. By reversing the substitution of κ, this leads to $\varphi_\Theta - \Psi + \chi = 0$ and therefore $\varphi_\Theta = \Psi - \chi$. This relation can be inserted into equation 2.62, and it follows that

$$
\begin{aligned}
I_\Theta(t) &= \frac{a^2 \cdot b^2}{a^2 \sin^2(-\chi) + b^2 \cos^2(-\chi)} \cdot \cos^2(\Psi - \chi - \Theta) \\
&= \frac{a^2 \cdot b^2}{a^2 \frac{\beta^2}{\gamma^2} + b^2 \frac{\alpha^2}{\gamma^2}} \cdot [\cos(\Psi - \Theta)\cos(\chi) + \sin(\Psi - \Theta)\sin(\chi)]^2 \\
&= \frac{a^2 b^2 \cdot [\frac{\alpha^2}{a^2\gamma} + \frac{\beta^2}{b^2\gamma}]^2}{\frac{1}{\gamma} \cdot [\frac{a^2\beta^2}{\gamma} + \frac{b^2\alpha^2}{\gamma}]} = \frac{\cancel{[\frac{a^2\beta^2}{\gamma} + \frac{b^2\alpha^2}{\gamma}]} \cdot [\frac{\alpha^2}{a^2\gamma} + \frac{\beta^2}{b^2\gamma}]}{\frac{1}{\gamma} \cdot \cancel{[\frac{a^2\beta^2}{\gamma} + \frac{b^2\alpha^2}{\gamma}]}} \\
&= a^2 \cdot \cos^2(\Theta - \Psi) + b^2 \cdot \sin^2(\Theta - \Psi) \ ,
\end{aligned}
$$

which equals equation 4.7 for the fitting procedure.

2.4.2 *Optical and Geometrical Chirality*

Chirality, in general, describes a property of *asymmetry*, which can be found all across nature. An intuitive example is certainly one's own hands, which are so-called *enantiomorphs*, i.e. one hand constitutes the object and the other one its mirror image. For chiral objects, those two objects cannot be superposed onto each other solely by rotations or translations, so that all major features coincidence across all axes. On the contrary, an achiral object is indistinguishable from its mirror image. Even though objects can be chiral in three dimensions, the geometrical chirality is limited to two dimensions in this thesis, as only planar nanostructures were investigated.
For *real* objects, it is easily understandable and decidable whether or not they are chiral, i.e. possess geometrical chirality, and the degree of chirality can even be quantified using the chiral coefficient χ_{2D}, as it has been introduced by G. Gilat in 1989 [108]. Figure 2.15 illustrates the structural chirality of different nanostructures investigated in this thesis. It shows the respective structures superposed with their mirror images and the corresponding chiral coefficients, which are given by the ratio between the non-overlapping (light grey-shaded areas) and projected total area of the structure and its mirror image. As can be seen, only the achiral nanorectangle can be superposed with its mirror image, while for the chiral rhomboids this is not possible by any translations and rotations (in two dimensions). It shall be mentioned that, in contrast to intrinsically chiral systems, chirality can also be introduced extrinsically to systems with symmetric structures ($\chi_{2D} = 0$). This can be achieved if the excitation geometry in optical measurements is chosen accordingly, exemplarily for excitation light coming in under oblique incidence or being circularly polarized [52, 109, 110].
Another important part of chirality, which on first sight might seem less intuitive, is the so-called optical chirality, which describes a fundamental property of electromagnetic fields and means that even light

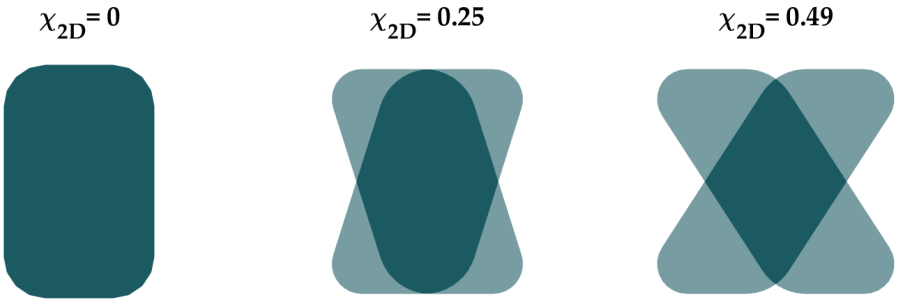

Figure 2.15: Concept of geometrical chirality for achiral and chiral nanostructures. The two-dimensional chiral coefficient χ_{2D} quantifies the geometrical chirality, as it is calculated from the geometrical overlap between the structure and its mirror image (exclusive disjunction).

can be chiral. Optical chirality is a scalar value that is odd in time and even in parity, i.e. symmetric under time reversal and asymmetric under mirror reflection. Since it is well known that chiral objects interact differently with chiral light, an effect called *circular dichroism* [111], many scientific works focus on finding a way to maximize chirality. A promising candidate are plasmonic nanostructures, as they have been shown to enhance optical chirality in their near fields [112].
Optical chirality can be quantified using an expression firstly introduced by Lipkin [113]

$$C \equiv \frac{\varepsilon_0}{2}\vec{E}\cdot\nabla\times\vec{E} + \frac{1}{2\mu_0}\vec{B}\cdot\nabla\times\vec{B} \quad , \tag{2.63}$$

and whose physical significance was firstly demonstrated by Tang and Cohen [114]. Considering its time-averaged form, C is then given by

$$C = -\frac{\varepsilon_0\omega}{2}\Im\left(\vec{E}^*\cdot\vec{B}\right) \quad , \tag{2.64}$$

where $\vec{E}^*$ is the complex conjugate of the electric field and $\vec{B}$ denotes the magnetic field, respectively. ε_0 is the electric permittivity of free space and ω the angular frequency of the electromagnetic field.
In the case of propagating plane waves, the optical chirality depends on their polarization state. For circularly polarized light, which can also be considered geometrically chiral, as the trajectories of the field vectors form helices in space, the optical chirality reaches a maximum. As the optical chirality is proportional to the dot product of the electric and magnetic fields, i.e. $C \propto \Im\left(\vec{E}^*\cdot\vec{B}\right)$, it is different from zero only for fields with parallel components of the respective fields, oscillating $\frac{\pi}{2}$ out of phase. This condition is fulfilled for circularly polarized light, but not for linear polarizations. For example, the electric and magnetic field amplitudes of left-handed circularly polarized light are given by

$\vec{E}_{LCP} = (E_0, iE_0, 0)^T$ and $\vec{B}_{LCP} = (-iB_0, B_0, 0)^T$ and with $B_0 = \frac{1}{c}E_0$ it follows that

$$C_{LCP} = \frac{-\varepsilon_0\omega}{2}\Im\left(\vec{E}^* \cdot \vec{B}\right) \tag{2.65}$$

$$= \frac{-\varepsilon_0\omega}{2}\Im\left((E_0, -iE_0, 0)^T \cdot \frac{1}{c}(-iE_0, E_0, 0)^T\right) \tag{2.66}$$

$$= \frac{\varepsilon_0\omega}{2c}|\vec{E}_{LCP}|^2 \ , \tag{2.67}$$

while for right-handed circularly polarized light $\vec{E}_{RCP} = (E_0, -iE_0, 0)^T$ and $\vec{B}_{RCP} = (iB_0, B_0, 0)^T$ and therefore $C_{RCP} = \frac{-\varepsilon_0\omega}{2c}|\vec{E}_{RCP}|^2$.

2.4.3 *Chirality Flux to the Far Field*

To characterize the optical chirality of plasmonic near fields, typically circular dichroism spectroscopy techniques are applied, which record the differences in the extinction or scattering spectra from the plasmonic nanostructures when excited with left- and right-handed circularly polarized light [115]. However, for the characterization of the near fields, this approach can be inaccurate, as the method yields two problems. Firstly, excitation with circularly polarized light introduces extrinsic chirality to the system and secondly, unwanted cancellation effects can occur due to investigating the difference of two spectra. To overcome these difficulties, *L. Poulikakos et al.* [53] identified the *chirality flux* $\mathcal{F}$ as a physical far-field probe to study the chirality of plasmonic near fields. They found the chirality flux to be proportional to the third Stokes parameter (cf. section 4.3.5), which is an experimentally accessible quantity and is studied in detail for the light scattered from chiral and achiral nanostructures in section 4.3.
An expression for the chirality flux $\mathcal{F}$ can be obtained by setting up a continuity equation in analogy with Poynting's theorem for lossy dispersive media. Therefore, a time-averaged, time-harmonic conservation law for the optical chirality density can be formulated

$$-2\omega\int_V \Im\left(C_e - C_m\right) d^3x + \int_V \Re\left(\nabla \cdot \mathcal{F}\right) d^3x = 0 \ , \tag{2.68}$$

where C_e and C_m are the electric and magnetic optical chirality densities (analogous to the harmonic electric and magnetic energy densities) and $\mathcal{F}$ is the optical chirality flux (analogous to the energy flux, i.e. Poynting vector $\mathcal{S}$) and are given by [53]

$$C_e = \frac{1}{8}\left(D^* \cdot (\nabla \times E) + E \cdot (\nabla \times D^*)\right) \tag{2.69}$$

$$C_m = \frac{1}{8}\left(H^* \cdot (\nabla \times B) + B \cdot (\nabla \times H^*)\right) \tag{2.70}$$

$$\mathcal{F} = \frac{1}{4}\left(E \times (\nabla \times H^*) - H^* \times (\nabla \times E)\right) \ . \tag{2.71}$$

When considering a circularly polarized plane wave, e.g. left-handed circularly polarized light with $\vec{E}_{LCP} = (E_0 \exp(i(kz - \omega t)), iE_0 \exp(i(kz - \omega t)), 0)^T$ and $\vec{B}_{LCP} = (-iB_0 \exp(i(kz - \omega t)), B_0 \exp(i(kz - \omega t)), 0)^T$, equation 2.71 reads as

$$\begin{aligned}
\mathcal{F}_{LCP} =& \frac{1}{4}\left[\begin{pmatrix} E_0 \\ iE_0 \\ 0 \end{pmatrix} \cdot e^{i(kz-\omega t)} \times \left(\begin{pmatrix} \frac{\partial}{\partial x} \\ \frac{\partial}{\partial y} \\ \frac{\partial}{\partial z} \end{pmatrix} \times \begin{pmatrix} iB_0 \\ B_0 \\ 0 \end{pmatrix} \cdot e^{-i(kz-\omega t)}\right)\right. \\
&\left. - \begin{pmatrix} iB_0 \\ B_0 \\ 0 \end{pmatrix} \cdot e^{-i(kz-\omega t)} \times \left(\begin{pmatrix} \frac{\partial}{\partial x} \\ \frac{\partial}{\partial y} \\ \frac{\partial}{\partial z} \end{pmatrix} \times \begin{pmatrix} E_0 \\ iE_0 \\ 0 \end{pmatrix} \cdot e^{i(kz-\omega t)}\right)\right] \\
=& \frac{1}{4}\left[\begin{pmatrix} E_0 \\ iE_0 \\ 0 \end{pmatrix} \times \begin{pmatrix} ikB_0 \\ kB_0 \\ 0 \end{pmatrix} - \begin{pmatrix} iB_0 \\ B_0 \\ 0 \end{pmatrix} \times \begin{pmatrix} kE_0 \\ ikE_0 \\ 0 \end{pmatrix}\right] \\
=& \frac{1}{4}\left[\begin{pmatrix} 0 \\ 0 \\ \frac{k}{c} 2E_0^2 \end{pmatrix} - \begin{pmatrix} 0 \\ 0 \\ \frac{-k}{c} 2E_0^2 \end{pmatrix}\right] = \frac{k}{c} E_0^2 \cdot \hat{e}_z \ . \qquad (2.72)
\end{aligned}$$

The complex Poynting vector denoting the energy flux is given by $\mathcal{S} = \frac{1}{2}(E \times H^*)$ and therefore

$$\mathcal{S}_{LCP} = \frac{1}{2}\left[\begin{pmatrix} E_0 \\ iE_0 \\ 0 \end{pmatrix} \times \begin{pmatrix} iB_0 \\ B_0 \\ 0 \end{pmatrix}\right] = \frac{1}{2c}\begin{pmatrix} 0 \\ 0 \\ 2E_0^2 \end{pmatrix} = \frac{1}{c} E_0^2 \cdot \hat{e}_z \ . \qquad (2.73)$$

Consequently, the chirality flux for a plane wave can be directly related to the energy flux via

$$\mathcal{F}_{LCP} = \frac{\omega}{c} \mathcal{S}_{LCP} \qquad (2.74)$$

$$\mathcal{F}_{RCP} = \frac{-\omega}{c} \mathcal{S}_{RCP} \qquad (2.75)$$

$$\mathcal{F} = \frac{\omega}{c}\left(|l|^2 \mathcal{S}_{LCP} - |r|^2 \mathcal{S}_{RCP}\right) \ , \qquad (2.76)$$

where $|l|^2$ and $|r|^2$ are weighting factors. As it has been mentioned before, the chirality flux is proportional to the third Stokes parameter S_3, as intensity I is given by the magnitude of the time-averaged energy flux $I = \langle \mathcal{S} \rangle_T$. In a circular basis the electric fields are given by $E_{LCP} = E_x + iE_y$ and $E_{RCP} = E_x - iE_y \exp(-i\Delta)$ and S_3 can therefore be written as

$$\begin{aligned}
S_3 &= I_{LCP} - I_{RCP} = |E_{LCP}|^2 - |E_{RCP}|^2 \\
&= E_x^2 + E_y^2 - (E_x^2 + E_y^2 - iE_xE_y \exp(-i\Delta) + iE_xE_y \exp(i\Delta)) \\
&= E_xE_y(i \exp(-i\Delta) - i \exp(i\Delta)) = 2E_xE_y \sin\Delta \ .
\end{aligned}$$

3 METHODS

This chapter focuses on the experimental methods used in this thesis. It includes sections on fabrication processes, optical measurement set-ups and simulations.
As plasmonic nanocones, and in particular hybrid systems consisting of nanocones and quantum emitters, constitute a substantial part of this thesis, detailed descriptions of the different fabrication processes for conical nanoantennas as well as recipes for the attachment of quantum dots to the apexes of such gold cones are described in the following. Also, the fabrication process of planar gold structures as they were used in the polarimetric dark-field scattering spectroscopy measurements is shortly discussed. Subsequently, the different optical set-ups that were used to perform the respective measurements described in chapter 4 are introduced. Lastly, a description of the different simulation models is given, which were used to buttress the experimental results.

3.1 FABRICATION

3.1.1 *Nanocones*

For the fabrication of gold nanocones, two top-down processes were used, as they have been successfully established in the group [116–119]. Figure 3.1 exemplarily shows a scheme of both processes for glass cover slips and gold, as these materials were chosen for most experiments in this thesis, yet there is no limitation to other materials, as long as they meet the requirements for the corresponding processing step.
To start from top to bottom in Figure 3.1, commercial glass cover slips (Menzel, borosilicate glass) serve as transparent substrates, which are firstly cleaned in a mixture of deionized water, potassium hydroxide and hydrogen peroxide in an ultrasonic bath, before being rinsed with deionized water and blow-dried with nitrogen. Afterwards, a thin layer ($\approx 50\,\mathrm{nm}$) of indium tin oxide (ITO) is sputtered (Leybold, Univex 300) to provide a conductive layer to facilitate electron beam lithography (EBL) and imaging of the finished structures with a scanning electron microscope (SEM). This step can be skipped if the substrate is conductive itself or if a conductive polymer is added before EBL (cf. section 3.1.4). Further processing is then chosen dependent on the desired (optical) properties of the conical nanostructures.

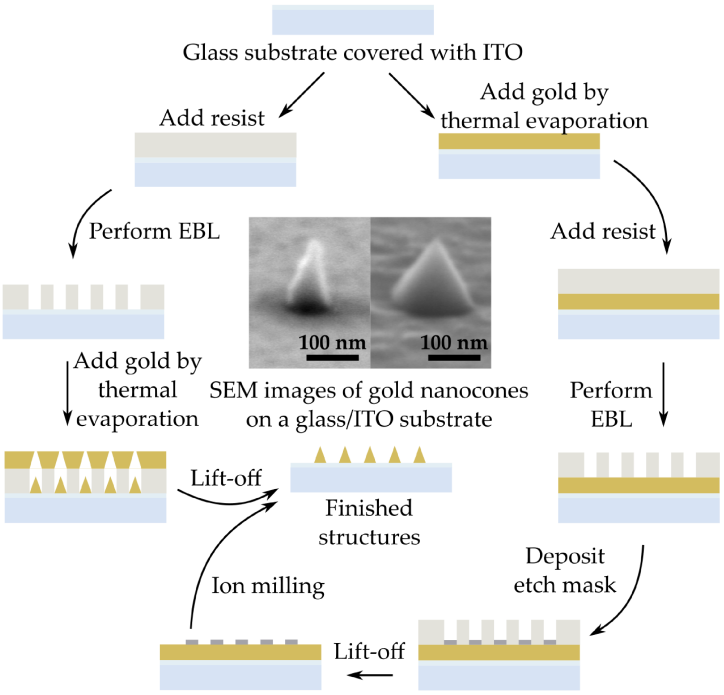

Figure 3.1: Schematic of the two used fabrication processes for nanocones with varying aspect ratios. Both methods have different advantages. While nanocones fabricated via thermal evaporation generally show higher aspect ratios, nanocones fabricated via ion-milling possess smaller tip radii. The scheme shows the processes for non-conductive substrates and gold as the structures' material, yet more general validity is also given for other commonly used materials in nanofabrication.

3.1.1.1 *Nanocones by Thermal Evaporation*

To obtain nanocones with higher aspect ratios ($\sim 1.2 - 2$), i.e. smaller base diameters compared to the height of the structures, thermal evaporation is the process of choice. The influence of such geometrical aspects on the optical properties is shortly discussed in section 3.2.1.1. So to proceed, an electron beam sensitive resist, namely polymethyl methacrylate, short PMMA (Mitsubishi Chemical America, Elvacite 2041), is dissolved in xylene and spin-coated onto the sample. The rotation parameters are chosen in such a way that the resist layer results in a smooth surface with a height dependent on the desired height of the nanocones. For structures with an envisaged height of $\approx$ 100 nm the resist thickness is adjusted to reach $\approx$ 300 nm, if need be in several spin-coating steps (cf. Appendix A for detailed process parameters). After being baked at 150 °C for about an hour to remove any remaining solvent, the sample is structured by performing EBL with the help of a pattern generator (Xenos, XPG) attached to a SEM (Philips/FEI, XL30). Exposed patterns are more easily soluble when placed in developer (IPA:MIBK, 3:1) than parts of the resist that

have not been exposed by the electron beam. The sample is rinsed with deionized water afterwards to remove any excess developer and blow-dried with nitrogen. Subsequently, the substrate with the structured resist layer is placed in an evaporator, and a gold film is deposited via thermal evaporation. The evaporation rate can be controlled by the applied current and is monitored with an oscillating quartz. Depending on the rate, the holes in the resist layer close, and consequently conical structures arise, thereby higher rates result in steeper slopes, whereas lower rates result in sharper tips, as has been observed experimentally. If structures are manufactured directly on glass or silicon substrates, an additional adhesive layer can be beneficial to enhance robustness against further processing. After metallization, the sample is placed in acetone for several minutes (up to hours) for the lift-off step, in which the resist gets dissolved and the nanocones remain. The SEM inset on the left-hand side in Figure 3.1 exemplarily shows such a nanocone fabricated via thermal evaporation.

3.1.1.2 *Nanocones by Ion Milling*

Nanocones fabricated via ion milling have aspect ratios around one. Beneficial in this approach are the high range of sizes and the extraordinarily sharp tips [120] that can be realized with this process. Disadvantageous, however, is the higher number of crucial steps that influence a successful fabrication. The SEM inset on the right-hand side in Figure 3.1 exemplarily shows such a nanocone fabricated via argon ion milling.
Here, the substrate is completely metallized, so that the thickness of the gold layer matches or exceeds the desired height of the structures. Similar to above, electron beam sensitive resist is spin-coated (on top of the metal layer) and baked, and EBL is performed. After development of the pattern, an etch mask consisting of aluminum oxide is deposited via electron beam evaporation. Due to different etching rates for different materials, the height of this aluminum oxide mask needs to be individually adjusted. For gold the chosen ratio lies at one fourth of the nominal gold thickness. A lift-off process is performed to remove residual resist, and the sample is then placed in an argon ion milling machine (Roth & Rau, UniLab). There it is kept under constant rotation and targeted with accelerated argon ions. As a result, the metal layer is gradually removed by the sputtering effect, yet regions underneath the disk-like etch masks are spared. As the overall etching rate of aluminum oxide is lower than that of gold, yet the lateral one is bigger than the vertical one, the resulting structures are conical. The importance of uniformity of the etch masks and the influence of their heights and diameters can be seen in Figure 3.2. The SEM image on the left-hand side shows structures of a successful process, resulting in similar nanocones with sharp tips. The image on the right-hand

side only shows individual cones with sharp tips, while most of the structures are highly over-etched. This is due to variations of the etch mask disk diameters, otherwise it would suggest that the height of the metal layer underneath fluctuates on spatial dimensions of several hundreds of nm, which is not the case. As the argon ions are relatively well directed and the sample rotates during the whole process, the etching profile is quite uniform over several centimeters.

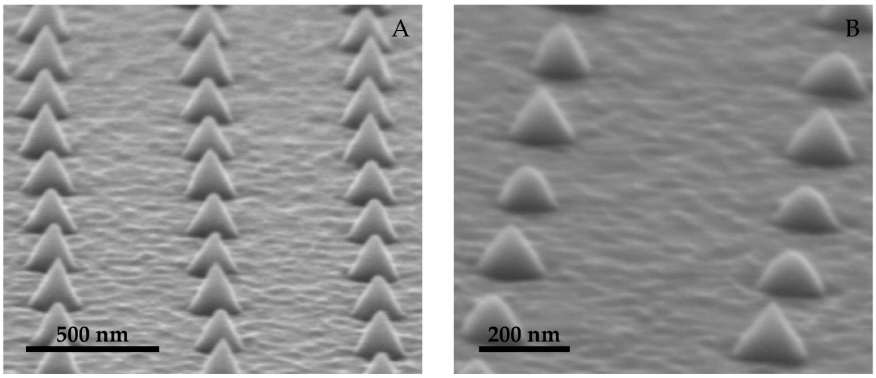

Figure 3.2: SEM images of arrays of gold nanocones fabricated via argon ion milling. The image on the left-hand side shows structures after a successful process resulting in quite uniform nanocones with sharp tips. The image on the right-hand side shows that only individual cones possess sharp tips, while others are over-etched. This is caused by an inhomogeneous etch mask with diverging disk diameters.

3.1.2 *Hybrid Systems*

Hybrid systems consisting of a plasmonic nanoantenna and a quantum emitter were fabricated using a self-aligned attachment process originally published in and adapted from *Fulmes et al., Self-aligned placement and detection of quantum dots on the tips of individual conical plasmonic nanostructures, Nanoscale, 2015* [121]. A schematic of the subsequent processing steps is shown in Figure 3.3. If the height of the structures to be embedded is already known, the process starts by spin-coating a layer of resist onto the sample, if need be in several steps, with its height being adjusted to exceed the cones' height by a few tens of nm. The sample is then prebaked at 150 °C for several minutes to evaporate any solvent residues. Unlike the process described in Reference [121], PMMA was chosen to embed the structures as residuals of the original resist (ma-P 1215 positive photoresist, Micro Resist Technology GmbH) could be detected as disruptive background signals in the optical measurements (cf. section 4.1.1). This problem could be solved by using the substitute. The first two SEM images below the schematic in Figure 3.3 show arrays of bare gold nanocones

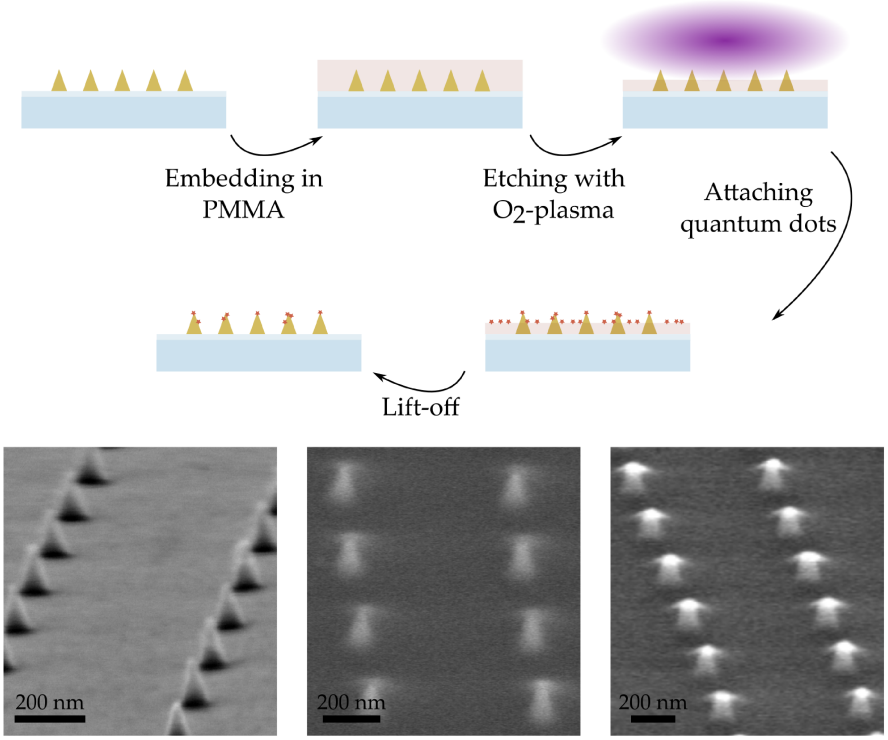

Figure 3.3: (Top) Schematic of the attachment process of quantum dots to the tips of gold nanocones. (Bottom) The SEM images show from left to right: array of gold nanocones fabricated via thermal evaporation, cones completely covered in PMMA and uncovered tips after the etching process with oxygen plasma.

or embedded in resist. The actual thickness of the resist is measured afterwards with a profilometer (Veeco, Dektak3030). To uncover the tips, oxygen plasma is applied using a reactive ion etching machine (Oxford Instruments, Plasmalab 80 Plus). The removal rate was tested before, and for process parameters of 20 W, 0.1 Torr, 100% O_2 the tips can be subsequently uncovered with 1.25 $\frac{\text{nm}}{\text{s}}$ [122]. It is advisable to split the etching process into several steps and to verify the remaining height in between times. It it also important to stop in time, as 4 s of additional oxygen plasma need to be added right before further processing steps can be carried out. This is done to activate the gold surface directly before the sample is functionalized. By the time the apexes are uncovered, one can see bright spots with enhanced contrast during SEM-imaging, as it is shown on the right-hand side at the bottom of Figure 3.3. For a quantitative study, an atomic force microscopy (AFM) raster scanning image (JPK Instruments, BioMAT Workstation, in the group of Prof. F. Schreiber) was taken of such a sample with unveiled tips, as it can be seen in the top panel of Figure 3.4. The positions of the nanocones can be clearly identified, however intensity, i.e. uncovered height, differs drastically for individual structures. The

white dotted line in the image displays the location at which a line scan was performed, as it can be seen in the bottom image of Figure 3.4. Irregularities in the structures' height forcedly result in an uneven profile, revealing bared tips ranging from 3 to 11 nm. This most likely is the biggest factor of uncertainty that influences the amount of quantum dots bound to the tips.
So, if the apexes are unveiled and the surface is activated, the sample is immediately immersed in a solution consisting of 3-mercaptopropionic acid (3-MPA) and deionized water for 30 min. This is done to adsorb a self-assembled monolayer to the tips' surface acting as linker molecules. The concentration is 0.02 g of 3-MPA in 20 mL of deionized water. The sample is rinsed with deionized water afterwards and exposed to CdSe/ZnS core-shell quantum dots (PlasmaChem GmbH, PL-QD-O-650) diluted in hexane (10 µg mL^{-1} for 24 h). Hexane was chosen over toluene (cf. Ref. [121]) as it does not dissolve the underlying PMMA layer. The quantum dots' ligand shell consisting of trioctylphosphine oxide (TOPO) and hexadecylamine (HDA) interlinks with the 3-MPA. Excess quantum dots are rinsed off with acetone and isopropanol, which simultaneously serves as gentle lift-off process. The overall attachment yield of quantum dots (single or few) bound to the apexes of gold nanocones was found to be ≈ 70% [121].

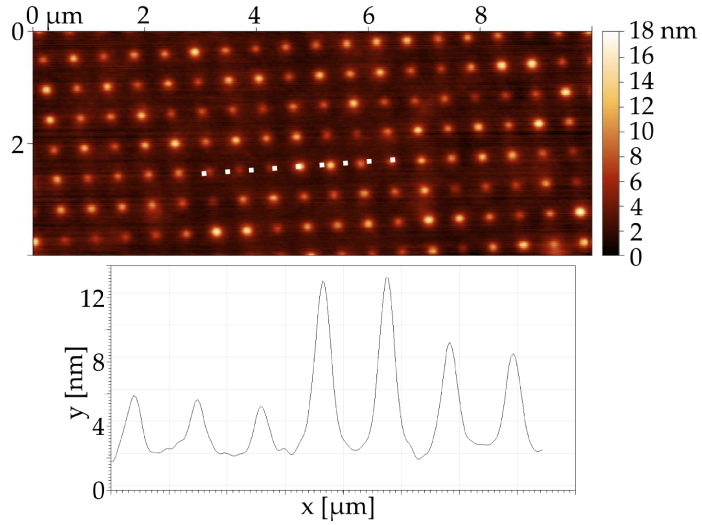

Figure 3.4: (Top) AFM raster scanning image of an array of gold nanocones embedded in PMMA with uncovered tips. (Bottom) Height profile at the position marked above as a white dotted line. The heights of the uncovered tips differ in a range from 3 - 11 nm.

3.1.3 *Bullseye Antennas*

Hybrid bullseye antennas, as they are introduced in section 2.3.2 and discussed in detail in section 4.2, are the promising result of a long-lasting cooperation with the group of Prof. R. Rapaport at the Racah Institute of Physics at the Hebrew University of Jerusalem in Israel (HUJI) and many joint efforts to combine two auspicious concepts of emission enhancement [123] and directionality modification [124, 125] in order to pave the way towards room-temperature quantum light sources.

Initial tries to design and individually optimize the antenna components, i.e. the bullseye and the nanocone, to fit together and divide the lithographic fabrication process of the device between both institutions have proven to be impractical. Figure 3.5 therefore shows a schematic of the finally applied fabrication process, split up between the two cooperation partners. The top part displays the processing steps for device fabrication [126] as it was done by Hamza Abudayyeh at HUJI using a template stripping method [127].

A silicon wafer is used as template material and is cleaned with piranha solution and acetone in a preparatory step. A focused gallium ion beam (1.1 pA) is used to etch an inverse nanocone (depth $\approx$ 180 nm, diameter $\approx$ 240 nm) into the substrate. Due to fabrication limitations, the resulting tip radii are rather big ($\approx$ 40 nm), which makes the precise attachment of quantum dots more difficult, yet offers simultaneously an obvious starting point for device optimization. Subsequently, the inverse bullseye rings are etched (240 pA) to reach a depth of 100 nm. To start the actual device fabrication, 250 nm of gold are deposited on the template. Labeled as glue in Figure 3.5, a layer of epoxy resist (SU8 3010) is spin-coated onto the gold film and prebaked at 95 °C for 5 min. A glass cover slip is attached to the SU8, and adhesion is enhanced by UV flood exposure (150 mJ/cm^2 for 15 s). As adhesion between bare silicon and gold is low, the gold film can then be stripped off with the glass/SU8 substrate, resulting in very smooth bullseye antennas. The silicon template can easily be reused for further fabrication cycles. The SEM image at the top of Figure 3.5 shows a nanocone in the center of the first few ring structures of such a fabricated device. The samples are then sent to *Tübingen* for the attachment of quantum dots to the nanocones' tips. The attachment process is similar to the one described in section 3.1.2, yet the process parameters need to be adjusted to cope with different materials. PMMA is spin-coated until a sufficient height is obtained ($\approx$ 220 nm). The prebaking step is done at 90 °C for 5 min, as higher temperatures lead to blisters, which destroy the (flatness of the) structures.

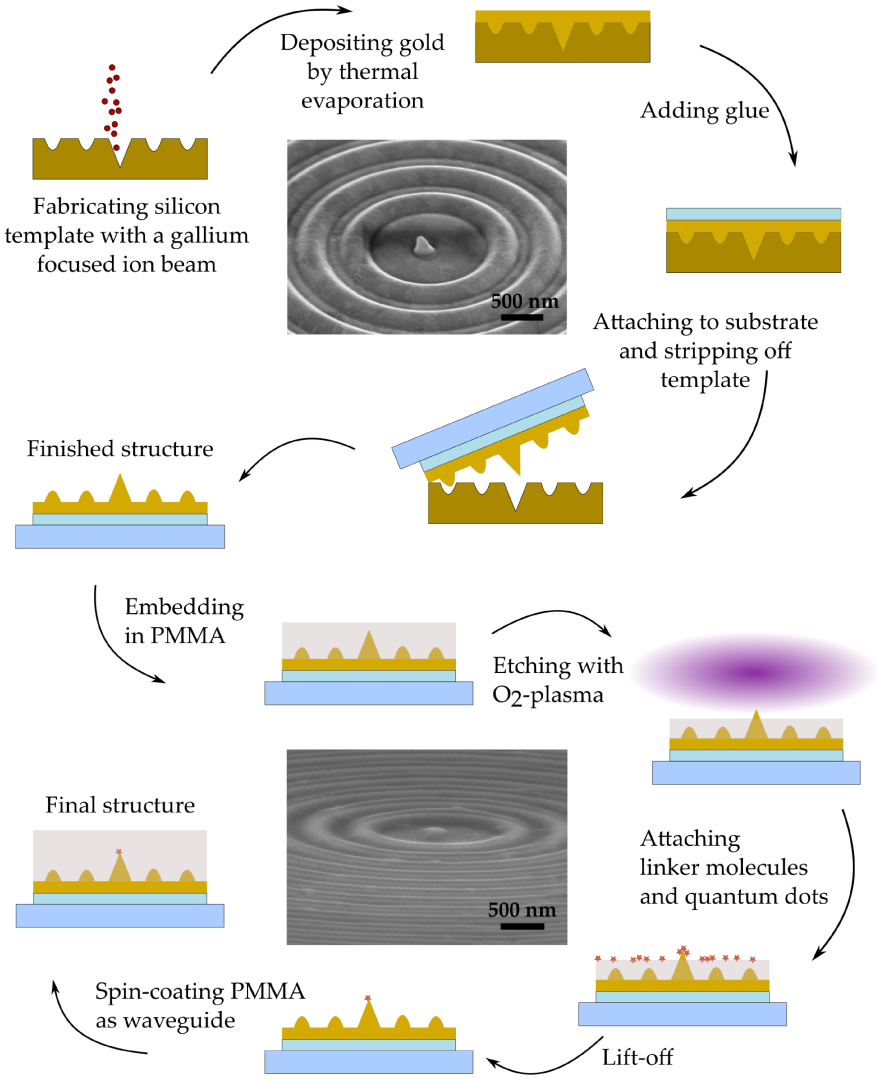

Figure 3.5: Schematic of the complete fabrication process of hybrid bullseye antennas. The upper part shows the template stripping method for antenna fabrictation as it is done at HUJI, while the lower part shows the attachment process for quantum dots as performed in this thesis. The SEM image at the top displays the center part of the finished device, the SEM image at the bottom shows the intermediate fabrication step of an antenna completely covered in PMMA.

Very careful handling is also required, as the height determination of the resist is more challenging. As there is a continuous gold layer underneath the structures, it can easily be scratched and thus falsify the height profile. Yet, looking at the resist layer with an electron beam in the SEM cross-links the PMMA and modifies its etching rates in the subsequent oxygen plasma treatments, leading to different height

profiles for regions that have and have not been imaged, respectively. Also, in regions on the sample that were overexposed during imaging, the resist layer can no longer be removed with the standard lift-off process using acetone, therefore leaving behind unusable devices. For this reason, SEM imaging is to be avoided during the attachment process.
Two different types of quantum dots were used, both possessing an emission maximum with $\lambda_{em} \approx 650\,\text{nm}$. For the devices described in section 4.2, commercial CdSe/ZnS core-shell quantum dots were used (cf. section 3.1.2), with a size of $\varnothing \sim 8\,\text{nm}$ and capped with trioctylphosphine oxide (TOPO) and hexadeclamine (HDA) ligands. As these quantum dots show relatively high fluorescence intermittency and fast bleaching behavior, a second type of quantum emitters (cf. [81, 126, 128, 129], giant CdSe/CdS core-shell quantum dots, $\varnothing \sim 17 - 19\,\text{nm}$) was used, which proved to be more stable. The attachment of quantum dots to the tips of the nanocones is verified at several antennas using the photoluminescence set-up described in section 3.2.5 and shown in Figure 3.17. If a luminescence signal can be detected (solely) at the positions of the nanocones, the samples are firstly stored in nitrogen atmosphere to prevent oxidation and are then vacuum sealed to be sent back to HUJI, where a final capping layer of PMMA ($h = 570\,\text{nm}$) is spin-coated to act as a waveguide. If no photoluminescence signal can be detected at the tips (or only occasionally) or if it appears at other positions than the tips, respectively, the samples are cleaned and the process needs to be repeated.

3.1.4 *Rectangles and Rhomboids*

The samples described in section 4.3 were fabricated by Andreas Horrer in the group of Prof. D. Gérard at the University of Technology of Troyes in France.
To start with, commercial microscope glass cover slips were cleaned, and a thin layer ($\approx 100\,\text{nm}$) of PMMA dissolved in MIBK (concentration of $30\,\frac{\text{g}}{\text{L}}$) was spin-coated. Afterwards, the samples covered in resist were baked at 160° for 1 h to remove any residual solvent. As no conductive ITO-layer was deposited and to still be able to perform EBL, a water-soluble conductive polymer was deposited before the pattern writing process and removed again by rinsing the sample in deionized water. Subsequently, the exposed structures were uncovered in a development step. The EBL process was performed on a Raith eLINE EBL system. Development was carried out in a mixture of MIBK and IPA (ratio 1 : 3) for 1 min. The samples were then rinsed with pure isopropanol and blow-dried afterwards with nitrogen. Subsequently, 3 nm of titanium dioxide were deposited by electron beam evaporation to serve as an adhesion layer. Even though it is more common to use pure titanium to enhance the adhesion, the use of titanium dioxide is

beneficial, as it does not increase absorption losses in the structures and also does not lower plasmonic enhancement [130]. Finally, a gold layer with a thickness of 25 nm was deposited by thermal evaporation. For the lift-off process, the samples were immersed in acetone for several minutes ($\approx$ 30 min), rinsed with isopropanol and again blow-dried with nitrogen.

3.2 OPTICAL SET-UPS

3.2.1 *Dark-field Scattering Spectroscopy*

Dark-field scattering spectra of different nanostructures discussed in this thesis were taken with modified commercial microscopes, namely with a Nikon Eclipse Ti-S inverted microscope in transmission and with a Zeiss Axio Scope A1 in reflection. Figure 3.6 shows the working principle of both microscopes, represented as boxes around the optical parts. For the transmission microscope, white light emitted from a 100 W halogen lamp is collimated, diffused and guided onto a dry dark-field condenser with a numerical aperture of $0.8 - 0.95$. The light is then focused onto the sample, which is located on a piezo scanning stage (Physik Instrumente, P-545.xR7). This enables accurate and repeatable positioning of the nanostructures for maximal signal detection. The scattered light is collected with an objective (Nikon, 60x Epiplan Achromat, NA = 0.7 or Nikon, 100x CFI Plan Fluor Oil Immersion, NA = $0.5 - 1.3$ if stated accordingly) and is then guided to a beam splitting device (20% reflection/ 80% transmission) outside of the microscope. From there, one part of the signal is sent to a fast-processing CCD-camera (XIMEA, MD028CU-SY) for imaging purposes and the other part is sent to a spectrometer (Andor, Shamrock SR-303i) equipped with a CCD-detector (Andor iDus DU416A-LDC-DD) cooled to $-40\,^{\circ}\mathrm{C}$.
For measurements in reflection, the excitation light originates from a 100 W halogen lamp as well and is also collimated and diffused. Dark-field illumination is achieved by using a microscope objective (Zeiss, 100x Epiplan Achromat and Epiplan Apochromat, NA = 0.95) with an integrated dark-field condenser with a numerical aperture of $0.97 - 0.99$. The sample is placed on a piezo scanning stage and the scattered light is collected with the very same objective and guided to the detection unit (camera and spectrometer) via mirrors.

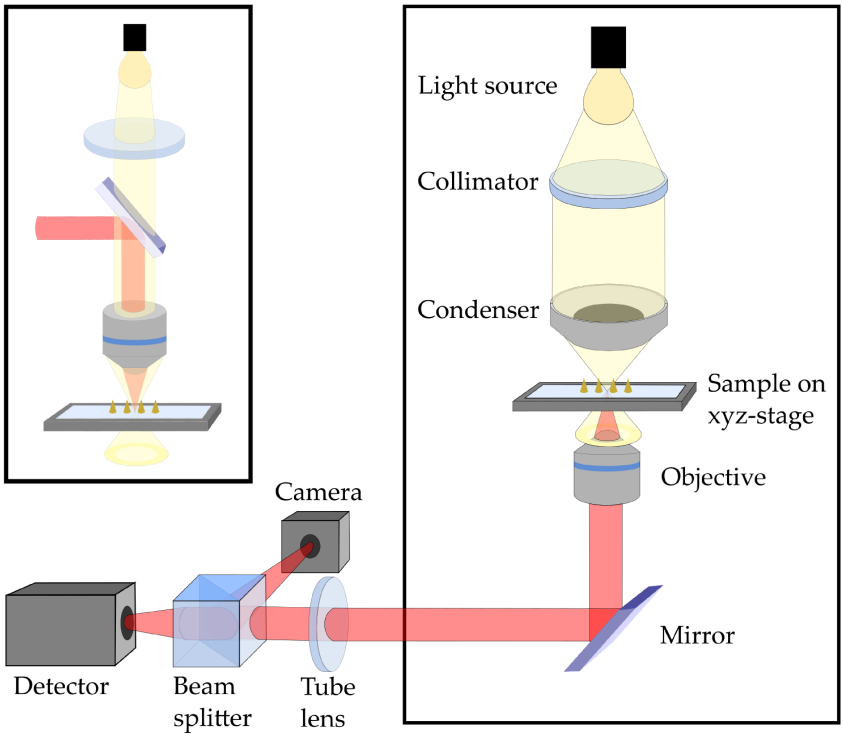

Figure 3.6: Schematic of the experimental set-up for transmission dark-field scattering spectroscopy. The smaller sketch shows the same principle for measurements in reflection. A collimated light beam originating from a halogen lamp is guided onto a dark-field condenser. There the middle part is blocked and the ring-shaped illumination beam is then focused onto the sample plane, where it can interact with the objects of interest. After passing through the sample, the excitation light misses the objective and is therefore not detected. Solely the scattered light is collected and can be measured with a detector.

3.2.1.1 *Influences of Optical Set-Ups on Experimental Results*

This parenthesis focuses on different appearances of experimental data dependent on the choice of optical set-up. For discussion, gold nanocones with high and low aspect ratios were investigated with the two dark-field scattering microscopes described above. Both geometries exhibit at least two plasmonic modes that are *spatially* separated, i.e. being oriented in-plane (base mode) and out-of-plane (tip mode). Naively, when thinking of two dark-field scattering spectra of an individual nanocone, one taken in transmission and one taken in reflection, respectively, one might expect to find the spectra to be quite similar. This expectation neglects the influence of the optical components in the set-up, i.e. the numerical apertures of the objectives and more importantly - of the condensers. Figure 3.7 illustrates the case for a nanocone with a slightly elliptical base, as it can be seen in the SEM image. The small inset shows a top view. The scattering spectra on the left were taken with the exact set-ups described in section 3.2.1 and are

normalized to unity for better comparability. While the discrepancy becomes apparent at first sight, the similarities are harder to detect.

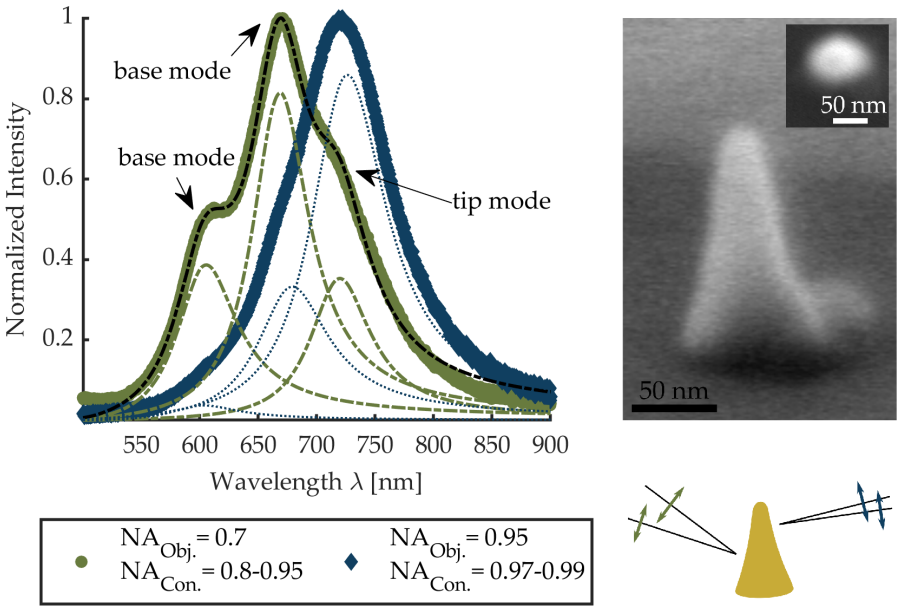

Figure 3.7: Dark-field scattering spectra of the individual nanocone shown in the SEM image (the inset shows the top view). The green spectrum is measured in transmission, the green dash-dotted lines show Lorentzian fits (sum in black) to the data. The blue spectrum is taken in reflection, and the blue dotted lines represent the corresponding Lorentzian fits. The sketch on the bottom right depicts the range of in-coming light vectors for the respective condenser together with the orientation of the electric field vectors for p-polarized light.

The dark blue curve represents the scattering spectrum taken in reflection and shows apparently two modes, where one peak is only visible as a small shoulder at $\sim 600\,\text{nm}$. In contrast, the green curve shows the scattering spectrum taken in transmission and exhibits three resonances, where one peak is hidden in the bulky slope at higher wavelengths and is again only discernible as a shoulder at $\sim 740\,\text{nm}$. Since for nanocones with high aspect ratios the out-of-plane resonance occurs at higher wavelengths than the in-plane resonance, the highest peak at $\sim 675\,\text{nm}$ could be easily attributed to the tip mode, yet the situation is more complex. As the base of the nanoantenna is elliptical and therefore two in-plane modes are expected, the out-of-plane resonance is actually visible as the shoulder at $\sim 740\,\text{nm}$. The resonance position of the tallest peak in the blue reflection spectrum coincidences with this mode. Also the other two modes can be found at a second glance, as the resonance at $\sim 675\,\text{nm}$ also hides in the slope of the out-of-plane mode. It is worth mentioning that the relative strengths of the two base-modes are similar in both measurements, i.e. the resonance along the major axis ($\sim 675\,\text{nm}$) exceeds the resonance along

the minor axis ($\sim 600\,\mathrm{nm}$) in intensity. This is consistent with the fact that intensity scales with the length of the particle, and excitation of different in-plane modes with unpolarized light is almost independent from the angles of the in-coming *k-vectors*, as s-polarized light contributes the most besides in-plane components of p-polarized light. In the spectrum (blue) taken at the reflection set-up, the intensity of the tip mode now clearly outvalues the intensities of the base modes compared to the transmission case. This is due to the changed excitation geometry, as the numerical aperture of the dark-field condenser at the reflection microscope is notably higher, and therefore the electric field components in the direction of the cone's axis predominate. The schematic at the bottom right of Figure 3.7 illustrates the incoming k-vectors and corresponding electric field vectors for p-polarized light. The importance of numerical apertures and their influence on the detected optical signals, for imaging purposes as well as for spectrally resolved responses, is visually depicted in Figure 3.8. The example shows dark-field scattering spectra for two individual nanocones with differing aspect ratios as shown in the SEM insets at the top. The varying geometries provide aspect ratios of < 1 and > 2, leading to spectrally reversed base- and tip modes. The spectra were taken in transmission and reflection, respectively (cf. section 3.2.1).
As mentioned before, the structures were therefore excited with different ratios of s- and p-polarized light. For both nanocones two peaks occur, representing the in-plane and out-of-plane resonance, respectively. For the low aspect ratio structure shown on the left-hand side of Figure 3.8 the in-plane resonance is more pronounced in both optical set-ups, yet the out-of-plane resonance (located at lower wavelengths) gains intensity when excited and detected more efficiently with higher NAs (blue spectrum). For the high aspect ratio nanocone shown on the right-hand side of Figure 3.8, the tip mode is now located at higher wavelengths and clearly outvalues the base mode in intensity in both set-ups. The in-plane resonance is not even visible when measured at the reflection set-up (blue spectrum), even though it is detected more efficiently than the out-of-plane resonance.
While spectra, i.e. spectrally resolved intensity distributions of scattered light, are obtained by integrating over a certain range (in y-direction) of the CCD-chip, some spatial information is lost. The two lower rows in Figure 3.8 show the corresponding full detector images of the first order of diffraction for the transmission set-up (center) and the reflection set-up (bottom). All images have been background-corrected and are normalized to the reference spectrum according to $I_{spectrum} = \frac{I_{structure} - I_{background}}{I_{reference} - I_{dark-current}}$. It can be seen that light originating from the out-of-plane mode shows a spatial modulation in y-direction, which will be further investigated in the following.

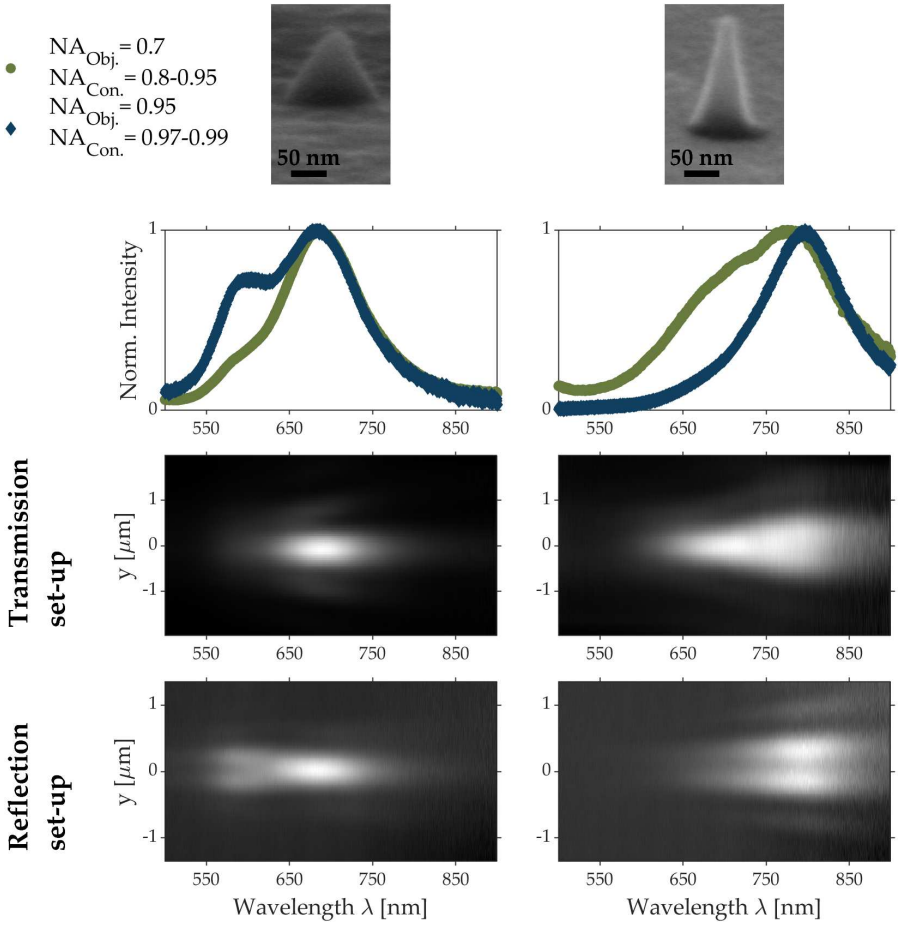

Figure 3.8: Comparison of dark-field scattering spectra for nanocones with two differing aspect ratios (shown in the SEM insets) taken at different optical set-ups. The green spectra are measured in transmission, while the blue spectra are taken in reflection, respectively. The lower rows show detector images of the first order of diffraction, i.e the spectrally resolved impacts of light on the detector. Different modes, i.e. dipole orientations in the structure, can be identified by the observed spatial pattern.

The influence of the numerical aperture of the objective in the detection path on the spectral shape becomes clear when the radiation pattern of a point-like dipole light source is considered. Figure 3.9 shows the computed scattering spectrum for a nanocone modeled after the SEM image (aspect ratio < 1) and placed on a semi-infinite glass substrate. The structure is illuminated with p-polarized light and an incoming k-vector with NA $= 0.98$. The two lower rows show corresponding cross-sectional radiation patterns (in the x-z-plane, 100x magnified) at the resonance wavelengths of both detected modes.

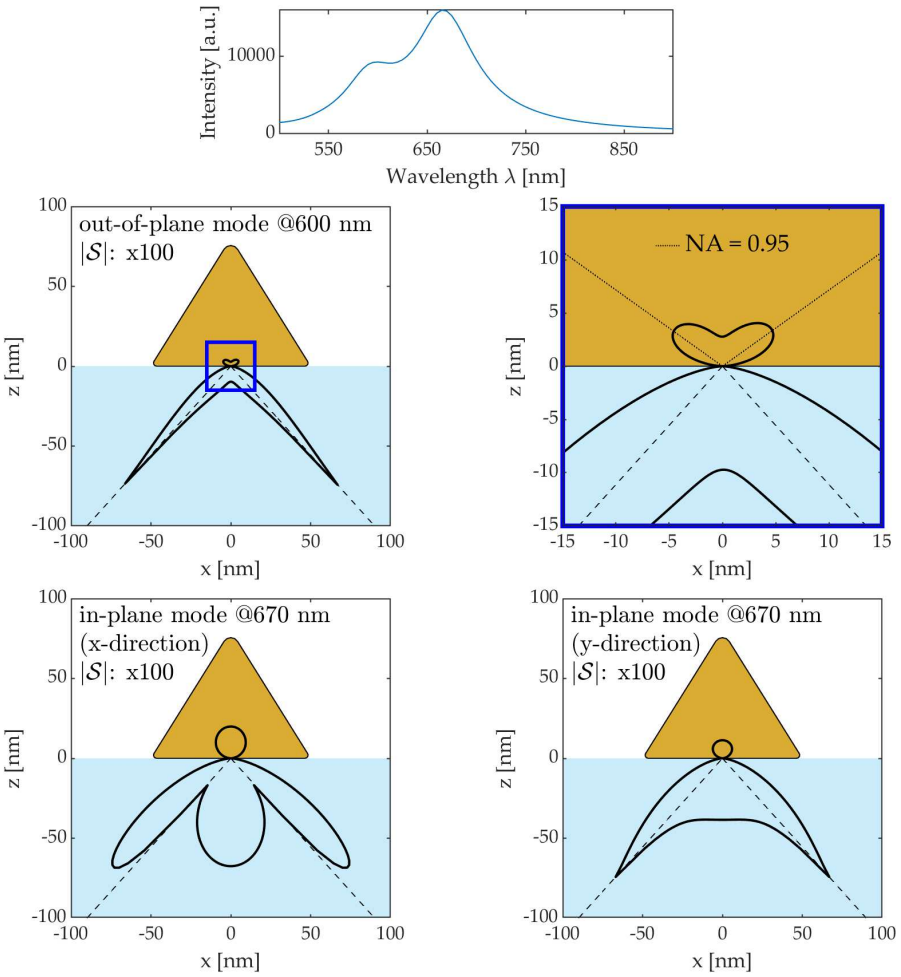

Figure 3.9: Computed scattering cross section (spectrum) and radiation patterns for a nanocone with aspect ratio of 0.75. The center row shows the radiation pattern at the resonance wavelength of the out-of-plane mode along the cone axis, while the bottom row shows radiation patterns at the resonance wavelengths of the in-plane modes along the base for an incoming plane wave polarized along x and y, respectively. The dashed lines indicate the critical angle for an air/glass interface.

These radiation patterns are calculated from the directional energy flux $\mathcal{S}$ according to

$$|\mathcal{S}| = \sqrt{\sum_{k=1}^{3} \left| \frac{1}{2} \cdot \Re(E \times H^*)_k \right|^2} \tag{3.1}$$

and clearly resemble the expected patterns [57] for differently oriented point dipoles located on a substrate. The center row in Figure 3.9 illustrates the directionality of light emission at $\lambda = 600\,\text{nm}$ and clearly validates the out-of-plane character of the plasmon resonance. To maximize intensity of the detected signal, transmission measurements seem preferential over reflection measurements, as most light

is irradiated into the lower half-space, i.e. the medium with higher refractive index. Yet, signal strength highly depends on the choice of objective. For an air-objective, as it was used in the transmission measurements shown in Figure 3.8 and Figure 3.10, the light needs to pass an interface upon leaving the substrate. The dashed lines in the lower part consequently mark the critical angle for a glass-air interface, above which no light can leave the substrate and therefore can not be detected. The already small amount of light that passes through the substrate finally gets diffracted at the interface before being collected with the objective. The case differs if an oil-objective is used, as the interface vanishes and even higher angles can be detected. The close-up on the right-hand side shows the emission pattern into the upper half space, i.e. into air. The pattern resembles the doughnut-shaped emission as known from dipoles oriented along z. The dotted line marks the collection NA of the used objective in reflection, and it can be seen that a high fraction of k-vectors can be detected. The lower row in Figure 3.9 shows radiation patterns for degenerate in-plane dipolar modes oriented along x (left) and y (right) at $\lambda = 670\,\mathrm{nm}$. It becomes clear that the detection of in-plane resonances is far less sensitive to the NAs of the collection objectives.

To substantiate these findings, Figure 3.10 shows the corresponding intensity distributions on the CCD-chip of the zeroth order of diffraction for the individual particles. While for particles with pronounced base modes the intensity distribution resembles a well-known *Airy* disk, the distribution clearly differs for the high aspect ratio nanocone excited with the high NA objective in the reflection set-up. The diffraction image shows a ring-shaped pattern, as it is expected for a point dipole oriented along z-direction. As for this structure the out-of-plane mode is also dominant in the spectrum measured in transmission, the ring shape also shows up in the diffraction image, but is superimposed with the point spread function of the in-plane mode. The bottom row in Figure 3.10 shows computed images of point dipoles oriented in different directions, calculated with the help of the *Nanopt Toolbox* accompanying the textbook [58] by U. Hohenester. The images show intensity distributions of electric fields emitted by point dipoles and imaged through lenses, dependent on the respective refractive indexes of surrounding medium and lens material, the wavelength of the emitted light and the NA of the collection lens. The first two pictures show the intensity distributions at the resonance positions of the respective modes and a NA of 0.7. Even though the intensities are not weighted and in reality more wavelengths contribute, the superposition of both distributions matches the measurement satisfactorily. The agreement can be seen even better in the reflection measurement, where only the out-of-plane resonance is visible.

A detailed description and derivation of the calculations can be found in [131], Chapter 6, 'Diffraction Limit and Beyond'

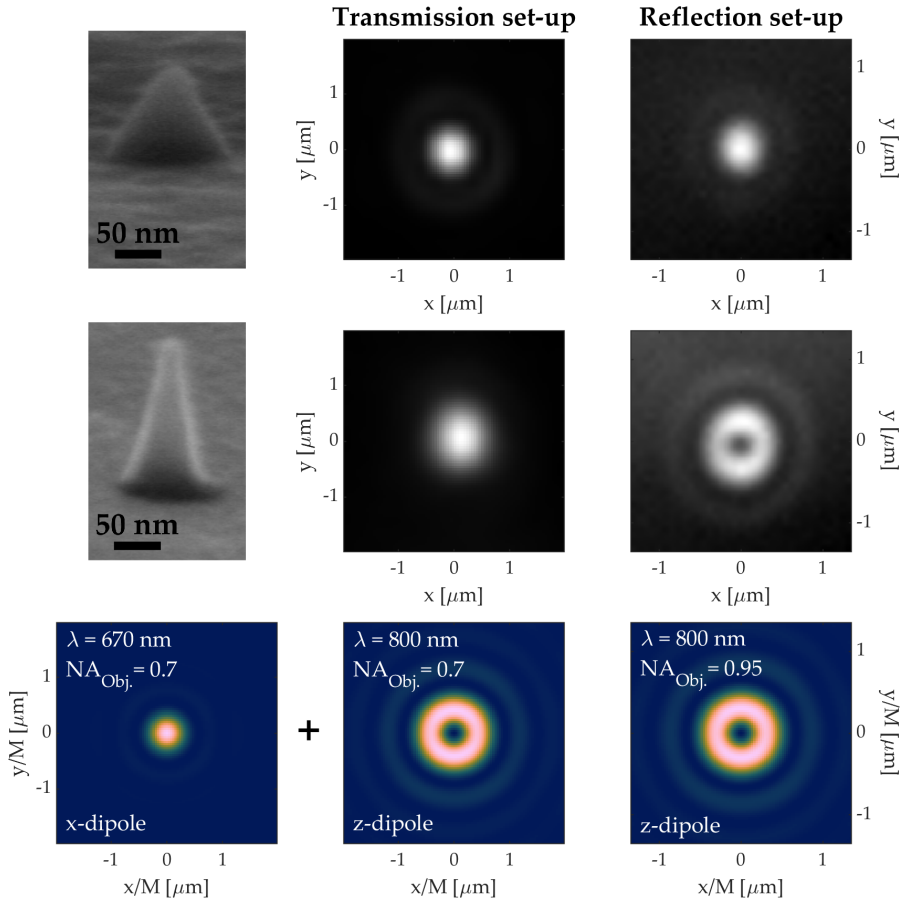

Figure 3.10: (Top and center row) Detector images of the zeroth order of diffraction, i.e. the diffraction limited images of the nanostructures shown on the left (acting as point-like light sources) in real-space. (Bottom row) Computed images, i.e. field intensities of dipoles oriented along x and z, respectively, for different wavelengths and NAs, calculated according to [131].

3.2.2 *Polarized Dark-field Scattering Spectroscopy*

The polarimetric measurements discussed in section 4.3 were taken with a modified dark-field set-up at the transmission microscope described in section 3.2.1. Figure 3.11 shows a scheme of the optical components and their location in the optical path. The additional crucial components are two rotatable polarization filters (Thorlabs, Ultra Broadband Wire Grid Polarizer, WP25M-UB) in the excitation and analyzation path, respectively, and a cross-like aperture, the necessity of which is described in the following. Finally, a removable back focal plane lens can be set in the optical path to get an image of the excitation beam in *k-space* on the detector.

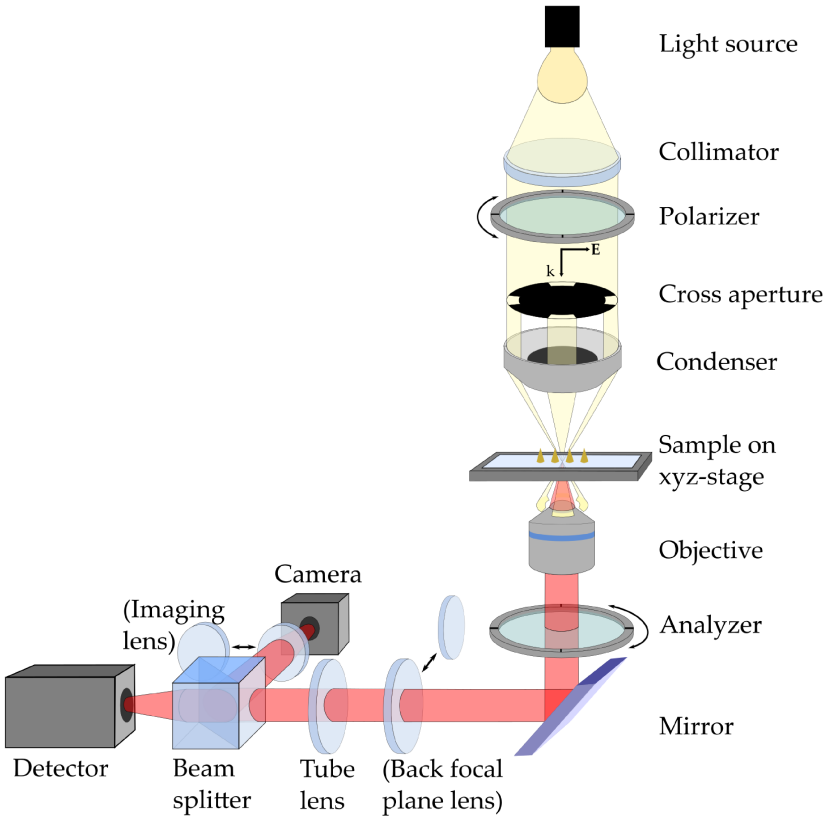

Figure 3.11: Schematic of the experimental set-up for polarization-resolved dark-field scattering spectroscopy. The back focal plane lens and the corresponding imaging lens in front of the camera are optional.

Figure 3.12 shows the white light reference spectrum (brown line) recorded with a polarization filter in the excitation path (oriented along $\Phi_{exc} = 45°$). When an additional cross-polarized analyzer is added to the detection path, complete cancellation of the light is expected, yet the green line shows some remaining signal on the order of one-tenth of the incoming light. As the manufacturer specifies an extinction ratio $> 1000 : 1$ for the polarizing components, the origin of this residual light must be due to some kind of depolarization in between the two filters, as the signal is too intense to originate solely from incoherent background scattering.

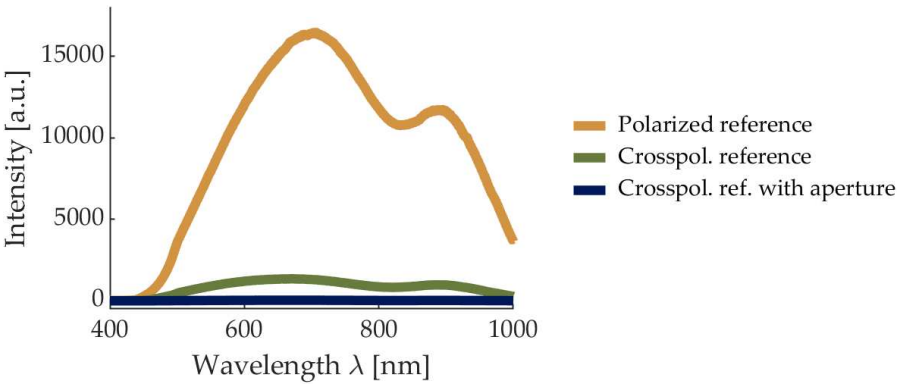

Figure 3.12: Reference spectra of the excitation for polarized light (brown), polarized excitation and cross-polarized analyzation (green), and the latter with additional cross-aperture (dark blue) in the optical path.

When linearly polarized light is focused with an optical element, the polarization orientation is not maintained for all k-vectors. Figure 3.13 shows a calculated top view image of this effect, where incoming light (k-vectors into the sample plane) is polarized along $\Phi_{exc} = 45°$ and then focused onto the sample with the condenser. It becomes clear that the polarization orientation is maintained only in a narrow angular range, see arrows highlighted with thicker lines, and for most of the light the polarization orientation is rotated by different extents, therefore leading to noteworthy signals even in the cross-polarized case. With the aperture mentioned above it is possible to explicitly select only the desired polarizations. A sketch of the cross-like aperture is shown in Figure 3.13. It was designed in such a way that it can be placed inside the dark-field condenser right before the collimated beam is focused and it is rotatable, so that it can be adjusted to the incoming excitation polarization orientation. The dark blue line in Figure 3.12 shows the reference spectrum for the cross-polarized case with the additional aperture placed in the detection path. Almost all intensity is cancelled out apart from a small background signal due to some stray light.

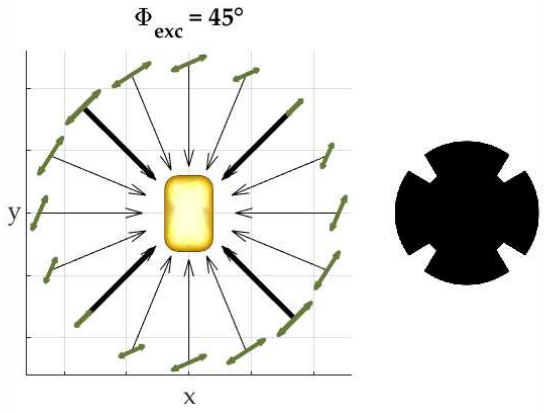

Figure 3.13: Left: Depolarization effect of the dark-field condenser for incoming light with the electric field being polarized along $\Phi_{exc} = 45°$. The polarization orientation maintaining k-vectors are highlighted with thicker lines. Right: Sketch of the rotatable cross-aperture.

This effect was further visualized by taking back focal plane images (see also section 3.2.3) of the excitation light. Therefore, the back focal plane lens is inserted into the optical path as can be seen in Figure 3.11. A clean and empty part of the sample is placed on the sample holder, and the 100x objective is focused using immersion oil (Zeiss, Immersol^{TM} 518F, n = 1.518). The adjustable Iris-aperture needs to be fully opened to maximize the collection angle. Figure 3.14 shows on the left-hand side a k-space image of the illumination ring (NA = $0.8 - 0.95$) of the dark-field condenser for polarized incoming light, the upper row displaying an excitation polarization of $\Phi_{exc} = 45°$ and the lower row of $\Phi_{exc} = 0°$ ($\Phi_{exc} = 90°$ looks similar). The three small black lines are a component-related feature of the blocking part of the condenser. The center images show the same illumination ring with an additional cross-polarized analyzer placed in the detection path. The polarization orientation maintaining angles can be easily identified by the black gaps, the bright parts correspond to the residual (compare to Figure 3.13 and note change in colorbar limits) depolarized signal. The images on the right-hand side finally show the illumination ring from before with the additional cross-aperture placed in the excitation path. By comparing the azimuthal angular range, it can be seen that the depolarized parts of the light can be sufficiently blocked, and only the polarization-maintaining parts reach the detector. As most of the excitation light is blocked in this set-up and additionally single particles are investigated, the plasmonic scattering intensities are also quite low. To maximize the detector sensitivity, the CCD-chip was cooled to $-60\,°C$, and the integration time for each spectrum was set to 20 s, averaging three times to reduce noise.

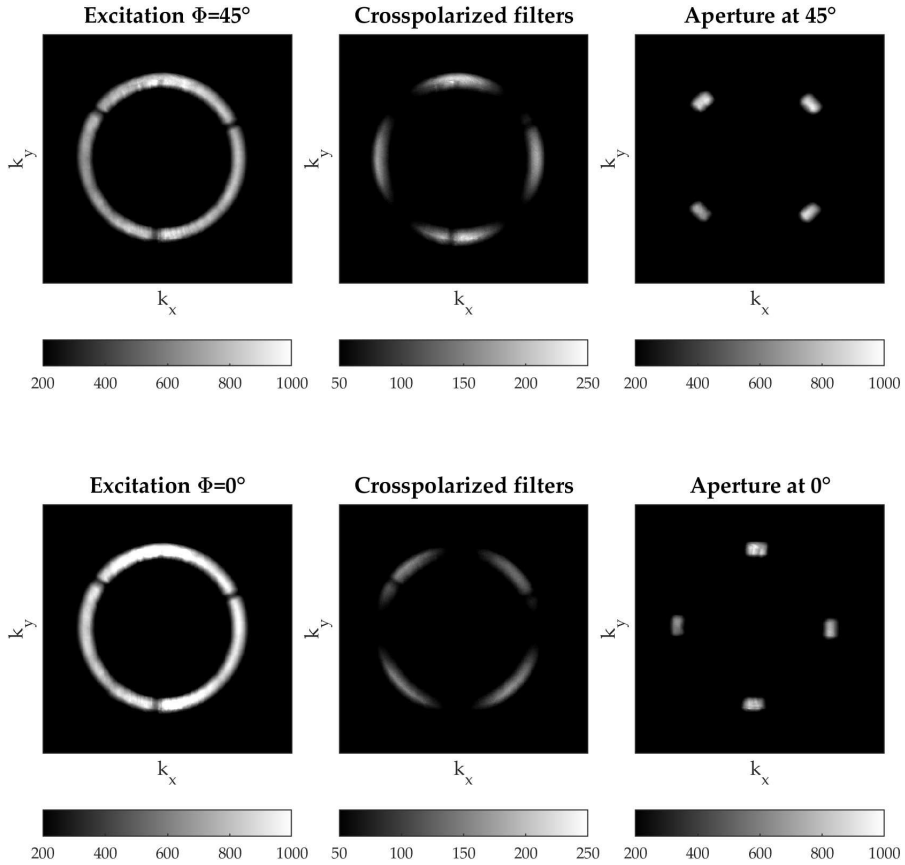

Figure 3.14: Back focal plane images of (left) the illumination ring of the dark-field condenser and polarized excitation for (upper row) $\Phi_{exc} = 45°$ and (lower row) $\Phi_{exc} = 0°$ (the three small black lines are a built-in condenser feature), (center) of the illumination ring with a cross-polarized analyzer but without aperture, and (right) the same pattern as on the left but with the designed cross-aperture placed in the excitation path.

3.2.3 *Back Focal Plane Imaging*

Back focal plane (BFP) measurements allow for visualizing radiation patterns, as the k-vectors of the (emitted) light are imaged on the detector plane. This means that each point in a back focal plane image corresponds to a direction in which the light propagates. The ability of detecting radiation patterns is of great interest when it comes to measuring fluorescence enhancement, as the amount of the detected light will be highly dependent on the propagation direction of the emitted light. It is also an essential tool when it comes to characterizing the directionality of an emitting quantum light source, as it was performed in section 4.2.
Figure 3.15 shows in the top panel the optical path of light for imaging an object, which is located in the sample plane, in real-space, while the bottom panel shows the optical path for imaging in k-space. Objectives used in standard microscopy are infinity corrected, meaning the light

is collimated upon exit, and the back focal plane of the lens system is located inside of the component. The 100x Nikon objective used in this set-up (cf. section 3.2.1) has a continuously variable Iris-aperture to set the NA to the desired value. As this diaphragm is located in the back focal plane, it can be adjusted in such a way that the edges can be used as the object in the sample plane. So to create an image of this back focal plane an additional lens is needed. A convenient configuration is the so-called *4f* set-up, in which the focal length of the BFP lens matches the focal length of the tube lens. The distances between the individual components is chosen in such a way that the *real* back focal plane is located in the front focal spot of the BFP lens. In this configuration an intermediate image plane is located right in between the two lenses at the shared focal spot. If a pinhole is placed at this exact position in the optical path, distinct points in the sample plane can be selected individually. This can be used in the dark-field set-up (see section 3.2.1) to image the emission of single nanostructures, even though a whole region is illuminated in the sample plane.

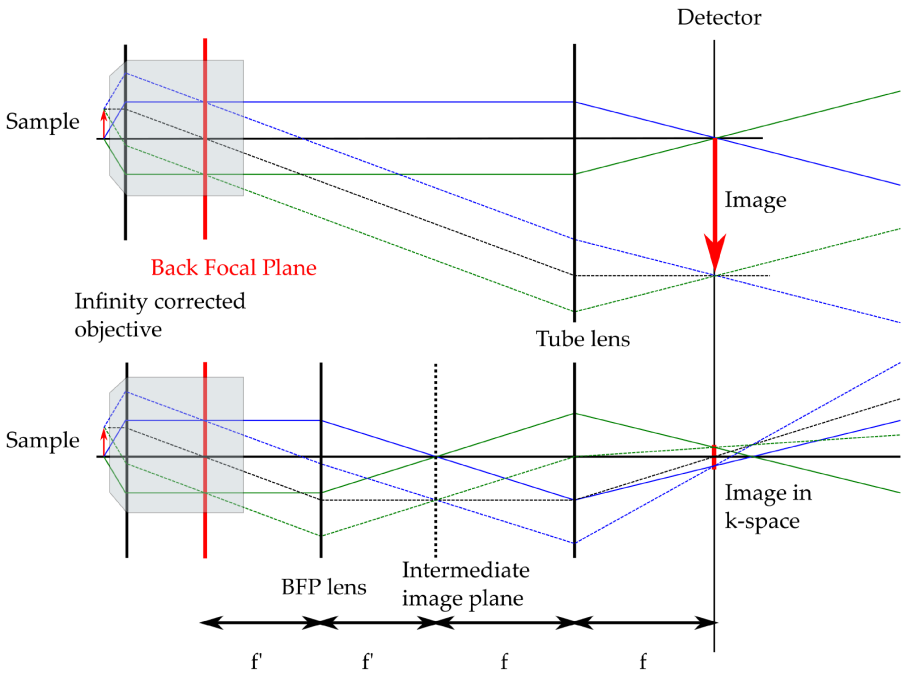

Figure 3.15: Optical paths for (top) real-space imaging and (bottom) k-space imaging in a 4f-configuration.

3.2.4 *Confocal Microscopy*

The (photoluminescence) measurements described in this thesis were conducted at different optical set-ups in varying laboratories. Yet, the common ground of all those set-ups is the usage of confocal microscopy, whose working principle is sketched in Figure 3.16. A collimated (laser) excitation beam (in blue) is focused onto the sample

through the (infinity corrected) microscope objective by passing a dichroic mirror, which is wavelength specific and blocks the reflected excitation light. The emitted light of the fluorescent specimen (in red) is collected through the very same objective, passes through the dichroic mirror and is focused onto a pinhole before reaching the detector. This method allows for detecting sharp images of the specimen originating only from the focal plane of the objective. Fluorescence light emitted from other regions or other unwanted background signals (in green) will leave the objective with random divergence and will therefore be mostly cut off by the pinhole.
In set-ups designed for spectroscopic purposes, as described in section 3.2.1, the pinhole is replaced by the built-in and adjustable slit at the entrance port of the spectrometer. In such set-ups, the collected light is focused by the tube lens onto the slit (i.e. pinhole) before it is detected after being spectrally split upon passing through the spectrometer.

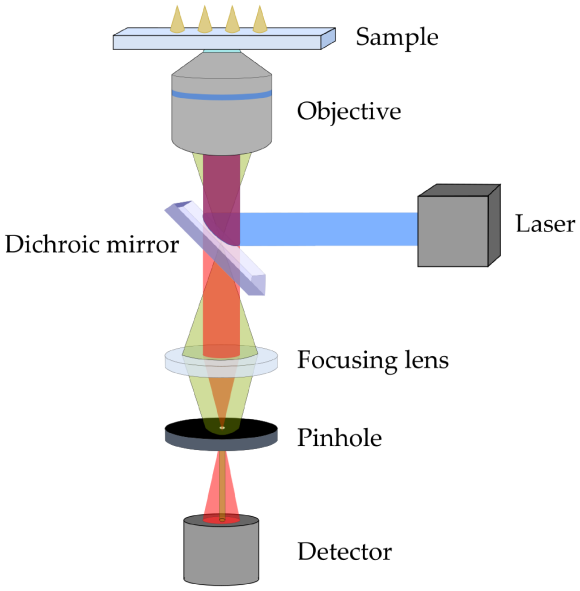

Figure 3.16: Working principle of confocal microscopy. A collimated excitation beam (blue) is focused onto the sample through a microscope objective. Emitted light originating from the focal plane (red) is focused through a pinhole to reach the detector. Light emitted from areas outside the focal volume (green) will barely pass the pinhole and therefore only a very small fraction will reach the detector.

3.2.5 *Photoluminescence Spectroscopy and Set-ups*

As mentioned before, various experiments described in this thesis were performed in different laboratories. Even though the measuring procedure for photoluminescence measurements is similar in all experiments, the focus is on different priorities. Therefore, the individual set-ups are described in the following.
The optical set-up described in section 3.2.2 has been extended for the possibility to conduct confocal photoluminescence spectroscopy measurements and back focal plane imaging, respectively. A scheme of the modified set-up is shown in Figure 3.17. A continuous wave, diode-pumped solid state laser (LaserQuantum, gem473) with a wavelength of $\lambda = 473\,\text{nm}$ and an output power range of $50 - 500\,\text{mW}$ is used as the excitation source. The excitation light is sent through a laser line filter to block remains of the pump laser before passing through a selectable set of neutral density (ND) filters with varying attenuation factors to adjust the power. The beam is cleaned by passing through a polarizing beam splitter cube which assures a defined linear polarization dependent on its orientation in the optical path. In this set-up, the polarization was adjusted to be horizontally oriented, yet it can be easily changed by inserting polarization optics into the optical path. (Optional optical elements are indicated by dashed lines in the figure.) The linear polarization of the light can be rotated by any amount by inserting a half-wave plate or it can be transformed to elliptical or circular polarization by inserting a quarter-wave plate. The light is then coupled into the objective by being directed towards a ND beam splitter (Chroma, ND-BS 20R/80T) via two vertically stacked mirrors. In most set-ups a dichroic mirror is the straightforward choice to guide the excitation light towards the sample and to block it from reaching the detector. Yet, here, a ND beam splitter was chosen followed by a notch filter (Semrock, NF03-473E-25), which only blocks the excitation wavelength in a small range of $\approx 13\,\text{nm}$. This choice is made to avoid unwanted side-effects concerning the retention of polarization in dichroic mirrors. Due to the nature of their working principle they show a wavelength-dependent phase shift between s- and p-polarized light, which becomes visible in polarimetric measurements. For the explicitly named components and supported by their data sheets, no differences could be observed in s- and p-polarized transmittance, therefore enabling polarimetric spectroscopy measurements. The choice of a notch filter provides the additional advantage of offering the possibility to measure anti-Stokes signals, for example in anti-Stokes Raman scattering [132] or anti-Stokes photoluminescence [133] (if higher excitation wavelengths are available). Lastly, the emitted light passes through the filter and is directed to the detection path, which is identical to that described in section 3.2.2.

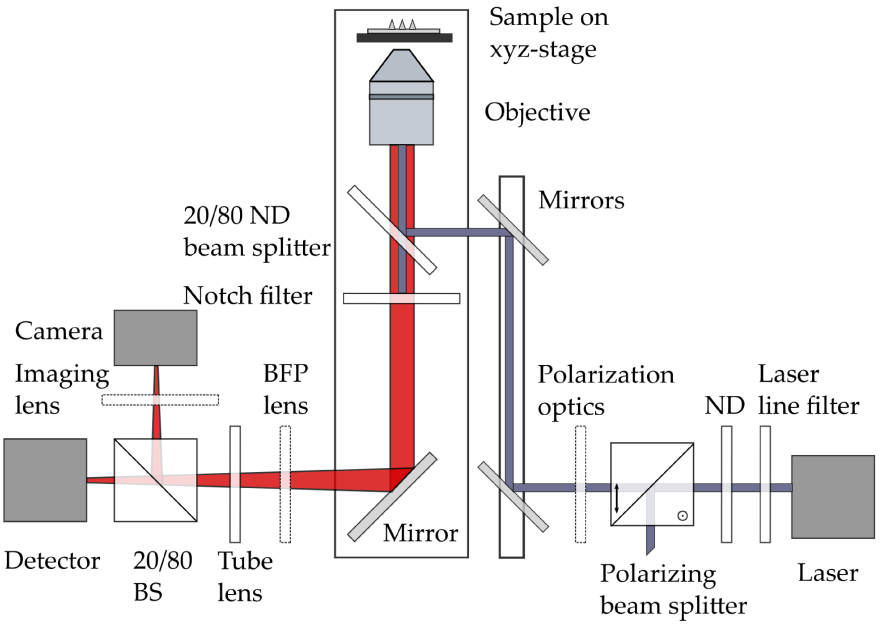

Figure 3.17: Schematic of the optical set-up for photoluminescence measurements at the transmission dark-field microscope. Elements sketched with dashed lines are optional.

3.2.5.1 *Photoluminescence Measurements of Quantum Dots on Nanocones*

Photoluminescence and lifetime measurements of the hybrid systems described in section 4.1 were performed by Regina Jäger and Kerstin Scherzinger in the group of Prof. A. Meixner at the Institute of Physical and Theoretical Chemistry.
The optical set-up consists of a home-built confocal microscope. A sketch of the set-up is given in Figure 3.18. It features the advantageous possibility to couple in different laser wavelengths [134]. For continuous-wave excitation, as it is used in photoluminescence imaging and spectroscopy measurements, it can be chosen from an Ar^+Kr^+ gas laser (Coherent Inc., Innova 300) providing several wavelengths between $\lambda = 450\,\text{nm}$ and $\lambda = 647\,\text{nm}$ and a HeNe laser at $\lambda = 632.8\,\text{nm}$. For the photoluminescence measurements described in section 4.1, the Ar^+Kr^+ laser was set to $\lambda = 488\,\text{nm}$. The excitation power can be controlled by inserting neutral density (ND) filters with different attenuation factors into the optical path. For the measurements the laser power was set to $1\,\mu\text{W}$. Before the beam is focused onto the sample, it is adjusted by the following steps: the beam is cleaned by passing a linear polarizer before it is converted to a radially (RPM) or azimuthally (APM) polarized Gaussian mode [135], respectively, by an electrically driven liquid crystal mode converter (ARCoptix, Radial Polarization Converter). The polarized beam is focused through a pinhole, which acts as a spatial filter to obtain a doughnut shape, the

so-called cylindrical vector beam, and then passes through a laser line filter to block unwanted wavelengths. Subsequently, it is guided towards the objective with a dichroic mirror, which blocks the excitation light in transmission. The excitation beam is focused through an oil immersion objective (Zeiss, 100x CP-Achromat, NA=1.46) onto the sample, which is located on a three-axis piezo scanning stage (Physik Instrumente, P-517.3CL). The emitted light is finally collected with the very same objective, transmitted through the dichroic mirror and guided towards the detector. Dependent on the respective application, also the detection path can be chosen individually with an optional flipping mirror.
For the raster scan images shown in section 4.1.1 (Figure 4.10), the excitation beam was converted to a radially polarized doughnut mode, and the sample was scanned through the diffraction limited focus of the RPM. The fluorescent signal was guided to an avalanche photo diode (APD) (Perkin Elmer, SPCM-AQR-14), and the integration time was set to 5 ms per pixel. The measurements showing fluorescence intermittency were also detected with the APD, followed by single photon counting electronics (PicoQuant, PicoHarp 300). The binning time was set to 5 ms. For the fluorescent spectra, the signal was guided to a spectrometer (Princeton Instruments, Acton 300 pro) equipped with a nitrogen-cooled CCD-detector (Princeton Instruments, Spec-10) and the integration time was set to 3 s.

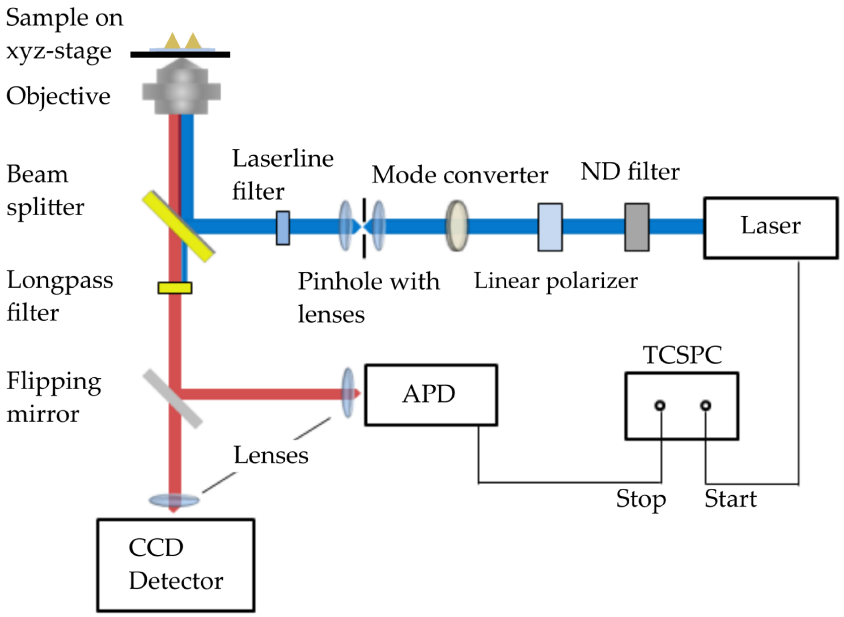

Figure 3.18: Schematic of the experimental set-up for confocal lifetime and photoluminescence measurements. Figure modified from Ref. [136].

Lifetime measurements were performed using a pulsed supercontinuum laser (NKT Photonics, SuperK Extreme EXB-4) operating at a repetition rate of 20 MHz as the excitation source. For reasons of consistency the laser wavelength was also set to $\lambda = 488$ nm by using an acousto-optical tunable filter (NKT Photonics, SuperK Select). The emitted light was guided to a spectrally integrating detector (Micro Photon Devices, PDM series) connected to a time-correlated single photon counting system (TCSPC), providing a photon timing resolution better than 50 ps FWHM, according to the manufacturer. With this, lifetime histograms as described in section 4.1.1 were taken by integrating the signal until a reasonable amount of counts was collected for further data evaluation.

3.2.5.2 *Photoluminescence Measurements of Hybrid Bullseye Antennas*

The optical measurements of the hybrid bullseye antennas described in section 4.2 were performed by Hamza Abudayyeh at the Hebrew University of Jerusalem in Israel.
A scheme of the optical set-up is shown in Figure 3.19. For excitation, laser pulses with a wavelength of $\lambda = 405$ nm and a repetition rate of 4 MHz are generated by a pulsed, frequency doubled femtosecond Ti:Sapphire laser. The excitation light is then coupled into the set-up by a dichroic mirror and focused onto the sample through an objective (Olympus, 100x MPlanFL N BD, NA = 0.9). The sample is mounted on a piezo stage and scanned through the focus of the excitation laser beam. The emitted fluorescence signal is collected with the same objective and guided alternately to different detectors by passing through the dichroic mirror, which blocks wavelengths below $\lambda = 567$ nm. Dependent on the respective application, the emitted light can be guided by inserting or removing flipping mirrors into the optical path. To determine the location on the sample, *real-space* images can be taken by guiding the light directly to a CMOS-camera (Hamamatsu, ORCA-Flash 4.0), which also serves as the detector for spectrally integrated back focal plane images when an additional BFP lens is inserted. Spectrally resolved back focal plane images can be acquired by guiding the light through a spectrometer equipped with a CCD-detector. Time-resolved and time-correlated single photon counting measurements can be done by directing the signal towards a Hanbury Brown Twiss module, consisting of a 50/50 beam splitter, two APDs (Excelitas, SPCM-AQRH-14-FC) and some time-resolved single photon counting electronics (Swabian Instruments, TimeTagger 2.0).
A Hanbury Brown Twiss experiment is used, inter alia, to determine whether photon antibunching is present, i.e. if a quantum light source truly emits single photons. For pulsed excitation, as given in the experiments described here, the quantum dot will get excited with every incoming pulse and relax again by emitting a photon within

the radiative lifetime τ_r after the trigger pulse. For a pulse separation $1/f_{trigger}$ much longer than τ_r, the photon stream will be controlled by the trigger pulse sequence, as no other photon can be emitted unless a new trigger pulse arrives. A corresponding measurement, as displayed in Figure 4.17 in section 4.2.1, shows the result of such a correlation measurement. A photon striking APD1 will start a timer, which measures the time that elapses until another photon striking APD2 will generate the stop signal. A vanishing (or small) peak at $\tau = 0$ therefore indicates that the two photons can not originate from the same trigger pulse, stating single photon emission.

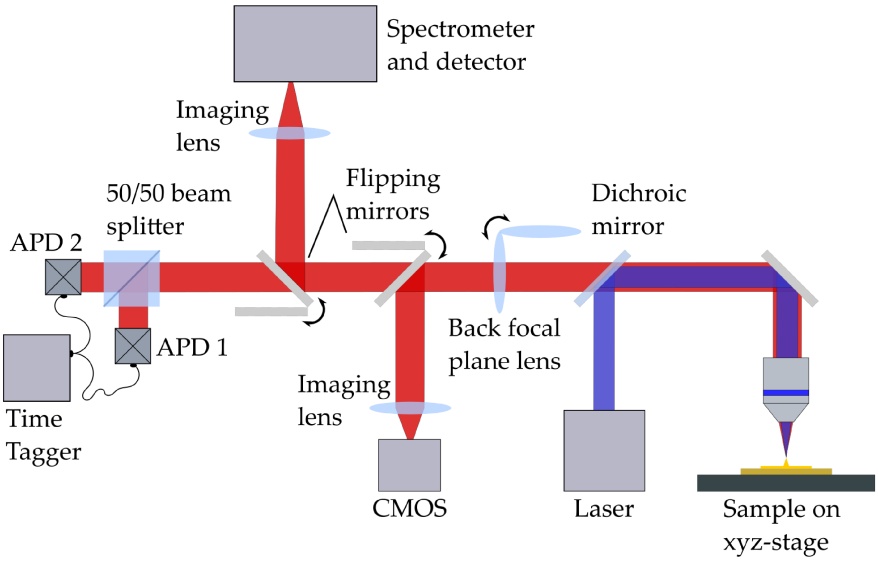

Figure 3.19: Schematic of the experimental set-up at HUJI for optical measurements on hybrid bullseye nanoantennas. The set-up combines two modules for real-space and k-space imaging and spectroscopy and a Hanbury Brown Twiss interferometer for time-correlation measurements. Image after [126].

3.3 SIMULATIONS

The simulated results discussed in different sections in this thesis were obtained with the help of the MATLAB toolbox *MNPBEM* by Hohenester et al. [137–139]. The toolbox has been devised for the simulation of **m**etallic **n**ano**p**articles (MNP), following F. J. Garcia de Abajo and A. Howie [140] with their **b**oundary **e**lement **m**ethod (BEM) approach to find exact solutions of Maxwell's equations for arbitrarily shaped particles in a dielectric environment. While details about the toolbox can be found in literature [137], its basic working principle is shortly introduced, and the models used for different simulations are presented.

As mentioned above, the toolbox was designed to find, i.e. compute the electromagnetic properties of metallic (plasmonic) nanoparticles in a dielectric environment. The toolbox differentiates between a quasi-static (quasi-static approximation) and a retarded approach. As the latter one includes retardation effects, it is more accurate for realistic structure dimensions and is therefore discussed here.

To start with, particles with volumes V_i in the simulations need to be generated in such a way that they are separated by closed interfaces ∂V_i from the environment and possess isotropic and homogeneous dielectric functions. By applying an external perturbation, i.e. exciting the particles through an incoming electromagnetic field, electromagnetic fields are consequently induced at the locations of the particles. The toolbox is used to compute these induced fields under consideration of the boundary conditions at the particles' closed surfaces. This is done with the help of Green's functions, which are used so solve linear partial differential equations such as the Helmholtz equation for the potentials, and are defined as

$$(\nabla^2 + k_i^2) G_i(\vec{r}, \vec{r}') = -4\pi\delta(\vec{r} - \vec{r}') \ , \ \ G_i(\vec{r}, \vec{r}') = \frac{e^{ik_i |\vec{r} - \vec{r}'|}}{|\vec{r} - \vec{r}'|} \tag{3.2}$$

Nonmagnetic materials are assumed in all simulations: permeability $\mu = 1$

where $k_i = \sqrt{\varepsilon_i} k$ denotes the wave number inside the particle, defined by positions $\vec{r} \in V_i$, with permittivity ε_i of medium i, and $k = \frac{\omega}{c}$ is the wave number in vacuum. Assuming that the boundary conditions for electromagnetic fields at interfaces are met, a solution for the scalar and vector potentials inside the particle ($\vec{r} \in V_i$, $\vec{r} \notin \partial V_i$) can be found, so that both fulfill the Helmholtz equation and are given by

$$\phi(\vec{r}) = \phi_{ext}(\vec{r}) + \oint_{V_i} G_i(\vec{r}, \vec{s}) \sigma_i(\vec{s}) da \tag{3.3}$$

$$\vec{A}(\vec{r}) = \vec{A}_{ext}(\vec{r}) + \oint_{V_i} G_i(\vec{r}, \vec{s}) \vec{h}_i(\vec{s}) da \ . \tag{3.4}$$

Here, ϕ_{ext} and $\vec{A}_{ext}$ denote the external perturbation given as scalar and vector potentials, G_i is the Green's function. σ_i are the surface

charge distributions at the particle boundary ∂V_i, consisting of surface elements da, and $\vec{h}_i$ denote the surface currents, respectively. As mentioned above, these two quantities need to be chosen in such a way that the resulting electromagnetic field satisfies the boundary conditions, i.e. continuity of the tangential component of the electric (magnetic) field inside and outside of the particle and continuity of the normal dielectric displacement. As the scalar and vector potentials ϕ and $\vec{A}$ are also linked through the Lorenz gauge condition

$$\nabla \cdot \vec{A} = ik\varepsilon\phi \ , \tag{3.5}$$

expressions for the surface charge and current distributions [140, 141] can be found, respectively, by performing some extended calculus including matrix inversions and multiplications. The boundary element method comes into account by approximating the integrals in equations 3.3 and 3.4 by a sum over discretized surface elements da. With the expressions for σ_i and $\vec{h}_i$ and with the help of equations 3.3 and 3.4, the electromagnetic fields at any other position can be determined via $\vec{E} = ik\vec{A} - \nabla\phi$ and $\vec{H} = \nabla \times \vec{A}$.
Apart from a homogeneous dielectric environment, the toolbox also allows for including layer structures, i.e. implementing substrates into the simulation, which is helpful to identify substrate-induced effects (such as resonance shifts due to a changed refractive index).
The simulations performed in this thesis were individually adapted for different research questions. Unless stated otherwise, a retarded approach was chosen to maintain phase-information of the surface charge distributions and electromagnetic fields. Furthermore, substrate layers were considered, differing between glass or glass/ITO for transparent samples (cf. section 4.1) and gold for the template-stripped cones discussed in section 4.2.

3.3.1 *Dipole Excitation*

The fields radiated by an oscillating dipole can act as an excitation source for plasmonic structures nearby. Vice versa, the nanostructures also modify the decay rates of the dipole emitter. Thus, for simulations including quantum emitters, a model was set up consisting of the desired structure placed on a substrate layer, and *dipole excitation* was chosen to compute the surface charge distributions on the particle. The position of the dipole can be chosen independently. For the simulations discussed in section 4.1.1, the dipole was placed at varying distances above the cone's apex while in section 4.2 the position was varied laterally. However, the computing scheme is as follows: Starting from the dyadic Green's function $\vec{E}(\vec{r}) = k^2\vec{G}(\vec{r},\vec{r}',\omega)\cdot\vec{d}$, which links the electric field at position $\vec{r}$ to an oscillating dipole at position $\vec{r}'$, potentials and surface charge distributions for a given wave number $k = \frac{\omega}{c}$ can be computed as described above, and from this the induced

fields can be obtained. The model allows for computing the total and radiative decay rates according to [57]

$$\Gamma_{tot} = \Gamma^0_{rad} + \frac{1}{2}\Im(\vec{d} \cdot \vec{E}_{ind}) \ , \ \Gamma^0_{rad} = \frac{4}{3} n_b k^3 \tag{3.6}$$

where $\vec{d}$ denotes the transition dipole moment, and $\vec{E}_{ind}$ is the induced electric field at the position of the dipole. Γ^0_{rad} is the free-space decay rate, dependent on the refractive index n_b of the surrounding medium, i.e. the decay rate of a dipole taking into account only the *background* layer structure. The toolbox also allows for computing the photonic local density of states for any given nanostructure.

3.3.2 *Plane Wave Excitation*

Simulations of electromagnetic fields scattered into the far field, i.e. spectra and radiation patterns, but also of near-field maps, as described in section 4.3 for example, were computed using an incoming plane wave as excitation source. The k-vector of the incoming light and also its polarization orientation can be specified. Again, the toolbox solves Maxwell's equations using the scheme described above to compute the surface charge distributions on the particle's surface. By the time the incoming fields $\vec{E}_{inc}$ and $\vec{B}_{inc}$ and more importantly the scattered electromagnetic fields $\vec{E}$ and $\vec{B}$ are known, the scattering cross sections can be computed from

$$P_{sca} = n_b \oint \Re\left(\vec{n} \cdot \{\vec{E} \times \vec{B}^*\}\right) da \tag{3.7}$$

and extinction is given by applying the optical theorem

$$P_{ext} = -\frac{1}{n_b} \oint \Re\left(\vec{n} \cdot \{\vec{E} \times \vec{B}^*_{inc} + \vec{E}^*_{inc} \times \vec{B}\}\right) da \ , \tag{3.8}$$

where n_b again denotes the refractive index of the surrounding medium. $\vec{n}$ is the unit vector in the propagation direction of light, and the integration is performed over the whole detector surface, i.e. a unit-sphere at infinity. The scattering cross section can then be obtained by dividing the radiated power P_{sca} by the intensity of the exciting plane wave. If layer structures are included in the simulations, the extinction cross section is computed according to [142, 143]

$$P_{ext} = \frac{4\pi}{k_r} \Im\left(\vec{E}^*_r \cdot \vec{F}_r + \vec{E}^*_t \cdot \vec{F}_t\right) \ , \tag{3.9}$$

where k_r is the wave number of the incoming wave reflected at the substrate. $\vec{E}_{r,t}$ denote the reflected and transmitted electric fields of the plane wave excitation, while $\vec{F}_{r,t}$ are the reflected and transmitted scattered fields, respectively. It should be emphasized once more that the toolbox allows direct access to the computed scattered electromagnetic fields, so that they can be used in further evaluations as it was done for instance in equation 3.1 for the energy flux.

4

RESULTS

4.1 HYBRID ANTENNAS - QUANTUM DOTS ON GOLD NANOCONES

The ability of plasmonic nanostructures to alter the emission characteristics of fluorescent molecules or quantum dots placed in close vicinity to the metal is a well-known phenomenon and widely studied [144, 145]. The enhancement of the emission rate is a key feature used in nano-optics, e.g. in tip-enhanced scanning near-field optical microscopy [146] or plasmon-enhanced stimulated Raman scattering microscopy [147], but also in nano-photonic applications such as nano-lasers [148] or photonic-crystal waveguides [149].
While many works focus on the improvement of the overall photoluminescence yield, containing both, excitation enhancement and quantum efficiency [150, 151], the mechanisms involved in the emission of a photon from such a hybrid system are far less investigated. This is also due to a quite challenging fabrication, as the precise placement of quantum emitters at distinct positions of nanostructures is no trivial task [152–154].
These issues shall be addressed by applying a process for the self-aligned placement of quantum dots at the apexes of gold nanocones [121] and studying the optical properties of such hybrid antennas [123]. The attachment process of the quantum dots was originally developed by Julia Fulmes and is adapted with some expedient changes in this work. A detailed description can be found in section 3.1.2. The photoluminescence and lifetime measurements were performed in the group of Prof. A. Meixner at the Institute of Physical and Theoretical Chemistry. The experimental results have been published in *Meixner et al., Coupling single quantum dots to plasmonic nanocones: optical properties, Faraday Discussions, 2015* [123].

4.1.1 *Optical Characterization of Hybrid Antennas*

One of the biggest advantages in plasmon-assisted photoluminescence enhancement is the high tunability of the structures themselves. Depending on size, material and geometry, the optical properties are adjustable over a wide wavelength range, spanning from ultraviolet, e.g. with aluminum [155], to mid-infrared with metal nitrides or doped semiconductors [156]. Also the variety of possibilities in tuning the geometry to obtain desired properties, e.g. clearly distinct resonances in very elongated structures or extremely confined and highly enhanced near fields at very sharp apexes, make plasmonic nanostructures well

suitable for studying the interaction with quantum emitters.
Here the focus lies on the interaction of CdSe/ZnS core-shell quantum dots[1] with an emission peak at 650 nm bound to the apexes of gold nanocones. This kind of structure was chosen for its three-dimensional geometry, as it simplifies exclusive access to the highly enhanced near field at the tip of an individual cone, and it also possesses two *spatially* separated dipolar modes (and also higher-order quadrupolar modes with resonances at shorter wavelengths), namely the (in-plane) base mode and the (out-of-plane) tip mode. By adjusting the nanocone's overall dimensions and also its aspect ratio, the resonance positions of the two modes and also their relative intensity can be controlled [157], so that the tip mode predominates over a background signal originating from the base mode.
Figure 4.1 shows a close-up of a single nanocone with a base diameter of ≈ 90 nm and a height of ≈ 100 nm located on a 50 nm thick conduction layer of indium tin oxide (ITO) on a glass cover slip. The array of cones on the right-hand side shows that uniformity of the structures is satisfactory.

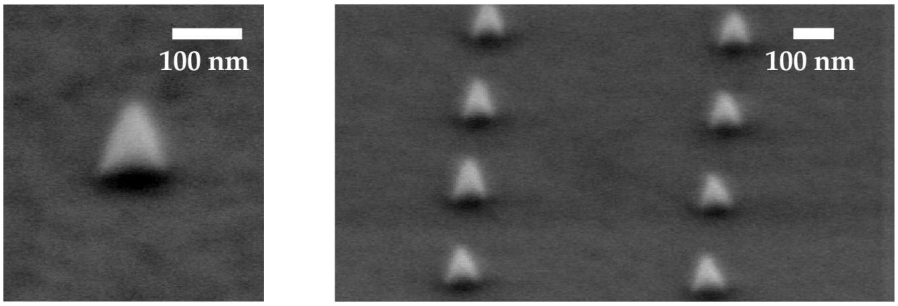

Figure 4.1: SEM images of gold nanocones at a viewing angle of 20° to the surface normal.
(Left) Single gold nanocone with a base diameter of $b \approx 90$ nm and a height of $h \approx 100$ nm. (Right) Overview of an array of nanostructures showing the consistency of shape.

To investigate the optical properties of the antenna alone, dark-field scattering spectroscopy was performed. Scattering spectra of individual nanocones are displayed in Figure 4.2 and show resonances at $\lambda \approx 650$ nm, thus being resonant to the emission wavelength of the chosen quantum dots. The average resonance $\lambda = 646$ nm is obtained from an averaged spectrum (black solid line in Figure 4.2) with a Gaussian fit. To unequivocally identify the modes in such nanostructures, simulations were performed for two distinct excitation polarizations, transverse magnetic (TM) and transverse electric (TE), i.e. p-polarized and s-polarized, respectively. The incident illumination angle of 71.8° was chosen to match the maximal experimental numerical aperture NA = 0.95 of the dark-field condenser.

1 CdSe/ZnS quantum dots with fluorescence maximum at (650 ± 5) nm, PlasmaChem GmbH, PL-QD-O-650.

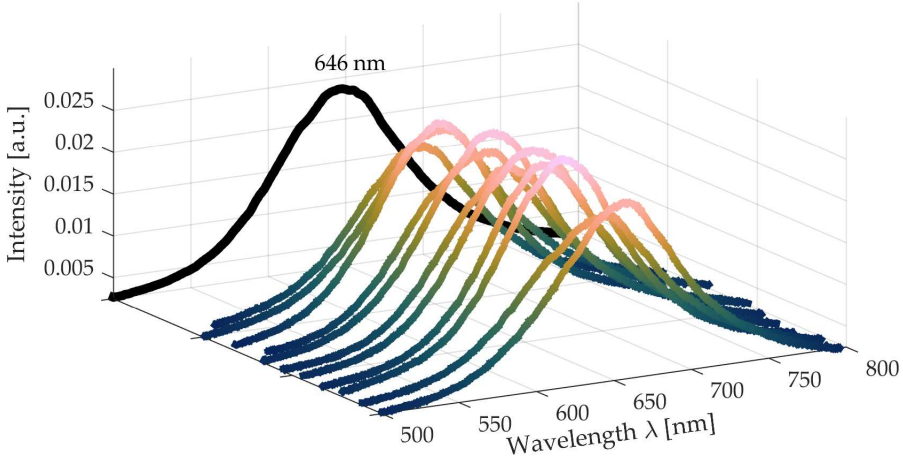

Figure 4.2: Dark-field scattering spectra of different nanocones as shown exemplarily in Figure 4.1. The black line shows the average spectrum with its maximum being located at $\lambda_{max} = 646\,\text{nm}$, as it is extracted from a Gaussian fit.

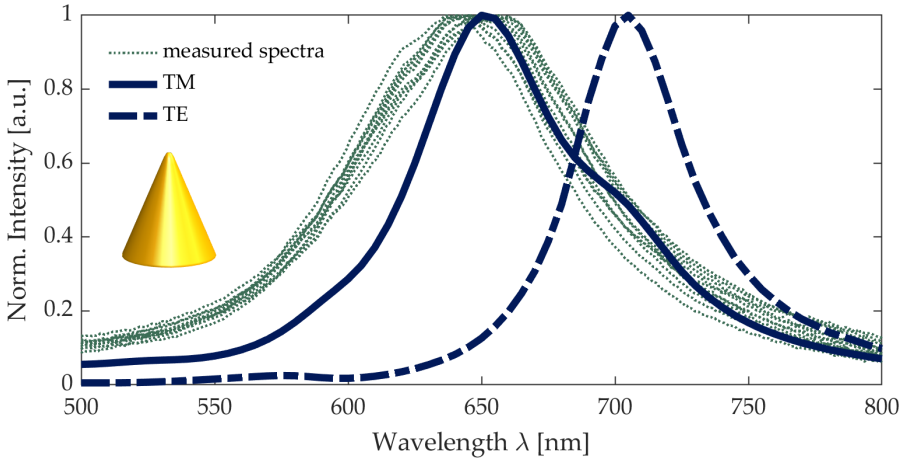

Figure 4.3: Computed scattering spectra for a gold nanocone located on a 50 nm thick ITO layer on a glass substrate. The solid line shows the normalized scattering for TM-excitation, the out-of-plane resonance position is $\lambda_{tip} = 650\,\text{nm}$. A higher-order mode shows up as a slight shoulder at $\lambda \approx 590\,\text{nm}$. The dashed line shows the normalized in-plane resonance at $\lambda_{base} = 705\,\text{nm}$, which is obtained for TE-excitation. The dotted lines represent data obtained from measurements.

Figure 4.3 shows the computed scattering spectra for a nanocone as modeled in the inset. The dashed line shows the light emitted to the far field for TE-excitation, therefore only exciting the in-plane (base) mode at $\lambda_{base} = 705\,\text{nm}$. TM-excitation leads to a resonance at $\lambda_{tip} = 650\,\text{nm}$, representing the out-of-plane (tip) mode and matching the experimental data (dotted lines) quite well. The in-plane resonance is visible as a slight shoulder, as p-polarized excitation under an angle other than 90° always has an in-plane contribution. The broadening

of the linewidths in the experimental data is caused by enhanced damping in realistic geometries and the polycrystalline nature of such nanostructures due to the fabrication process (cf. section 3.1.1).
Figure 4.4 shows maps of the near-field enhancement for TM-excitation at $\lambda_{tip} = 650\,\text{nm}$ and for TE-excitation at $\lambda_{base} = 705\,\text{nm}$. These confirm the expected high field confinement at the tip and the edges of the nanostructure and show a maximal enhancement factor of $E/E_0 = 89$ at the tip. They also illustrate that for the chosen geometry and excitation, the out-of-plane resonance exceeds the in-plane resonance in intensity of the electromagnetic fields, which is of relevance in our approach of studying the optical properties of quantum dots bound to the nanocones' tips.

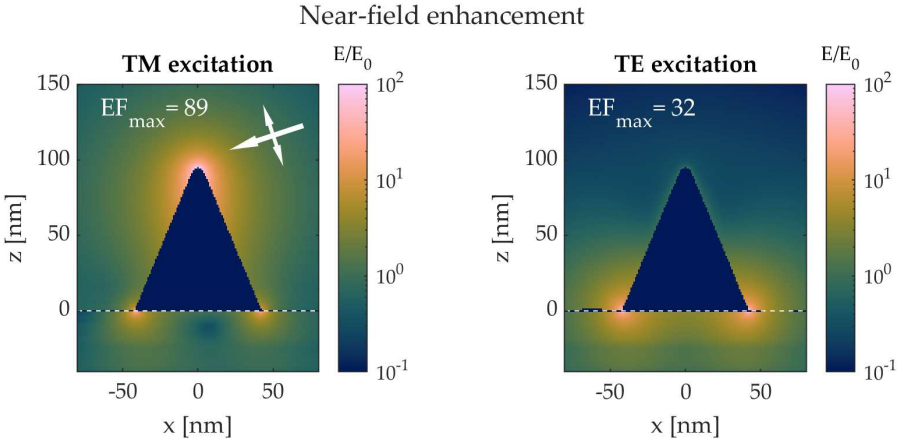

Figure 4.4: (Left) Near-field enhancement for TM-excitation at the resonance wavelength $\lambda_{tip} = 650\,\text{nm}$ of the out-of-plane mode. (Right) Near-field enhancement for TE-excitation at the resonance wavelength $\lambda_{base} = 705\,\text{nm}$ of the in-plane mode. The white dotted line marks the surface of the ITO-layer.

As mentioned before, CdSe/ZnS quantum dots were chosen to study the optical properties, i.e. the emission characteristics of the hybrid antennas. Those quantum dots exhibit broad absorption and a narrow luminescence emission band[2] as can be seen in Figure 4.5. The Stokes shift between these bands is beneficial for our approach, as excitation and emission are spectrally distinct. So for a wavelength of $\lambda_{exc} = 488\,\text{nm}$, the excitation is far off-resonance, and the emission of photons originating from direct excitation of the out-of-plane plasmon mode can be neglected. Also, the power of the excitation laser is chosen to be low enough (see section 3.2.5.1 for a detailed description of the experimental set-up) to not excite plasmons via energy transfer from gold photoluminescence.

While the excitation transition dipole moment has been shown to be isotropic [77] in individual CdSe/ZnS quantum dots, its lumines-

2 Spectra extracted from datasheet for PL-QD-O-650, PlasmaChem GmbH.

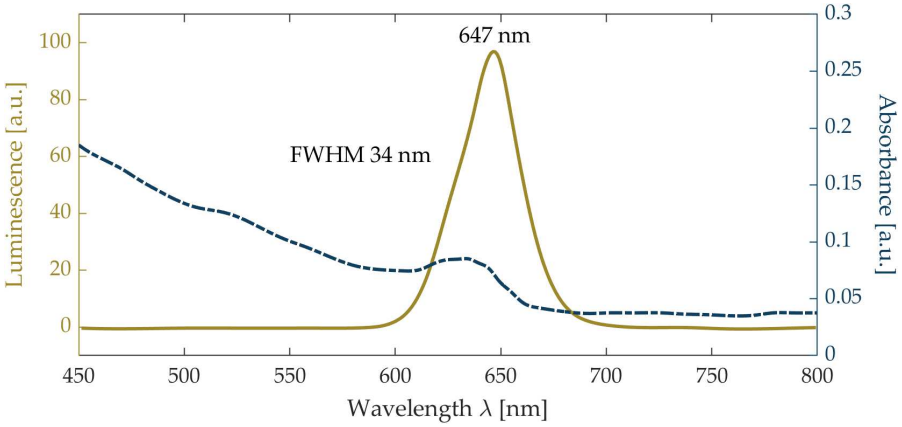

Figure 4.5: Luminescence (solid line) and absorbance (dash-dotted line) of commercial CdSe/ZnS quantum dots. Data extracted from datasheet.

cence emission is anisotropic and dependent on its orientation due to its crystallographic properties [76]. Also, as discussed in detail in section 2.3, the excitation and emission rates, γ_{exc} and γ_{em}, of such a nanocrystal are modified when the quantum emitter is brought close to a metallic nanostructure. Both rates depend, inter alia, on the photonic local density of states $\rho(\vec{r}, \omega)$ via

$$\gamma_{exc}(\vec{r}, \omega_0) = \frac{2\pi}{\hbar^2} \left|\vec{p}\vec{E}(\vec{r})\right|^2 \rho(\vec{r}, \omega_0) \tag{4.1}$$

$$\gamma_{em}(\vec{r}, \omega_{em}) = \frac{2\pi}{\hbar^2} \left|M_{ge}(\vec{r}, \omega_{em})\right|^2 \rho(\vec{r}, \omega_{em}) \tag{4.2}$$

where $\vec{p}$ is the excitation transition dipole moment, $\vec{E}(\vec{r})$ is the electric field amplitude at the position $\vec{r}$ of the dipole emitter, and $M_{ge}(\vec{r}, \omega_{em})$ is the matrix element of the transition, i.e. gives the magnitude of the quantum dot's emission dipole moment. These local densities of states are displayed in Figure 4.6. For reasons of simplicity, a substrate was not considered in these simulations. The upper row shows $\rho(\vec{r}, \omega_0)$ for the excitation wavelength, while the lower row shows $\rho(\vec{r}, \omega_{em})$ for the emission wavelength. The columns differentiate between an x- and z-orientation of the dipole moment. While the density of states for the excitation wavelength is almost independent from different dipole orientations and is also distributed quite uniformly around the nanostructure, one can see a clear difference for the density of states at the emission wavelength. $\rho(\vec{r}, \omega_{em})$ is clearly enhanced around the tip for photons emitted from dipoles oriented along z, simultaneously, following the cone's axis in vertical direction, there are essentially no states to occupy for photons emitted from dipoles oriented along x (and y consequently). The local density of states represents the total amount of states that can be occupied by a photon, that includes radiative states as well as non-radiative ones.

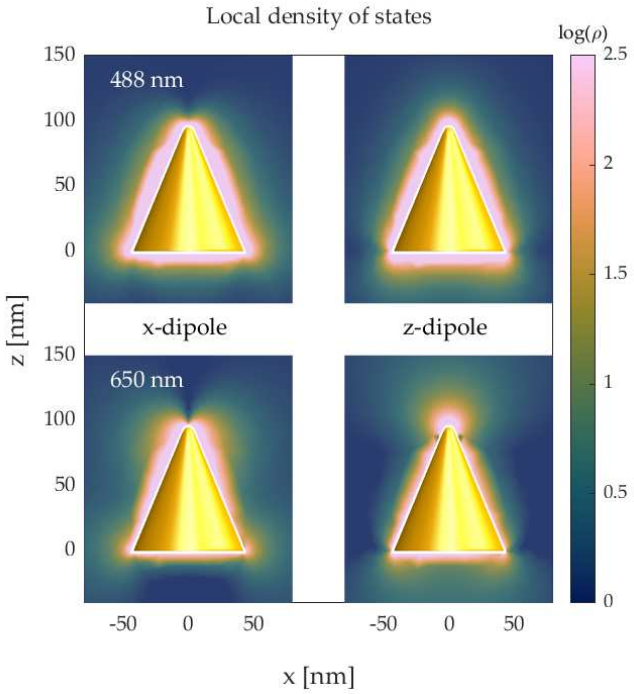

Figure 4.6: Photonic local density of states presented on a logarithmic color scale. The upper row shows $\rho(\vec{r}, \omega_0)$ for the excitation wavelength $\lambda_{exc} = 488\,\text{nm}$, and the lower row shows $\rho(\vec{r}, \omega_{em})$ for the emission wavelength $\lambda_{em} = 650\,\text{nm}$ of the quantum dots for dipole moments oriented in (left) x- and (right) z-direction, respectively.

The modification of the transition rates is known to be dependent on the distance of the quantum emitter to the metal nanostructure [158]. Therefore, the energy-dependent modification of the transition rates for a dipole emitter placed at varying distances above the nanocone's tip is investigated in more detail. For weak excitation, which is given in the experiment, the total decay rate is given by $\gamma_{em} = \gamma = \gamma_{rad} + \gamma_{nr}$, where γ_{rad} represents the radiative and γ_{nr} the non-radiative decay rate, respectively, and the emission rate γ_{em} can be linked to the excitation rate γ_{exc} via

$$\gamma_{em} = \gamma_{exc} \frac{\gamma_{rad}}{\gamma} \,. \tag{4.3}$$

Figure 4.7 depicts the spectrally resolved decay rates in dependence of the vertical displacement Δz of the dipole emitter from the tip of the nanocone. It shows that the total decay rate γ is enhanced for dipole positions close to the nanocone's tip, i.e. in regions where the near-field enhancement is highest, and over a wide spectral range, compared to the free-space decay rate γ_0, calculated without the nanostructure being present. While the non-radiative decay rate γ_{nr} is also mostly enhanced for shorter wavelengths, yet showing distinguishable features at the resonance positions of the out-of-plane dipolar mode and also a higher-order mode (compare spectrum in Figure

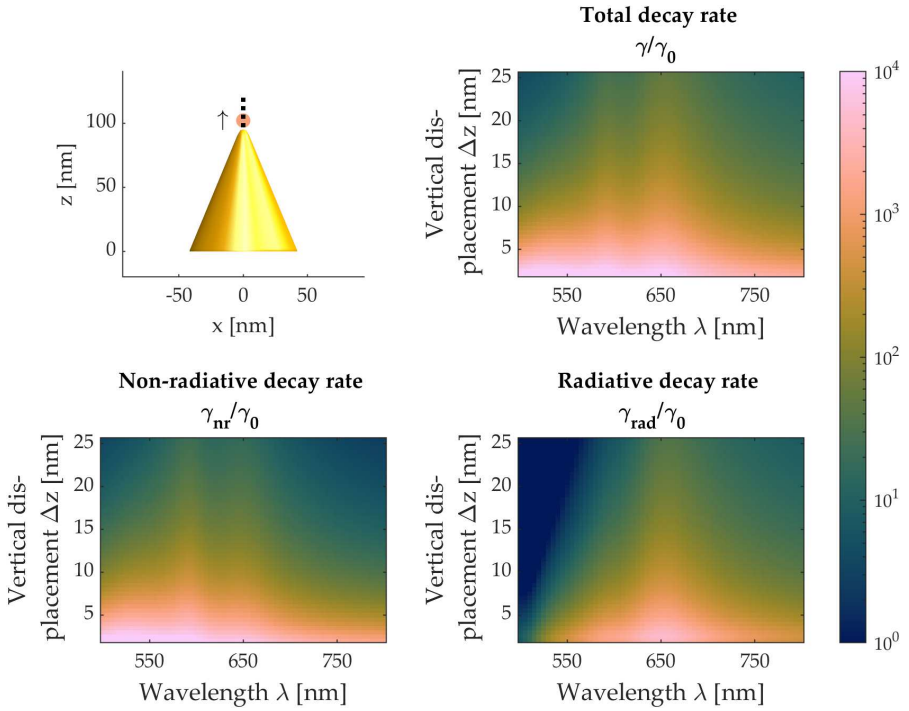

Figure 4.7: Spectrally resolved decay rates for a dipole emitter oriented along z close to the tip of a nanocone antenna. The decay rates are normalized to the free-space decay rate γ_0 computed without a nanostructure and are shown for different dipole positions, varying in a vertical direction above the nanocone's tip.

4.3), the radiative decay rate γ_{rad} clearly shows its highest values around the out-of-plane resonance of the nanostructure. Attention is now drawn to the radiative and non-radiative decay rates at these two resonance positions. The uppermost row in Figure 4.8 shows the decay rates (solid lines) as a function of the vertical displacement Δz. (The dotted lines show the same data on a semi-logarithmic scale to improve the visibility of the differences for higher displacements.) At the wavelength of the higher-order mode (left), the enhancement of the non-radiative decay rate predominates for all distances, while for the resonance wavelength of the dipolar mode (right), the enhancement of γ_{nr} dominates only for very small distances, and the enhancement of γ_{rad} prevails. The lower two rows in Figure 4.8 show the decay rates as a function of the wavelength for different displacements, accordingly. Very close to the tip, the non-radiative decay rate clearly predominates over the full spectral range, an effect known as quenching. This quenching is also highest for shorter wavelengths, as the enhancement of the non-radiative decay rate is proportional to the amount of Ohmic losses (high absorption for wavelengths below the plasma frequency ω_p) in the environment of the quantum emitter [159]. For increasing distances between quantum dot and nanostructure, the enhancement of the non-radiative decay rate decreases drastically, while - at the

wavelength of the out-of-plane resonance - the radiative decay rate starts to prevail. So, while the total enhancement reduces notably, the ratio of radiative to non-radiative decay improves, i.e. the emission probability $q_a = \frac{\gamma_{rad}}{\gamma}$ or so-called quantum yield increases.

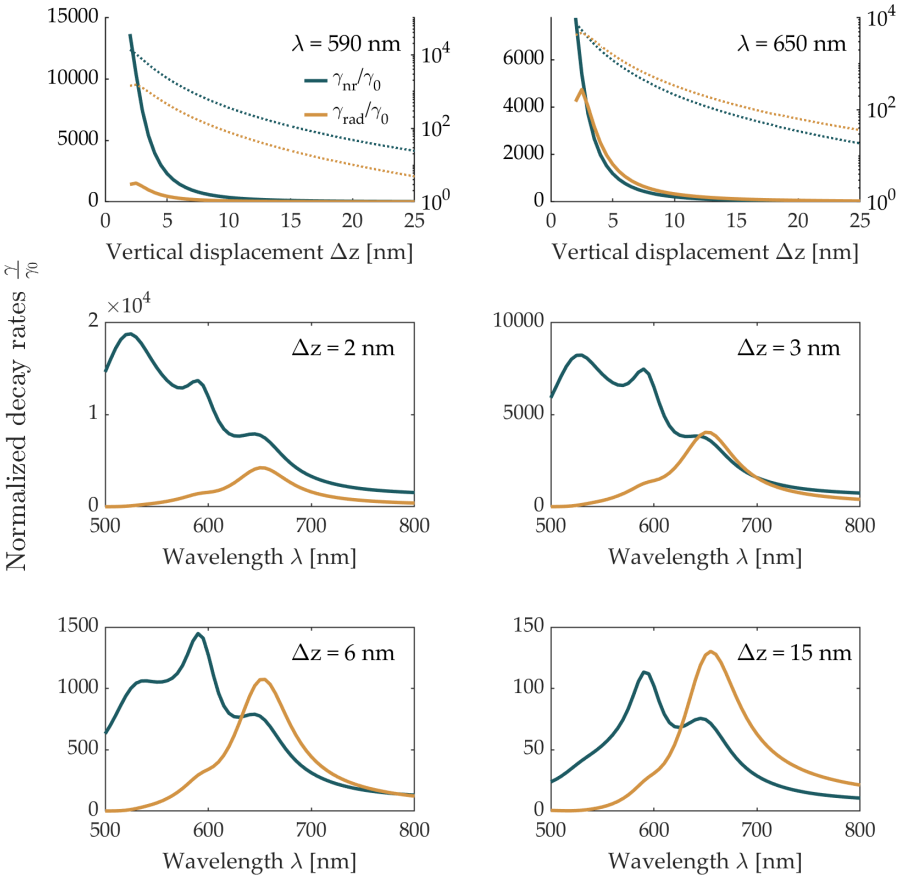

Figure 4.8: (Upper row) Radiative and non-radiative decay rates for increasing distances of the dipole emitter to the nanocone's tip, evaluated at the wavelengths of the plasmon resonances $\lambda = 590\,\text{nm}$ and $\lambda = 650\,\text{nm}$. The dotted lines show the same data on a semilogarithmic scale to improve the visibility of the differences for higher displacements. (Lower rows) Radiative and non-radiative decay rates for different vertical displacements as noted in the figures. For very small distances, the non-radiative decay rate and therefore quenching dominates the fluorescence process, while for greater distances the enhancement of the radiative rate prevails at the dipolar resonance (cross-over at $\sim 3\,\text{nm}$), and the emission probability increases. The mode at $\lambda \approx 525\,\text{nm}$ shows a dark mode, which consequently does not radiate photons to the far field.

Therefore, as given in equation 4.3, the emission rate can be calculated. It depends on this quantum yield and also the excitation rate. The normalized excitation rate, as described in section 2.3, is depicted on the left side in Figure 4.9 together with the distance-dependent quantum yield, while on the right-hand side the calculated emission

rate enhancement can be seen, showing a maximum at $\Delta z = 2.5\,\text{nm}$. The rate enhancement found in the experiment is around an order of magnitude, while the quantum dot is assumed to be located at a distance of $\Delta z \approx 3.7\,\text{nm}$ due to the binding by thiol chemistry [121].

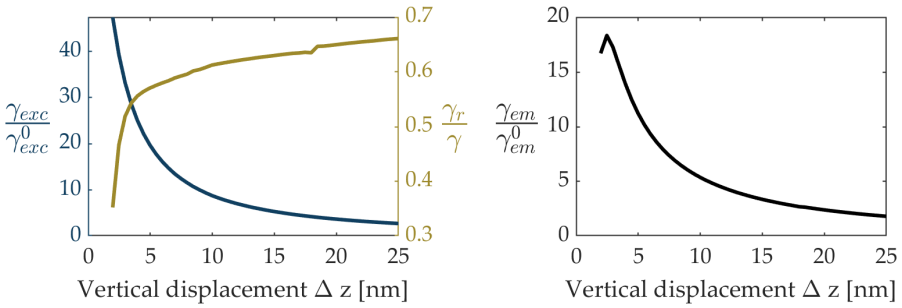

Figure 4.9: (Left) Excitation rate enhancement and quantum yield for a dipole emitter placed at varying distances above a nanocone. (Right) Emission rate enhancement for this particular system.

4.1.2 *Experimental Characterization*

To experimentally investigate such hybrid systems, photoluminescence and lifetime measurements were performed in the group of Prof. A. Meixner. Photoluminescence raster scan images and spectra were taken using a home-built inverted confocal microscope (see section 3.2.5.1 for more details on the experimental set-up). Figure 4.10 shows such photoluminescence raster scan images of quantum dots dispersed on a glass cover slip and bound to the tips of individual gold nanocones. The quantum dots dispersed on glass show intensity fluctuations and also fluorescence intermittency, i.e blinking behavior, which is often observed in such types of single quantum dots. Contrarily, fluorescence intensity fluctuations of quantum dots bound to the tips of the nanocones are by far less pronounced. The lower row in Figure 4.10 displays typical photoluminescence spectra for the two cases shown above. While the emission peaks were fitted with Lorentzian line profiles, a Gaussian peak was superimposed to the spectra recorded on the nanocones sample, as they show some background luminescence. Corresponding residuals are shown to display the goodness of fits for individual spectra. The background signal originates from the fabrication process and is due to some residual resist. Yet, the binding process could be modified successfully to eliminate this unwanted signal. See section 3.1.2 for details on the modified process and recorded photoluminescence spectra without such background signal.

As it can be seen from the raster scan images, fluorescence intermittency seems to decrease for quantum dots placed on nanocones.

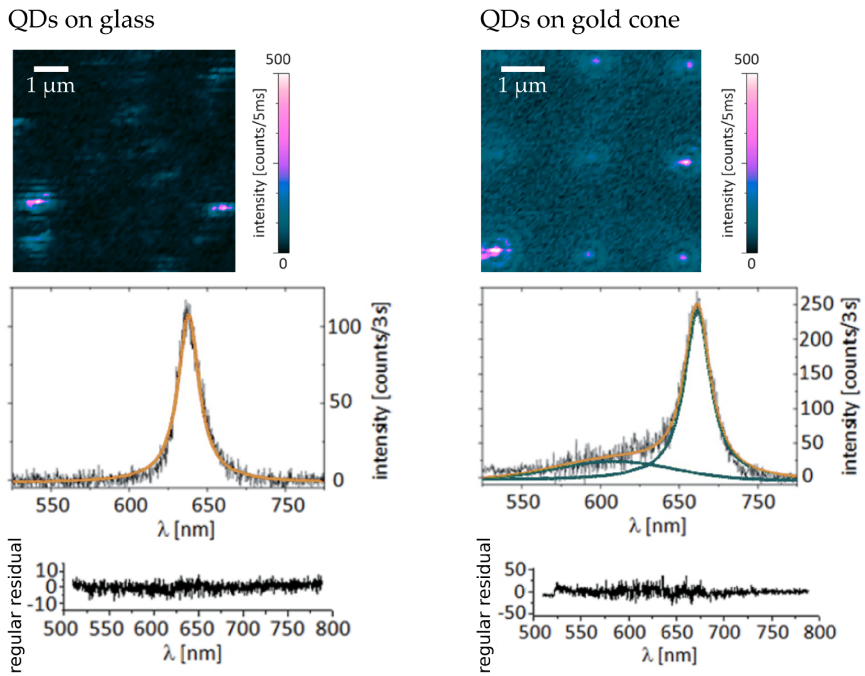

Figure 4.10: (Upper row) Photoluminescence raster scan images of quantum dots (left) dispersed on glass and (right) bound to the tips of individual gold nanocones. (Lower row) Photoluminescence emission spectra of a single quantum dot on glass and on a gold cone fitted with a Lorentzian line profile and on the nanocone sample with an additional Gaussian line profile accounting for the background signal. Corresponding residuals are shown to demonstrate the goodness of fits. Figure modified from Ref. [123].

Therefore, spectral time series of the emission of individual quantum dots were recorded. Figure 4.11 shows such time series for the different surroundings described above. Additionally, quantum dots embedded in PMMA were investigated as a reference, as it is known that the emission of a quantum dot is altered when placed in different media [160–164]. Also the background signal of a bare cone, i.e. with no quantum dot at the tip, was recorded. All time series were taken under the same experimental conditions to ensure comparability of intensity values. While the photoluminescence spectra of quantum dots on glass show highly varying intensities, the average count rate is rather low. Contrarily, when looking at the luminescence signal measured for quantum dots on cones, intensity fluctuations are highly reduced, and the average count rate exceeds that of the reference on glass by one order of magnitude, which is in good agreement with the computed values obtained from the simulations for the emission rate enhancement (cf. Figure 4.9). Quantum dots embedded in PMMA also show reduced fluorescence intermittency, yet the average intensity is still rather low. The background signal obtained from a nanocone with

no linked quantum dot shows the lowest count rates and no intensity fluctuations at all, which confirms the assumption that the signal is due to some residual resist originating from the fabrication process. The laser power used in the experiments was set too low to efficiently excite gold photoluminescence (cf. section 3.2.5.1), and what is even more convincing, the background signal vanished after modifying the attachment process.

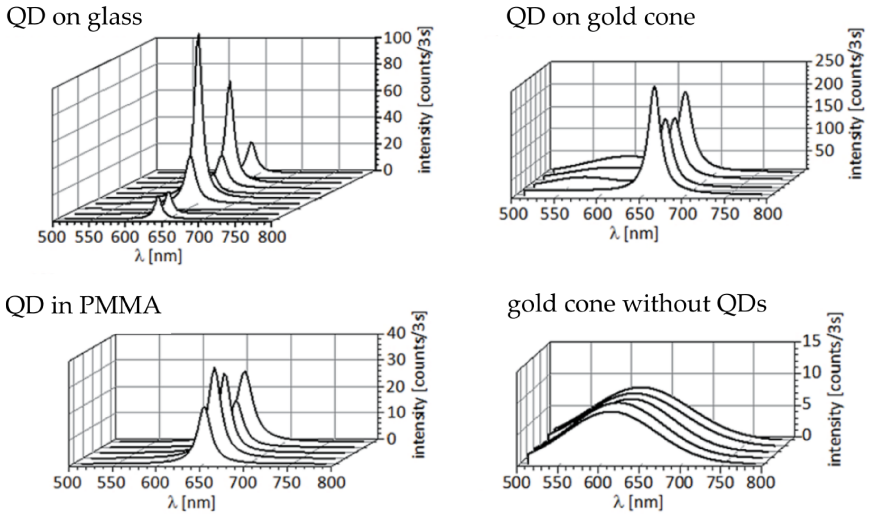

Figure 4.11: Time series of photoluminescence spectra for single quantum dots on glass, bound to the tip of a nanocone, and embedded in PMMA, and of the background signal of a nanocone with no quantum dot attached. The photoluminescence signal of a quantum dot on glass shows high intensity fluctuations at a rather low overall count rate. On average, the signal on a gold cone is enhanced by an order of magnitude compared to the one on glass and shows less emission intermittency. The emission signal of quantum dots embedded in PMMA is also less fluctuating, however at low overall count rates. The background signal is of low intensity and shows no intensity fluctuations, as it is expected for a luminescence signal originating from some residual resist. Figure modified from Ref. [123].

To decide whether a single quantum dot system or several quantum dots are investigated, the full width at half maximum can be considered, yet the occurrence of fluorescence intermittency with distinguishable states is an even stronger argument for the presence of a single quantum dot [165, 166], if no time-correlation measurements are available. Figure 4.12 shows a typical two-level intensity trajectory for a single quantum dot on glass, recorded with a single photon counting avalanche photo diode. Time bins were chosen to last 5 ms for an overall time interval of 60 s. Next to the intensity trajectories, histograms are given, displaying the number of occurrences for a

certain intensity value. Even though blinking is a highly complex phenomenon, involving a variety of different effects, such as multi-exciton decay, Auger recombination, and charge trapping [83, 84, 167], the kind of quantum dots used in our study shows two distinguishable states, namely the on- and off-states. While the on-state seems to last for time scales on the order of seconds, the system seems to *prefer* the off-state, i.e. non-radiative processes have the upper hand, and energy is transferred without emitting a photon, as those states last for tens of seconds.

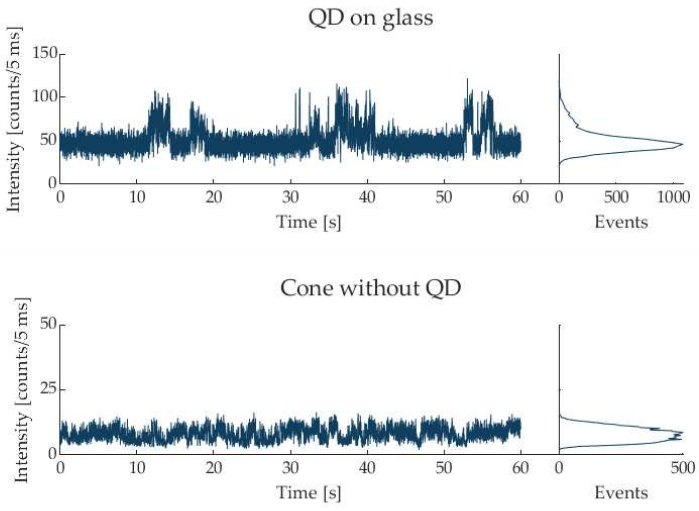

Figure 4.12: Spectrally integrated intensity trajectories of a quantum dot on glass and of a bare nanocone with no quantum dot linked to the tip, and histogram plots displaying the number of occurrences of a certain intensity value. The quantum dot on glass shows a two-level blinking behavior, while the bare gold cone expectedly shows no fluorescence intermittency.

For comparison, the luminescence signal of a bare gold cone with no quantum dot linked to the tip expectedly shows no such features, as can be also seen in Figure 4.12. Contrarily, intensity trajectories recorded for the hybrid systems differ clearly, as even three-level blinking can be resolved. Figure 4.13 exemplarily shows an intensity trajectory of a *single* quantum dot bound to the tip of a gold nanocone for a time interval of 120 s with a binning time of again 5 ms. It can be seen that the occupation time of the on-state increased compared to before and also the total amount of counts per time bin. One would also expect an increased photoluminescence intensity if two or more quantum dots were bound to the tip. Yet, the data gives strong indication that the signal originates from solely one quantum dot. The grey-shaded areas labeled *A* - *D* mark periods of 5 s each, which are investigated in more detail below. The blinking behavior observed

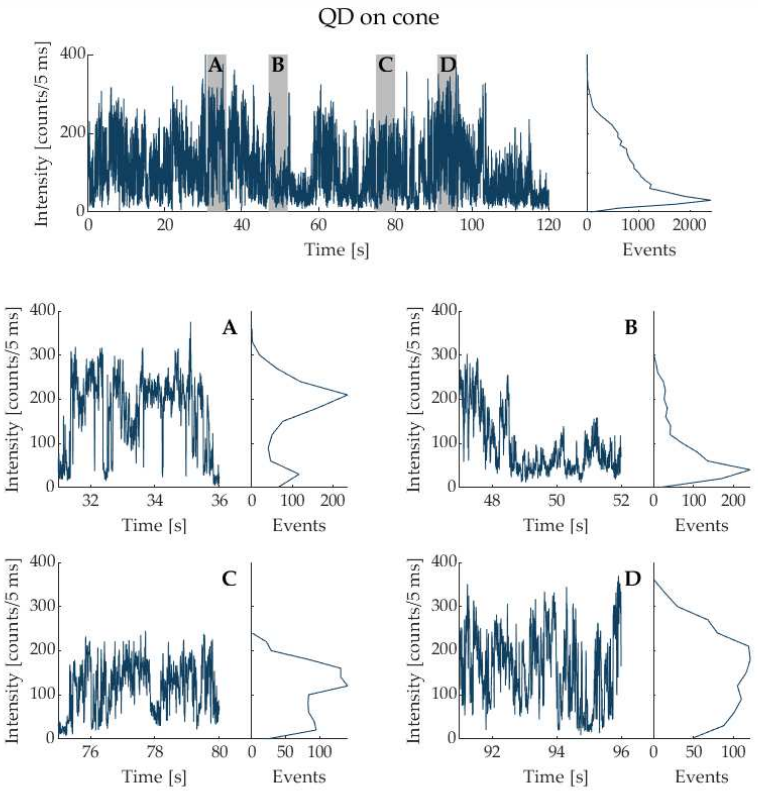

Figure 4.13: Spectrally integrated intensity trajectory of a quantum dot bound to the tip of a gold nanocone and corresponding intensity value occurrence histogram. Shown is a time interval of 120 s with a binning time of 5 ms. The grey-shaded areas mark periods of 5 s each which are displayed as close-ups below. *A* shows two-level blinking with an enhanced occupation of the on-state, while in *B* the off-state predominates. *C* shows the occupation of an intermediate *grey* state, which is due to adsorption and desorption of molecules from the ambient air. *D* shows random switching between the three levels, uncovering the unpredictability of fluorescence intermittency.

in time interval *A* is the strongest argument for a single quantum dot in the system, as it clearly shows two-level blinking, with the system even being preferably in the on-state. If the signal originated from two or more quantum dots, those quantum dots would need to emit photons in an absolutely synchronized fashion, otherwise more intensity levels or even an average continuous intensity value would be visible. This is highly unlikely, as blinking of individual quantum dots has no characteristic time scales. Yet, here, two-level blinking persist over several seconds. In time interval *B* the system is mostly in the off-state, similar to what has been observed for a quantum dot on glass, and also gives strong indication to only one quantum dot, as again a persisting off-state would require two (or even more) quantum dots to not emit simultaneously. Time interval *C* now shows

the occupation of an intermediate *grey* state, which has been reported before [168–171] in the blinking statistics of single nanocrystals and is due to changes in the surface passivation of the individual quantum dot, when adsorption and desorption events of molecules from the ambient air occur at its surface [172]. Bleaching due to photo-induced oxidation would also cause a decrease of intensity, yet this effect is irreversible, and intensity would not increase again, as it does in time interval *D*. The event histogram in *D* shows an almost evenly distributed occupation of the three states for also a time period of 5 s, which highlights the unpredictability of blinking behavior.

To further characterize the hybrid system, fluorescence lifetime measurements were performed on single quantum dots on nanocones, and for comparison also on glass and embedded in PMMA, using a pulsed supercontinuum laser and a time-correlated single photon counting system together with a spectrally integrating detector (see section 3.2.5.1 for more details).
Figure 4.14 exemplarily shows such lifetime histograms for different environments. These were fitted with a bi-exponential decay function convoluted with the instrument response function, i.e. the convolution of excitation pulse and response function of the detector.

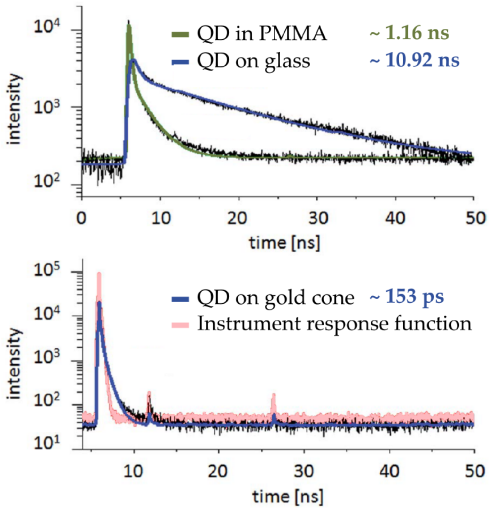

Figure 4.14: Fluorescence lifetime measurements for a single quantum dot on glass, embedded in PMMA, and attached to the tip of a gold nanocone. Also shown is the instrument response function. The displayed lifetimes are intensity-weighted average lifetimes. Figure modified from Ref. [123].

From the obtained amplitudes and lifetimes, the intensity-weighted average fluorescence lifetimes were calculated according to

$$\langle \tau \rangle = \frac{\sum_i A_i \cdot \tau_i^2}{\sum_i A_i \cdot \tau_i} \,. \tag{4.4}$$

While for a quantum dot on glass the average lifetime is on the order of $\langle \tau \rangle \approx 11\,\text{ns}$, it is slightly decreased when the quantum dot is embedded in PMMA, as the lifetimes are found to be related to the stabilization energy of charges in the direct environment [160]. The average lifetime in PMMA is then found to be around $\langle \tau \rangle \approx 1\,\text{ns}$. Both values are in good agreement with lifetimes found in literature [173–176]. A drastic decrease in lifetime can be observed for quantum dots on nanocones, as it is found to be on the order of $\langle \tau \rangle \approx 150\,\text{ps}$. Similar lifetimes have been found in other hybrid systems consisting of single quantum dots and metallic nanoparticles or rough gold films [177, 178]. The average fluorescence lifetime of a quantum emitter in a similar hybrid system, as it is described in section 4.2, was found to be $\langle \tau \rangle \approx 940\,\text{ps}$, while for the reference measurement of a quantum dot on glass the lifetime was $\langle \tau \rangle \approx 20\,\text{ns}$ [41]. A remotely similar system is described in [154], where a quantum dot is picked up with a glass fiber tip of a shear-force microscope and is subsequently positioned above a plasmonic nanocone. The average lifetimes found in this work were $\langle \tau \rangle \approx 1.4\,\text{ns}$ for the quantum dot above the nanocone and $\langle \tau \rangle \approx 62\,\text{ns}$ for a reference quantum dot on glass. This comparison demonstrates once again the crucial influence of the surroundings on the radiative properties of a quantum emitter. The record-low lifetime reported in this work might even be undercut, as due to resolution restrictions of the experimental set-up, the value is close to the instrument response function, and therefore represents an upper limit.

4.2 HYBRID BULLSEYE ANTENNAS

The knowledge transfer from fundamental research to industry, i.e. its implementation in the development of specific applications, is the supreme discipline for applied scientists. Semiconductor quantum dots serve as a prime example for such a successful evolution, as basic research and application development go hand in hand. Due to their high tuneability of chemical, electrical and optical properties, scientists strive to find new compositions, and the engineering and improvement of their properties is still in the focus of contemporary research. Additionally, due to their large-scale availability, reproducibility and reliability in synthesis and performance, they proved to be well-suited candidates for usage in commercial applications.
Semiconductor nanocrystals are already used in a variety of fields, such as in light emitting diodes [179], in hybrid solar cells for up-conversion [180], to enhance performance in photo-detectors [181] or as active media in quantum dot lasers [182]. Quantum dots are also in the focus of attention for implementation in quantum information and communication technologies [183]. A major step towards successful quantum applications is the development of single photon light sources, which are able to provide individual photons *on demand*, preferably deterministic with a well-defined polarization and indistinguishable from each other. This challenging task therefore constitutes a highly investigated topic for a large number of researchers with different scientific backgrounds [184–189]. While there are many approaches of using quantum dots [36, 190–193] (coupled into photonic cavities) as photon sources, there still are some obstacles that need to be overcome. The brightness, for example, is limited by the intrinsic optical properties of such nanocrystals, as it depends on the decay rates of the excited state and also the omnidirectional emission characteristics. As it has been extensively discussed before [57], plasmonic nanostructures can alter the emission rates of quantum emitters when placed in close vicinity to each other (cf. section 4.1). Additionally, such metal structures can also redirect fluorescence signals when designed as directional antennas, as is has been demonstrated, e.g. in [69, 124, 194].
With the antenna design discussed in the following, both concepts are combined in a monolithic device, so that the emission rates as well as the emission directionality of a quantum emitter can be modified simultaneously, which is no trivial task for applications working at room-temperature. As the projected photon emission rates of this engineered quantum light source approach the GHz range, this study marks a significant step towards ultra-bright deterministic single photon sources operating at room-temperature. The optical measurements for characterizing such hybrid systems were performed in the group of Prof. R. Rapaport at the Racah Institute of Physics at the Hebrew

University of Jerusalem. The experimental results have been published in *Abudayyeh et al., Overcoming the Rate-Directionality Trade-off: A Room-Temperature Ultrabright Quantum Light Source, ACS Nano, 2021* [41].

4.2.1 *Characterization of Hybrid Bullseye Antennas*

To address both, emission rate enhancement and emission directionality modification, a hybrid device was designed that combines two proven concepts to overcome the trade-off between the two properties mentioned above. In such a structure, a semiconductor nanocrystal is coupled to the tip of a gold nanocone that acts as a plasmonic resonator and enhances the emission rate of the quantum dot, enclosed by a Bragg (bullseye) antenna that modifies the emission directionality, as it was previously demonstrated in different works by the Rapaport group [124–126, 195].
Figure 4.15 shows a SEM image of such a hybrid structure together with a cross-sectional scheme of the center part displaying the according dimensions of the individual elements. The antenna consists of a gold nanocone with a base diameter of $\approx 240\,\text{nm}$ and a height of $\approx 180\,\text{nm}$ and is located in the center of a bullseye structure consisting of 15 concentric rings. The grid period is $\approx 560\,\text{nm}$ and the height of the rings is $\approx 100\,\text{nm}$, therefore being lower than the height of the cone, which enables the attachment of quantum emitters solely at the resonator. A detailed description of the fabrication process can be found in section 3.1.3.

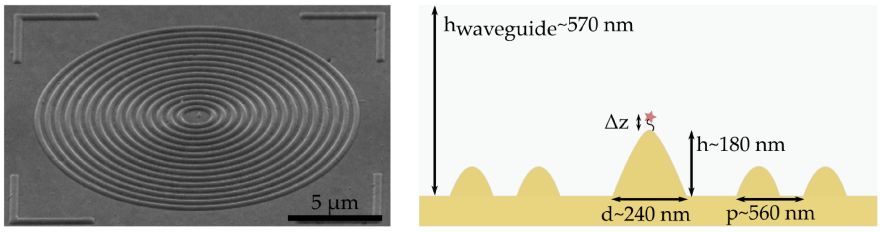

Figure 4.15: SEM image and cross-sectional scheme of a hybrid bullseye antenna with according dimensions.

As already mentioned above, the nanocone in the center of the bullseye antenna acts as an optical resonator that modifies the emission rate of a quantum emitter by the Purcell factor, which is proportional to the ratio of quality factor Q over mode volume V. Figure 4.16 shows a close-up SEM image of the nanocone in the central ring next to a computed near-field map for a dipole emitter placed closely ($\approx 7\,\text{nm}$) above the cone's apex. The whole structure is embedded in PMMA,

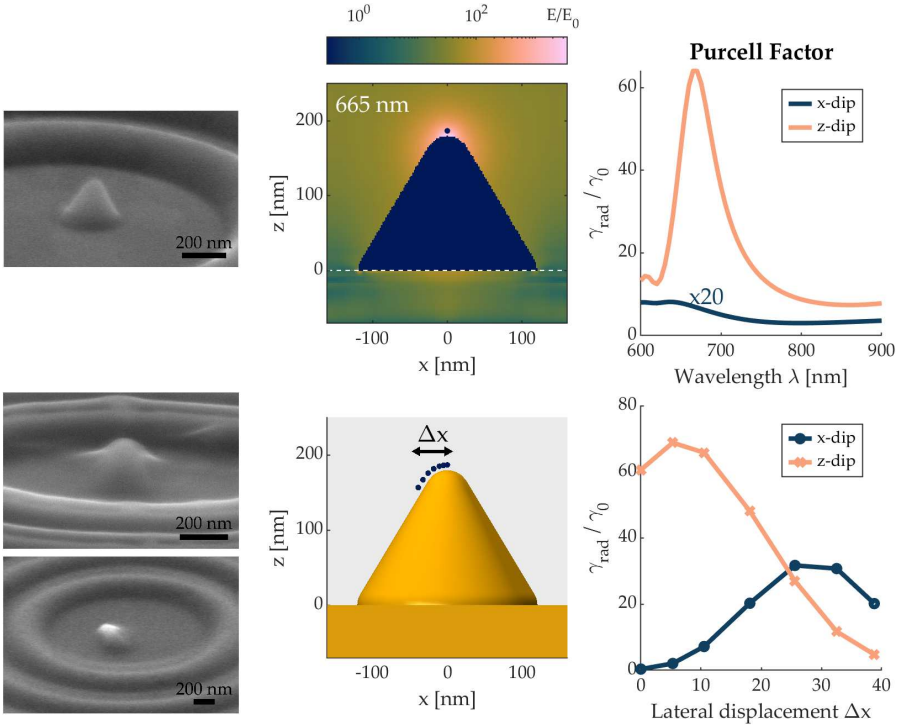

Figure 4.16: (Left column) SEM images of a gold nanocone in the center of a hybrid bullseye device - bare, embedded and with an uncovered tip. (Upper row) Near-field enhancement for a dipole emitter placed above the tip with its dipole moment being oriented in z-direction and for an emission wavelength of $\lambda = 665\,\text{nm}$ (center). Comparison of wavelength-dependent Purcell factors for dipoles oriented in x- and z-direction, respectively (right). (Lower row) Sketch of simulation model for different quantum dot positions at the tip (center) and comparison of enhancement factors for different dipole orientations depending on the lateral displacement Δx for $\lambda = 665\,\text{nm}$ (right).

which constitutes the waveguide layer. It shows that the near fields around the tip are highly enhanced for an emitter with a dipole moment oriented in z-direction and with an emission wavelength of 665 nm. The graph on the right-hand side compares the corresponding wavelength-dependent enhancement factors for dipoles oriented in x- and z-direction, respectively, and clearly demonstrates the predominance of one orientation over the other. However, this is only valid for dipole emitters placed exactly above the tip. As realistic structures in the hybrid devices exhibit relatively large tip radii ($\approx 20\,\text{nm}$) due to the fabrication method, the placement of quantum dots is not as accurate as simulations suggest.

The SEM images in the lower row of Figure 4.16 show intermediate steps of the attachment process (cf. section 3.1.3). They show the nanocone being completely embedded in PMMA and the tip being already uncovered after oxygen plasma treatment. As the attachment of quantum dots is performed by a self-aligned process, emitters statisti-

cally bind anywhere in the uncovered region. To investigate the impact of lateral displacement, simulations were performed with varying positions around the tip (Δx) but with a constant distance $\Delta z = 7\,\text{nm}$ to the surface, as it is also displayed in the lower row of Figure 4.16. For evaluation, the wavelength was again set to $\lambda = 665\,\text{nm}$ to coincidence with the maximal enhancement factor for the chosen geometry. It becomes clear that for increasing (yet still realistic) displacements the enhancement factors vary and dominate for dipole moments oriented in x-direction or rather any other *in-plane* orientation, as the x-direction was only chosen representatively. The importance of this result comes to light when interpreting the experimental results discussed in the following. A description of the experimental set-up that was used to perform the optical measurements described below can be found in section 3.2.5.2.

Figure 4.17 shows an optical image next to a confocal raster scanning fluorescence image of such an investigated hybrid device. It can be seen that the detected fluorescence signal solely originates from the center of the antenna, i.e. from quantum dots coupled to the nanocone, and therefore demonstrates the successful positioning of quantum emitters exclusively at the desired hot spot. The lower left panel in Figure 4.17 shows spectrally resolved and normalized fluorescence signals taken at 15 different devices (light grey lines) and their averaged spectrum in green. For comparison, a reference spectrum was taken for quantum dots dispersed on glass (light pink) and also for an *empty* device with no quantum dots attached to the nanocone (blue). The differences in signal strengths and line shapes demonstrate that plasmonic background contributions of the device can be neglected and confirms that the detected signal indeed originates from quantum dot fluorescence.

In order to achieve single photon emission, single or very few nanocrystals need to be attached to the apexes of the gold nanocones. To determine the number of quantum emitters in individual devices, i.e. to decide whether single or few emitters are investigated, time-filtered second-order correlation measurements were performed using the Hanbury Brown Twiss module as sketched in Figure 3.19 and explained in section 3.2.5.2. The graph on the bottom right of Figure 4.17 shows the result of such a correlation measurement, displaying photon anti-bunching and therefore representing a device containing only a single quantum emitter. Time-filtering with a time-gate of 2 ns was applied to temporally separate photons originating from the biexciton (XX) state in the colloidal quantum dots, as those states are known to emit multiple photons in the relaxation process [196].

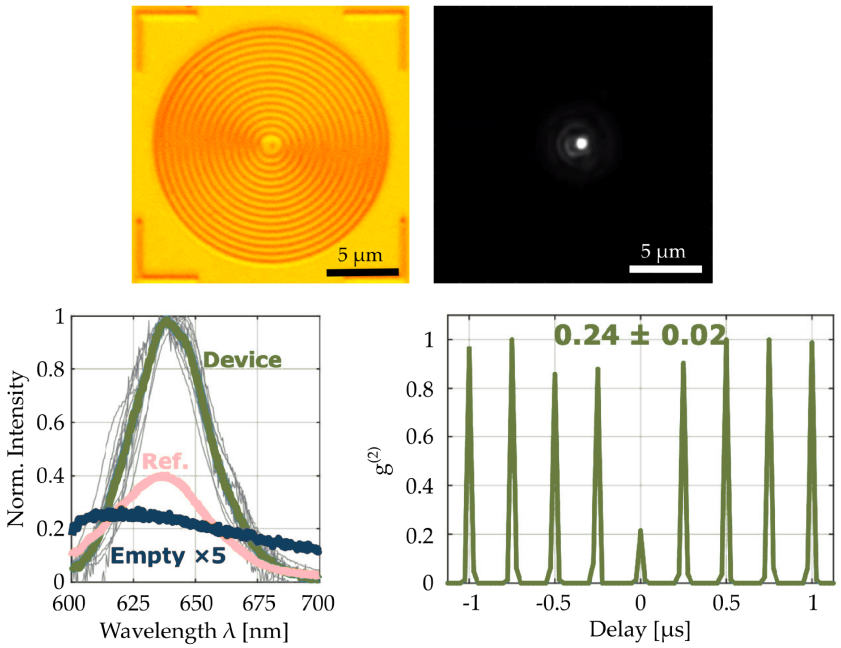

Figure 4.17: (Upper row) Top view image of a hybrid device taken with an optical microscope and confocal raster scanning fluorescence image showing that light emission solely originates from quantum dots coupled to the nanocone located in the center of the device. (Lower row) Fluorescence spectra taken for 15 different devices (light grey) with quantum dots coupled to the nanocone and the normalized averaged spectrum in green compared to an empty device without any quantum dots (blue) and a reference spectrum of quantum dots on glass (light pink). The graph on the right-hand side shows a time-filtered second order correlation measurement displaying single quantum dot emission. Graphs modified with permission from Ref. [41].

To investigate the emission directionality of the fabricated hybrid devices, back focal plane imaging was performed (cf. section 3.2.3), and some of the results are exemplarily displayed in Figure 4.18. The top row shows the obtained angular emission pattern for one of the investigated full hybrid devices containing a quantum dot, next to the emission pattern of an empty device and a quantum dot dispersed on glass. For the full hybrid device, highly directional emission can be observed. While there is a clear emission peak in the forward direction, i.e into 0°, the whole amount of light is emitted into angles below 20°. This high directivity is accompanied by a high overall emission intensity, as it is expected for quantum dots coupled to plasmonic resonators due to the enhanced emission rates. In comparison, the empty device shows no emission directionality and demonstrates once again that plasmonic effects hardly contribute to the observed signals. The pattern of the quantum dot on glass shows

emission into a wide angular range, as it is expected in absence of the redirecting bullseye antenna. The graph in the lower row of Figure 4.18 shows the dependence of the respective fluorescence signals on the radial coordinate θ when integrated over the azimuthal angle φ and normalized to the maximum intensity of the device. The superiority of the hybrid device, both in directivity and intensity enhancement, compared to the reference is clearly demonstrated. The image on the right-hand side of Figure 4.18 shows the computed radiation pattern of a full hybrid device obtained from FDTD simulations. The observed ring-like angular emission pattern originates from the high z-dipole emission enhancement for dipoles placed accurately above the tip and clearly differs from the measurement, which is likely due to an inaccurate positioning (lateral displacement) of the quantum emitter in the experiment (cf. Figure 4.16).

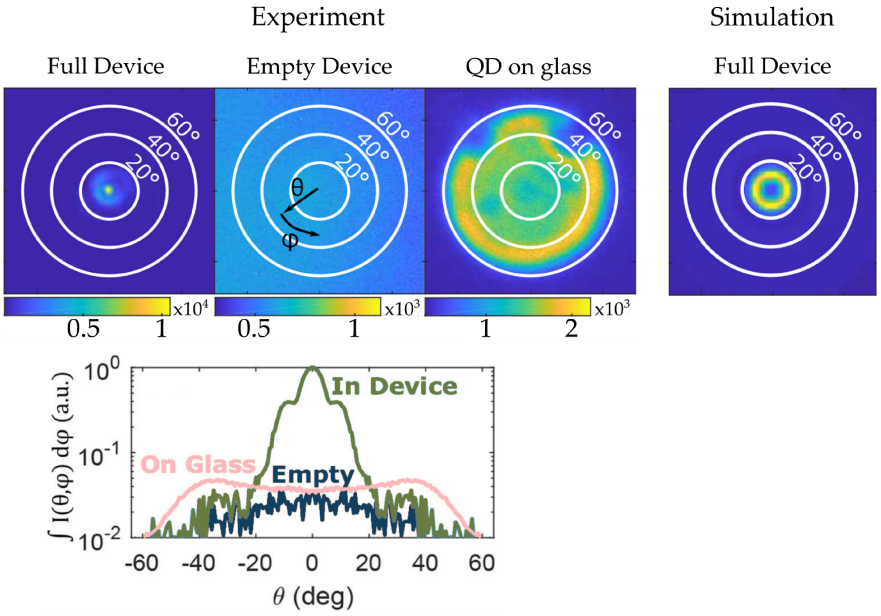

Figure 4.18: Back focal plane images (from left to right) for the radiation patterns of a full hybrid device including a quantum dot, an empty device without quantum dot and a quantum dot dispersed on glass. The rightmost image shows a FDTD simulation of a full device for a dipole placed 7 nm above the tip and shows strong enhancement of the z-dipole emission. The lower image shows the intensity profiles for the three cases dependent on the radial coordinate θ after integration over azimuthal angle φ. Images and graph modified with permission from Ref. [41].

The position of the quantum emitter on the nanocone and the resulting varying enhanced dipole emission rates also have an impact on the collection efficiency $\eta_{coll}(\mathrm{NA})$ of the investigated system. The collection efficiency is a variable that quantifies the directionality of

the emitting device as it is visualized in the back focal plane images and is given by

$$\eta_{coll}(\theta_{\mathrm{NA}}) = \frac{\int_0^{2\pi} d\varphi \int_0^{\theta_{\mathrm{NA}}} d\theta \; I(\theta,\varphi)}{\int_0^{2\pi} d\varphi \int_0^{\pi} d\theta \; I(\theta,\varphi)} \quad .$$

Figure 4.19 shows the collection efficiency for 20 measured devices (grey lines), with the best performing device being highlighted by a slightly thicker black line. The average is shown with the green solid line. This is compared to the collection efficiency of a quantum dot on glass (pink) serving as reference, and to the computed collection efficiency of the simulated device (red). As can be seen, the measurements clearly surpass η_{coll} for the reference and even for the simulation for a majority of the investigated devices. The performance improvement of the hybrid devices (on average) is highest for low numerical apertures, for example reaching values (70%) 88-fold greater than the reference (0.8%) at NA $= 0.22$. This high collection efficiency is also due to the enhanced x-dipole emission observed in the experiments, which is radiated into the forward direction (into 0°). While this effect is advantageous to reach high values of η_{coll}, it is disadvantageously accompanied by a reduction of the Purcell factor for the z-dipole component, for which the highest enhancement factors are expected (cf. Figure 4.16).
To quantify the rate enhancement, fluorescence lifetime measurements were performed for both, quantum dots in hybrid devices and dispersed on glass. The graph on the right-hand side in Figure 4.19 shows the decay curves of the quantum dots' emission in the measured devices with grey lines and their average in green. The pink curve again shows the reference decay for quantum dots on glass, and the yellow line represents the instrument response function of the detection diode.

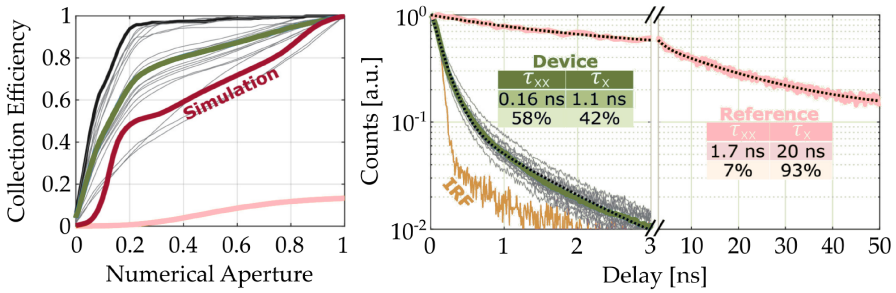

Figure 4.19: (Left) Collection efficiency and (right) lifetime measurements for 20 investigated devices (grey lines), their average (green) and reference quantum dots on glass (pink). For comparison, the computed collection efficiency is also shown for a full hybrid device (red). Graphs modified with permission from Ref. [41].

The data was fitted with a bi-exponential decay function, showing a drastic decrease for both lifetime components. While the exciton (X) state's lifetime τ_x declines from 20 ns to 1.1 ns, the biexciton (XX) state's lifetime τ_{xx} reduces from 1.7 ns to 0.16 ns. In addition, the contributions from the exciton and biexciton states are altered, respectively, which is due to a modified quantum efficiency of the respective state. As mentioned above, only photons originating from the exciton state are of interest in a single photon device, as the relaxation of the biexciton state results in multiphoton emission. With an average lifetime of $\tau_x = 1.1$ ns for the X state, filtering with a time gate of 2 ns sufficiently dismisses XX contributions in the detected signal. The modification of the quantum efficiencies originates from the changed photonic environment due to the plasmonic nanostructure in close proximity to the quantum emitter. As discussed before, the metallic resonator modifies the decay rate $\gamma = \frac{1}{\tau} = \gamma_{rad} + \gamma_{nr}$ of each state (X,XX) of a quantum emitter compared to the decay rate γ_0 of an emitter in free space according to

$$\gamma = F\gamma_0 = \underbrace{F_{rad}\,\gamma_{0,rad}}_{\gamma_{rad}} + \underbrace{F_{nr}\,\gamma_{0,rad} + \gamma_{0,nr}}_{\gamma_{nr}} \,, \tag{4.5}$$

where F is the Purcell factor and γ_{rad} is the radiative and γ_{nr} the non-radiative decay rate of the respective state, respectively. The enhancement factors as well as the intrinsic quantum yield QY_0 and the device quantum yield QY can be quantitatively extracted from the measurements by solving a set of rate equations that describe the photon statistics in the device [41] and by fitting the obtained decay function to the lifetime curves. Additionally, a power saturation measurement is needed to determine the final overall quantum yield of the device, and saturation is reached at 0.35 photons/pulse. According to the supplier[3], the initial overall quantum yield is $QY_0 = 0.2 - 0.4$. The obtained parameters are summarized in Table 4.1:

i	F_i	$F_{i,rad}$	$F_{i,nr}$	$QY_{0,i}$	QY_i
X	19 ± 2	9 ± 5	21 ± 7	0.28 ± 0.09	0.147 ± 0.009
XX	11 ± 1	23 ± 10	9 ± 1	0.023 ± 0.009	0.203 ± 0.012

Table 4.1: Purcell factors and quantum yields

The overall enhancement factors F are found to be on the order of 20 and therefore demonstrate the ability of the device to increase the decay rates of the quantum emitters compared to the reference. Also, the extracted quantum efficiencies show a moderate decrease of the value for the exciton state in the device, accompanied by a drastic increase of the quantum yield for the biexciton state. This explains

3 PlasmaChem GmbH, PL-QD-O-650.

the remarkable changes in the contributions from the two states in the lifetime measurements.
From these findings the brightness enhancement factor BE (for each state separately, with the focus lying on the exciton state) can be obtained, which is defined as

$$BE(\mathrm{NA}) = \frac{QY\,\gamma\,\eta_{coll}(\mathrm{NA})}{QY_0\,\gamma_0\,\eta_{0,coll}(\mathrm{NA})}\,. \tag{4.6}$$

As the hybrid device combines both, enhanced collection efficiency and enhanced emission rates, BE is a quantity to describe the modified (single) photon flux into a given numerical aperture compared to that of a reference quantum dot on glass. The graph on the left-hand side in Figure 4.20 shows the brightness enhancement for the measured devices (average in green), compared to that obtained from simulations (red). While the high discrepancy at low NA values is again due to the differing dipole orientations in experiment and simulation, the increase of detectable single photons is clearly demonstrated.

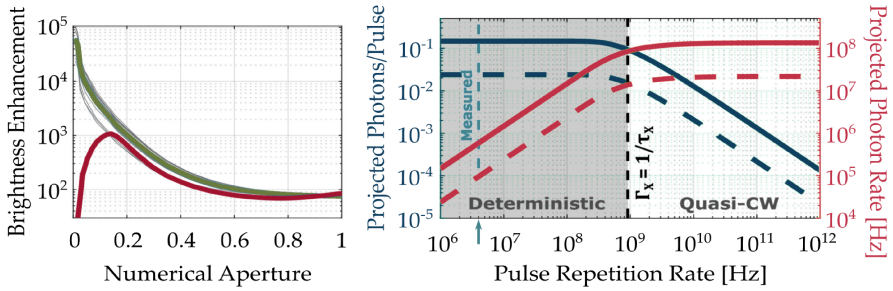

Figure 4.20: (Left) Brightness enhancement factor and (right) projected single photon rates for quantum dots in hybrid devices. Right: The solid lines show the projected rates extrapolated from the measurement for photons originating from the exciton state, whereas the dashed lines show the projected rates with additional time-gated filtering applied. Graphs modified with permission from Ref. [41].

The graph on the right-hand side of Figure 4.20 shows the projected single photon rates that can be expected for varying excitation laser repetition rates. Those projected photon rates and projected photons per pulse, respectively, can be calculated by extrapolating the results obtained from the measurements. The laser used in the experiment was operated at 4 MHz at saturation, therefore resulting in a detected (NA$=0.9$) single photon rate of 0.6 MHz, where the photons originate solely from exciton emission ($4 \cdot 10^6 \frac{\text{pulse}}{s} \cdot 0.35 \frac{\text{photons}}{\text{pulse}} \cdot 42\%$). The corresponding projected photons per pulse (ppp) can also be calculated by solving a rate equation, which results in $ppp(\Gamma_{Laser}) = QY_X(1 - \exp(-\frac{\gamma_X}{\Gamma_{Laser}}))$, where Γ_{Laser} denotes the excitation laser's repetition rate. Therefore, the projected photons per pulse are given by

$ppp \approx QY_X = 0.147$ for $\Gamma_{Laser} = 4\,\mathrm{MHz}$ and $\gamma_X = (1.1\,\mathrm{ns})^{-1}$. Those values (on solid lines) are marked in the graph with a vertical dashed line and an arrow indicating the experimental laser repetition rate. In the deterministic regime, i.e. for laser repetition rates lower than the decay rate of the exciton state, the achievable single photon rate approaches $1 \cdot 10^8 \frac{\mathrm{photons}}{s}$, whereas in the quasi-continuous wave regime even rates as high as $1.4 \cdot 10^8 \frac{\mathrm{photons}}{s}$ should be possible.
Even though the numbers shown in Figure 4.20 are only related to the exciton state, the single photon purity can be questioned due to simultaneous multiphoton emission originating from the biexciton state. For comparison, the dashed lines show the obtained projected photon rates with additional time-gated filtering (2 ns) applied, which sufficiently dismisses those biexciton photons [196]. The projected photon rates are therefore reduced to 16%, yet they still reach values as high as $2 \cdot 10^7 \frac{\mathrm{photons}}{s}$ and represent a lower limit for high purity single photons in the hybrid device.

4.3 POLARIMETRIC SPECTROSCOPY AND ANALYSIS OF PLANAR GOLD NANOSTRUCTURES

The exploitation of locally strongly enhanced near fields originating from the confinement of light in close vicinity to plasmonic nanostructures is the basic principle in a variety of plasmon-enhanced sensing applications [197, 198], with achievable sensitivities reaching even down to the single molecule level [199]. The influence of plasmonic nanoantennas on the emission behavior of semiconductor nanocrystals was part of the studies described in sections 4.1 and 4.2 and the occurring modifications of the emission rates were extensively discussed. Fluorescent quantum emitters, in return, can be also utilized to detect plasmonic near fields [200]. While there is a variety of experimental approaches to image such near fields, above all scanning near-field optical microscopy (SNOM) techniques [201–204], but also methods based on local ablation of materials in combination with fast laser excitation pulses [205] or photochemical processes in photoactive molecules [206–209] as well as photoemission electron microscopy [210, 211], it is a further challenge to gain information on the optical properties of the detected fields [212]. This is important though, e.g. in order to acquire a better understanding of the mechanisms involved in selective fluorescence enhancement, as it is observed for chiral molecules close to plasmonic nanostructures [213–216]. As also electromagnetic fields can possess optical chirality, and the enantiomer-selectivity originates from the plasmonic near fields, it is of high interest to investigate their chiroptical properties.

Chiral plasmonics constitutes a complete field of research on its own, and substantial efforts are put into finding and optimizing structure designs with tailored optical properties, solitary as well as arranged in metasurfaces [47, 48, 112, 217, 218].

The study presented here contributes to a better understanding of the formation of chiroptical fields in single plasmonic nanostructures. Therefore, single planar gold structures with varying geometries, ranging from achiral to chiral, were investigated experimentally with the help of polarized single-particle dark-field scattering spectroscopy and also theoretically, supported by simulations. A strategy was developed to determine the full set of Stokes parameters from the polarimetric spectroscopy measurements, which was used to demonstrate the chirality flux to the far field [53]. In addition, a dipole model was set up to describe the findings analytically, and a remarkable agreement between measurement, simulation and calculation could be found. The results of this study have been published in *Mildner et al., Decoding Polarization in a Single Achiral Gold Nanostructure from Emitted Far-Field Radiation, ACS Nano, 2023* [107].

4.3.1 *Polarimetric Spectroscopy*

As mentioned before, it is of broad scientific interest to study the chiroptical properties of electromagnetic fields emerging from plasmonic nanostructures, both in the near and far field. Apart from sophisticated imaging techniques, the characterization usually relies on ensemble far-field measurements, namely linear circular dichroism spectroscopy, which records the difference in extinction, i.e. includes absorption and scattering, for circularly polarized excitation light with opposed handedness. Non-zero responses are then used to draw conclusions on the near-field optical properties [219].
Here, in contrast, single particles were investigated with a modified dark-field scattering spectroscopy set-up, which is described in detail in sections 3.2.1 and 3.2.2, and therefore only takes scattered signals into account. The set-up allows for maintaining the polarization of the incoming electric field, even though the light gets focused through a dark-field condenser. This is of fundamental importance for the interpretation of the obtained data, as will be discussed in the following sections. In the experiments described below, the incoming electric field was chosen to be linearly polarized. This is achieved by inserting a broadband polarization filter in the excitation path, followed by a rotatable cross-like aperture, which is placed directly into the dark-field condenser, and which selectively lets pass certain incoming k-vectors and otherwise blocks light that gets depolarized, i.e. whose polarization is rotated from the initial one during the focusing process. Details on how the aperture was designed can be found in section 3.2.2.

Figure 4.21 illustrates the depolarization effect on the electromagnetic fields for different numerical apertures. The graph on the left-hand side shows the situation for the condenser used in the experiment. The incoming light enters the condenser under normal incidence (not shown) and gets focused onto the sample. The black arrows show the resulting k-vectors, i.e. oblique incidence, for the boundary values of the angular range of the dark-field condenser, while the colored arrows depict the electric field vectors. For an initially linearly polarized electric field in x-direction, the polarization is only maintained for k-vectors originating from a small angular range around directions parallel or perpendicular to the polarization orientation, after passing through the condenser. The graph on the right-hand side demonstrates the effect more clearly, as it shows the deviation from the x-axis in a top view image and as a bigger range of NA values was chosen. While for a NA of 0.6 the depolarization effect is almost negligible, the difference to a NA of 0.95 becomes even clearer.

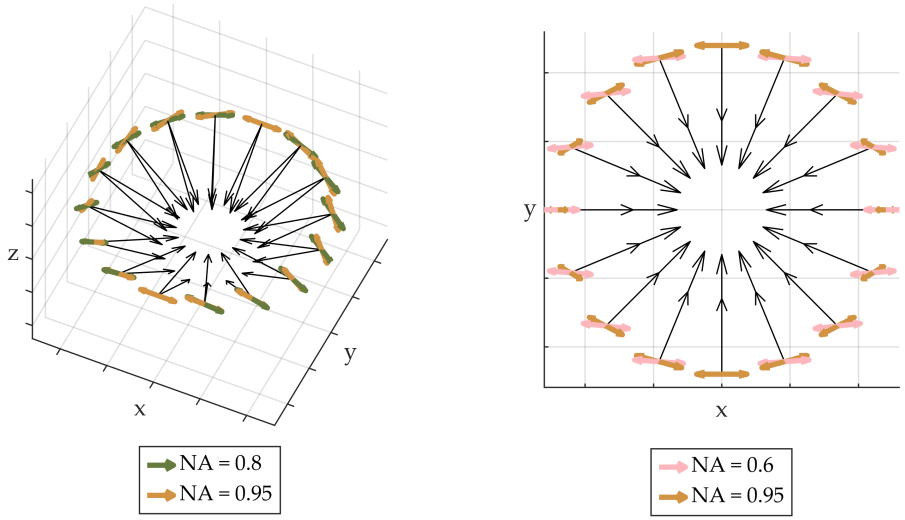

Figure 4.21: (Left) Depolarization of the electric field of linearly polarized (in x-direction) incoming light in a dark-field condenser for different NAs. The black arrows show the resulting k-vectors of the light and the colored arrows the corresponding electric field vectors. (Right) Exemplification of the effect for a greater range of numerical apertures in top view.

4.3.2 *Optical Far-Field Characterization of Rectangles and Rhomboids*

In this study, several planar nanostructures with different geometries were investigated with the help of polarized dark-field scattering spectroscopy measurements. The structures discussed here consist of gold with a thickness of $h \approx 25\,\text{nm}$ and are located on a transparent glass substrate, so that transmission measurements could be performed. A detailed description of the fabrication process can be found in section 3.1.4. Figure 4.22 shows SEM images of the according nanostructures, which are named A, B, and C in order to simplify the reading flow. While the widths ($\approx 80\,\text{nm}$) and lengths ($\approx 120\,\text{nm}$) of the structures are kept constant, the angle between the short and the long axis is varied from $\alpha_A = 90°$ for the rectangular structure to $\alpha_B = 105°$ and $\alpha_C = 120°$ for the rhomboids. The rectangular structure therefore is achiral, while the rhomboids are 2D-chiral structures with increasing values of geometrical chirality χ_{2D}.
The lower row in Figure 4.22 shows the corresponding normalized dark-field scattering spectra for each structure, each for unpolarized excitation (black solid line) and also linearly polarized light oriented along $\Phi_{exc} = 0°$ (blue dotted line), i.e. parallel to the rectangle's short axis, along $\Phi_{exc} = 45°$ (brown dash-dotted line) and along $\Phi_{exc} = 90°$ (green dashed line), i.e. parallel to the rectangle's long axis. For each structure, the unpolarized spectrum shows two peaks, typifying the longitudinal (LR) and transverse (TR) localized surface plasmon resonances and their relative strengths, showing that the longitudinal

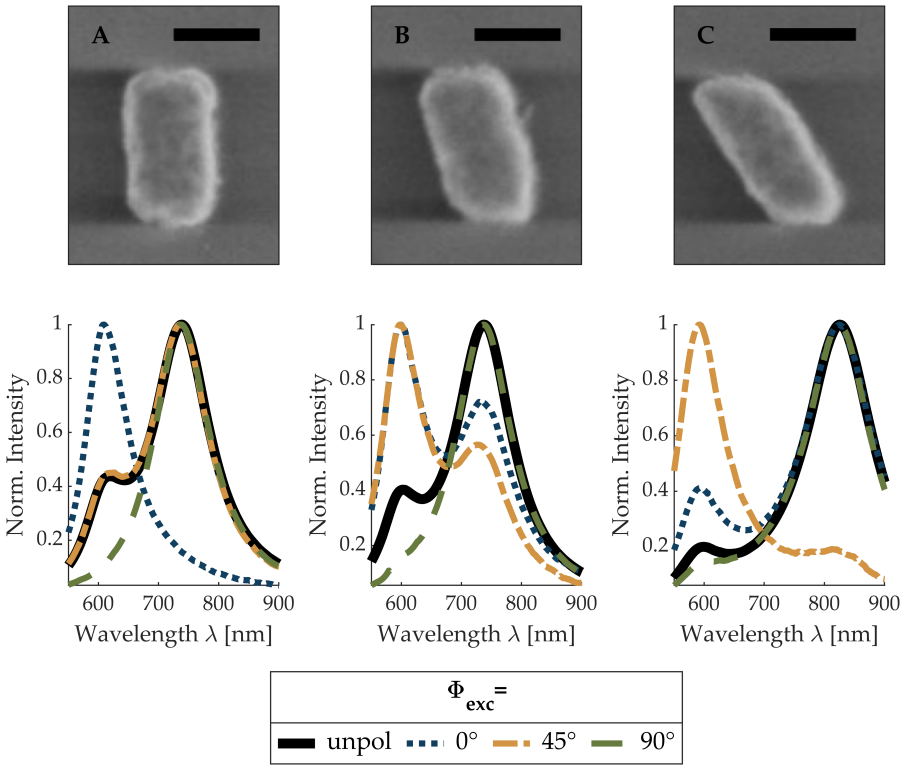

Figure 4.22: SEM images of the investigated achiral (A) and chiral (B, C) nanostructures with varying angles between the short and the long axis (scale bar is 100 nm) and according normalized dark-field scattering spectra for different excitation polarizations Φ_{exc}. $\Phi_{exc} = 0°$ is oriented parallel to the rectangle's short axis, while $\Phi_{exc} = 90°$ is oriented parallel to its long axis.

mode clearly outnumbers the transverse mode in intensity.

As expected for particle A, illumination with light polarized along $\Phi_{exc} = 0°$ only excites the transverse dipolar mode with a resonance at $\lambda_{TR} = 615\,\text{nm}$, while polarized illumination with $\Phi_{exc} = 90°$ only excites the longitudinal mode at $\lambda_{LR} = 740\,\text{nm}$ and $\Phi_{exc} = 45°$ reproduces the unpolarized spectrum. The cases differ for particles B and C, where both modes are excited with varying intensities for all three linear polarization orientations of the illuminating white light source. As can be seen in the spectra of particle C, excitation with linear polarization in $\Phi_{exc} = 45°$ almost solely excites the *transverse* mode, while illumination with $\Phi_{exc} = 0°$ and $\Phi_{exc} = 90°$ clearly excites both modes to a notable amount, which suggests that the orientations of the dipolar modes changed related to the change in geometry. A strategy to experimentally obtain the eigenmodes' orientations will be discussed in section 4.3.6. Additionally, a red-shift of the longitudinal resonance in particle C can be observed, as the geometrical length increases even though the overall dimensions are kept constant.

To further investigate the optical far-field responses of the different nanostructures, additional analyzation of the emitted signals was per-

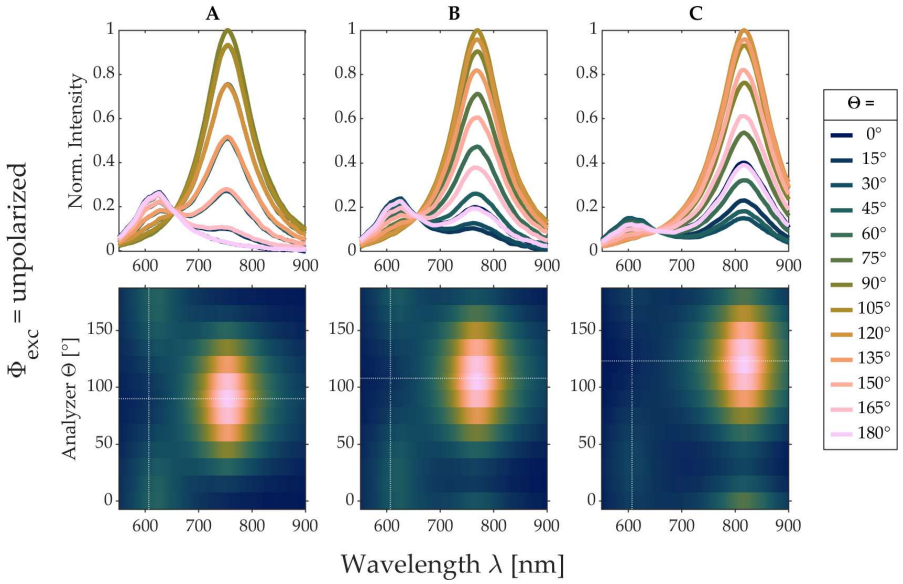

Figure 4.23: Analyzed dark-field scattering spectra for unpolarized excitation with analyzation angles Θ ranging from 0° to 180° for all three kinds of particle geometries A-C. The vertical white dotted lines in the bottom row images mark a wavelength at which the intensity course was fitted with a sine function for each data set. The horizontal dotted lines mark the respective positions of the intensity minimum.

formed by introducing a linear polarizer in the detection path. This analyzer was inserted directly after the collection objective to avoid possible influences of any other optical components in the optical path (cf. section 3.2.2). Figure 4.23 shows analyzed dark-field scattering spectra for all three kinds of particle geometries A-C, obtained from similar structures in an array. The structures were excited with unpolarized illumination, i.e. no polarization filter and aperture were inserted in the excitation path, resulting in an annular distribution of incoming k-vectors (cf. Figure 4.21). The analyzer was varied from $\Theta = 0°$ to 180° in steps of 15°, as polarization is π-periodic and the measurements suffice for further evaluation. Finally, all spectra were normalized to the maximum value of each set for better comparability. So, for unpolarized excitation and simultaneous analyzation, the intensities of both modes vary dependently on each other, while one mode gains intensity, the other one decreases, which results in a joint intersection of all analyzed spectra. Interestingly, while for the achiral rectangular structure the intensities cancel out for *cross-polarization*, i.e. analyzer and eigenmode's dipole moment being oriented orthogonal, the case differs for chiral particles B and C, as the longitudinal modes do not vanish. The intensity of the transverse mode, conversely, is too low to be detectable in the slope of the longitudinal resonance.
The lower row in Figure 4.23 shows a heat map visualization of the spectrally resolved intensity patterns in dependence of the analyzer an-

gle Θ. At first glance, an alternating increase and decrease of intensity is found for all three particles. The vertical white dotted lines mark a wavelength ($\lambda = 606\,\text{nm}$) at which the intensity course was fitted with a sine function in each image. The horizontal white dotted lines mark the found minimum positions of the respective sine functions, namely $\Theta_A = (89.5 \pm 1.6)^\circ$, $\Theta_B = (107.9 \pm 1.5)^\circ$ and $\Theta_C = (122.7 \pm 1.5)^\circ$. Those values coincidence quite well with the maximal intensity found at wavelengths of the longitudinal resonances and also with the deflection angle of the respective nanostructure.
As already mentioned in the description of Figure 4.22, the eigenmodes' orientations seemingly were altered with the change in geometry, yet their orientations remain still unclear. If the longitudinal mode's dipole moment were to follow the particle's geometry (and the transverse mode remains orthogonal), the intensity should vanish for an analyzer orientation of $\Theta = 15^\circ$ in particle B and $\Theta = 30^\circ$ in particle C, which is not the case.
For further investigations, the structures were excited with linearly polarized light, therefore the cross-like aperture was placed in the condenser, i.e. limiting the illumination to originate from four opposite directions (cf. section 3.2.2). The spectra were then analyzed simultaneously. The results for all three geometries and excitation polarization orientations are summarized in Figure 4.24.

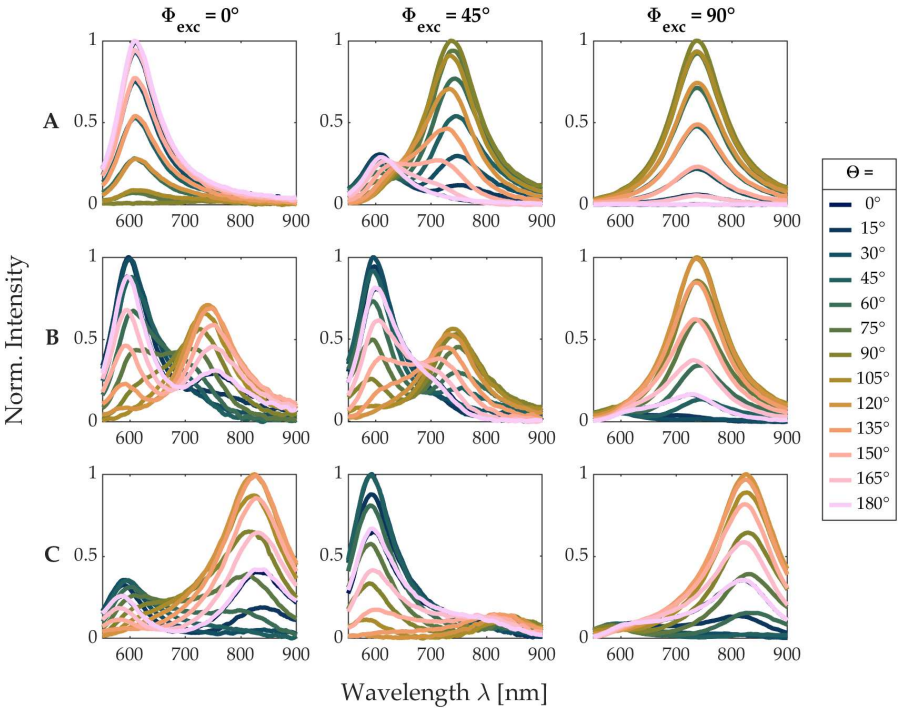

Figure 4.24: Analyzed dark-field scattering spectra with analyzation angles Θ ranging from 0° to 180° for all three particle geometries A-C (rows) for linearly polarized excitation Φ_{exc} illuminations (columns).

For structure A, i.e. the achiral rectangle, and excitation with light polarized along the short axis ($\Phi_{exc} = 0°$), the measurement results in a varied decrease and increase of the intensity of the solely detected transverse resonance, respectively, and the signal vanishes, as expected, at cross-polarization of the excitation and analyzation filter. For excitation with light polarized along the long axis ($\Phi_{exc} = 90°$), only the longitudinal resonance is detected and its intensity increases and decreases again for varying analyzation angles, starting and ending at zero counts.
More interesting, however, is the case for linearly polarized excitation in $\Phi_{exc} = 45°$, which excites both modes simultaneously. Additional analyzation of the spectra does not solely result in an alternating decrease and increase of intensity of both modes, as it might be naively expected and as it was observed for unpolarized excitation. It rather shows an additional shifting of the respective resonances for different analyzation angles, and the signal also does not vanish for cross-polarized excitation and analyzation filters. Analyzed measurements on particles B and C show a similar, therefore confirming behavior, as for the chosen excitation polarization orientations always both modes are excited simultaneously, even though to varying extents (cf. Figure 4.23).
For a more profound study, the rectangular structure was chosen to be investigated in more detail, as will be discussed in the following. To facilitate comparison, Figure 4.25 again visualizes the analyzed spectra of structure A for linear excitation polarizations oriented along $\Phi_{exc} = 0°$ and $\Phi_{exc} = 90°$ in a heat map. As discussed before, both dipolar modes are excited exclusively for the respective incoming polarization, and the signal vanishes for cross-polarization. The lower row shows polar plots of the intensity at distinct wavelengths, chosen to cover the whole spectral range of interest, including the resonance positions.
As described and discussed in section 2.4.1, such intensity patterns hold information on the polarization states of the electric fields, i.e. their polarization ellipses, at the respective wavelengths. The intensity data was therefore fitted (solid lines in polar representation) by

$$I(\Theta) = a^2 \cdot \cos^2(\Theta - \Psi) + b^2 \cdot \sin^2(\Theta - \Psi) \ , \tag{4.7}$$

where Θ is the analyzer angle, a and b are the major and minor axis of the polarization ellipse and Ψ gives the orientation of the polarized light. As a result, the intensity plots for the emitted light both show linear polarization over the whole spectral range, rotated by 90°, and parallel to the excitation polarization orientation.
In contrast, the spectrally resolved intensity pattern for $\Phi_{exc} = 45°$, as shown in Figure 4.26, differs noticeably, as there no longer is a symmetry axis for varying analyzer orientations. The peculiarities in the analyzed spectral responses are exemplarily discussed for analyzer

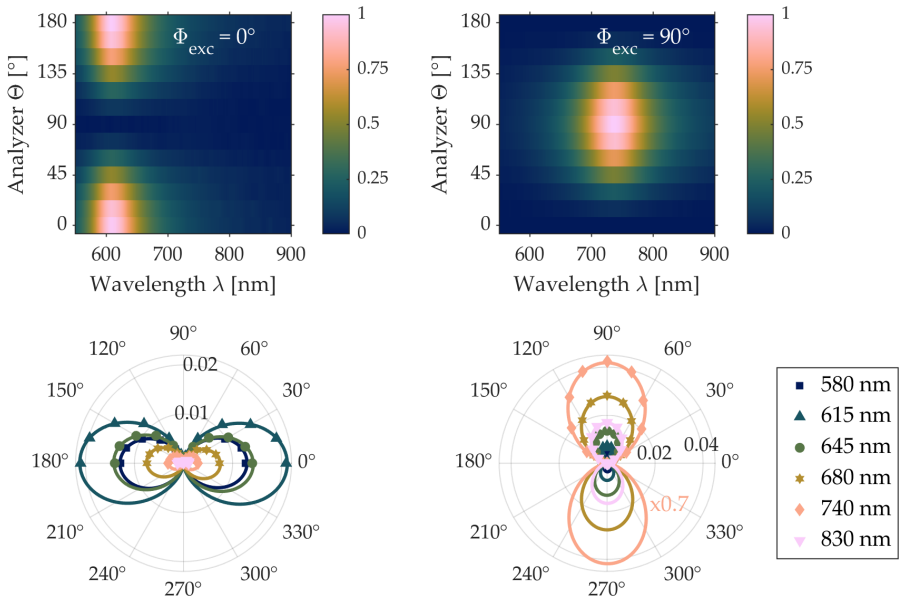

Figure 4.25: (Top) Heat map visualization of the analyzed dark-field scattering spectra for particle A excited with linearly polarized light oriented in $\Phi_{exc} = 0°$ (left) and $\Phi_{exc} = 90°$ (right) and (bottom) corresponding polar plot representations of the obtained intensities for different wavelengths.

angles of $\Theta = 45°$ and $\Theta = 135°$ (positions highlighted with horizontal white dashed lines), i.e. parallel and cross-polarized analyzation. The corresponding spectra are also shown in Figure 4.26, depicted with a vertical offset to facilitate comparison to the reference spectrum without analyzation. First of all, it can be seen that the line shapes of both analyzed spectra differ from the reference, which is clearly visible in the overlap region of both modes. Additionally, the resonance positions of both modes vary, as it has already been mentioned in Figure 4.24. To bring out the shifts more clearly, the *unfiltered* resonance positions $\lambda_{TR} = 615\,\text{nm}$ and $\lambda_{LR} = 740\,\text{nm}$, obtained from Lorentzian fits to the reference spectrum, are marked with vertical black lines in the graph. While for parallel filters ($\Theta = 45°$) one could naively expect a similar spectrum as the reference, there instead appear two clearly distinct peaks, and their resonance positions are shifted apart. For cross-polarized filters, the signal does not cancel out, but rather shows two resonance peaks that seem to merge. To visualize the shifting behavior for all analyzer angles, the graph on the right-hand side in the lower row of Figure 4.26 shows the resonance positions of all spectra as obtained from Lorentzian fitting. The origin of these effects can be understood by looking at the angular intensity patterns, again shown exemplarily for several wavelengths in the bottom left panel in Figure 4.26. Here, the individual intensity plots show varying orientations, i.e. the polarization orientations differ for different wavelengths. Also, for some wavelengths the emitted light now shows polarizations di-

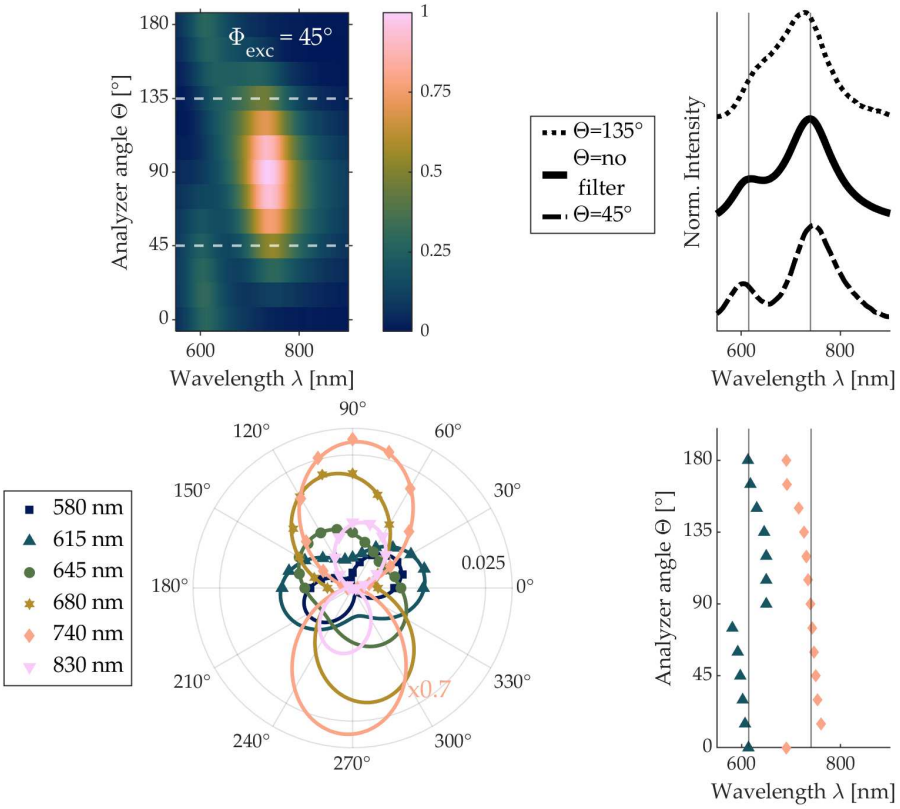

Figure 4.26: Heat map visualization (top left) of the analyzed dark-field scattering spectra for particle A excited with linearly polarized light oriented in $\Phi_{exc} = 45°$ and corresponding polar plot representation of the obtained intensities for different wavelengths (bottom left). Comparison of analyzed spectra (parallel- and cross-polarized to excitation) to the unpolarized spectrum (top right) and analyzer angle-dependent resonance positions of both dipolar modes as obtained from fits (bottom right). The vertical black lines mark the resonance positions found for the unpolarized spectrum.

verging from purely linear polarization, as it has been observed before for excitation polarizations oriented along the eigenmodes' dipole moments (cf. Figure 4.25). So, by adding an analyzer to the optical path, the measured spectra show wavelength-dependent projections of the electric fields on the transmission axis of the analyzer, and the detected signal strength therefore clearly depends on the relative orientation of the respective polarization ellipse for each wavelength. These findings are well supported by far-field simulations conducted with *MNPBEM* (cf. section 3.3), which are described in the following section 4.3.3.

4.3.3 *Computed Far-Field Characterization of Rectangular Nanostructures*

In this work, simulations on the optical near- and far-field properties of plasmonic nanostructures were performed with the help of the MATLAB toolbox *MNPBEM* (cf. section 3.3).
Here, the gold nanostructures, located on a glass substrate, were modeled to match the experimental data. Plane wave excitation was chosen to compute the scattered far fields for light coming in from two directions. These depend on the respective excitation polarization orientation, as in the experiment the cross-like aperture in the condenser limited the directions of the incoming light (cf. section 3.2.2). Illumination was also chosen to come in under oblique incidence (NA= 0.9), to mimic the condenser.
Figure 4.27 shows a sketch of the modeled rectangular nanostructure together with the according illumination vectors, which characterize the excitation light being polarized along $\Phi_{exc} = 45°$.

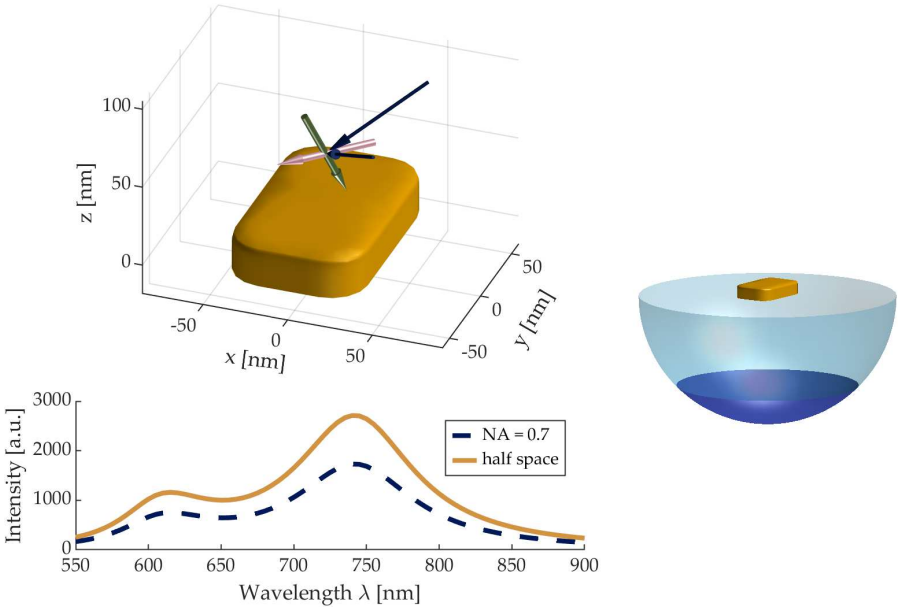

Figure 4.27: Simulation model and computed scattering spectra for the rectangular nanostructure. The dark blue arrows depict the k-vectors of the illumination coming in from two sides and the colored arrows show the electric field vectors for TE (pink) and TM (green) illumination for an excitation polarization orientation along $\Phi_{exc} = 45°$.

The dark blue arrows depict two of the incoming k-vectors and the pink and green arrows show the electric field vectors for TE and TM illumination, respectively. The resulting far-field spectrum, as shown in the bottom graph, is then given by the superposition of both individual scattered spectra obtained from each excitation. The graph also shows the computed spectrum when a limitation of the collection angle due to the numerical aperture of the objective is included in the

evaluation. This situation is depicted in the inset on the right-hand side of Figure 4.27 for an exemplarily chosen NA of 0.7. The hemisphere depicts a unit-sphere discretization at which the electromagnetic fields are computed at infinity. The spectral response is then given by the sum of all segmental electromagnetic fields. By restricting the number of elements that are taken into account (dark blue area in the inset), intensity scaling is observed. The spectral properties however, remain unchanged. Therefore, the NA of the objective was neglected in further simulations.

In the experiment, the scattered light (in the far field) is collected with an *infinity-corrected* objective, it is therefore collimated upon exiting the objective. Subsequently, the light fields are analyzed as they hit the linear polarization filter under normal incidence, i.e. the electric field vectors are oriented perpendicular to the direction of propagation and parallel to the filter's plane.
The situation was modeled in simulations to study its impact on the spectral responses and compared to simulations, in which simplifications were assumed, i.e. normal incidence of the incoming light or negligence of the collimation effect (cf. Figure 4.28). This was done to justify the used simplifications in further simulations on the near fields and in the applied dipole model described in section 4.3.6.
As already mentioned before, the electromagnetic fields in the far field are computed at a discretized unit-sphere at infinity. The top image in Figure 4.28 once again depicts the investigated rectangular nanostructure, which is excited with plane wave illumination $\vec{k}_{in}$ coming in either at an angle (NA= 0.9) or at normal incidence (bold dark blue arrows on top). The excitation polarization orientation in the examples described in the following is along $\Phi_{exc} = 45°$ (not shown here). The computational hemisphere is illustrated, and the blue grid shows how the surface is meshed into segments j. The blue arrows on some exemplarily selected elements show vectors that are oriented parallel to the respective surface normal vectors. The computed and directly accessible electric (and magnetic) fields are of the form $\vec{E}(\vec{r}) = \vec{E}_r(\vec{r}) + i\vec{E}_i(\vec{r})$ $\left(\vec{H}(\vec{r}) = \vec{H}_r(\vec{r}) + i\vec{H}_i(\vec{r})\right)$, where $\vec{E}_{r,i}$ $(\vec{H}_{r,i})$ are complex amplitudes and propagate in those arrow directions, so that $\vec{k}_{sca} || \vec{e}_n$.
To mimic the collimation effect, by applying a rotation matrix, the normal vector of every element was rotated by an individual angle β_j around the axis $\vec{t}_j$, which is given by the corresponding horizontally oriented tangential vector of each element j. Each resulting vector points in $-\vec{e}_z$ direction, as shown with the green arrows (plotted with a radial offset) in Figure 4.28. The respective electric field vectors were consequently rotated as well by multiplying the same rotation matrix, and therefore eliminating the $E_{j,z}$-components.
The electric fields were subsequently analyzed by calculating the pro-

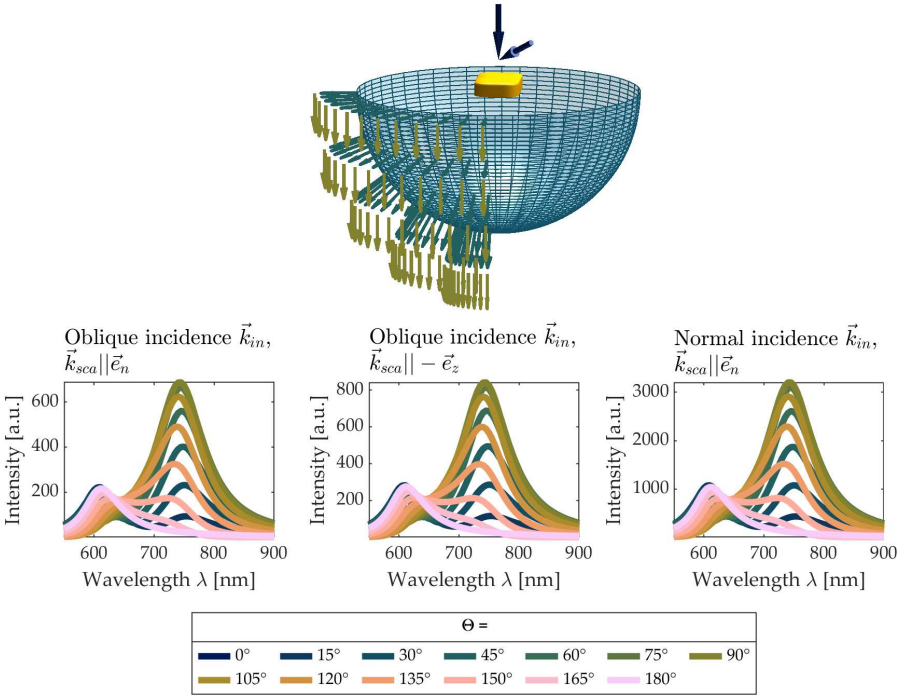

Figure 4.28: Simulation model for the rectangular nanostructure, both for oblique and normal incidence excitation $\vec{k}_{in}$ (dark blue bold arrows on top). The hemisphere is discretized into individual elements as shown with the grid. The blue arrows show k-vectors of the scattered light $\vec{k}_{sca}$ on exemplarily selected elements, which are oriented parallel to the normal vectors $\vec{e}_n$ on the respective segments. The green arrows show the k-vectors being rotated into $-\vec{e}_z$ direction, to mimic the collimation of light with the objective. The bottom row compares *analyzed* spectra, each for an excitation polarization orientation along $\Phi_{exc} = 45°$ and for oblique or normal incidence, as stated in the titles of each graph. The scattered intensity was calculated from the computed electric fields, either directly ($\vec{k}_{sca}||\vec{e}_n$) or with previous rotation ($\vec{k}_{sca}|| - \vec{e}_z$).

jections in the direction of the transmission axis Θ of the analyzer via

$$E_{j,\Theta} = E_{j,x} \cdot \cos\Theta + E_{j,y} \cdot \sin\Theta \ . \tag{4.8}$$

As intensity is proportional to the absolute square of the complex electric field, $I \propto |E|^2$, the fields were added up ($E_\Theta = \sum_j E_{j,\Theta}$) and multiplied by their complex conjugate.
The lower row in Figure 4.28 shows the obtained *intensities* for three different situations. The left and center graph both show the evaluation for oblique incidence excitation, yet on the left the computed fields were analyzed directly, while in the center they were rotated as described above. The most apparent difference that can be located is the change in intensity, which is due to the excluded $E_{j,z}$-component.

This is hardly relevant though, as absolute values are not of interest. The graph on the right-hand side shows the obtained spectra for normal incidence excitation, and the electric fields were evaluated directly as computed. Again, a similar spectral behavior is observed. These results, i.e. the similarities of the obtained spectral responses, strongly justify the simplification of normal incidence in the following simulations of the optical near fields.

4.3.4 *Computed Near-Field Characterization of Rectangular Nanostructures*

The experimental results on the analyzation of dark-field scattering spectra of achiral planar gold nanorectangles, as discussed in section 4.3.2, indicate that there are, contrary to common expectations, chiroptical effects detectable in the far-field responses of such structures. The polarization states of the emitted light were found to be wavelength-dependent. They also vary in their degree of ellipticity and their relative orientation, depending on the linear polarization orientation of the excitation light. To further investigate these effects, additional simulations were performed on the particle's near field, as it contains both, evanescent waves and waves propagating to the far field. It therefore offers insights on the optical properties at the origin of the plasmonically enhanced fields. Moreover, the occurrence of chiroptical effects in the near field of achiral nanostructures has been previously reported, even for linearly polarized excitation [51, 220].

The working principle of the *MNPBEM* toolbox can be shortly summarized as follows: After setting up the particle's geometry and dielectric properties, the surface charges σ, located at the boundaries of the nanoparticle, are computed. This is done for a given excitation (cf. section 3.3) and in such a way that the boundary conditions of Maxwell's equations are fulfilled. Further measurement quantities, as absorption or scattering cross sections but also electric fields, can thus be deduced from these surface charge distributions.

For the simulations discussed in the following, the particle and its dielectric environment were set up as described above (cf. section 4.3.3), yet linearly polarized plane wave excitation was chosen to come in under normal incidence.

So, the computed surface charges are complex quantities and contain the time evolution via $\sigma(\vec{r}, t) = \Re\{\tilde{\sigma}(\vec{r}) \exp(-i\omega t)\}$ [221]. This time dependence is important to note, as the wavelength-dependent surface charge distributions are often used to identify the respective plasmonic modes in computed scattering spectra. Figure 4.29 exemplarily illustrates the time evolution of the surface charge distribution at the resonance wavelength $\lambda_{LR} = 740\,\text{nm}$ of the longitudinal dipolar mode, for half a period ranging within $\omega t = \mathcal{T} \in [0, \pi]$ and for two different

excitation polarization orientations $\Phi_{exc} = 90°$ and $\Phi_{exc} = 45°$. It becomes clear that the temporal course of the respective surface charge distribution highly depends on the polarization of the excitation light, as for $\Phi_{exc} = 90°$ the charges oscillate along the polarization direction of the incoming electric field, while for $\Phi_{exc} = 45°$ the charges seem to rotate azimuthally. Also, if the time dependence were to be neglected, the resulting surface charge distributions would be similar to the ones shown for $\mathcal{T} = 0$. The difficulties in identifying the longitudinal mode from these brief snapshots are clearly apparent.

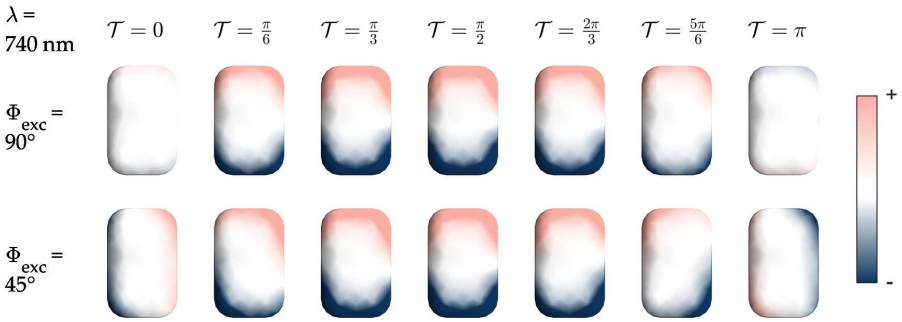

Figure 4.29: Time evolution of the computed surface charge distributions for $\lambda_{LR} = 740\,\text{nm}$ for two different excitation polarization orientations $\Phi_{exc} = 90°$ (top) and $\Phi_{exc} = 45°$ (bottom).

The uppermost row in Figure 4.30 shows the surface charge distributions for the rectangular nanostructure at selected wavelengths (same as in Figure 4.26) as stated in the top panel, and excited with linearly polarized light along $\Phi_{exc} = 45°$. The distributions were plotted for different times $\mathcal{T}$, such that the corresponding time-dependent dipole moments $\vec{p}(t)$ reach a maximum (see next paragraph). The second row shows consequential near-field maps for the same set of wavelengths, computed in a plane located at $z = -10\,\text{nm}$, i.e. below the particle. This was done to stay true to the direction of light propagation, as experimental measurements were performed in transmission, and reversal of light propagation (i.e. reflection) would lead to a change in sign in further discussions on the handedness of the scattered light. Be that as it may, the resemblance of both, surface charge distributions and enhanced near fields is clearly notable. Additionally, for the resonance positions ($\lambda_{TR} = 615\,\text{nm}$, $\lambda_{LR} = 740\,\text{nm}$) the field distributions look quite as expected for two orthogonally oriented linear dipoles, as they are oriented along the transverse and longitudinal dipolar modes' axes. The near-field maps for the remaining wavelengths show highest field enhancements oriented in different azimuthal directions. However, by calculating the electric field enhancements, the information on the temporal courses of the electric field vectors is lost, and therefore no conclusions can be drawn on the respective polarization states. The time evolution of the surface charge distributions (cf. bottom row

in Figure 4.29) shows more of a rotational behavior than an oscillating one, though, i.e. resulting in rotating dipole moments, as will be discussed in the forthcoming paragraph. Prior to that, the electric near-field maps were calculated to show the circularly polarized electric field components, as can be seen in the two lower rows in Figure 4.30. The images likewise show the electric near-field enhancements, yet in a circular basis, i.e. the components with different handedness, which are given by $E_{LCP} = E_x + E_y \exp(i\frac{\pi}{2})$ and $E_{RCP} = E_x + E_y \exp(-i\frac{\pi}{2})$. The superposition of left- and right-handed circularly polarized light with no relative phase shift results in linear polarization. This can be observed at the near-field maps for $\lambda = 830\,\text{nm}$, where the portions (and locations) of E_{LCP} and E_{RCP} are quite similar and therefore resemble the distribution obtained in a linear basis. For the remaining wavelengths, the field distributions differ clearly, not only in intensity, but also the locations with highest field enhancements around the particle. This strongly indicates that the superposition of both circular components does not result in linearly polarized light. Lastly, it shall be mentioned that the intensity of the sum of E_{LCP} and E_{RCP} is different to that of the total field shown above in the second row, as the E_z-component is not included.

As mentioned above, for an excitation polarization of $\Phi_{exc} = 45°$, the surface charges were evaluated at some distinct wavelengths and were partly found to rotate azimuthally in the plane of the nanoparticle. To visualize this effect, the time-dependent dipole moments, given by $\vec{p}(t) = \oint \sigma(\vec{r}', t)\vec{r}' dS'$ were therefore calculated for the discussed wavelengths and are displayed in the bottom row of Figure 4.31. In order to allow for an interpretation of the data, the uppermost row once again displays the fits $I(x, y)$ to the intensity values that were experimentally obtained from measurements including an analyzation filter (cf. Figure 4.26), while the center row shows the electric field ellipses $\vec{E}(t)$ calculated from these measurements as described in section 2.4.1. The black dashed lines denote the 95% confidence interval for the calculated fields. All plots in Figure 4.31 are normalized to their maximal amplitude to facilitate comparison. As can be seen, the polarization ellipses strongly vary in their degree of ellipticity, i.e. the ratio between the lengths of the minor and major axes, and therefore clearly demonstrate chiroptical behavior in the far field. Also, the overall orientations of the polarization ellipses vary across the investigated spectral range, showing an almost horizontal orientation at the resonance position of the transverse mode ($\lambda_{TR} = 615\,\text{nm}$) and an almost vertical orientation at the resonance wavelength of the longitudinal mode ($\lambda_{LR} = 740\,\text{nm}$). Those experimentally obtained overall orientations of the electric field ellipses (and even of the intensity patterns) coincide with the positions of the highest field enhancements in the computed near-field maps displayed in Figure 4.30. Comparison to

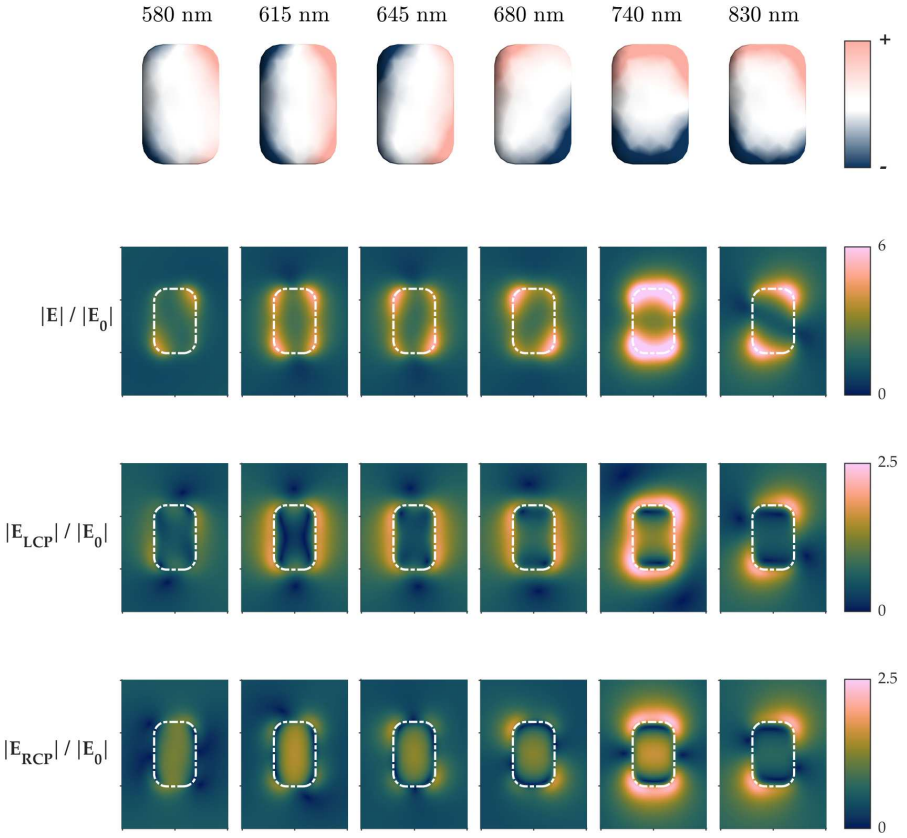

Figure 4.30: Computed surface charge distributions (top row) and near-field maps (located at $z = -10\,\text{nm}$) for the rectangular nanostructure in a linear (second row) and a circular base (third and fourth row), i.e. showing linear electric field components and circularly polarized electric field components with different handedness. The excitation polarization is oriented along $\Phi_{exc} = 45°$.

the time-dependent dipole moments also shows excellent agreement, therefore demonstrating that the chiroptical properties are already determined in the near field.

As the results discussed before already imply that chiroptical effects are to be expected in the near fields surrounding the achiral nanostructure, it is a logical extension to compute optical chirality maps with the help of the simulations described above. The desired normalized optical chirality enhancements $\hat{C}$ were computed in a plane located at $z = -10\,\text{nm}$ below the particle, similar to before, for incident light coming in under normal incidence and with different excitation polarizations. The optical chirality is given by $C = -\frac{\varepsilon_0 \omega}{2} \Im\left(\vec{E}^* \cdot \vec{B}\right)$, as introduced in section 2.4.2, and can be calculated directly from the computed electromagnetic fields. The term *normalization* in $\hat{C}$, accounts for dividing the obtained C values by the absolute value of a factor $C_0^{\pm} = \pm\frac{\varepsilon_0 \omega}{2c}|\vec{E}|^2$, which denotes the optical chirality of circularly polarized light, where the + and - signs refer to the respective

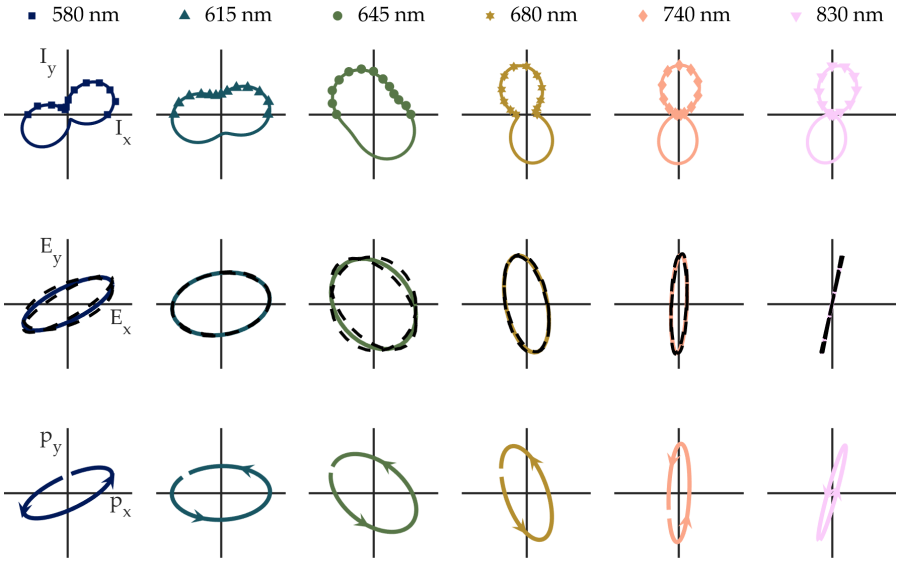

Figure 4.31: (Top row) Analyzed far-field intensity measurements and corresponding fits for the rectangular nanostructure excited with linearly polarized light under $\Phi_{exc} = 45°$ and (center row) thereof extracted electric field ellipses (with confidence interval) for the wavelengths given in the top panel. (Bottom row) Time evolution of the wavelength-dependent dipole moments calculated from the time-dependent surface charge distributions. All plots are normalized to their maximal amplitude for better comparability.

handedness, i.e left- and right-handed circular polarization. $|C_0^{\pm}|$ is calculated from the incoming fields at the same frequency, but without the nanostructure. The normalized optical chirality values $\hat{C}$ are therefore independent of the intensity of the incident light, and show the enhancement of chirality, as regions with $|\hat{C}| > 1$ correspond to superchiral fields [213].

The computed complex electromagnetic fields are given by the superposition of the induced and incoming fields, i.e. are of the form $\vec{E}_{tot} = \vec{E}_{ind} + \vec{E}_{inc}$ ($\vec{H}_{tot} = \vec{H}_{ind} + \vec{H}_{inc}$). To broaden the discussion, Figure 4.32 firstly shows the optical chirality densities calculated solely from the induced fields, while Figure 4.33 finally shows the obtained maps calculated from the total fields. The simulations were performed for all three of the experimentally investigated incident linear light polarizations (i.e. 0°, 45°, 90°) and additionally for left- and right-handed circular polarizations (i.e. LCP and RCP).

As can be seen in Figure 4.32, a non-zero optical chirality is found for all excitation polarizations, even if the incoming light has no chirality on its own, i.e. does not introduce extrinsic chirality to the system. As in these simulations the excitation light is set up to come in under normal incidence, there is also no extrinsic chirality introduced through broken symmetry aspects of the system's 2D geometry.

For $\Phi_{exc} = 0°$ and $\Phi_{exc} = 90°$, the optical chirality patterns look very similar, showing four main lobes with alternating signs, i.e. alternat-

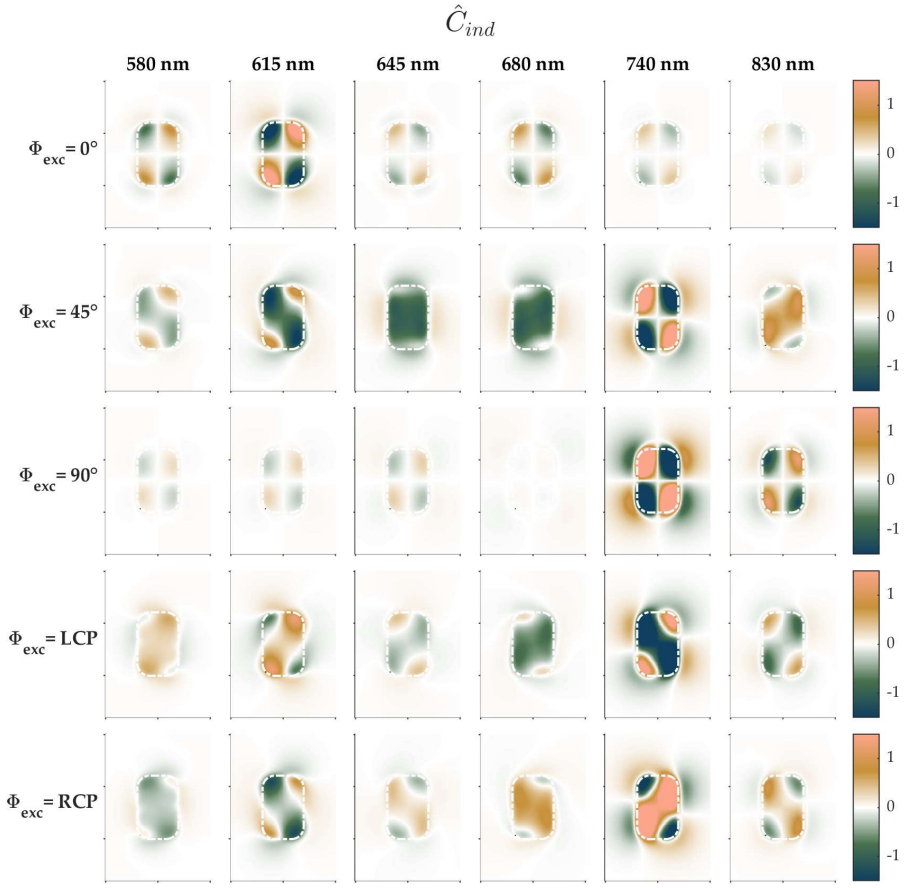

Figure 4.32: Normalized optical chirality $\hat{C}$ calculated from the induced electromagnetic fields for different wavelengths (columns) and different linear or circular polarization orientations of the incoming plane-wave excitation (rows). LCP and RCP denote left- and right-handed circular polarization, respectively. Regions where $|\hat{C}| > 1$ show superchiral hot spots, i.e. fields with a chirality larger than that of circularly polarized light.

ing handedness of the chiral fields, at positions below the particle, whose outline is indicated with a white dash-dotted line. Those lobes are encircled by another set of four lobes, again showing alternating signs that are opposed to those of the inner lobes. For both excitation cases, chirality is highest at the respective resonance positions, even showing superchirality, i.e. $|\hat{C}| > 1$, for the *inner* lobes/fields. This complies with the work of *T.J. Davis and E. Hendry* [50], where they show theoretically that superchiral fields can be generated close to achiral nanostructures, if the (longitudinal) dipolar localized surface plasmon resonance is excited. As can be seen from the patterns discussed here, this equally holds for both, the transverse and longitudinal dipolar resonances. The patterns also show that chirality decreases with increasing distance from the structure, which indicates a dependence on the choice of the computational domain, i.e. the volume over which integration is performed, when calculating the net

chirality. It shall be mentioned, that the computed chirality patterns are in good accordance to the ones found by *M. Schäferling et al.* [222] in their theoretical work on the occurrence of chiroptical fields in the environment of achiral nanostructures. It is also straightforward to see that due to the symmetry of the obtained patterns, the integral over the optical chirality vanishes for each wavelength. For the just-discussed excitation polarizations, this also holds true if the optical chirality is computed in different planes normal to the direction of the incident light.

The case clearly differs for the optical chirality patterns obtained for $\Phi_{exc} = 45°$. While the pattern obtained at the resonance wavelength $\lambda_{LR} = 740\,\text{nm}$ of the longitudinal dipolar mode looks quite similar to before, the one obtained at $\lambda_{TR} = 615\,\text{nm}$ differs clearly. Interestingly, this pattern resembles pretty much the one obtained for right-handed circularly polarized excitation, which is displayed in the bottom row and was computed for the sake of completeness. The chirality patterns obtained for circularly polarized excitation are also in good accordance to the theoretical ones from *M. Schäferling et al.* [222] and also to the ones shown in the work by *S. Hashiyada et al.* [223]. As can be seen from the patterns obtained at the remaining wavelengths for $\Phi_{exc} = 45°$, symmetry seems to be lost, leading to a preponderance of fields with one handedness over the other, therefore resulting in a (computed) non-zero net chirality in the discussed plane. However, in a symmetric environment the sign of the optical chirality flips for fields computed at an equidistant plane in the backwards direction, as has been already mentioned above and was impressively shown in [222]. In conclusion, the computed net optical chirality represents integrated values that depend on the choice of the computational domain, and therefore self-explanatorily hinder comparability. Amongst other reasons, *L. Poulikakos et al.* [53] therefore introduced the quantity $\mathcal{F}$, which describes the optical chirality flux to the far field (cf. section 2.4.3) and is independent of the size of the computational domain. Experimental results on the chirality flux will be discussed in the next section 4.3.5.

The optical chirality patterns discussed above were computed solely from the induced electromagnetic fields and therefore do not represent realistic, i.e. experimentally accessible, results. To comply with this, Figure 4.33 shows maps of the optical chirality computed from the superposition of incoming and induced electromagnetic fields, as the total fields near a nanoparticle consist of both.

To start with, the chirality maps obtained for linearly polarized excitation oriented in $\Phi_{exc} = 0°$ and $\Phi_{exc} = 90°$ again show highly symmetric patterns. Consistent to before, superchiral fields occur at the resonance positions of the dipolar modes. Yet different to before, the appearance of the patterns changed, as the lobes showing superchiral fields spatially increased to form only four symmetric lobes

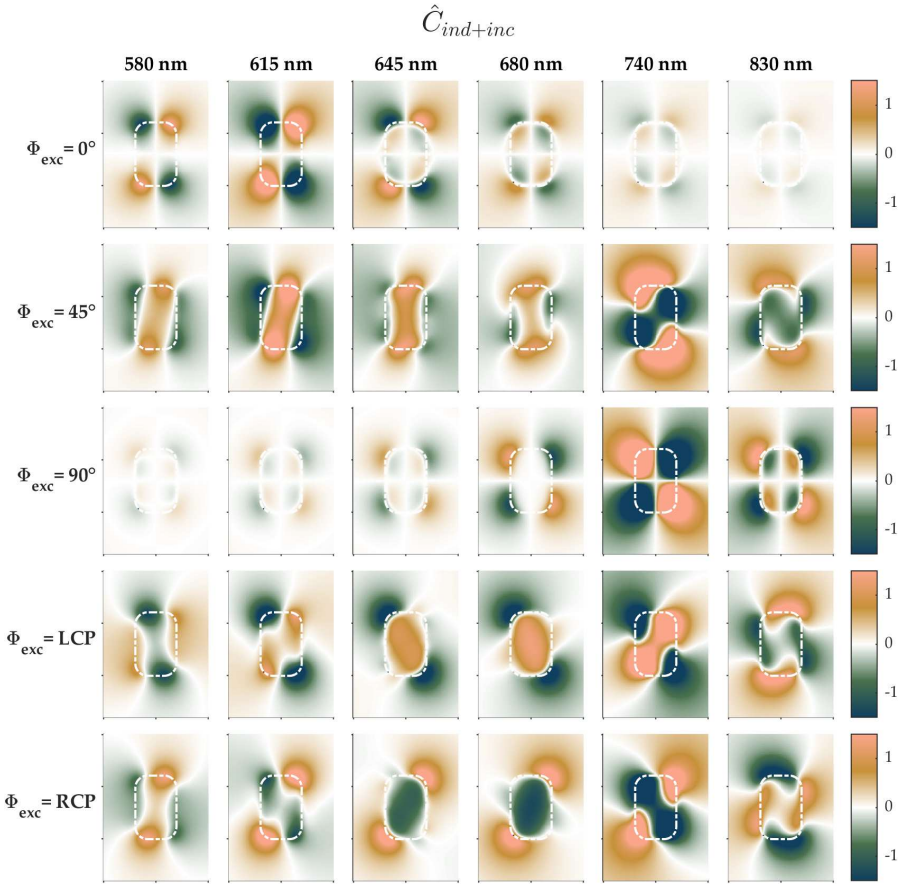

Figure 4.33: Normalized optical chirality $\hat{C}$ calculated from the total electromagnetic fields, i.e. from the superposition of induced and incoming fields, for different wavelengths (columns) and different linear or circular polarization orientations of the incoming plane-wave excitation (rows). LCP and RCP denote left- and right-handed circular polarization, respectively. Regions where $|\hat{C}| > 1$ show superchiral hot spots, i.e. fields with a chirality larger than that of circularly polarized light.

with alternating signs. For off-resonant wavelengths the encircled lobe geometry remains, and in contrast to $\hat{C}_{ind}$, the signs do not change throughout the investigated spectral range. It shall be mentioned that the four-lobe symmetry (at resonance) resembles the chirality pattern of a point-like Hertzian dipole [222], which fits to the common simplification of nanoantennas acting as point light sources in a background field. For $\Phi_{exc} = 45°$, the lobes now change their appearance and begin to rotate for all of the investigated wavelengths, which is consistent with recently obtained experimental patterns on the degree of circular polarization found by *S. Hashiyada et al.* [220]. The chirality patterns obtained for left- and right-handed circular polarizations are again opposed to each other, in sign as well as spatial orientation of the lobes, and resemble the ones obtained for $\Phi_{exc} = 45°$.

The theoretical examination of the optical chirality density for the

rectangular nanostructure shows to be in line with what is found in literature on the formation of chiral near fields in the surroundings of achiral nanostructures [50, 222, 224, 225] and demonstrates appropriateness of the applied simulation model. The computed patterns illustrate the intricate polarization behavior of the plasmonic near fields, as there are regions with high and low chirality, being located at different spatial positions for different wavelengths and being clearly dependent on the polarization of the incoming light. However, it turns out to be quite difficult to draw conclusions from the optical near-field chirality on the polarization properties of the scattered light in the far field. This is partly due to the fact that the optical chirality is proportional to both electric and magnetic fields, while the far field is governed by the properties of the electric fields [52].

To investigate the chirality of the electric field only, a dissymmetry factor [226] can be calculated according to $V = \frac{|E_{LCP}|^2 - |E_{RCP}|^2}{|E_{LCP}|^2 + |E_{RCP}|^2}$, where E_{LCP} and E_{RCP} are the circularly polarized electric field components as displayed in Figure 4.30. This quantity can be interpreted as the local circular dichroism of the near-field intensity [52, 227] and is equivalent to the third Stokes parameter (cf. sections 2.4.1 and 4.3.5) normalized to the total intensity at the respective positions, i.e. $V = S_3 / I_{CP}$, where $S_3 = I_{LCP} - I_{RCP}$ and $I_{CP} = |E_{LCP}|^2 + |E_{RCP}|^2 = I_{LCP} + I_{RCP}$.

The upper row in Figure 4.34 exemplarily shows the dissymmetry factor V, calculated from the electric fields obtained for $\Phi_{exc} = 90°$ at the resonance wavelength λ_{LR} (center column) and one each for a wavelength blue-shifted (left) and red-shifted (right) to the resonance. As can be seen, again an expanded four-leafed pattern can be observed with alternating signs between the single areas, where positive values correspond to left-handed rotations and negative values denote right-handed rotations of the electric field, respectively. The outline of the particle is again indicated with a white line. The background is found to be $V = 0$ and displays the linearly polarized incoming field. A second, much less pronounced four-leafed pattern is enclosed in the center, with alternating signs matching the outer ones. From left to right, i.e. from *blue* to *red*, the outer lobes seem to shift from the vertical ends of the nanostructure to the sides, while the inner pattern seems to be mostly stationary. For wavelengths $\lambda > \lambda_{LR}$ the areas of (circular) polarization reduce drastically in size and are located at the horizontal symmetry axis.

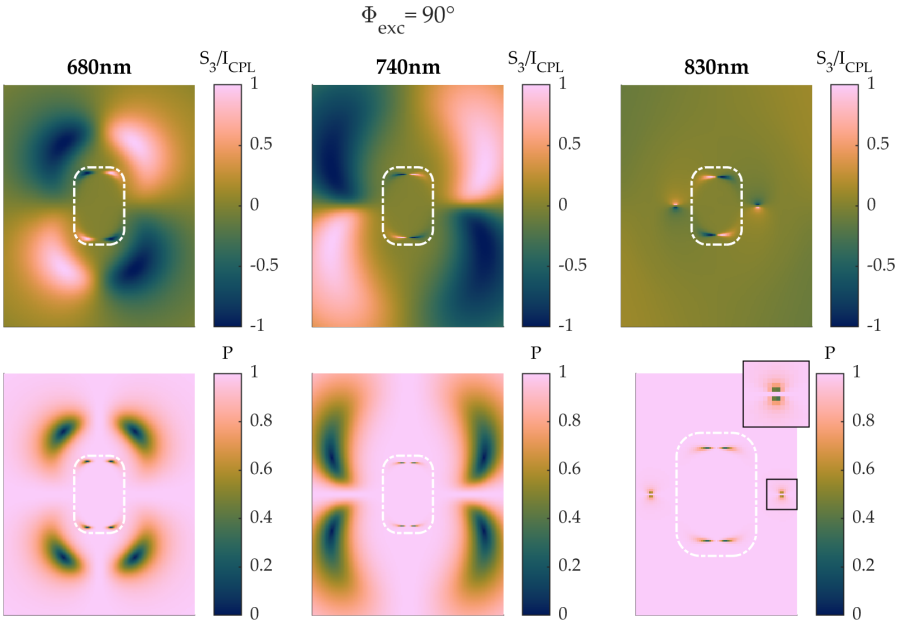

Figure 4.34: Dissymmetry factor (upper row) and degree of polarization (lower row) for the electric near fields at different wavelengths, calculated for $\Phi_{exc} = 90°$ in a plane located at $z = -10\,\text{nm}$ below the particle. The displayed section changes in the lower right image (bigger size of nanostructure) to enhance visibility. The inset shows a close-up of the pattern marked with the box.

From the dissymmetry factor the degree of polarization can be calculated according to $P = \sqrt{1 - V^2}$, where the color scale reaches from 0 to 1, i.e. from circular polarization to linear polarization, and where values lying in between denote elliptical polarizations. The patterns clearly demonstrate that even for linearly polarized excitation, which is oriented in the direction of the plasmonic longitudinal dipolar mode, the electric near field is found to be selectively circularly polarized in some regions around the nanoparticle.
It shall be mentioned that the results discussed above are in reasonable accordance to the work of *E. Chubchev et al.* [228], where they analytically investigated the wavelength-dependent near-field polarization distributions for a prolate nanospheroid. As they varied the incoming excitation polarizations, they also found the electric near field to be circularly polarized for linearly polarized excitation, while for circularly polarized excitation the near field exhibits regions in which the electric fields are linearly polarized. Additionally, by introducing the dissymmetry factor, the dependence of the polarization on the third Stokes parameter is introduced, which is an experimentally accessible quantity that describes the chirality flux to the far field, as will be discussed in the next section.

4.3.5 *Stokes Parameters and Chirality Flux to the Far Field*

The theoretical results discussed above clearly suggest that the enhanced near fields generated in the surroundings of the planar achiral nanostructure exhibit optical chirality, even under excitation with linearly polarized light. The experimental results on the polarization analysis measured in the far field also imply that the detected signals of the dark-field scattering spectra possess chiroptical properties. As introduced and discussed in section 2.4.3, *L. Poulikakos et al.* [53] introduced the aforementioned chirality flux $\mathcal{F}$ as a measurable far-field quantity to probe chiral near fields. They showed that $\mathcal{F}$ can be directly related to the energy flux $\mathcal{S}$ with opposite handedness via

$$\mathcal{F} = \frac{\omega}{c}\left(|l|^2\mathcal{S}_{LCP} - |r|^2\mathcal{S}_{RCP}\right) \ ,$$

where $|l|^2$ and $|r|^2$ are weighting factors. In general, intensity I is given by the magnitude of the time-averaged energy flux $I = \langle\mathcal{S}\rangle_T$ and by expressing the energy flux in a circular basis, the chirality flux is found to be proportional to the preponderance of the intensity of circularly polarized light with one handedness over the other $\mathcal{F} \propto I_{LCP} - I_{RCP}$ (cf. section 2.4.3). $\mathcal{F}$ is therefore proportional to the third Stokes parameter S_3 (cf. section 2.4.1), which is used to describe the degree of circular polarization in the detected signals.
The third Stokes parameter is given by $S_3 = I_{LCP} - I_{RCP} = 2E_{0x}E_{0y}\sin\Delta$ and can be calculated from the experimentally obtained analyzed angular intensity patterns by fitting equation 4.7 (cf. section 4.3.2)

$$a^2 \cdot \cos^2(\Theta - \Psi) + b^2 \cdot \sin^2(\Theta - \Psi)$$

and by thereof extracting the electric field components E_{0x} and E_{0y} and the relative phase Δ between the two components via

$$E_{0x} = \sqrt{a^2\cos^2\Psi + b^2\sin^2\Psi} \tag{4.9}$$

$$E_{0y} = \sqrt{a^2\sin^2\Psi + b^2\cos^2\Psi} \tag{4.10}$$

$$\cos\Delta = \frac{E_{0x}^2 - E_{0y}^2}{2E_{0x}E_{0y}}\tan 2\Psi \ . \tag{4.11}$$

As those values are obtained from the measured dark-field scattering spectra, S_3 (and also the other Stokes parameters $S_0 - S_2$) can be calculated for each wavelength individually, therefore providing the full set of spectrally resolved Stokes parameters from a single set of measurements. The upper row in Figure 4.35 displays the thereof obtained normalized (to S_0) Stokes parameters for the two linearly polarized excitation polarizations $\Phi_{exc} = 45°$ and $\Phi_{exc} = 90°$. As can be seen in the left graph, for $\Phi_{exc} = 45°$ there is a considerable contribution of circular polarization for the widest part of the considered spectral range. The spectral position, where S_3 reaches its maximal magnitude is marked with a vertical line (●, $\sim 640\,\text{nm}$). Values of $|\frac{S_3}{S_0}| = 1$

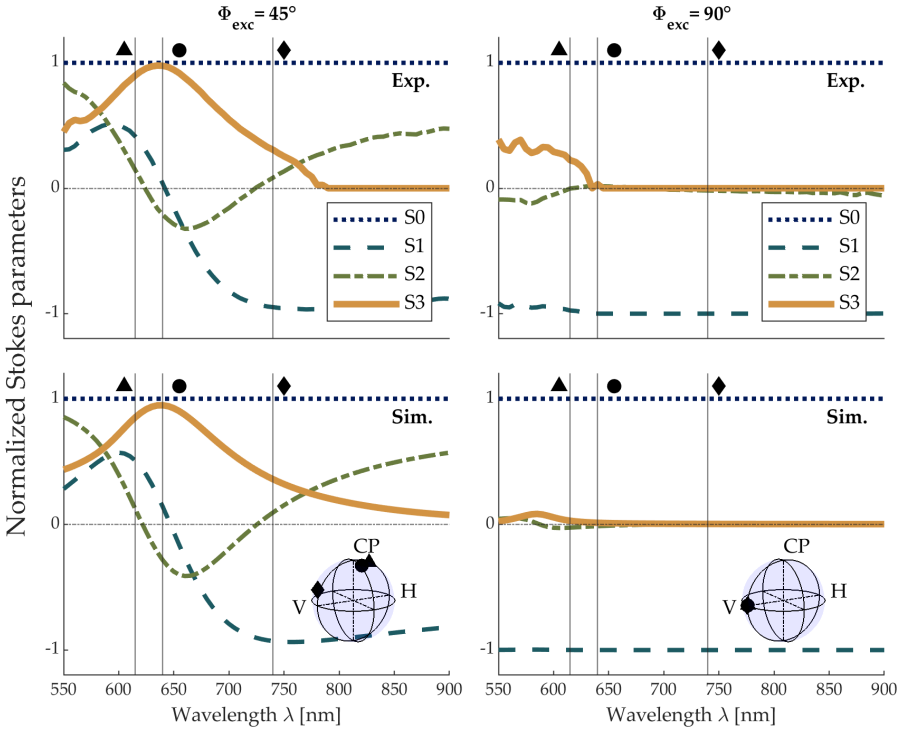

Figure 4.35: Spectrally resolved full set of Stokes parameters as obtained from the measurements (upper row) and from the computed electromagnetic far fields (lower row) for two different linear excitation polarizations: $\Phi_{exc} = 45°$ (left column) and $\Phi_{exc} = 90°$ (right column). The vertical lines mark the resonance positions λ_{TR} (▲) and λ_{LR} (◆) and the position with a maximal magnitude of circular polarization (●). The insets in the lower row depict the positions of the marked wavelengths on a *Poincaré* sphere.

(and S_1,$S_2 = 0$) correspond to circular polarization, while values in-between denote elliptical polarizations and for $\frac{S_3}{S_0} = 0$ the scattered light is purely linearly polarized. The vertical lines in all plots mark the resonance positions λ_{TR} (▲) and λ_{LR} (◆). For $\Phi_{exc} = 90°$, S_3 is zero for almost all wavelengths, which is in excellent accordance to the intensity patterns found in Figure 4.25, displaying linear polarization in the direction of the longitudinal dipolar mode. Small deviations are found at shorter wavelengths, however, which are partly due to small measurement inaccuracies. For verification, the *experimental* results were compared to simulations. The lower row in Figure 4.35 therefore shows the normalized Stokes parameters as calculated from the computed complex electromagnetic far fields. In the far-field simulation model, the excitation light comes in under oblique incidence from two directions, as it has been already described above (cf. section 4.3.3). The electric field components are of the form $E_{x,y} = E_{r_{x,y}} + E_{i_{x,y}} i$ and can be rewritten as $|E_{x,y}| \cdot \exp(i\varphi_{x,y})$, where $\varphi_{x,y}$ denote the phase angles. The electric field components are then given by $E_{0x} \hat{=} |E_x|$ and $E_{0y} \hat{=} |E_y|$ and the relative phase between the two components is therefore obtained

from $\Delta = \varphi_x - \varphi_y$. To visualize the obtained Stokes parameters more descriptively, the insets depict the three chosen wavelengths on the surface of a *Poincaré* sphere. While for $\Phi_{exc} = 45°$ the markers are located at random positions on the upper hemisphere and therefore denote elliptical polarizations, the case differs for $\Phi_{exc} = 90°$, where the light is found to be vertically polarized for all three wavelengths. The simulation also shows a small contribution of circular polarization for small wavelengths. To investigate the origin of this effect, the Stokes parameters were computed once more, each for TE and TM contributions of the exciting field separately.

As can be seen in Figure 4.36, the deviations also occur for TE polarized fields, while for TM excitation the scattered electric field is purely linearly polarized for all considered wavelengths. The effect therefore might be due to retardation effects, yet a more profound study still needs to be done for clarification.

The results discussed above clearly demonstrate that the light emitted from an achiral nanostructure can exhibit chiroptical properties in the far field, when excited with linearly polarized light. The degree of circular polarization in the detected signal, described in form of the S_3 parameter, was found to depend on the wavelength, besides the orientation of the excitation polarization. The observed polarization behavior of the scattered electric fields can be understood, when looking at the superposition of two orthogonally oriented fields and taking into account the relative phase φ between the two components. Circular polarization, exemplarily, can be described as the superposition of two orthogonally oriented, linearly polarized electric fields with the same amplitude and a relative phase of $\varphi = \pm\frac{\pi}{2}$. In analogy, an analytical model was set up to describe the interplay of the electric fields emerging from the two dipolar modes, as will be discussed in the following section 4.3.6.

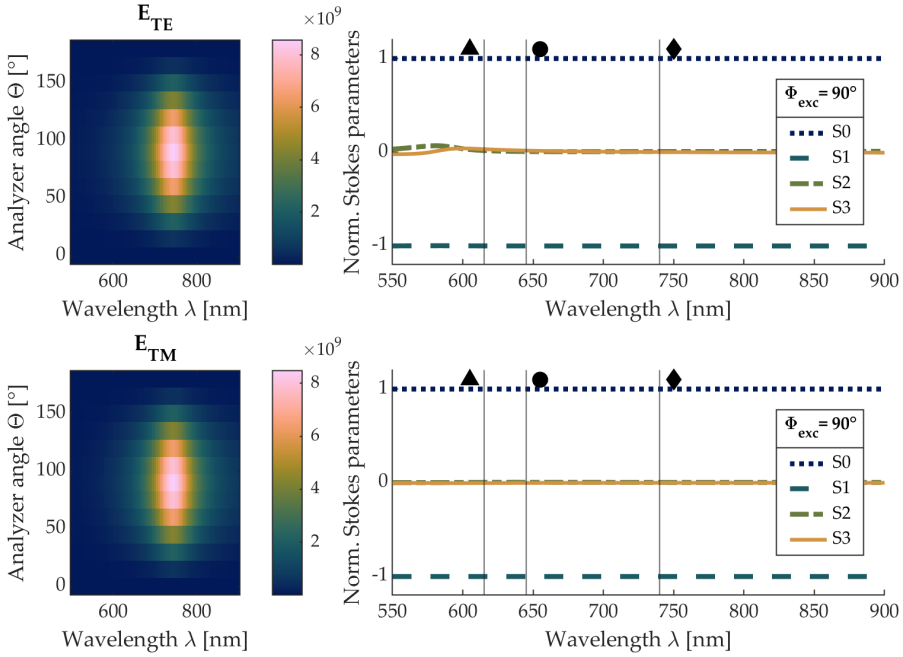

Figure 4.36: Computed full set of Stokes parameters of the scattered electric fields for linear excitation polarizations $\Phi_{exc} = 90°$, separated into sole TE and TM contributions of the incoming plane wave, respectively.

4.3.6 *Analytical Dipole Model*

The formation of chiral light emerging from a plasmonic nanostructure can be described by the superposition of the electric fields originating from the structure's eigenmodes by taking into consideration the relative phase between the contributing resonances. As will be discussed in the following, an analytical model was set up with generous help of Prof. Dieter P. Kern to describe the polarization characteristics of the emitted light for the investigated structures. While the model in general is devised for arbitrary illumination angles and arbitrary geometries, i.e. eigenmodes' orientations, a few simplifications were made in the evaluation process, which are justified for the investigated planar structures and will be mentioned when applied.
To start with, the far-field spectrum of a nanostructure with n resonances under excitation with unpolarized light can be fitted by the superposition of n Lorentzians, each with a resonance wavelength $\lambda_{i,res}$ and a full width at half maximum $\gamma_{i,fwhm} = 2\gamma_i$ via $f(\lambda) = \sum_{i=1}^{n} f_i(\lambda) = A_i \cdot \frac{\gamma_i}{\gamma_i^2 + (\lambda - \lambda_{i,res})^2}$. By assuming that the resonantly oscillating electrons act as harmonic oscillators, the emission phase follows the excitation frequency according to

$$\varphi_i(\lambda) = \arctan\left(\frac{\lambda \gamma_{i,fwhm}}{\lambda^2 - \lambda_{i,res}^2}\right) \quad , \tag{4.12}$$

i.e. is in-phase with the driving field for $\lambda \gg \lambda_{res}$ (excitation red-shifted relative to the resonance), out-of-phase for $\lambda \ll \lambda_{res}$ (excitation blue-shifted relative to the resonance) and $\varphi = \frac{\pi}{2}$ for $\lambda = \lambda_{res}$. For illustration purposes, the green solid line in Figure 4.37 therefore shows the dark-field scattering spectrum of the rectangular nanostructure, and the black dashed line its corresponding fit for unpolarized excitation. The two individual Lorentzian fits, representing the transverse (blue) and longitudinal (pink) dipolar resonances, are also plotted together with the respective phase angles (black dotted lines) according to equation 4.12. The black dash-dotted line finally shows the relative phase $\Delta = \varphi_{LR} - \varphi_{TR}$ between the two modes. In the regime of a

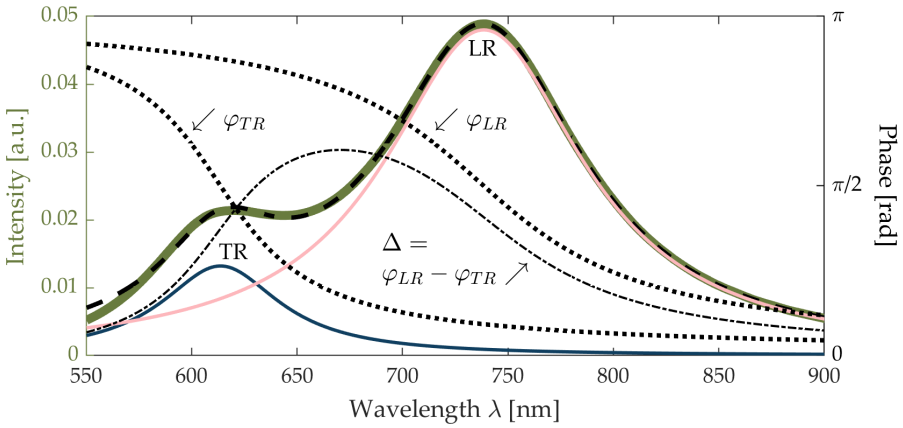

Figure 4.37: Dark-field scattering spectrum (green solid line) of the rectangular nanostructure for unpolarized excitation and corresponding fit (black dashed line) composed of two Lorentzian fits representing the transverse (blue solid line) and longitudinal (pink solid line) dipolar resonances. The phase shifts (back dotted lines) towards the excitation are shown for each mode, and also the resulting wavelength-dependent relative phase $\Delta = \varphi_{LR} - \varphi_{TR}$ (black dash-dotted line).

quasi-static approximation, the oscillations of the free electron gas density in a plasmonic nanostructure follow distinguishable modes, which can be modeled by dipoles with varying strength and different orientations $\vec{p}_i(\lambda) = p_i(\lambda) \cdot \vec{e}_i$ for $i = 1, ..., n$, where $\lambda = \lambda_i$ denotes a wavelength of maximal oscillator strength. The wavelength-dependent dipole strengths $p_i(\lambda)$ can be obtained from the functional values of the respective Lorentzian fits to the *unpolarized* spectrum.
So, for an incoming plane-wave propagating in the direction of

$$\vec{n}_{exc} = \sin\theta_{exc}\cos\phi_{exc} \cdot \vec{e}_x + \sin\theta_{exc}\sin\phi_{exc} \cdot \vec{e}_y + \cos\theta_{exc} \cdot \vec{e}_z$$

with inclination θ and azimuth ϕ, the electric excitation field can be written as $\vec{E} = \vec{E}_0 \exp(-i\omega t)$, where $\vec{E}_0 = E_0 (\cos\phi \cdot \vec{a}_1 + \sin\phi \cdot \vec{a}_2)$, so that $\vec{a}_1 \perp \vec{a}_2$ and $\vec{a}_i \perp \vec{n}_{exc}$, i.e. $\vec{a}_1$ and $\vec{a}_2$ are orthogonal unit vectors in

the plane perpendicular to the direction of incidence.
For oblique incidence, the unit vectors $\vec{a}_i$ are given by

$$\vec{n}_{exc} \neq \pm\vec{e}_z, \begin{cases} \vec{a}_1 = -\sin\phi_{exc} \cdot \vec{e}_x + \cos\phi_{exc} \cdot \vec{e}_y \\ \vec{a}_2 = \vec{n}_{exc} \times \vec{a}_1 \end{cases} ,$$

while for normal incidence they are given by

$$\vec{n}_{exc} = \pm\vec{e}_z, \begin{cases} \vec{a}_1 = \vec{e}_x \\ \vec{a}_2 = \vec{e}_y \end{cases} .$$

The electric far field of a dipole $\vec{p}$, radiated into the direction $\vec{n}$, is of the form

$$\begin{aligned} \vec{E}_D &\sim \frac{\exp(ikr - i\omega t)}{r} (\vec{n} \times \vec{p}) \times \vec{n} \\ &= \frac{\exp(ikr - i\omega t)}{r} (\vec{p} - (\vec{n} \cdot \vec{p})\, \vec{n}) \quad , \end{aligned}$$

where $k = \frac{2\pi}{\lambda}$ denotes the wave number, and r is the distance to the observer. For an incoming excitation field $\vec{E}_0$ in the direction of the ith 'eigen'-dipole, i.e. for $E_i = \vec{E}_0 \cdot \vec{e}_i$, the excited dipole therefore radiates into the far field according to

$$\begin{aligned} \vec{E}_i &= A \cdot \left(\vec{E}_0 \cdot \vec{e}_i\right) \exp(-i\omega t + i\varphi_i) (\vec{p}_i - (\vec{n} \cdot \vec{p}_i)\, \vec{n}) \\ &= A \cdot p_i(\lambda) \exp(-i\omega t + i\varphi_i) \left(\vec{E}_0 \cdot \vec{e}_i\right) (\vec{e}_i - (\vec{n} \cdot \vec{e}_i)\, \vec{n}) \quad , \end{aligned}$$

where A is some proportionality factor including the distance dependence, and φ_i is the phase difference between the exciting field and the dipole (cf. equation 4.12). The total electric field, radiated by all dipoles, is consequently given by

$$\vec{E} = \sum_{i=1}^{n} \vec{E}_i = A \cdot \exp(-i\omega t) \sum_{i=1}^{n} p_i(\lambda) \exp(i\varphi_i) \left(\vec{E}_0 \cdot \vec{e}_i\right) (\vec{e}_i - (\vec{n} \cdot \vec{e}_i)\, \vec{n}) \quad .$$

The polarization of the electric field is analyzed subsequently by inserting a linear polarization filter with transmission axis Θ into the optical path. In the model, the electric field component for a given polarization in direction $\vec{e}_p$, determined by the analyzer angle Θ, can be obtained from the projection of the electric field on the transmission axis and is given by

$$\begin{aligned} \vec{E}_p &= \vec{E} \cdot \vec{e}_p \\ &= A \cdot \exp(-i\omega t) \sum_{i=1}^{n} p_i(\lambda) \exp(i\varphi_i) \left(\vec{E}_0 \cdot \vec{e}_i\right) \left(\vec{e}_i \cdot \vec{e}_p - (\vec{n} \cdot \vec{e}_i) \left(\vec{n} \cdot \vec{e}_p\right)\right) \\ &= A \cdot \exp(-i\omega t) \sum_{i=1}^{n} p_i(\lambda) \exp(i\varphi_i) \cdot R_i \cdot S_i \, , \end{aligned}$$

where $R_i = \left(\vec{E}_0 \cdot \vec{e}_i\right)$ and $S_i = \left(\vec{e}_i \cdot \vec{e}_p - \left(\vec{n} \cdot \vec{e}_i\right)\left(\vec{n} \cdot \vec{e}_p\right)\right)$.
In the experimental set-up, the emitted light is collimated after leaving the objective and before impinging on the polarizer. For simplification purposes, it can therefore be assumed that the polarizer axis is parallel to the propagation direction of the emitted light, i.e. $\vec{e}_p \perp \vec{n}$ and therefore $\left(\vec{n} \cdot \vec{e}_p\right) = 0$. The corresponding intensity, depending on the transmission axis of the linear polarizer Θ, is consequently given by

$\cos x = \Re(\exp(ix))$

$$\begin{aligned} I_p &= |E_p|^2 = E_p \cdot E_p^* \\ &= A^2 \sum_{i=1}^{n} \sum_{k=1}^{n} p_i(\lambda) p_k(\lambda) R_i \cdot R_k \cdot S_i \cdot S_k \cdot \exp(-i(\varphi_k - \varphi_i)) \\ &= A^2 \left(\sum_{i=1}^{n} p_i^2(\lambda) R_i^2 S_i^2 + 2 \sum_{i=1}^{n} \sum_{k>i}^{n} p_i(\lambda) p_k(\lambda) R_i R_k S_i S_k \cdot \cos(\varphi_k - \varphi_i) \right) . \end{aligned} \tag{4.13}$$

For planar plasmonic nanostructures oriented in the x, y-plane, as they were investigated in this thesis, it can be assumed that the eigenmodes are also oriented in-plane, and contributions of out-of-plane plasmonic modes can hence be neglected. As the investigated structures all show two resonances in the scattering spectra, it can be assumed that the two eigenmodes point in different directions $\vec{e}_1 = \cos\beta \cdot \vec{e}_x + \sin\beta \cdot \vec{e}_y$ and $\vec{e}_2 = \cos\gamma \cdot \vec{e}_x + \sin\gamma \cdot \vec{e}_y$. For plane-wave excitation with linearly polarized light oriented in Φ, equation 4.13 becomes

$$\begin{aligned} I_p(\lambda) = E_0^2 A^2 \cdot (& p_1^2(\lambda) \cdot \cos^2(\Phi - \beta) \cdot \cos^2(\beta - \Theta) \\ &+ p_2^2(\lambda) \cdot \cos^2(\Phi - \gamma) \cdot \cos^2(\gamma - \Theta) \\ &+ 2 \cdot p_1(\lambda) \cdot p_2(\lambda) \cdot \cos(\Phi - \beta) \cdot \cos(\beta - \Theta) \\ &\cdot \cos(\Phi - \gamma) \cdot \cos(\gamma - \Theta) \cdot \cos(\varphi_2 - \varphi_1)) . \end{aligned} \tag{4.14}$$

$E_0^2 A^2$ therein is a scaling factor, Θ denotes the analyzer angle, and β and γ are the dipoles' orientations.
Equation 4.14 therefore describes the expected intensity curves for distinct analyzation angles Θ under excitation with linearly polarized light in direction Φ. The validity of the model was tested for the achiral rectangular nanostructure, but also for tilted rhomboids, i.e. for structures with increasing geometrical chirality coefficients χ_{2D} (cf. section 2.4.2).
The model was applied by simultaneously fitting equation 4.14 to the experimentally obtained spectra and by using the dipoles' orientations β and γ as fitting parameters. Figure 4.38 exemplarily shows a summary of the obtained results for one excitation polarization, namely $\Phi_{exc} = 45°$. The upper part shows SEM images together with the modeled structures as implemented in the numerical simulations with dimensions and corresponding geometrical chirality coefficients χ_{2D}. The lower part shows a comparison of the experimentally obtained analyzed dark-field scattering spectra and the intensity curves

obtained from the analytical dipole model. Both show the expected behavior of alternating intensities with varying analyzation angles, as it has already been discussed before (cf. section 4.3.2).

As has been mentioned above, the dipoles' orientations β and γ were

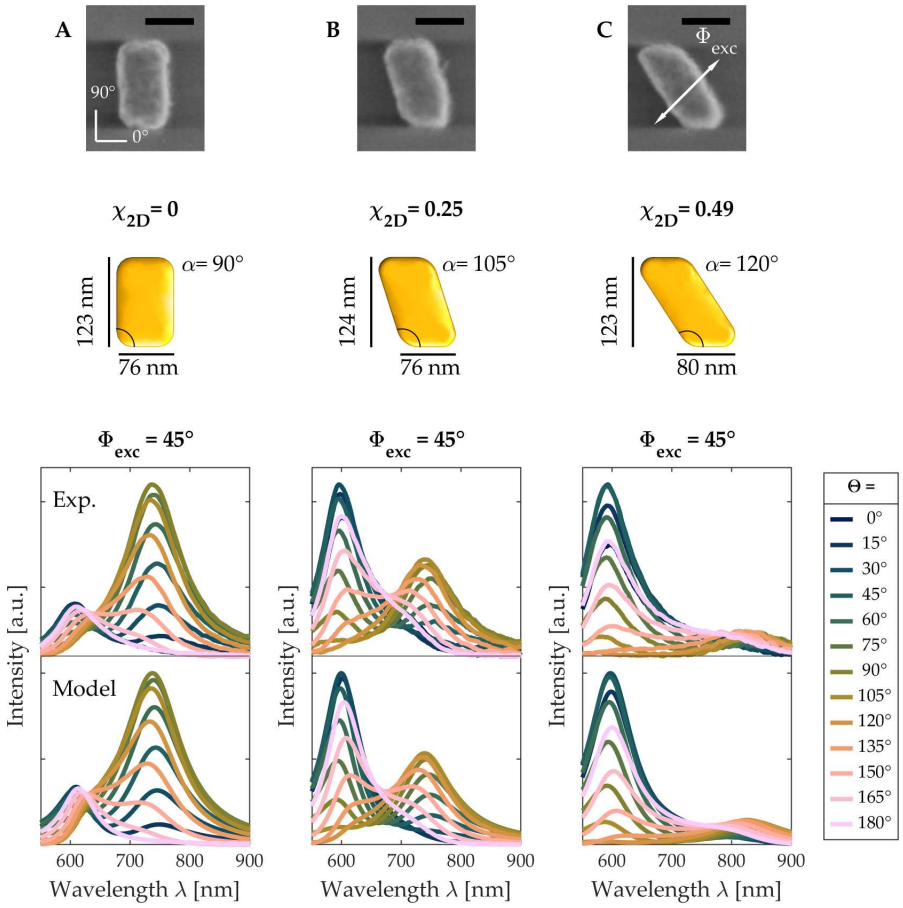

Figure 4.38: (Upper part) SEM images and model extracted from simulations of the investigated nanostructures with dimensions and corresponding chirality coefficients χ_{2D}. (Lower part) Experimentally obtained analyzed dark-field scattering spectra (top) and intensity curves from the analytical dipole model (bottom) for $\Phi_{exc} = 45°$.

used as fitting parameters in equation 4.14 for each set of measurements with given excitation and analyzation angles. The obtained results are summarized in Table 4.2 for all three particle geometries A-C. For particle A it is clearly demonstrated that, according to the model, the dipoles are oriented along the transverse and longitudinal dipolar modes of the particle. For particles B and C the dipoles' orientations vary, yet a direct relation to the variation of the structure's geometry is not apparent on first sight, as they do not follow the particles' sides. However, by keeping in mind that the model was set up with dipoles following a particle's eigenmodes, simulations were performed with the eigenmode solver implemented in *MNPBEM*.

The solver uses a quasi-static approach to find solutions to Maxwell's equations on the particle's surface. From the obtained surface charge distributions, the dipole moments were calculated similar to before (cf. section 4.3.3). The extracted orientations are summarized in the bottom part of Table 4.2 and prove to be in good accordance to the ones obtained from the model. Figure 4.39 finally visualizes the computed eigenmodes.

	A	B	C
β_{Model}	$(-2.5 \pm 1.2)°$	$(23.4 \pm 0.5)°$	$(34.8 \pm 0.5)°$
γ_{Model}	$(89.9 \pm 0.2)°$	$(114.2 \pm 0.4)°$	$(126.4 \pm 0.4)°$
$\beta_{Simulation}$	0°	24°	40°
$\gamma_{Simulation}$	90°	116°	130°

Table 4.2: Dipole orientations extracted from analytical dipole model and numerical simulations

The results discussed above demonstrate that the model allows for calculating polarization states solely from an *unpolarized* spectrum if the orientation of the respective structure and its eigenmodes are known. Or vice versa, it exemplarily allows for determining the azimuthal orientations of the longitudinal modes of randomly distributed nanorods if polarized measurements are available. This approach was taken in [229].

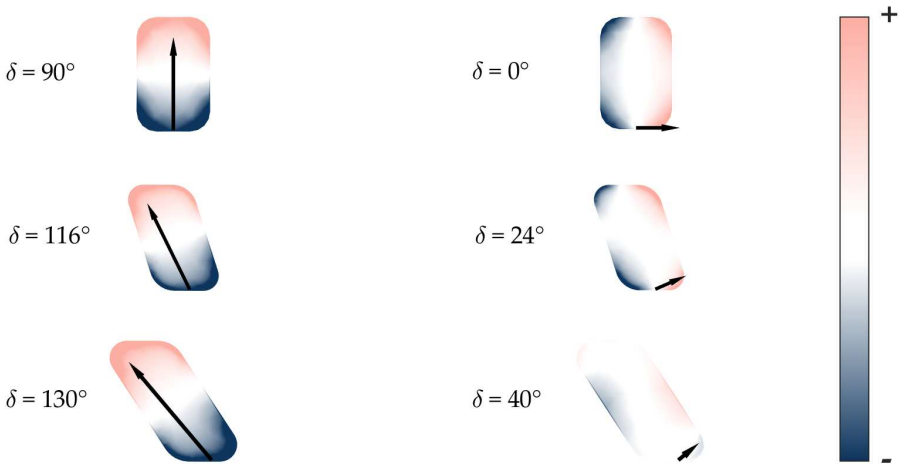

Figure 4.39: Surface charge distributions of the dipolar eigenmodes and thereof obtained orientations of their dipole moments for structures A-C.

For the sake of completeness, Figures 4.40 - 4.42 show the comparisons of measurement, numerical simulation and analytical model for each particle A-C for all three of the investigated linear excitation

polarizations. The intensities are normalized to the maximum of each set for better comparability.

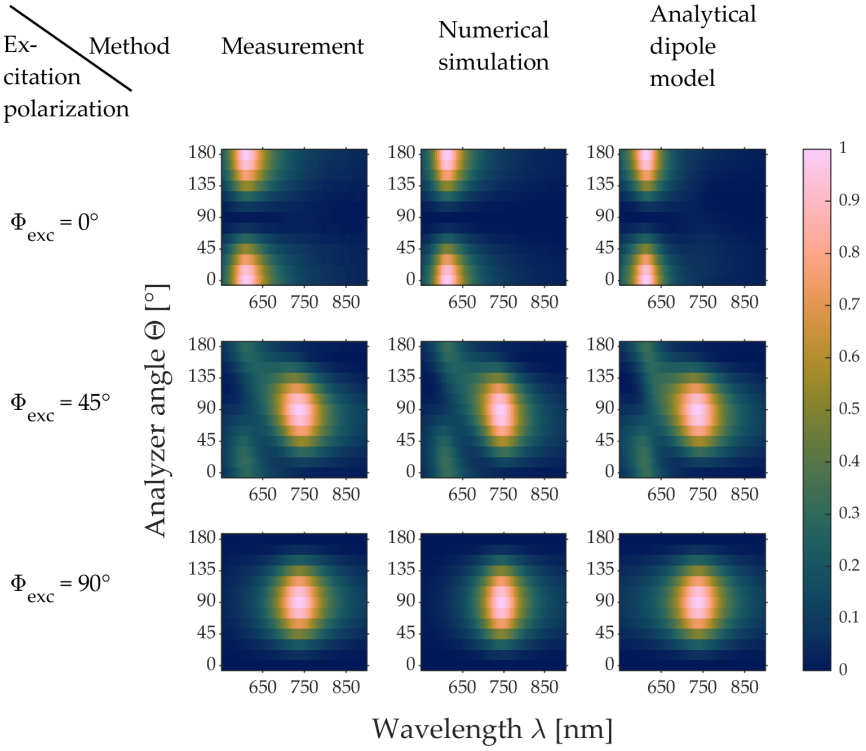

Figure 4.40: Particle A: Comparison of normalized intensities of measurement, simulation and model for three different linear excitation polarization orientations.

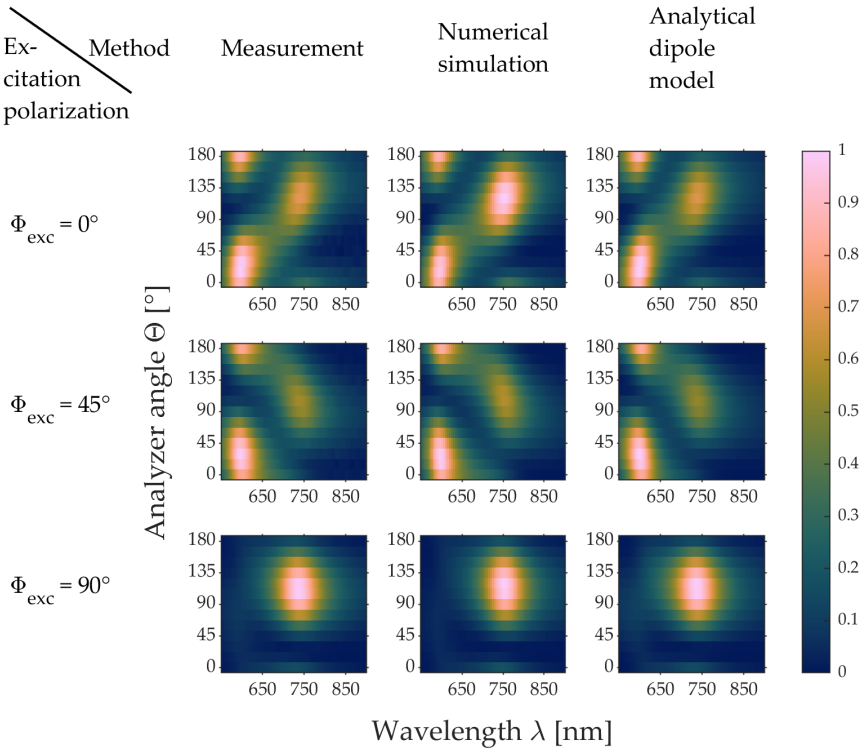

Figure 4.41: Particle B: Comparison of normalized intensities of measurement, simulation and model.

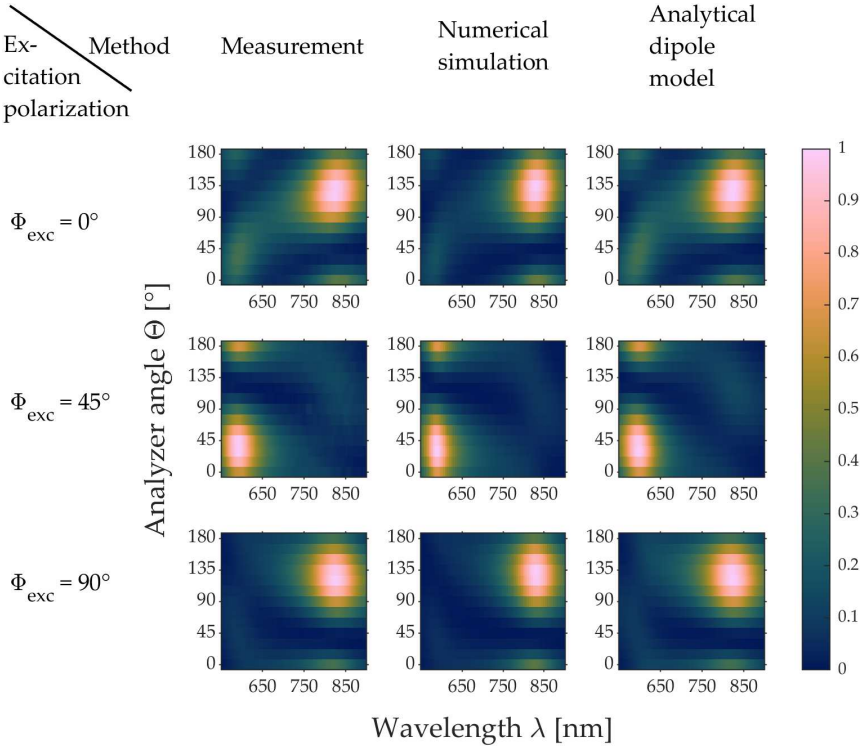

Figure 4.42: Particle C: Comparison of normalized intensities of measurement, simulation and model.

4.3.7 *Circular Dichroism-like Behavior in Achiral Rectangular Nanostructures*

Circular dichroism spectroscopy describes the differential absorption of left- and right-handed circularly polarized light and is the method of choice for determining whether or not a structure shows chiroptical effects [230]. For ensemble measurements, extinction is usually measured, which consists of the sum of absorption and scattering. For structures with relatively large dimensions ($> 100\,\text{nm}$) their scattering cross-sections can exceed their absorption cross-sections, so that circular differential scattering measurements can be favorable [231], as it also allows for investigating single particles [109].
According to earlier discussions on the preservation of incoming polarizations using a dark-field condenser, there are some boundary conditions to be taken into account when implementing circularly polarized excitation into the experimental set-up [232]. Be that as it may, for achiral nanostructures, optical chirality in the far-field response is widely neglected, as it is not visible in standard circular dichroism spectroscopy measurements.
However, with the results discussed before, a differing far-field signal can be expected for excitation with left- and right-handed circularly polarized light, if the spectra are analyzed as described before. As a proof of concept, measurements were performed on a similar achiral rectangular nanostructure, excited with linearly polarized light oriented in $\Phi_{exc} = 45^\circ$ and $\Phi_{exc} = 135^\circ$. Both polarizations can be interpreted as the superposition of left- and right-handed circularly polarized light of the same amplitude and with complex coefficients, i.e. with a phase shift of $\pm\frac{\pi}{2}$ between the two components:

$$\begin{aligned}
E_{LCP} + E_{RCP}\exp(i\frac{\pi}{2}) &= E_x + iE_y + \big(E_x - iE_y\big)\exp(i\frac{\pi}{2}) \\
&= E_x + iE_x + E_y + iE_y \\
&= (E_x + E_y) + i(E_x + E_y) \mathrel{\widehat{=}} E_{45^\circ} \\
E_{LCP} + E_{RCP}\exp(-i\frac{\pi}{2}) &= E_x + iE_y + \big(E_x - iE_y\big)\exp(-i\frac{\pi}{2}) \\
&= E_x - iE_x - E_y + iE_y \\
&= (E_x - E_y) - i(E_x - E_y) \mathrel{\widehat{=}} E_{135^\circ} \quad ,
\end{aligned}$$

where $E_{45^\circ,135^\circ}$ denote complex amplitudes, and the corresponding electric fields are given by $\mathcal{E} = \Re(E_{45^\circ,135^\circ}\exp(i\omega t))$. The top row in Figure 4.43 shows far-field scattering spectra for both linearly polarized excitation polarization orientations, as obtained from simulations (left column) and also measurements (center column). The graph on the right-hand side shows double-Lorentzian fits to the measurements. As can be seen, the scattering spectra do not show any differences, which is clearly expected for an achiral nanostructure. However, when looking at the analyzed spectral responses, as can be seen in the center

row for $\Phi_{exc} = 45°$ and in the bottom row for $\Phi_{exc} = 135°$, one can easily distinguish between the two excitation polarizations, and the importance of a phase-correct interpretation becomes clear. The column on the right-hand side shows analyzed and spectrally resolved intensity maps calculated according to equation 4.14, for fixed dipole positions of $\beta = 0°$ and $\gamma = 90°$ and with the dipoles' strength being extracted from the Lorentzian fits in the top panel.
This experiment again shows a high qualitative accordance between simulation, measurement and model and confirms once more the predictive power of the analytical model.

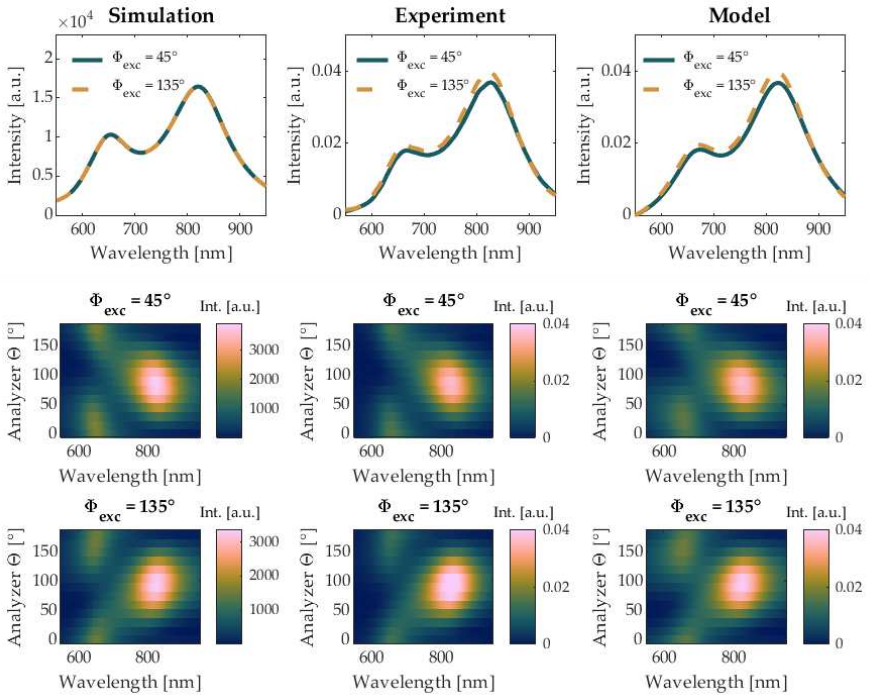

Figure 4.43: (Top) Comparison of scattering spectra obtained from simulations, measurements and Lorentzian fits to the experimental data for linearly polarized excitation polarizations $\Phi_{exc} = 45°$ and $\Phi_{exc} = 135°$. (Center and bottom) Analyzed and spectrally resolved intensity maps for both excitation orientations.

5

SUMMARY AND OUTLOOK

In this thesis, the optical characterization of different plasmonic systems was paramount, but also the production of nanostructures with common methods of nanofabrication made up a significant share. Additionally, numerical simulations were performed to forecast geometrical requirements on nanostructures, and to verify experimental findings theoretically.
Firstly, plasmonic hybrid systems consisting of gold nanocones and semiconductor quantum dots were fabricated on transparent substrates, to facilitate optical transmission measurements. The gold nanocones were designed in such a way that their dipolar out-of-plane resonance matches the quantum dots' photoluminescence emission wavelength. The nanocones were fabricated using electron beam lithography and a thermal evaporation process for metallization. The geometrical parameters were determined beforehand, and the optical properties were consequently investigated theoretically with various simulations on their scattering cross-sections, near-field distributions and photonic densities of optical states. They were also investigated experimentally by performing white-light dark-field scattering spectroscopy. A self-aligned process was co-developed and applied to attach single or few quantum dots solely to the apexes of the nanocones. The optical properties of the resulting hybrid systems were further investigated in the group of Prof. A. Meixner at the Institute of Physical and Theoretical Chemistry at the University of Tübingen. This was done by confocal photoluminescence spectroscopy, using a laser as excitation source. The resulting luminescence spectra were compared to different reference systems, and an intensity enhancement of roughly an order of magnitude could be obtained for a quantum dot bound to the tip of a gold nanocone compared to the luminescence intensity of a single quantum dot on glass. Spectrally integrated intensity trajectories were taken for both, the hybrid and the reference system, respectively, to investigate the changes in the fluorescence intermittency. It could be shown that the blinking statistics change significantly for a quantum dot in the vicinity of a metallic nanostructure, and the times in which the system is in an on-state increase compared to the reference on glass. As such changes in the emission behavior go hand in hand with modified lifetimes of the excited states, additional lifetime measurements were performed. For a quantum dot coupled to the tip of a gold nanocone the intensity-weighted average fluorescence lifetime was found to be $\langle \tau \rangle \approx 150\,\mathrm{ps}$, while for the reference system, i.e. a quantum dot on glass, the average lifetime was found to be

$\langle\tau\rangle \approx 11\,\text{ns}$, which demonstrates a 70-fold acceleration of the emission process.
The investigated hybrid system proved to be an interesting candidate to study the influence of resonantly tuned metallic nanoantennas on the emission properties of closely positioned quantum emitters and provided the promising opportunity to be further applicable in proceeding studies.

To efficiently exploit the effects of luminescence enhancement and the preferred coupling to the out-of-plane plasmonic mode, as they were found in the hybrid system consisting of nanocone and quantum emitter, a similar system was incorporated in a hybrid metal-dielectric bullseye device, which was designed and implemented by the group of Prof. R. Rapaport at the Racah Institute of Physics at the Hebrew University of Jerusalem, to overcome the rate-directionality trade-off in the photon emission of a single quantum emitter.
The device consisted of a quantum dot coupled to the tip of a gold nanocone, which was located in the center of a concentric Bragg grating, i.e. the bullseye antenna, and the whole device was embedded in a dielectric waveguide layer. The metallic part of the device was fabricated using a monolithic template stripping method, where the antenna components were preliminary etched into a silicon template, using focused gallium ion beam milling, before being covered in gold by thermal evaporation. By attaching a glass substrate with the help of an additional adhesion layer, the whole layer system could be stripped off, resulting in a very smooth bullseye antenna and nanocone.
For the optical characterization of the device, different spectroscopy and imaging techniques were applied. In order to determine the number of quantum dots bound to the tips of the nanocones, time-filtered second-order correlation measurements were performed and single-photon emission could be detected, therefore confirming the successful attachment of single to few quantum dots. As expected, enhanced luminescence could be observed compared to a reference quantum dot on glass. By performing back focal plane imaging, also the modified emission directionality could be investigated accordingly. The collection efficiency improvement was highest at low numerical apertures, reaching values 88-fold greater than the reference (at NA $= 0.22$). Again, lifetime measurements were performed to identify the contributions of exciton and biexciton excitations and to calculate the hybrid system's quantum yield. An overall enhancement factor $F \sim 20$ could be found, therefore demonstrating the ability of the device to increase the decay rates compared to the reference. From the obtained results, it could be shown theoretically that with such a device, photon emission rates reaching the GHz regime should be achievable.
As is often the case in hindsight of proof-of-concept measurements, some adjustment screws could be identified to improve the overall

performance of the device. Most importantly, due to fabrication restrictions of the applied methods, the nanocones had rather big tip radii, which was found to be disadvantageous for the single quantum dot yield in the attachment process. It could also be shown through simulations, that a lateral displacement of the quantum emitter leads to a decrease of the radiative decay rate of the out-of-plane dipole, which results in a reduction of the Purcell factor and should therefore be prevented. The Purcell factor could also be enhanced theoretically by adjusting the device's geometry, so that the nanocone's dipolar out-of-plane resonance could be exploited, as this mode shows the highest rate enhancements. Nevertheless, the presented device may be regarded as a success, as the optical performance and the feasible on-chip design make it an important component towards deterministic GHz-rate single photon sources operating at room-temperature.

Finally, in this thesis, polarimetric dark-field scattering spectroscopy measurements were performed on different single gold nanostructures, to study the polarization of the detected scattered signals dependent on the incoming excitation polarization.
Therefore, individual planar achiral rectangular nanostructures and chiral rhomboidal nanostructures with different degrees of geometrical chirality were fabricated in the group of Prof. D. Gérard at the University of Technology of Troyes in France using electron beam lithography and a thermal evaporation process. Regarding the set-up for the optical characterization, a commercial transmission dark-field scattering microscope was modified with respective polarization filters to enable polarized excitation and subsequent analyzation of the scattered signals. Additionally, a cross-like aperture was designed and implemented to maintain linear polarization in the excitation path, even though focusing through a condenser, and the functionality was verified using back focal plane imaging. The obtained spectra were evaluated for their wavelength-dependent degree of circular polarization and the results were compared to numerical simulations, pertaining the near field, but also the far field, respectively. For the rectangular nanostructure, it could be shown exemplarily amongst other things, that for linear excitation polarizations oriented along directions not coinciding with the eigenmodes' dipole moments, chiroptical far-field responses could be detected. From the experimental data, polarization ellipses could be calculated for each wavelength. The findings were compared to numerical simulations of the surface charge distributions, showing the temporal course of the excited dipole moments, and reasonable accordance could be found, underlining the statement that the polarization state of the emitted light is already determined in the near field. For the sake of completeness, also simulations on the optical chirality distributions in the surroundings of the nanostructure were performed and the results compared to liter-

ature. Furthermore, an alternative method to determine the full set of Stokes parameters from the detected signals could be presented, and the findings were also successfully compared to simulations of the scattered far fields. The importance of this finding comes to light, when considering the assumption that the chirality flux from the near field to the far field is proportional to the third Stokes parameter. As the existence of chiroptical far-field responses is widely neglected for achiral nanostructures, additional proof-of-concept measurement were performed, showing differing analyzed far-field responses for the rectangular nanostructure for two linear excitation polarizations oriented in 45° and 135° relative to the structure's main axes, as those two excitation polarizations can be interpreted as a superposition of left- and right-handed circularly polarized light with complex coefficients. Last but not least, an analytical dipole model could be set up with the help of Prof. Dieter P. Kern to describe the emergence of circular polarization in arbitrarily shaped, planar nanostructures with two (or even more) spectrally overlapping eigenmodes for a given linear excitation polarization. For a successful application of the model, an *unpolarized* scattering spectrum of the investigated nanostructure is needed, and at least three analyzed spectra for a given excitation polarization. By fitting the unpolarized spectrum with n Lorentzians, representing the n eigenmodes, the phase shift towards the excitation can be calculated for each resonance. With the obtained phase shifts, the modeled equation to describe the analyzed intensities can be fitted to the experimentally obtained spectra, where the dipoles' orientations are the fitting parameters. A good accordance could be found for the measured and modeled spectra, for the achiral but also the chiral structures, respectively. It could also be shown, through measurements and also simulations, that for the rhomboidal nanostructures, the eigenmodes' dipole moments are not necessarily aligned to the geometrical axes.

In conclusion, it can be said that the work presented here demonstrates both, experimentally and through simulations, that achiral nanostructures can exhibit far-field chiroptical effects under linearly polarized excitation, which is an effect widely neglected in literature. It therefore contributes to a better understanding of the formation of polarization in the light emerging from plasmonic nanostructures and might be a useful tool in designing structures with desired polarization characteristics for various applications, e.g. in sensing applications, metasurfaces or polarization optics.

However, the work also highlighted the importance of further studies to resolve pending issues. This in turn can also be considered a chance, as it simultaneously opens up the opportunity to gain deeper insights into the interplay of different modes within such single structures. For example, it would be a straight-forward approach to perform analyzed extinction measurements on similar nanostructures with

circularly polarized excitation light, as this kind of measurements would meet the requirements of circular dichroism spectroscopy, and the expected differences in the CD spectra should become observable. It could also be of interest to perform photoluminescence measurements on chiral nanostructures with different handedness to study the phenomenon of intrinsic chirality. For excitation wavelengths below the interband transition threshold, the incoming photons are absorbed and excite interband and intraband transitions, which in turn can decay radiatively, preferably into plasmon modes due to the enhanced photonic density of states. Due to the incoherence of the process, it could be interesting to investigate the detected signals for their degree of circular polarization. Ultimately, it could be demonstrated from simulations and preliminary measurements, that for planar triangular nanostructures with increasing values of tip deflection and therefore increasing degrees of geometrical chirality, the dipolar resonances start to show an avoided-crossing behavior. This gives hint to some kind of mode-hybridization and clearly offers an interesting starting point for further studies.

A

APPENDIX

The following appendix gives a review on the recipes of the nanofabrication processes used in this thesis. It shall be emphasized that the given parameters might need to be adjusted for individual purposes, as they are highly dependent on environmental conditions, such as room-temperature or humidity in the laboratory.

A.1 SUBSTRATE PREPARATION

1. Put 5-8 pellets of potassium hydroxide in beaker (20 ml) and fill halfway up with deionized water
2. Put glass cover slips in and place beaker in ultrasonic bath for 3 min
3. Add one third of hydrogen peroxide and use ultrasonic bath for further 5 min
4. Transfer sample to new beaker filled with deionized water and use ultrasonic bath for 1 min
5. Take sample out and rinse with deionized water
6. Blow-dry sample with nitrogen
7. Optional: Add conductive layer of indium tin oxide via sputter deposition

A.2 PROCESS PARAMETERS FOR NANOCONE FABRICATION

1. Optional: Deposit gold layer with desired thickness, i.e. envisaged height of nanocones
2. Spin-coat PMMA layer (2.5%, dissolved in MIBK) with 2600 rpm for 6 s and 5000 rpm for 60 s (resulting resist thickness $\approx$ 120 nm)
3. Bake at 150°C for $\approx$ 15 min
4. Optional: Repeat step 2 to 3 to receive a higher resist layer, adjust rotation parameters if needed (higher rotation parameters decrease resulting height)
5. Bake sample at 150°C for 60 min

6. Perform EBL, acceleration voltage: 30 kV, point dose ≈ 50-120 fC/dot, area dose ≈ 300 μC/cm^2, working distance: 6 mm
7. Develop sample in mixture of IPA:MIBK with a ratio of 3:1 for ≈ 60 s (Important: The time needed for development is highly dependent on several parameters such as exposure dose or the temperature of the developer and needs to be checked before)
8. Stop development step by placing sample in beaker with IPA for 30 s
9. Blow-dry with nitrogen

The following steps depend on the respective fabrication process used for nanocone fabrication. For nanocones by thermal evaporation follow steps 10 to 13.

10. Deposit gold with desired thickness via thermal evaporation, deposition rate ≈ 2-3 Å/s
11. Place sample in acetone for at least 60 min for lift-off process
12. Rinse sample with IPA
13. Blow dry with nitrogen

For nanocones by argon ion milling follow steps 14 to 18.

14. Deposit aluminum oxide with a thickness of one fourth of the nominal gold thickness
15. Place sample in acetone for at least 60 min for lift-off process
16. Rinse sample with IPA
17. Blow dry with nitrogen
18. Use argon ion milling machine to etch nanocones. The time needed to etch away the whole metal layer strongly varies and the progress of the process needs to be checked individually after short etching time intervals (∼ several seconds) via SEM imaging

A.3 PROCESS PARAMETERS FOR ATTACHMENT OF QUANTUM DOTS

1. Spin-coat PMMA with a thickness of ≈ *nanocone height + 20 nm*. Check actual height with profilometer
2. Apply oxygen plasma (using reactive ion etching) to uncover tips. Process parameters: 20 W, 0.1 Torr, 100% O_2, etch rate: 1.25 nm/s
3. Check progress via SEM imaging, repeat steps 2 to 3 if needed

4. Place sample in beaker filled with 20 ml deionized water and 0.02 g 3-MPA for 30 min
5. Rinse with deionized water and immediately place in quantum dot suspension diluted in hexane (10 µg/ml) for 24 h
6. Rinse with acetone for several minutes to remove embedding layer and excess quantum dots
7. Rinse with IPA
8. Blow-dry with nitrogen

BIBLIOGRAPHY

[1] S. Eustis and M. A. El-Sayed. "Why gold nanoparticles are more precious than pretty gold: Noble metal surface plasmon resonance and its enhancement of the radiative and nonradiative properties of nanocrystals of different shapes." In: *Chemical Society Reviews* 35.3 (2006), pp. 209–217. DOI: 10.1039/b514191e.

[2] J. L. Lee. "Better living through plasmonics." In: *Science News* 176.10 (2009).

[3] A. Naldoni, V. M. Shalaev, and M. L. Brongersma. "Applying plasmonics to a sustainable future." In: *Science* 356.6341 (June 2017), pp. 908–909. ISSN: 1095-9203. DOI: 10.1126/science.aan5802.

[4] K. Liu et al. "Review and perspective on ultrafast wavelength-size electro-optic modulators." In: *Laser & Photonics Reviews* 9.2 (Feb. 2015), pp. 172–194. ISSN: 1863-8880. DOI: 10.1002/lpor.201400219.

[5] P. Mandal and S. Sharma. "Progress in plasmonic solar cell efficiency improvement: A status review." In: *Renewable and Sustainable Energy Reviews* 65 (Nov. 2016), pp. 537–552. ISSN: 1364-0321. DOI: 10.1016/j.rser.2016.07.031.

[6] P. Mandal. "Application of Plasmonics in Solar Cell Efficiency Improvement: a Brief Review on Recent Progress." In: *Plasmonics* 17.3 (Mar. 2022), pp. 1247–1267. ISSN: 1557-1963. DOI: 10.1007/s11468-022-01616-9.

[7] Y. H. Jang et al. "Plasmonic Solar Cells: From Rational Design to Mechanism Overview." In: *Chemical Reviews* 116.24 (Dec. 2016), pp. 14982–15034. ISSN: 1520-6890. DOI: 10.1021/acs.chemrev.6b00302.

[8] S. Pillai and M. A. Green. "Plasmonics for photovoltaic applications." In: *Solar Energy Materials and Solar Cells* 94.9 (2010), pp. 1481–1486. DOI: 10.1016/j.solmat.2010.02.046.

[9] L. Mascaretti et al. "Plasmon-Enhanced Photoelectrochemical Water Splitting for Efficient Renewable Energy Storage." In: *Advanced Materials* 31.31 (Feb. 2019). ISSN: 1521-4095. DOI: 10.1002/adma.201805513.

[10] M. Valenti et al. "Plasmonic nanoparticle-semiconductor composites for efficient solar water splitting." In: *Journal of Materials Chemistry A* 4.46 (2016), pp. 17891–17912. ISSN: 2050-7496. DOI: 10.1039/c6ta06405a.

[11] J. Lee et al. "Plasmonic Photoanodes for Solar Water Splitting with Visible Light." In: *Nano Letters* 12.9 (2012), pp. 5014–5019. DOI: 10.1021/nl302796f.

[12] E. Liu et al. "Photocatalytic Reduction of CO2 into Methanol over Ag/TiO2 Nanocomposites Enhanced by Surface Plasmon Resonance." In: *Plasmonics* 9.1 (July 2013), pp. 61–70. ISSN: 1557-1963. DOI: 10.1007/s11468-013-9598-7.

[13] Z. Wang et al. "Photo-assisted methanol synthesis via CO2 reduction under ambient pressure over plasmonic Cu/ZnO catalysts." In: *Applied Catalysis B: Environmental* 250 (Aug. 2019), pp. 10–16. ISSN: 0926-3373. DOI: 10.1016/j.apcatb.2019.03.003.

[14] E. B. Creel et al. "Directing Selectivity of Electrochemical Carbon Dioxide Reduction Using Plasmonics." In: *ACS Energy Letters* 4.5 (Apr. 2019), pp. 1098–1105. ISSN: 2380-8195. DOI: 10.1021/acsenergylett.9b00515.

[15] R. Brisbin et al. "Plasmonics-Enhanced UV Photocatalytic Water Purification." In: *The Journal of Physical Chemistry C* 125.18 (May 2021), pp. 9730–9735. ISSN: 1932-7455. DOI: 10.1021/acs.jpcc.1c00613.

[16] C. Chen et al. "Dual functional asymmetric plasmonic structures for solar water purification and pollution detection." In: *Nano Energy* 51 (Sept. 2018), pp. 451–456. ISSN: 2211-2855. DOI: 10.1016/j.nanoen.2018.06.077.

[17] E. C. Dreaden et al. "The golden age: gold nanoparticles for biomedicine." In: *Chemical Society Reviews* 41.7 (2012), pp. 2740–2779. ISSN: 1460-4744. DOI: 10.1039/c1cs15237h.

[18] M. Kim, J.-H. Lee, and J.-M. Nam. "Plasmonic Photothermal Nanoparticles for Biomedical Applications." In: *Advanced Science* 6.17 (July 2019). ISSN: 2198-3844. DOI: 10.1002/advs.201900471.

[19] X. Yang et al. "Gold Nanomaterials at Work in Biomedicine." In: *Chemical Reviews* 115.19 (Aug. 2015), pp. 10410–10488. ISSN: 1520-6890. DOI: 10.1021/acs.chemrev.5b00193.

[20] N. G. Khlebtsov and L. A. Dykman. "Optical properties and biomedical applications of plasmonic nanoparticles." In: *Journal of Quantitative Spectroscopy and Radiative Transfer* 111.1 (Jan. 2010), pp. 1–35. ISSN: 0022-4073. DOI: 10.1016/j.jqsrt.2009.07.012.

[21] N. L. Rosi and Ch. A. Mirkin. "Nanostructures in Biodiagnostics." In: *Chemical Reviews* 105.4 (Mar. 2005), pp. 1547–1562. ISSN: 1520-6890. DOI: 10.1021/cr030067f.

[22] W. Zhou et al. "Gold Nanoparticles for In Vitro Diagnostics." In: *Chemical Reviews* 115.19 (June 2015), pp. 10575–10636. ISSN: 1520-6890. DOI: 10.1021/acs.chemrev.5b00100.

[23] X. Huang et al. "Cancer Cell Imaging and Photothermal Therapy in the Near-Infrared Region by Using Gold Nanorods." In: *Journal of the American Chemical Society* 128.6 (Jan. 2006), pp. 2115–2120. ISSN: 1520-5126. DOI: 10.1021/ja057254a.

[24] D. Pissuwan, S. M. Valenzuela, and M. B. Cortie. "Therapeutic possibilities of plasmonically heated gold nanoparticles." In: *Trends in Biotechnology* 24.2 (Feb. 2006), pp. 62–67. ISSN: 0167-7799. DOI: 10.1016/j.tibtech.2005.12.004.

[25] P. R. West et al. "Searching for better plasmonic materials." In: *Laser & Photonics Reviews* 4.6 (2010), pp. 795–808.

[26] W. O. F. Carvalho and J. R. Mejía-Salazar. "Plasmonics for Telecommunications Applications." In: *Sensors* 20.9 (Apr. 2020), p. 2488. ISSN: 1424-8220. DOI: 10.3390/s20092488.

[27] Y. Salamin et al. "Microwave plasmonic mixer in a transparent fibre–wireless link." In: *Nature Photonics* 12.12 (Oct. 2018), pp. 749–753. ISSN: 1749-4893. DOI: 10.1038/s41566-018-0281-6.

[28] X. G. Zhang et al. "A metasurface-based light-to-microwave transmitter for hybrid wireless communications." In: *Light: Science & Applications* 11.1 (May 2022). ISSN: 2047-7538. DOI: 10.1038/s41377-022-00817-5.

[29] V. J. Sorger et al. "Toward integrated plasmonic circuits." In: *MRS Bulletin* 37.8 (Aug. 2012), pp. 728–738. ISSN: 1938-1425. DOI: 10.1557/mrs.2012.170.

[30] S. I. Bozhevolnyi and N. A. Mortensen. "Plasmonics for emerging quantum technologies." In: *Nanophotonics* 6.5 (Jan. 2017), pp. 1185–1188. ISSN: 2192-8614. DOI: 10.1515/nanoph-2016-0179.

[31] A. S. Solntsev, G. S. Agarwal, and Y. S. Kivshar. "Metasurfaces for quantum photonics." In: *Nature Photonics* 15.5 (Apr. 2021), pp. 327–336. ISSN: 1749-4893. DOI: 10.1038/s41566-021-00793-z.

[32] P. Ma et al. "Ultrafast cryptography with indefinitely switchable optical nanoantennas." In: *Light: Science & Applications* 7.1 (Oct. 2018). ISSN: 2047-7538. DOI: 10.1038/s41377-018-0079-9.

[33] E. Meyer-Scott, C. Silberhorn, and A. Migdall. "Single-photon sources: Approaching the ideal through multiplexing." In: *Review of Scientific Instruments* 91.4 (Apr. 2020). ISSN: 1089-7623. DOI: 10.1063/5.0003320.

[34] S. Fasel et al. "High-quality asynchronous heralded single-photon source at telecom wavelength." In: *New Journal of Physics* 6 (Nov. 2004), pp. 163–163. ISSN: 1367-2630. DOI: 10.1088/1367-2630/6/1/163.

[35] Q. Li, M. Davanço, and K. Srinivasan. "Efficient and low-noise single-photon-level frequency conversion interfaces using silicon nanophotonics." In: *Nature Photonics* 10.6 (Apr. 2016), pp. 406–414. ISSN: 1749-4893. DOI: 10.1038/nphoton.2016.64.

[36] P. Senellart, G. Solomon, and A. White. "High-performance semiconductor quantum-dot single-photon sources." In: *Nature Nanotechnology* 12.11 (2017), pp. 1026–1039. DOI: 10.1038/nnano.2017.218.

[37] N. Somaschi et al. "Near-optimal single-photon sources in the solid state." In: *Nature Photonics* 10.5 (Mar. 2016), pp. 340–345. ISSN: 1749-4893. DOI: 10.1038/nphoton.2016.23.

[38] A. M. Glass et al. "Interaction of metal particles with adsorbed dye molecules: absorption and luminescence." In: *Optics Letters* 5.9 (Sept. 1980), p. 368. ISSN: 1539-4794. DOI: 10.1364/ol.5.000368.

[39] D.A. Weitz et al. "Flourescent lifetimes and yields of molecules adsorbed on silver-island films." In: *Journal of Luminescence* 24–25 (Nov. 1981), pp. 83–86. ISSN: 0022-2313. DOI: 10.1016/0022-2313(81)90226-x.

[40] T. Ming et al. "Plasmon-Controlled Fluorescence: Beyond the Intensity Enhancement." In: *The Journal of Physical Chemistry Letters* 3.2 (Jan. 2012), pp. 191–202. ISSN: 1948-7185. DOI: 10.1021/jz201392k.

[41] H. Abudayyeh et al. "Overcoming the Rate-Directionality Tradeoff: A Room-Temperature Ultrabright Quantum Light Source." In: *ACS Nano* 15.11 (2021), pp. 17384–17391. DOI: 10.1021/acsnano.1c08591.

[42] J. Liu et al. "Quantum photonics based on metasurfaces." In: *Opto-Electronic Advances* 4.9 (2021), pp. 200092–200092. ISSN: 2096-4579. DOI: 10.29026/oea.2021.200092.

[43] P. Zheng et al. "Metasurface-based key for computational imaging encryption." In: *Science Advances* 7.21 (May 2021). ISSN: 2375-2548. DOI: 10.1126/sciadv.abg0363.

[44] Y. Hu et al. "All-dielectric metasurfaces for polarization manipulation: principles and emerging applications." In: *Nanophotonics* 9.12 (June 2020), pp. 3755–3780. ISSN: 2192-8606. DOI: 10.1515/nanoph-2020-0220.

[45] J.P. B. Mueller et al. "Metasurface Polarization Optics: Independent Phase Control of Arbitrary Orthogonal States of Polarization." In: *Physical Review Letters* 118.11 (Mar. 2017), p. 113901. ISSN: 1079-7114. DOI: 10.1103/physrevlett.118.113901.

[46] P. Lodahl et al. "Chiral quantum optics." In: *Nature* 541.7638 (Jan. 2017), pp. 473–480. ISSN: 1476-4687. DOI: 10.1038/nature21037.

[47] M. Hentschel et al. "Chiral Plasmonics." In: *Science Advances* 3.5 (2017), e1602735. DOI: 10.1126/sciadv.1602735.

[48] Y. Luo et al. "Plasmonic Chiral Nanostructures: Chiroptical Effects and Applications." In: *Advanced Optical Materials* 5.16 (June 2017). ISSN: 2195-1071. DOI: 10.1002/adom.201700040.

[49] W. Ma et al. "Chirality-Based Biosensors." In: *Advanced Functional Materials* 29.1 (Nov. 2018). ISSN: 1616-3028. DOI: 10.1002/adfm.201805512.

[50] T. J. Davis and E. Hendry. "Superchiral electromagnetic fields created by surface plasmons in nonchiral metallic nanostructures." In: *Physical Review B* 87.8 (Feb. 2013), p. 085405. ISSN: 1550-235X. DOI: 10.1103/physrevb.87.085405.

[51] S. Hashiyada, T. Narushima, and H. Okamoto. "Imaging Chirality of Optical Fields near Achiral Metal Nanostructures Excited with Linearly Polarized Light." In: *ACS Photonics* 5.4 (2018), pp. 1486–1492. DOI: 10.1021/acsphotonics.7b01511.

[52] A. Horrer et al. "Local Optical Chirality Induced by Near-Field Mode Interference in Achiral Plasmonic Metamolecules." In: *Nano Letters* 20.1 (2019), pp. 509–516. DOI: 10.1021/acs.nanolett.9b04247.

[53] L. V. Poulikakos et al. "Optical Chirality Flux as a Useful Far-Field Probe of Chiral Near Fields." In: *ACS Photonics* 3.9 (2016), pp. 1619–1625. DOI: 10.1021/acsphotonics.6b00201.

[54] J. D. Jackson. *Klassische Elektrodynamik*. Walter de Gruyter, 2006.

[55] S. A. Maier. *Plasmonics: fundamentals and applications*. Springer Science & Business Media, 2007.

[56] E. Hecht. *Optik*. De Gruyter, 2018. DOI: 10.1515/9783110526653.

[57] L. Novotny and B. Hecht. *Principles of nano-optics*. Cambridge University Press, 2012.

[58] U. Hohenester. *Nano and Quantum Optics*. Springer International Publishing, 2020. DOI: 10.1007/978-3-030-30504-8.

[59] X. Zhang et al. "Transient localized surface plasmon induced by femtosecond interband excitation in gold nanoparticles." In: *Scientific Reports* 8.1 (July 2018). ISSN: 2045-2322. DOI: 10.1038/s41598-018-28909-6.

[60] A. Vial et al. "Improved analytical fit of gold dispersion: Application to the modeling of extinction spectra with a finite-difference time-domain method." In: *Physical Review B* 71.8 (Feb. 2005), p. 085416. ISSN: 1550-235X. DOI: 10.1103/physrevb.71.085416.

[61] P. B. Johnson and R.-W. Christy. "Optical constants of the noble metals." In: *Physical Review B* 6.12 (1972), p. 4370.

[62] J.J. Quinn. "Bulk and surface plasmons in solids." In: *Nuclear Instruments and Methods in Physics Research Section B: Beam Interactions with Materials and Atoms* 96.3–4 (May 1995), pp. 460–464. ISSN: 0168-583X. DOI: 10.1016/0168-583x(95)00246-4.

[63] J. M. Pitarke et al. "Theory of surface plasmons and surface-plasmon polaritons." In: *Reports on Progress in Physics* 70.1 (Dec. 2006), pp. 1–87. DOI: 10.1088/0034-4885/70/1/r01.

[64] F. Crameri. *Scientific colour maps*. en. 2021. DOI: 10.5281/ZENODO.1243862.

[65] F. Crameri, G. E. Shephard, and P. J. Heron. "The misuse of colour in science communication." In: *Nature Communications* 11.1 (2020). DOI: 10.1038/s41467-020-19160-7.

[66] L. Novotny and N. Van Hulst. "Antennas for light." In: *Nature Photonics* 5.2 (2011), p. 83.

[67] L. Novotny. "Optical antennas tuned to pitch." In: *Nature* 455.7215 (Oct. 2008), pp. 887–887. ISSN: 1476-4687. DOI: 10.1038/455887a.

[68] P. Bharadwaj, B. Deutsch, and L. Novotny. "Optical Antennas." In: *Advances in Optics and Photonics* 1.3 (Aug. 2009), p. 438. ISSN: 1943-8206. DOI: 10.1364/aop.1.000438.

[69] A. G. Curto et al. "Unidirectional Emission of a Quantum Dot Coupled to a Nanoantenna." In: *Science* 329.5994 (2010), pp. 930–933. DOI: 10.1126/science.1191922.

[70] I. S. Maksymov et al. "Optical Yagi-Uda nanoantennas." In: *Nanophotonics* 1.1 (June 2012), pp. 65–81. ISSN: 2192-8606. DOI: 10.1515/nanoph-2012-0005.

[71] G. Blanquer et al. "Waveguide efficient directional coupling and decoupling via an integrated plasmonic nanoantenna." In: *Optics Express* 29.18 (Aug. 2021), p. 29034. ISSN: 1094-4087. DOI: 10.1364/oe.432637.

[72] D. Vercruysse et al. "Single Asymmetric Plasmonic Antenna as a Directional Coupler to a Dielectric Waveguide." In: *ACS Photonics* 4.6 (May 2017), pp. 1398–1402. ISSN: 2330-4022. DOI: 10.1021/acsphotonics.7b00038.

[73] J. Kim et al. "Directional radiation of Babinet-inverted optical nanoantenna integrated with plasmonic waveguide." In: *Scientific Reports* 5.1 (July 2015). ISSN: 2045-2322. DOI: 10.1038/srep11832.

[74] J. Kim et al. "Recent Progress of Quantum Dot-Based Photonic Devices and Systems: A Comprehensive Review of Materials, Devices, and Applications." In: *Small Structures* 2.3 (Dec. 2020). ISSN: 2688-4062. DOI: 10.1002/sstr.202000024.

[75] M. G. Bawendi, M. L. Steigerwald, and L. E. Brus. "The quantum mechanics of larger semiconductor clusters ("quantum dots")." In: *Annual Review of Physical Chemistry, Vol 61* 41.1 (1990), pp. 477–496.

[76] F. Koberling et al. "Fluorescence Anisotropy and Crystal Structure of Individual Semiconductor Nanocrystals." In: *The Journal of Physical Chemistry B* 107.30 (2003), pp. 7463–7471. DOI: 10.1021/jp027800b.

[77] A. I. Chizhik et al. "Excitation Isotropy of Single CdSe/ZnS Nanocrystals." In: *Nano Letters* 11.3 (2011), pp. 1131–1135. DOI: 10.1021/nl1040385.

[78] B. G. Jeong et al. "Colloidal Spherical Quantum Wells with Near-Unity Photoluminescence Quantum Yield and Suppressed Blinking." In: *ACS Nano* 10.10 (Oct. 2016), pp. 9297–9305. ISSN: 1936-086X. DOI: 10.1021/acsnano.6b03704.

[79] O. Chen et al. "Compact high-quality CdSe–CdS core–shell nanocrystals with narrow emission linewidths and suppressed blinking." In: *Nature Materials* 12.5 (2013), pp. 445–451. DOI: 10.1038/nmat3539.

[80] A. M. Dennis et al. "Suppressed Blinking and Auger Recombination in Near-Infrared Type-II InP/CdS Nanocrystal Quantum Dots." In: *Nano Letters* 12.11 (Oct. 2012), pp. 5545–5551. ISSN: 1530-6992. DOI: 10.1021/nl302453x.

[81] Y. Chen et al. "Giant Multishell CdSe Nanocrystal Quantum Dots with Suppressed Blinking." In: *Journal of the American Chemical Society* 130.15 (Mar. 2008), pp. 5026–5027. ISSN: 1520-5126. DOI: 10.1021/ja711379k.

[82] S. Hohng and T. Ha. "Near-Complete Suppression of Quantum Dot Blinking in Ambient Conditions." In: *Journal of the American Chemical Society* 126.5 (Jan. 2004), pp. 1324–1325. ISSN: 1520-5126. DOI: 10.1021/ja039686w.

[83] A. L. Efros and D. J. Nesbitt. "Origin and control of blinking in quantum dots." In: *Nature Nanotechnology* 11.8 (2016), pp. 661–671. DOI: 10.1038/nnano.2016.140.

[84] G. Yuan et al. "Two Mechanisms Determine Quantum Dot Blinking." In: *ACS Nano* 12.4 (2018), pp. 3397–3405. DOI: 10.1021/acsnano.7b09052.

[85] A. L. Efros. "Almost always bright." In: *Nature Materials* 7.8 (Aug. 2008), pp. 612–613. ISSN: 1476-4660. DOI: 10.1038/nmat2239.

[86] A. Zhang et al. "Blinking Behavior of CdSe/CdS Quantum Dots Controlled by Alkylthiols as Surface Trap Modifiers." In: *The Journal of Physical Chemistry C* 117.46 (Nov. 2013), pp. 24592–24600. ISSN: 1932-7455. DOI: 10.1021/jp408544x.

[87] A. M. Kern, A. J. Meixner, and O. J. F. Martin. "Molecule-Dependent Plasmonic Enhancement of Fluorescence and Raman Scattering near Realistic Nanostructures." In: *ACS Nano* 6.11 (Oct. 2012), pp. 9828–9836. ISSN: 1936-086X. DOI: 10.1021/nn3033612.

[88] A. M. Fox. *Quantum optics: an introduction*. Vol. 15. Oxford University Press, USA, 2006.

[89] A. M. Kern et al. "Enhanced single-molecule spectroscopy in highly confined optical fields: from $\lambda/2$-Fabry–Pérot resonators to plasmonic nano-antennas." In: *Chemical Society Reviews* 43.4 (2014), pp. 1263–1286. DOI: 10.1039/c3cs60357a.

[90] E. M. Purcell. "Proceedings of the American Physical Society." In: *Physical Review* 69.11–12 (June 1946), pp. 674–674. ISSN: 0031-899X. DOI: 10.1103/physrev.69.674.

[91] R. X. Bian et al. "Single Molecule Emission Characteristics in Near-Field Microscopy." In: *Physical Review Letters* 75.26 (Dec. 1995), pp. 4772–4775. ISSN: 1079-7114. DOI: 10.1103/physrevlett.75.4772.

[92] N. Livneh et al. "Efficient Collection of Light from Colloidal Quantum Dots with a Hybrid Metal–Dielectric Nanoantenna." In: *ACS Photonics* 2.12 (Dec. 2015), pp. 1669–1674. ISSN: 2330-4022. DOI: 10.1021/acsphotonics.5b00433.

[93] M. G. Harats, N. Livneh, and R. Rapaport. "Design, fabrication and characterization of a hybrid metal-dielectric nanoantenna with a single nanocrystal for directional single photon emission." In: *Optical Materials Express* 7.3 (Feb. 2017), p. 834. ISSN: 2159-3930. DOI: 10.1364/ome.7.000834.

[94] M. Davanço et al. "A circular dielectric grating for vertical extraction of single quantum dot emission." In: *Applied Physics Letters* 99.4 (July 2011). ISSN: 1077-3118. DOI: 10.1063/1.3615051.

[95] J.-M. Liu. *Photonic Devices*. Cambridge University Press, Apr. 2005. ISBN: 9780511614255. DOI: 10.1017/cbo9780511614255.

[96] X. Chen et al. "Scalable and highly efficient approach for an on-chip single-photon source." In: *Photonics Research* 10.9 (Aug. 2022), p. 2066. ISSN: 2327-9125. DOI: 10.1364/prj.462318.

[97] J. Hu et al. "Linearly Polarized Emission from Colloidal Semiconductor Quantum Rods." In: *Science* 292.5524 (June 2001), pp. 2060–2063. ISSN: 1095-9203. DOI: 10.1126/science.1060810.

[98] M. Ren et al. "Linearly Polarized Light Emission from Quantum Dots with Plasmonic Nanoantenna Arrays." In: *Nano Letters* 15.5 (Apr. 2015), pp. 2951–2957. ISSN: 1530-6992. DOI: 10.1021/nl5047973.

[99] T. Zuo et al. "Rotation of Single-Molecule Emission Polarization by Plasmonic Nanorods." In: *The Journal of Physical Chemistry Letters* 10.17 (2019), pp. 5047–5054. DOI: 10.1021/acs.jpclett.9b02270.

[100] T. Ming et al. "Experimental Evidence of Plasmophores: Plasmon-Directed Polarized Emission from Gold Nanorod–Fluorophore Hybrid Nanostructures." In: *Nano Letters* 11.6 (May 2011), pp. 2296–2303. ISSN: 1530-6992. DOI: 10.1021/nl200535y.

[101] D. Jameson and J. Croney. "Fluorescence Polarization: Past, Present and Future." In: *Combinatorial Chemistry & High Throughput Screening* 6.3 (May 2003), pp. 167–176. ISSN: 1386-2073. DOI: 10.2174/138620703106298347.

[102] H. Ni et al. "Tunable polarization control with self-assembled arrays of anisotropic plasmonic coaxial nanocavities." In: *Optics Express* 32.10 (Apr. 2024), p. 16901. ISSN: 1094-4087. DOI: 10.1364/oe.519827.

[103] X. Yin et al. "Active Chiral Plasmonics." In: *Nano Letters* 15.7 (June 2015), pp. 4255–4260. ISSN: 1530-6992. DOI: 10.1021/nl5042325.

[104] J. Xu et al. "Manipulating optical polarization by stereo plasmonic structure." In: *Optics Express* 19.2 (Jan. 2011), p. 748. ISSN: 1094-4087. DOI: 10.1364/oe.19.000748.

[105] A. H. Dorrah et al. "Metasurface optics for on-demand polarization transformations along the optical path." In: *Nature Photonics* 15.4 (Jan. 2021), pp. 287–296. ISSN: 1749-4893. DOI: 10.1038/s41566-020-00750-2.

[106] B. Schaefer et al. "Measuring the Stokes polarization parameters." In: *American Journal of Physics* 75.2 (Feb. 2007), pp. 163–168. ISSN: 1943-2909. DOI: 10.1119/1.2386162.

[107] A. Mildner et al. "Decoding Polarization in a Single Achiral Gold Nanostructure from Emitted Far-Field Radiation." In: *ACS Nano* 17.24 (Dec. 2023), pp. 25656–25666. ISSN: 1936-086X. DOI: 10.1021/acsnano.3c10398.

[108] G. Gilat. "Chiral coefficient-a measure of the amount of structural chirality." In: *Journal of Physics A: Mathematical and General* 22.13 (1989), p. L545.

[109] X. Lu et al. "Circular dichroism from single plasmonic nanostructures with extrinsic chirality." In: *Nanoscale* 6.23 (Oct. 2014), pp. 14244–14253. ISSN: 2040-3372. DOI: 10.1039/c4nr04433a.

[110] T. Oshikiri et al. "Extrinsic Chirality by Interference between Two Plasmonic Modes on an Achiral Rectangular Nanostructure." In: *ACS Nano* 15.10 (Sept. 2021), pp. 16802–16810. ISSN: 1936-086X. DOI: 10.1021/acsnano.1c07137.

[111] W. C. Johnson Jr. "Secondary structure of proteins through circular dichroism spectroscopy." In: *Annual Review of Biophysics and Biophysical Chemistry* 17.1 (1988), pp. 145–166.

[112] M. Schäferling et al. "Tailoring Enhanced Optical Chirality: Design Principles for Chiral Plasmonic Nanostructures." In: *Physical Review X* 2.3 (2012), p. 031010. DOI: 10.1103/physrevx.2.031010.

[113] D. M. Lipkin. "Existence of a New Conservation Law in Electromagnetic Theory." In: *Journal of Mathematical Physics* 5.5 (May 1964), pp. 696–700. ISSN: 1089-7658. DOI: 10.1063/1.1704165.

[114] Y. Tang and A. E. Cohen. "Optical chirality and its interaction with matter." In: *Physical Review Letters* 104.16 (2010), p. 163901.

[115] S. Zhou et al. "Polarization-dispersive imaging spectrometer for scattering circular dichroism spectroscopy of single chiral nanostructures." In: *Light: Science & Applications* 11.1 (Mar. 2022). ISSN: 2047-7538. DOI: 10.1038/s41377-022-00755-2.

[116] M. Fleischer et al. "Three-dimensional optical antennas: Nanocones in an apertureless scanning near-field microscope." In: *Applied Physics Letters* 93.11 (2008), p. 111114.

[117] M. Fleischer et al. "Fabrication of metallic nanocones by induced deposition of etch masks and ion milling." In: *Microelectronic Engineering* 88.8 (2011), pp. 2247–2250. DOI: 10.1016/j.mee.2011.02.090.

[118] M. Fleischer et al. "Tailoring gold nanostructures for near-field optical applications." In: *Nanotechnology* 21.6 (2010), p. 065301. DOI: 10.1088/0957-4484/21/6/065301.

[119] M. Fleischer et al. "Nanocones on transparent substrates for investigations in scanning probe microscopes." In: *Microelectronic Engineering* 86.4-6 (2009), pp. 1219–1221. DOI: 10.1016/j.mee.2008.11.091.

[120] M. Fleischer et al. "Gold nanocone near-field scanning optical microscopy probes." In: *ACS Nano* 5.4 (2011), pp. 2570–2579.

[121] J. Fulmes et al. "Self-aligned placement and detection of quantum dots on the tips of individual conical plasmonic nanostructures." In: *Nanoscale* 7.35 (2015), pp. 14691–14696.

[122] L. Lüder. "Kopplungseffekte in Hybridsystemen aus plasmonischen Gold-Nanokegeln und Quantenpunkten als Einzelphotonenquelle." MA thesis. Universität Tübingen, 2017.

[123] A. J. Meixner et al. "Coupling single quantum dots to plasmonic nanocones: optical properties." In: *Faraday Discussions* 184 (2015), pp. 321–337. DOI: 10.1039/c5fd00074b.

[124] M. G. Harats et al. "Full Spectral and Angular Characterization of Highly Directional Emission from Nanocrystal Quantum Dots Positioned on Circular Plasmonic Lenses." In: *Nano Letters* 14.10 (2014), pp. 5766–5771. DOI: 10.1021/nl502652k.

[125] H. Abudayyeh and R. Rapaport. "Quantum emitters coupled to circular nanoantennas for high-brightness quantum light sources." In: *Quantum Science and Technology* 2.3 (2017), p. 034004. DOI: 10.1088/2058-9565/aa73e4.

[126] H. Abudayyeh et al. "Single photon sources with near unity collection efficiencies by deterministic placement of quantum dots in nanoantennas." In: *APL Photonics* 6.3 (2021).

[127] P. Nagpal et al. "Ultrasmooth Patterned Metals for Plasmonics and Metamaterials." In: *Science* 325.5940 (2009), pp. 594–597. DOI: 10.1126/science.1174655.

[128] Y. Ghosh et al. "New Insights into the Complexities of Shell Growth and the Strong Influence of Particle Volume in Nonblinking "Giant" Core/Shell Nanocrystal Quantum Dots." In: *Journal of the American Chemical Society* 134.23 (May 2012), pp. 9634–9643. ISSN: 1520-5126. DOI: 10.1021/ja212032q.

[129] N. J. Orfield et al. "Photophysics of Thermally-Assisted Photobleaching in "Giant" Quantum Dots Revealed in Single Nanocrystals." In: *ACS Nano* 12.5 (Apr. 2018), pp. 4206–4217. ISSN: 1936-086X. DOI: 10.1021/acsnano.7b07450.

[130] H. Aouani et al. "Crucial role of the adhesion layer on the plasmonic fluorescence enhancement." In: *ACS Nano* 3.7 (2009), pp. 2043–2048.

[131] U. Hohenester. "Diffraction Limit and Beyond." In: *Graduate Texts in Physics*. Springer International Publishing, 2019, pp. 115–137. DOI: 10.1007/978-3-030-30504-8_6.

[132] J.-X. Cheng, A. Volkmer, and S. Xie. "Theoretical and experimental characterization of coherent anti-Stokes Raman scattering microscopy." In: *JOSA B* 19.6 (2002), pp. 1363–1375.

[133] Y.-Y. Cai et al. "Anti-Stokes Emission from Hot Carriers in Gold Nanorods." In: *Nano Letters* 19.2 (2019), pp. 1067–1073. DOI: 10.1021/acs.nanolett.8b04359.

[134] S. Jäger. "Symmetry matching excitation of rotational symmetric plasmonic nanostructures." PhD thesis. University of Tübingen, 2013.

[135] K. S. Youngworth and T. G. Brown. "Focusing of high numerical aperture cylindrical-vector beams." In: *Optics Express* 7.2 (2000), p. 77. DOI: 10.1364/oe.7.000077.

[136] K. Scherzinger. "Untersuchung der Kopplung von CdSe/ZnS Quantenpunkten mit plasmonischen Goldnanokegeln mittels Konfokalmikroskopie und Spektroskopie." MA thesis. University of Tübingen, 2015.

[137] U. Hohenester and A. Trügler. "MNPBEM – A Matlab toolbox for the simulation of plasmonic nanoparticles." In: *Computer Physics Communications* 183.2 (2012), pp. 370–381. DOI: 10.1016/j.cpc.2011.09.009.

[138] U. Hohenester. "Simulating electron energy loss spectroscopy with the MNPBEM toolbox." In: *Computer Physics Communications* 185.3 (2014), pp. 1177–1187. DOI: 10.1016/j.cpc.2013.12.010.

[139] J. Waxenegger, A. Trügler, and U. Hohenester. "Plasmonics simulations with the MNPBEM toolbox: Consideration of substrates and layer structures." In: *Computer Physics Communications* 193 (2015), pp. 138–150. DOI: 10.1016/j.cpc.2015.03.023.

[140] F. J. García de Abajo and A. Howie. "Retarded field calculation of electron energy loss in inhomogeneous dielectrics." In: *Physical Review B* 65.11 (2002). DOI: 10.1103/physrevb.65.115418.

[141] F. J. García de Abajo. "Optical excitations in electron microscopy." In: *Reviews of Modern Physics* 82.1 (2010), pp. 209–275. DOI: 10.1103/revmodphys.82.209.

[142] D. R. Lytle et al. "Generalized optical theorem for reflection, transmission, and extinction of power for electromagnetic fields." In: *Physical Review E* 71.5 (2005), p. 056610. DOI: 10.1103/physreve.71.056610.

[143] N. Dahan and J.-J. Greffet. "Enhanced scattering and absorption due to the presence of a particle close to an interface." In: *Optics Express* 20.104 (2012), A530–A544.

[144] S. A. Maier and H. A. Atwater. "Plasmonics: Localization and guiding of electromagnetic energy in metal/dielectric structures." In: *Journal of Applied Physics* 98.1 (2005), p. 011101. DOI: 10.1063/1.1951057.

[145] K. A. Willets and R. P. Van Duyne. "Localized Surface Plasmon Resonance Spectroscopy and Sensing." In: *Annual Review of Physical Chemistry* 58.1 (2007), pp. 267–297. DOI: 10.1146/annurev.physchem.58.032806.104607.

[146] B. Hecht et al. "Scanning near-field optical microscopy with aperture probes: Fundamentals and applications." In: *The Journal of Chemical Physics* 112.18 (2000), pp. 7761–7774. DOI: 10.1063/1.481382.

[147] C. Zong et al. "Plasmon-enhanced stimulated Raman scattering microscopy with single-molecule detection sensitivity." In: *Nature Communications* 10.1 (2019). DOI: 10.1038/s41467-019-13230-1.

[148] R.-M. Ma and S.-Y. Wang. "Plasmonic nanolasers: fundamental properties and applications." In: *Nanophotonics* 10.14 (2021), pp. 3623–3633. DOI: 10.1515/nanoph-2021-0298.

[149] P. Lodahl and S. Stobbe. "Solid-state quantum optics with quantum dots in photonic nanostructures." In: *Nanophotonics* 2.1 (2013), pp. 39–55. DOI: 10.1515/nanoph-2012-0039.

[150] A. Kinkhabwala et al. "Large single-molecule fluorescence enhancements produced by a bowtie nanoantenna." In: *Nature Photonics* 3.11 (2009), pp. 654–657. DOI: 10.1038/nphoton.2009.187.

[151] F. Tam et al. "Plasmonic enhancement of molecular fluorescence." In: *Nano Letters* 7.2 (2007), pp. 496–501.

[152] B. Ji et al. "Non-blinking quantum dot with a plasmonic nanoshell resonator." In: *Nature Nanotechnology* 10.2 (2015), pp. 170–175. DOI: 10.1038/nnano.2014.298.

[153] G. P. Acuna et al. "Fluorescence Enhancement at Docking Sites of DNA-Directed Self-Assembled Nanoantennas." In: *Science* 338.6106 (2012), pp. 506–510. DOI: 10.1126/science.1228638.

[154] K. Matsuzaki et al. "Strong plasmonic enhancement of biexciton emission: controlled coupling of a single quantum dot to a gold nanocone antenna." In: *Scientific Reports* 7 (2017), p. 11. DOI: 10.1038/srep42307.

[155] J. M. Sanz et al. "Metals for UV Plasmonics." In: *Research in Optical Sciences*. OSA, 2014. DOI: 10.1364/opm.2014.ow4d.3.

[156] Y. Zhong et al. "Review of mid-infrared plasmonic materials." In: *Journal of Nanophotonics* 9.1 (2015), p. 093791. DOI: 10.1117/1.jnp.9.093791.

[157] C. Schäfer et al. "A single particle plasmon resonance study of 3D conical nanoantennas." In: *Nanoscale* 5.17 (2013), pp. 7861–7866.

[158] P. Anger, P. Bharadwaj, and L. Novotny. "Enhancement and Quenching of Single-Molecule Fluorescence." In: *Physical Review Letters* 96.11 (2006), p. 113002. DOI: 10.1103/physrevlett.96.113002.

[159] R. R. Chance, A. Prock, and R.J.A.C.P. Silbey. "Molecular fluorescence and energy transfer near interfaces." In: *Advances in Chemical Physics* 37 (1978), pp. 1–65.

[160] A. Issac, C. von Borczyskowski, and F. Cichos. "Correlation between photoluminescence intermittency of CdSe quantum dots and self-trapped states in dielectric media." In: *Physical Review B* 71.16 (Apr. 2005), p. 161302. ISSN: 1550-235X. DOI: 10.1103/physrevb.71.161302.

[161] D. Valerini et al. "Temperature dependence of the photoluminescence properties of colloidal CdSe/ZnS core/shell quantum dots embedded in a polystyrene matrix." In: *Physical Review B* 71.23 (June 2005), p. 235409. ISSN: 1550-235X. DOI: 10.1103/physrevb.71.235409.

[162] V. Pilla et al. "Fluorescence quantum efficiency of CdSe/ZnS quantum dots embedded in biofluids: pH dependence." In: *Journal of Applied Physics* 112.10 (Nov. 2012). ISSN: 1089-7550. DOI: 10.1063/1.4767470.

[163] E. Zanazzi et al. "Photoluminescence enhancement of colloidal CdSe/ZnS quantum dots embedded in polyvinyl alcohol after 2MeV proton irradiation: crucial role of the embedding medium." In: *Optical Materials* 88 (Feb. 2019), pp. 271–276. ISSN: 0925-3467. DOI: 10.1016/j.optmat.2018.11.047.

[164] A. Issac et al. "Influence of the Dielectric Environment on the Photoluminescence Intermittency of CdSe Quantum Dots." In: *ChemPhysChem* 13.13 (June 2012), pp. 3223–3230. ISSN: 1439-7641. DOI: 10.1002/cphc.201101040.

[165] D. P. Shepherd et al. "Fluorescence Intermittency and Energy Transfer in Small Clusters of Semiconductor Quantum Dots." In: *The Journal of Physical Chemistry C* 114.35 (Aug. 2010), pp. 14831–14837. ISSN: 1932-7455. DOI: 10.1021/jp105150x.

[166] M. Yu and A. Van Orden. "Enhanced Fluorescence Intermittency of CdSe-ZnS Quantum-Dot Clusters." In: *Physical Review Letters* 97.23 (Dec. 2006), p. 237402. ISSN: 1079-7114. DOI: 10.1103/physrevlett.97.237402.

[167] R. Schmidt et al. "The Fluorescence Intermittency for Quantum Dots Is Not Power-Law Distributed: A Luminescence Intensity Resolved Approach." In: *ACS Nano* 8.4 (2014), pp. 3506–3521. DOI: 10.1021/nn406562a.

[168] N. Amecke and F. Cichos. "Intermediate intensity levels during the emission intermittency of single CdSe/ZnS quantum dots." In: *Journal of Luminescence* 131.3 (Mar. 2011), pp. 375–378. ISSN: 0022-2313. DOI: 10.1016/j.jlumin.2010.10.026.

[169] G. Schlegel et al. "Fluorescence Decay Time of Single Semiconductor Nanocrystals." In: *Physical Review Letters* 88.13 (2002), p. 137401. DOI: 10.1103/physrevlett.88.137401.

[170] J. M. Pietryga et al. "Spectroscopic and Device Aspects of Nanocrystal Quantum Dots." In: *Chemical Reviews* 116.18 (2016), pp. 10513–10622. DOI: 10.1021/acs.chemrev.6b00169.

[171] Y. Sun and J. Zhao. "Unconventional Blinking Characteristics of Single Quantum Dots Revealed by Timing Analyses." In: *The Journal of Physical Chemistry C* 125.2 (2020), pp. 1171–1179. DOI: 10.1021/acs.jpcc.0c09721.

[172] D. E. Gómez et al. "Exciton-Trion Transitions in Single CdSe–CdS Core–Shell Nanocrystals." In: *ACS Nano* 3.8 (2009), pp. 2281–2287. DOI: 10.1021/nn900296q.

[173] A. Issac, S. Jin, and T. Lian. "Intermittent Electron Transfer Activity From Single CdSe/ZnS Quantum Dots." In: *Journal of the American Chemical Society* 130.34 (2008), pp. 11280–11281. DOI: 10.1021/ja8043085.

[174] L. Zhu et al. "Spontaneous decay of CdSe/ZnS core-shell quantum dots at the air-dielectric interface." In: *Optics Express* 20.3 (2012), p. 3144. DOI: 10.1364/oe.20.003144.

[175] W. G. J. H. M. van Sark et al. "Blueing, Bleaching, and Blinking of Single CdSe/ZnS Quantum Dots." In: *ChemPhysChem* 3.10 (2002), pp. 871–879. DOI: 10.1002/1439-7641(20021018)3:10<871::aid-cphc871>3.0.co;2-t.

[176] Y. Zhai et al. "Experimental investigation of energy transfer between CdSe/ZnS quantum dots and different-sized gold nanoparticles." In: *Physica E: Low-dimensional Systems and Nanostructures* 88 (2017), pp. 109–114. DOI: 10.1016/j.physe.2016.12.007.

[177] D. Ratchford et al. "Manipulating Coupling between a Single Semiconductor Quantum Dot and Single Gold Nanoparticle." In: *Nano Letters* 11.3 (2011), pp. 1049–1054. DOI: 10.1021/nl103906f.

[178] K. T. Shimizu et al. "Surface-Enhanced Emission from Single Semiconductor Nanocrystals." In: *Physical Review Letters* 89.11 (2002), p. 117401. DOI: 10.1103/physrevlett.89.117401.

[179] D. Tian et al. "A Review on Quantum Dot Light-Emitting Diodes: From Materials to Applications." In: *Advanced Optical Materials* 11.2 (2022). DOI: 10.1002/adom.202201965.

[180] S. Asahi et al. "Two-step photon up-conversion solar cells." In: *Nature Communications* 8.1 (2017). DOI: 10.1038/ncomms14962.

[181] J. Liu et al. "Organic and quantum dot hybrid photodetectors: towards full-band and fast detection." In: *Chemical Communications* 59.3 (2023), pp. 260–269. DOI: 10.1039/d2cc05281d.

[182] A. Yadav et al. "Edge emitting mode-locked quantum dot lasers." In: *Progress in Quantum Electronics* 87 (2023), p. 100451. DOI: 10.1016/j.pquantelec.2022.100451.

[183] A. Alfieri et al. "Nanomaterials for Quantum Information Science and Engineering." In: *Advanced Materials* 35.27 (2022). DOI: 10.1002/adma.202109621.

[184] M. B. Gaither-Ganim et al. "Organic molecule single-photon sources." In: *Oxford Open Materials Science* 3.1 (2022). DOI: 10.1093/oxfmat/itac017.

[185] S. Gupta et al. "Single-Photon Emission from Two-Dimensional Materials, to a Brighter Future." In: *The Journal of Physical Chemistry Letters* 14.13 (2023), pp. 3274–3284. DOI: 10.1021/acs.jpclett.2c03674.

[186] T. M. Babinec et al. "A diamond nanowire single-photon source." In: *Nature Nanotechnology* 5.3 (2010), pp. 195–199. DOI: 10.1038/nnano.2010.6.

[187] A. Högele et al. "Photon Antibunching in the Photoluminescence Spectra of a Single Carbon Nanotube." In: *Physical Review Letters* 100.21 (2008), p. 217401. DOI: 10.1103/physrevlett.100.217401.

[188] T. Gao et al. "Atomically-thin single-photon sources for quantum communication." In: *npj 2D Materials and Applications* 7.1 (2023). DOI: 10.1038/s41699-023-00366-4.

[189] G. Murtaza et al. "Efficient room-temperature molecular single-photon sources for quantum key distribution." In: *Optics Express* 31.6 (2023), p. 9437. DOI: 10.1364/oe.476440.

[190] J. Claudon et al. "A highly efficient single-photon source based on a quantum dot in a photonic nanowire." In: *Nature Photonics* 4.3 (2010), pp. 174–177. DOI: 10.1038/nphoton.2009.287x.

[191] J. Jurkat et al. "Single-Photon Source in a Topological Cavity." In: *Nano Letters* 23.3 (2023), pp. 820–826. DOI: 10.1021/acs.nanolett.2c03693.

[192] T. Strobel et al. "A Unipolar Quantum Dot Diode Structure for Advanced Quantum Light Sources." In: *Nano Letters* 23.14 (2023), pp. 6574–6580. DOI: 10.1021/acs.nanolett.3c01658.

[193] M. De Gregorio et al. "Plug-and-Play Fiber-Coupled Quantum Dot Single-Photon Source via Photonic Wire Bonding." In: *Advanced Quantum Technologies* (2023). DOI: 10.1002/qute.202300227.

[194] S. D. Choudhury, R. Badugu, and J. R. Lakowicz. "Directing Fluorescence with Plasmonic and Photonic Structures." In: *Accounts of Chemical Research* 48.8 (2015), pp. 2171–2180. DOI: 10.1021/acs.accounts.5b00100.

[195] N. Livneh et al. "Highly Directional Room-Temperature Single Photon Device." In: *Nano Letters* 16.4 (2016), pp. 2527–2532. DOI: 10.1021/acs.nanolett.6b00082.

[196] H. Abudayyeh et al. "Purification of Single Photons by Temporal Heralding of Quantum Dot Sources." In: *ACS Photonics* 6.2 (Jan. 2019), pp. 446–452. ISSN: 2330-4022. DOI: 10.1021/acsphotonics.8b01396.

[197] M. Bauch et al. "Plasmon-Enhanced Fluorescence Biosensors: a Review." In: *Plasmonics* 9.4 (Dec. 2013), pp. 781–799. ISSN: 1557-1963. DOI: 10.1007/s11468-013-9660-5.

[198] M. Li, S. K. Cushing, and N. Wu. "Plasmon-enhanced optical sensors: a review." In: *Analyst* 140.2 (2015), pp. 386–406.

[199] A. B. Taylor and P. Zijlstra. "Single-Molecule Plasmon Sensing: Current Status and Future Prospects." In: *ACS Sensors* 2.8 (2017), pp. 1103–1122. DOI: 10.1021/acssensors.7b00382.

[200] R. C. Boutelle, D. Neuhauser, and S. Weiss. "Far-Field Superresolution Detection of Plasmonic Near-Fields." In: *ACS Nano* 10.8 (Aug. 2016), pp. 7955–7962. ISSN: 1936-086X. DOI: 10.1021/acsnano.6b03873.

[201] D. W. Pohl, U. Ch. Fischer, and U. T. Dürig. "Scanning near-field optical microscopy (SNOM)." In: *Journal of Microscopy* 152.3 (Dec. 1988), pp. 853–861. ISSN: 1365-2818. DOI: 10.1111/j.1365-2818.1988.tb01458.x.

[202] V. Sandoghdar and J. Mlynek. "Prospects of apertureless SNOM with active probes." In: *Journal of Optics A: Pure and Applied Optics* 1.4 (Jan. 1999), pp. 523–530. ISSN: 1741-3567. DOI: 10.1088/1464-4258/1/4/319.

[203] T. Lacoste et al. "Contrast enhancement using polarization-modulation scanning near-field optical microscopy (PM-SNOM)." In: *Ultramicroscopy* 71.1–4 (Mar. 1998), pp. 333–340. ISSN: 0304-3991. DOI: 10.1016/s0304-3991(97)00093-4.

[204] V. J. Rao et al. "AFM-IR and IR-SNOM for the Characterization of Small Molecule Organic Semiconductors." In: *The Journal of Physical Chemistry C* 124.9 (Feb. 2020), pp. 5331–5344. ISSN: 1932-7455. DOI: 10.1021/acs.jpcc.9b11056.

[205] P. Leiderer et al. "Imaging optical near-fields of nanostructures." In: *Applied Physics Letters* 85.22 (Nov. 2004), pp. 5370–5372. ISSN: 1077-3118. DOI: 10.1063/1.1819990.

[206] C. Hubert et al. "Near-Field Photochemical Imaging of Noble Metal Nanostructures." In: *Nano Letters* 5.4 (Mar. 2005), pp. 615–619. ISSN: 1530-6992. DOI: 10.1021/nl047956i.

[207] C. Hubert et al. "Near-Field Polarization Effects in Molecular-Motion-Induced Photochemical Imaging." In: *The Journal of Physical Chemistry C* 112.11 (Feb. 2008), pp. 4111–4116. ISSN: 1932-7455. DOI: 10.1021/jp7096263.

[208] C. Deeb et al. "Size Dependence of the Plasmonic Near-Field Measured via Single-Nanoparticle Photoimaging." In: *The Journal of Physical Chemistry C* 117.20 (May 2013), pp. 10669–10676. ISSN: 1932-7455. DOI: 10.1021/jp4020564.

[209] Y. Kawata et al. "Non-optically probing near-field microscopy." In: *Optics Communications* 161.1–3 (Mar. 1999), pp. 6–12. ISSN: 0030-4018. DOI: 10.1016/s0030-4018(98)00621-x.

[210] M. Cinchetti et al. "Photoemission Electron Microscopy as a Tool for the Investigation of Optical Near Fields." In: *Physical Review Letters* 95.4 (July 2005), p. 047601. ISSN: 1079-7114. DOI: 10.1103/physrevlett.95.047601.

[211] Q. Sun et al. "Direct imaging of the near field and dynamics of surface plasmon resonance on gold nanostructures using photoemission electron microscopy." In: *Light: Science & Applications* 2.12 (Dec. 2013), e118–e118. ISSN: 2047-7538. DOI: 10.1038/lsa.2013.74.

[212] G. Lévêque et al. "Polarization state of the optical near field." In: *Physical Review E* 65.3 (Feb. 2002), p. 036701. ISSN: 1095-3787. DOI: 10.1103/physreve.65.036701.

[213] Y. Tang and A. E. Cohen. "Enhanced Enantioselectivity in Excitation of Chiral Molecules by Superchiral Light." In: *Science* 332.6027 (Apr. 2011), pp. 333–336. ISSN: 1095-9203. DOI: 10.1126/science.1202817.

[214] M. L. Solomon et al. "Enantiospecific Optical Enhancement of Chiral Sensing and Separation with Dielectric Metasurfaces." In: *ACS Photonics* 6.1 (Dec. 2018), pp. 43–49. ISSN: 2330-4022. DOI: 10.1021/acsphotonics.8b01365.

[215] J. García-Guirado et al. "Enantiomer-Selective Molecular Sensing Using Racemic Nanoplasmonic Arrays." In: *Nano Letters* 18.10 (Sept. 2018), pp. 6279–6285. ISSN: 1530-6992. DOI: 10.1021/acs.nanolett.8b02433.

[216] K.-T. Lee et al. "Enantiomer-Selective Molecular Sensing in the Nonlinear Optical Regime via Upconverting Chiral Metamaterials." In: *Advanced Functional Materials* 32.43 (Aug. 2022). ISSN: 1616-3028. DOI: 10.1002/adfm.202208641.

[217] V. K. Valev et al. "Chirality and chiroptical effects in plasmonic nanostructures: fundamentals, recent progress, and outlook." In: *Advanced Materials* 25.18 (2013), pp. 2517–2534.

[218] X. Lan and Q. Wang. "Self-Assembly of Chiral Plasmonic Nanostructures." In: *Advanced Materials* 28.47 (June 2016), pp. 10499–10507. ISSN: 1521-4095. DOI: 10.1002/adma.201600697.

[219] K. W. Smith, S. Link, and W.-S. Chang. "Optical characterization of chiral plasmonic nanostructures." In: *Journal of Photochemistry and Photobiology C: Photochemistry Reviews* 32 (2017), pp. 40–57. DOI: 10.1016/j.jphotochemrev.2017.05.004.

[220] S. Hashiyada, T. Narushima, and H. Okamoto. "Active Control of Chiral Optical near Fields on a Single Metal Nanorod." In: *ACS Photonics* 6.3 (2019), pp. 677–683. DOI: 10.1021/acsphotonics.8b01500.

[221] T. V. Raziman and O. J. F. Martin. "Does the real part contain all the physical information?" In: *Journal of Optics* 18.9 (2016), p. 095002. DOI: 10.1088/2040-8978/18/9/095002.

[222] M. Schäferling, X. Yin, and H. Giessen. "Formation of chiral fields in a symmetric environment." In: *Optics Express* 20.24 (2012), p. 26326. DOI: 10.1364/oe.20.026326.

[223] S. Hashiyada, T. Narushima, and H. Okamoto. "Local Optical Activity in Achiral Two-Dimensional Gold Nanostructures." In: *The Journal of Physical Chemistry C* 118.38 (2014), pp. 22229–22233. DOI: 10.1021/jp507168a.

[224] A. García-Etxarri and J. A. Dionne. "Surface-enhanced circular dichroism spectroscopy mediated by nonchiral nanoantennas." In: *Physical Review B* 87.23 (June 2013), p. 235409. ISSN: 1550-235X. DOI: 10.1103/physrevb.87.235409.

[225] A. Vázquez-Guardado and D. Chanda. "Superchiral Light Generation on Degenerate Achiral Surfaces." In: *Physical Review Letters* 120.13 (Mar. 2018), p. 137601. ISSN: 1079-7114. DOI: 10.1103/physrevlett.120.137601.

[226] S. Zu et al. "Deep-Subwavelength Resolving and Manipulating of Hidden Chirality in Achiral Nanostructures." In: *ACS Nano* 12.4 (Apr. 2018), pp. 3908–3916. ISSN: 1936-086X. DOI: 10.1021/acsnano.8b01380.

[227] T. Aoudjit et al. "Photochemical Imaging of Near-Field and Dissymmetry Factor in Chiral Nanostructures." In: *Advanced Optical Materials* 11.9 (2023). DOI: 10.1002/adom.202203015.

[228] E. D. Chubchev, Y. V. Vladimirova, and V. N. Zadkov. "Controlling near-field polarization distribution of a plasmonic prolate nanospheroid by its aspect ratio and polarization of the incident electromagnetic field." In: *Optics Express* 22.17 (Aug. 2014), p. 20432. ISSN: 1094-4087. DOI: 10.1364/oe.22.020432.

[229] P. C. Simo et al. "Dipole Determination by Polarimetric Spectroscopy Yielding the Orientation of Gold Nanorods." In: *Submitted* (2024).

[230] X. Wang and Z. Tang. "Circular Dichroism Studies on Plasmonic Nanostructures." In: *Small* 13.1 (June 2016), p. 1601115. ISSN: 1613-6810. DOI: 10.1002/smll.201601115.

[231] M. A. van Dijk et al. "Absorption and scattering microscopy of single metal nanoparticles." In: *Physical Chemistry Chemical Physics* 8.30 (2006), p. 3486. ISSN: 1463-9076, 1463-9084. DOI: 10.1039/b606090k. (Visited on 10/25/2016).

[232] L.-Y. Wang et al. "Circular Differential Scattering of Single Chiral Self-Assembled Gold Nanorod Dimers." In: *ACS Photonics* 2.11 (Nov. 2015), pp. 1602–1610. ISSN: 2330-4022. DOI: 10.1021/acsphotonics.5b00395.